AFRL-RY-HS-TR-2010-0001

PROCEEDINGS OF THE 2009 ANTENNA APPLICATIONS SYMPOSIUM, VOLUME I

Dr. Daniel Schaubert
University of Massachusetts Amherst
Electrical and Computer Engineering
100 Natural Resources Road
Amherst MA 01003

12 December 2009

Final Report

APPROVED FOR PUBLIC RELEASE – DISTRIBUTION UNLIMITED

AIR FORCE RESEARCH LABORATORY
Sensors Directorate
Electromagnetics Technology Division
80 Scott Drive
Hanscom AFB MA 01731-2909

NOTICE AND SIGNATURE PAGE

Using Government drawings, specifications, or other data included in this document for any purpose other than Government procurement does not in any way obligate the U.S. Government. The fact that the Government formulated or supplied the drawings, specifications, or other data does not license the holder or any other person or corporation; or convey any rights or permission to manufacture, use, or sell any patented invention that may relate to them.

This report was cleared for public release by the 66th Air Base Wing Public Affairs Office for the Air Force Research Laboratory Electromagnetic Technology Division and is available to the general public, including foreign nationals. Copies may be obtained from the Defense Technical Information Center (DTIC) (http://www.dtic.mil).

AFRL-RY-HS-TR-2010-0001 HAS BEEN REVIEWED AND IS APPROVED FOR PUBLICATION IN ACCORDANCE WITH ASSIGNED DISTRIBUTION STATEMENT.

DAVID D. CURTIS
Chief, Antenna Technology Branch

MICHAEL N. ALEXANDER
Technical Advisor
Electromagnetic Technology Division

This report is published in the interest of scientific and technical information exchange, and its publication does not constitute the Government's approval or disapproval of its ideas or findings.

REPORT DOCUMENTATION PAGE

Form Approved
OMB No. 0704-0188

1. REPORT DATE *(DD-MM-YYYY)*	2. REPORT TYPE	3. DATES COVERED *(From - To)*
20-12-2009	FINAL REPORT	22 Sep 2009 – 24 Sep 2009

4. TITLE AND SUBTITLE

Proceedings of the 2009 Antenna Applications Symposium, Volume I

5a. CONTRACT NUMBER
F33615-02-D-1283

5b. GRANT NUMBER

5c. PROGRAM ELEMENT NUMBER

6. AUTHOR(S)

Daniel Schaubert et al.

5d. PROJECT NUMBER
4916

5e. TASK NUMBER
HA

5f. WORK UNIT NUMBER
01

7. PERFORMING ORGANIZATION NAME(S) AND ADDRESS(ES)

University of Massachusetts Amherst
Electrical and Computer Engineering
100 Natural Resources Road
Amherst, MA 01003

8. PERFORMING ORGANIZATION REPORT

9. SPONSORING / MONITORING AGENCY NAME(S) AND ADDRESS(ES)

Electromagnetics Technology Division
Sensors Directorate
Air Force Research Laboratory
80 Scott Drive
Hanscom AFB MA 01731-2909

10. SPONSOR/MONITOR'S ACRONYM(S)
AFRL-RY-HS

11. SPONSOR/MONITOR'S REPORT NUMBER(S)
AFRL-RY-HS-TR-2010-0010

12. DISTRIBUTION / AVAILABILITY STATEMENT

APPROVED FOR PUBLIC RELEASE; DISTRIBUTION UNLIMITED

13. SUPPLEMENTARY NOTES

Volume I contains pages 1 – 257 Public Affairs release Number 66ABW-2010-0005
Volume II contains pages 258-509

14. ABSTRACT

The Proceedings of the 2009 Antenna Applications Symposium is a collection of state-of-the art papers relating to antenna arrays and elements, millimeter wave antennas, simulation and measurement of antennas, integrated antennas, and antenna bandwidth and radiation improvements.

15. SUBJECT TERMS

Antennas, phased arrays, digital beam forming, millimeter waves, metamaterials, antenna measurements, airborne antenna applications, Vivaldi antennas, waveguide antenna arrays, broadband arrays, electrically small antennas

16. SECURITY CLASSIFICATION OF:			17.LIMITATION OF ABSTRACT	18.NUMBER OF PAGES	19a. NAME OF RESPONSIBLE PERSON
a. REPORT	b. ABSTRACT	c. THIS PAGE			David D. Curtis
Unclassified	Unclassified	Unclassified	UU	520	19b. TELEPHONE NUMBER *(include area code)* N/A

Standard Form 298 (Rev. 8-98)
Prescribed by ANSI Std. Z39.18

2009 ANTENNA APPLICATIONS SYMPOSIUM Volume I

22 - 24 September 2009
Monticello, Illinois

Identifiers for Proceedings of Symposia

The USAF Antenna Research and Development Program

Year	Symp. No.	Identifier
1951	First	_____
1952	Second	ADB870006
1953	Third	ADB283180
1954	Fourth	AD63139
1955	Fifth	AD90397
1956	Sixth	AD114702
1957	Seventh	AD138500
1958	Eighth	AD301151
1959	Ninth	AD314721
1960	Tenth	AD244388 (Vol. 1) AD319613 (Vol. 2)
1961	Eleventh	AD669109 (Vol. 1) AD326549 (Vol. 2)
1962	Twelfth	AD287185 (Vol. 1) AD334484 (Vol. 2)
1963	Thirteenth	AD421483
1964	Fourteenth	AD609104
1965	Fifteenth	AD474238L
1966	Sixteenth	AD800524L
1967	Seventeenth	AD822894L
1968	Eighteenth	AD846427L
1969	Nineteenth	AD860812L
1970	Twentieth	AD875973L
1971	Twenty-First	AD888641L
1972	Twenty-Second	AD904360L
1973	Twenty-Third	AD914238L

Antenna Applications Symposium

Year	Symposium	Technical Report #	Identifier
1977	First	None	ADA 955413
1978	Second	None	ADA 955416
1979	Third	_____	ADA 077167
1980	Fourth	_____	ADA 205907
1981	Fifth	_____	ADA 205816
1982	Sixth	_____	ADA 129356
1983	Seventh	_____	ADA 142003; 142754
1984	Eighth	85-14	ADA 153257; 153258
1985	Ninth	85-242	ADA 166754; 165535
1986	Tenth	87-10	ADA 181537; 181536
1987	Eleventh	88-160	ADA 206705; 206704
1988	Twelfth	89-121	ADA 213815; 211396
1989	Thirteenth	90-42	ADA 26022; 226021
1990	Fourteenth	91-156	ADA 37056; 237057
1991	Fifteenth	92-42	ADA 253681; 253682
1992	Sixteenth	93-119	ADA 268167; 266916
1993	Seventeenth	94-20	ADA 277202; 277203
1994	Eighteenth	95-47	ADA 293258; 293259
1995	Nineteenth	96-100	ADA 309715; 309723
1996	Twentieth	97-189	ADA 341737
1997	Twenty First	1998-143	ADA 355120
1998	Twenty Second	1999-86	ADA 364798
1999	Twenty Third	2000-008 (I) (II)	ADA 386476; 386477
2000	Twenty Fourth	2002-001 Vol I & II	ADA 405537; 405538
2001	Twenty Fifth	2002-002 Vol I & II	ADA 405328; 405327
2002	Twenty Sixth	2005-001 Vol I & II	ADA 427799; 427800
2003	Twenty Seventh	2005-005 Vol I & II	ADA 429122
2004	Twenty Eighth	2005-016 Vol I & II	ADA431338; 431339
2005	Twenty Ninth	2005-039 Vol I & II	ADM001873
2006	Thirtieth	2006-0047 Vol I & II	ADA464059
2007	Thirty First	2007-0037 Vol I & II	ADA475327, 475333
2008	Thirty Second	2008-0026 Vol I & II	ADA494632, 494633

2009 Author Index

BANDWIDTH ENHANCEMENT OF A SMALL ANTENNA BY MODAL SUPERPOSITION

Jacob J. Adams and Jennifer T. Bernhard
Electromagnetics Laboratory
University of Illinois at Urbana-Champaign, Urbana, IL 61801
http://antennas.ece.illinois.edu; E-mail: jbernhar@illinois.edu, jjadams@illinois.edu

Abstract: In this study, we demonstrate the use of characteristic mode theory (CMT) in designing a multiresonant electrically small antenna. Several characteristic modes are evaluated for their potential use in a multiresonant structure. A combination of a first order mode and higher order mode are shown to produce a set of resonances and antiresonances that can achieve bandwidth beyond Chu's limit for a single resonance.

Previous work has demonstrated an electrically small spherical antenna which excites the TM_{10} spherical mode. The antenna exhibits low quality factor (Q) relative to the Chu limit. For a singly resonant antenna, bandwidth is inversely proportional to Q, so the TM_{10} antenna achieves a large bandwidth for its size. However, since the Q-bandwidth relationship is only valid for antennas with a single resonance, further bandwidth enhancement can be achieved by making the antenna multiresonant.

1. Fundamental Limitations of Electrically Small Antennas

One of the key parameters for electrically small antennas is the radiation quality factor (Q). The Q of an antenna represents the ratio of the energy stored per cycle to the power radiated and is typically defined as

$$Q_{rad} = \frac{2\omega_0 |W_{\max}|}{P} \tag{1}$$

Radiation Q is critical for a singly resonant antenna, because the antenna's bandwidth is inversely proportional to Q [1]. Thus, a low Q antenna is desirable.

However, the minimum Q has been shown to be constrained by the electrical size of the antenna. In 1948, Chu published his well-known work investigating the fundamental limitations of antennas [2]. He showed that the radiation Q of an antenna has a lower limit determined by the electrical size of a sphere of radius a which circumscribes the antenna [2], [3].

$$Q_{Chu} \approx \frac{1}{ka} + \frac{1}{(ka)^3} \tag{2}$$

An antenna that approaches Chu's limit has been sought for decades. It has been taken as a rule of thumb that an antenna that most fully occupies a spherical volume exhibits the lowest *Q*. Foltz and McLean showed mathematically that the minimum *Q* is achievable with an antenna occupying a spherical volume rather than a dipole or planar structure [4]. In our previous work [5], [6], we described a spherical antenna (TM_{10} antenna) that approaches the stricter limit derived by Thal [7] and is easily matched over a large range of electrical sizes. According to Thal, Chu's limit is optimistic and in a more realistic scenario, the minimum Q that can be achieved is 1.5 times Chu's original limit.

In this paper, we address methods of extending the bandwidth of the TM_{10} antenna beyond that predicted by Chu for a singly resonant antenna by exciting multiple resonant modes. While Chu's limit still applies to the Q of each mode, the inverse relationship between Q and bandwidth no longer holds when resonances are closely spaced [8]. In order to clearly evaluate the individual modes, we will use Characteristic Mode Theory (CMT) to evaluate individual modes for use in the multiresonant antenna.

2. Characteristic Mode Theory

The Theory of Characteristic Modes originated as a result of work by Garbacz and Turpin [9] and was refined soon after by Harrington and Mautz [10], [11]. Characteristic current modes form an orthogonal basis for the current on a metal structure such as an antenna. Thus, they serve as an expansion of the current on the structure. For a more complete review of CMT see the recent article by Cabedo-Fabrés *et al.* [12].

For the n^{th} mode there is an associated eigenvalue (λ_n) and eigenvector (J_n) which are the solution to the generalized eigenvalue problem

$$[\mathrm{X}]J_n = \lambda_n[\mathrm{R}]J_n \tag{3}$$

where [R] and [X] are the real and imaginary parts of the Moment Method impedance matrix, respectively.

This eigenvalue problem is solved at every frequency of interest, yielding a full set of eigenmodes at each frequency. The eigenvectors generate the modal current distribution and the eigenvalues determine how capacitive or inductive the mode is and how well it radiates. The eigenvalues and eigenvectors vary with frequency, but the eigenvectors tend to vary slowly, retaining the same general modal pattern.

To solve the eigenvalue problem, we first used FEKO [13] to model the antenna and generate the impedance matrix. Then a Matlab program was used to solve the eigenvalue

problem, organize solutions, and export the results back to FEKO where current distributions and fields can be plotted.

The total current on the antenna can be represented as a weighted sum of the eigencurrents. Similarly, the input admittance can be expressed as a summation of the admittances of each mode. For the case of a gap voltage source on a wire, the input admittance can be calculated as [14]

$$Y_{in}(\vec{r}_{feed}) = \sum_{n} \frac{J_n(\vec{r}_{feed})^2}{1+\lambda_n{}^2}(1-j\lambda_n) \tag{4}$$

There are two types of characteristic modes: resonant and non-resonant modes. Resonant modes are capacitive at low frequencies, resonate, and become inductive beyond their resonance. Non-resonant modes (inductive modes) begin as inductive modes and never resonate, only ever contributing inductive susceptance to the antenna.

This suggests that resonances ($dX/df > 0$) and antiresonances ($dX/df < 0$) of the entire structure are caused by fundamentally different phenomena. Resonances are caused by the resonance of a single dominant characteristic mode while antiresonances are caused by the interaction of two characteristic modes, one that is capacitive and one that is inductive (either non-resonant or at a frequency above its resonance).

Because resonances are the result of a single characteristic mode, resonant properties depend entirely on the mode itself. Resonant conductance is very high for electrically small antennas due to large currents at the feed, resulting in the small resonant resistance that is often observed. In the electrically small region, reducing this current and controlling the antenna's resonant is difficult. In previous work, we have shown that because antiresonances result from the combination of two modes, they are often easier to control than resonances [15].

3. A TM_{10} Antenna

The TM_{10} antenna fundamentally operates by exciting the TM_{10} spherical mode, which Thal showed to have the lowest possible Q [7]. The TM_{10} mode can be excited by a surface current distribution of the form

$$J_\theta = \sin(\theta) \tag{5}$$

The antenna structure consists of helical wires coiled along the constant-φ lines of a sphere which support the current distribution of Eq. 5 [5], [6]. The sphere is bisected by a ground plane along $\theta = \pi/2$. A conducting trace suspended above the ground plane contacts all of the arms at their base. The trace is fed in the center by a probe from behind the ground plane. Figure 1 shows the structure using four arms.

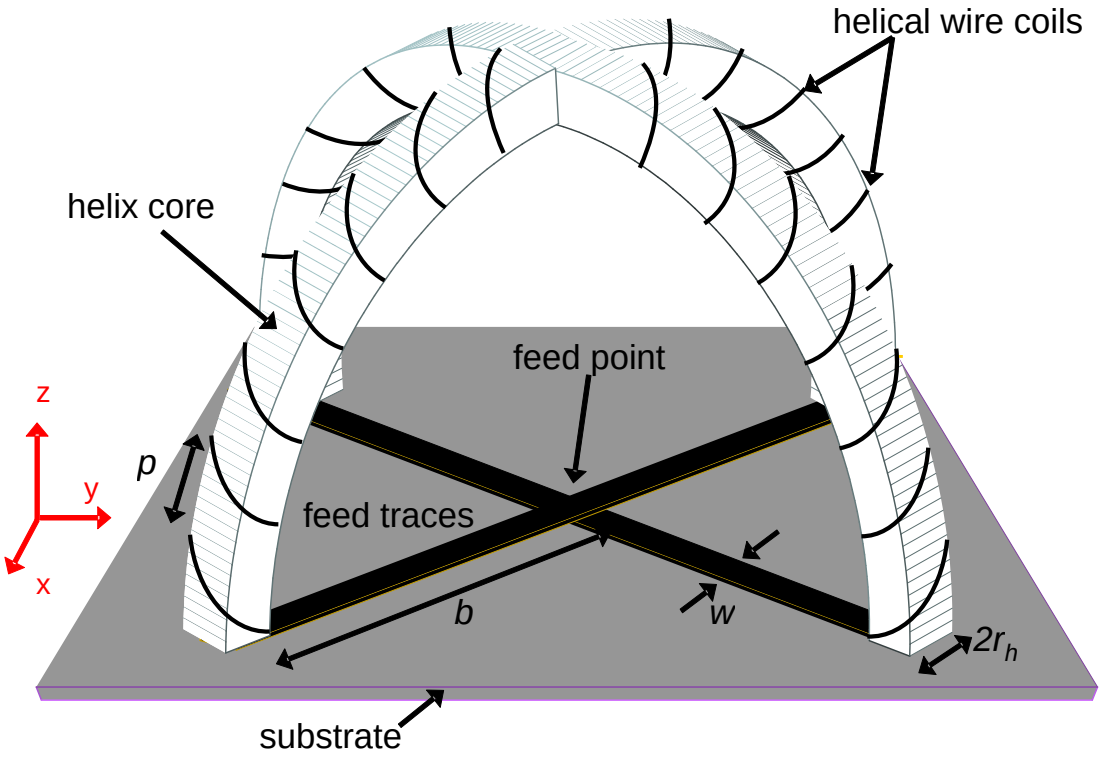

Figure 1: A four arm TM_{10} antenna. The pitch, p, is measured on the outer radius of the arm coils. The arm coils have radius r_h and their centerline follows a circle of radius b from the center of the structure. The width of the trace is w.

4. Characteristic modes of the TM_{10} antenna

Since we are interested in the behavior of the TM_{10} antenna in the electrically small region, the number of significant characteristic modes is small. The superposition of just two modes results in the tunable, low Q antiresonance described in [5], [6].

Both modes are standard resonant characteristic modes as discussed in Section 2 (i.e., they are not special inductive modes). Mode 1 has the smallest eigenvalue over the operating band and provides most of the antenna's radiation. The mode 1 resonance falls at the same frequency as the resonance of the entire structure. As we expect for an electrically small antenna, the resonant resistance of the mode is quite small and the only way to increase it is to increase the size of the antenna. As with all resonant characteristic modes, the mode is capacitive before the resonance and inductive after the resonance.

To tune out the inductive susceptance of mode 1, mode 2 is used to provide capacitive susceptance, causing an antiresonance. Mode 2 has a higher current along the feed trace than in the arms, so its resonant frequency is more strongly influenced by the substrate properties and feed trace width. Mode 1's resonance is moved primarily by changing the wire pitch. By adjusting these parameters, the antenna's antiresonant resistance can be controlled as shown in [15].

5. Multiple resonant behavior of antennas

In order to create multiband behavior, multiple modes are strung together and centered at successive frequencies. The important factors for multiband design become the frequency spacing of the modes and their conductance maxima and minima. The Q of an individual mode no longer has critical importance, although it will affect how far apart in frequency modes can be before VSWR specifications are violated.

Few multiresonant electrically small antennas have been reported. Recently Stuart and Tran designed a multiresonant small antenna with $ka = 0.54$ [16]. The antenna achieved 2:1 VSWR bandwidth approximately equal to the Chu limit with a matching network. Stuart and Best also reported a wideband antenna with $ka = 0.54$ and 1.9 times the impedance bandwidth predicted by Chu's limit. However, it remains unclear whether the radiation pattern is tolerable and whether a matching network has been included with the design [17]. Best has a recent review of "small" multiresonant antennas [18], but these antennas are the border of the electrically small region with *ka* values just less than one and may not be comparable to smaller antennas.

In a multiband antenna, in order for the VSWR to remain below a desired value between a resonance and an antiresonance, the ratio of the resonant conductance to the antiresonant conductance must be less than or equal to the square of the desired VSWR in the best case. For example, if the half-power bandwidth ($VSWR = 5.828$) is to extend from a resonance to the following antiresonance, G_R/G_{AR} must be less than 34.0. This of course assumes that we use a matching network to move the system impedance to the geometric mean of the resonant and antiresonant resistances and match out any reactance.

This observation is easily derived from the equations for VSWR. At a resonant point ($Y_{ant} = G_{ant}$) then the VSWR can be written

$$VSWR = \begin{cases} \dfrac{G_C}{G_{ant}} & G_C > G_{ant} \\ \dfrac{G_{ant}}{G_C} & G_C < G_{ant} \end{cases} \tag{6}$$

We then assume that at a resonance, $G_R > G_C$ and at an antiresonance $G_C > G_{AR}$ since we desire that the antenna's impedance encircle the center of the Smith chart for minimum VSWR over the entire bandwidth. If assume the VSWR is equal $VSWR_{max}$ at both resonances, it can easily be seen that $G_R/G_{AR} = VSWR_{max}^2$.

This resonance-antiresonance conductance ratio (RACR) is useful because it allows us to quickly evaluate an antenna's multiband potential even when the conductance values are not centered about 20 mS (assuming the design targets a 50 Ω feed). If the conductance has a swing greater than the square of the maximum VSWR between resonances and antiresonances, it is clear that it cannot have a VSWR below the desired value at both the resonant and antiresonant frequencies.

6. Low order characteristic modes for multiband behavior

The goal of this study is to create an electrically small antenna with bandwidth beyond that predicted by the Chu limit by matching the antenna at several resonances caused by the interaction of multiple modes. We will focus on antennas with $ka \approx 0.5$ to be certain the antennas we are working with are truly electrically small.

The most obvious way to create an additional mode in the TM_{10} antenna is to offset the pitches of two of the helices so two low order, TM_{10}-like modes appear and resonate at different frequencies. The initial design consists of two arms with pitch p_a and two arms with pitch p_b, where the arms with the same pitch are opposite each other. As anticipated, this approach leads to two characteristic modes with slightly offset resonant frequencies. In the low frequency mode (mode 1a), the current is highest is the arms with the smaller pitch and in the high frequency mode (mode 1b), the current exists in the arms with the larger pitch. Figure 2 has a schematic showing these modes.

However, while both modes are, for the most part, well excited by the feed location, an anomalous drop in the conductance of mode 1a occurs with this configuration. A typical example of this response can be seen in Figure 3. When the conductance drops to nearly zero in the band of interest, the RACR blows up and multiresonant behavior is not possible.

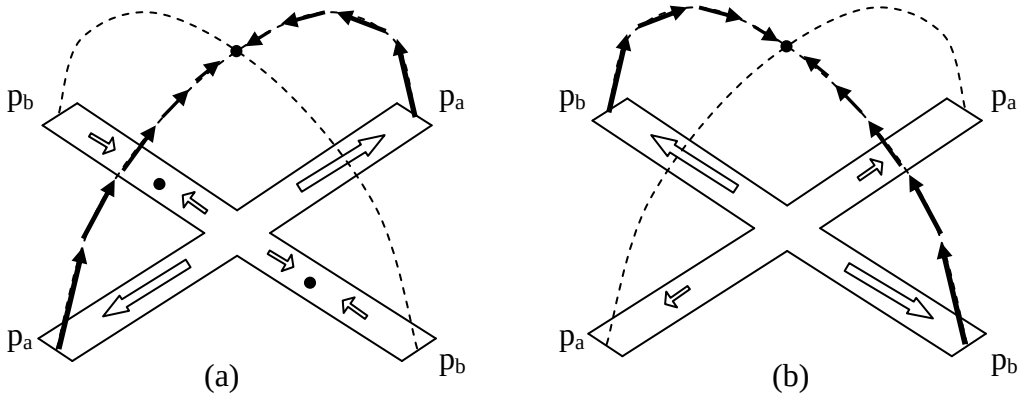

Figure 2: Schematic representation of low order characteristic modes 1a and 1b. The arms have one of two pitches, p_a or p_b, as shown. If $p_a < p_b$, then mode 1a will have a lower resonant frequency. Filled arrows represent currents in the helical wires and unfilled arrows represent currents on the feed trace. Circles represent current nulls.

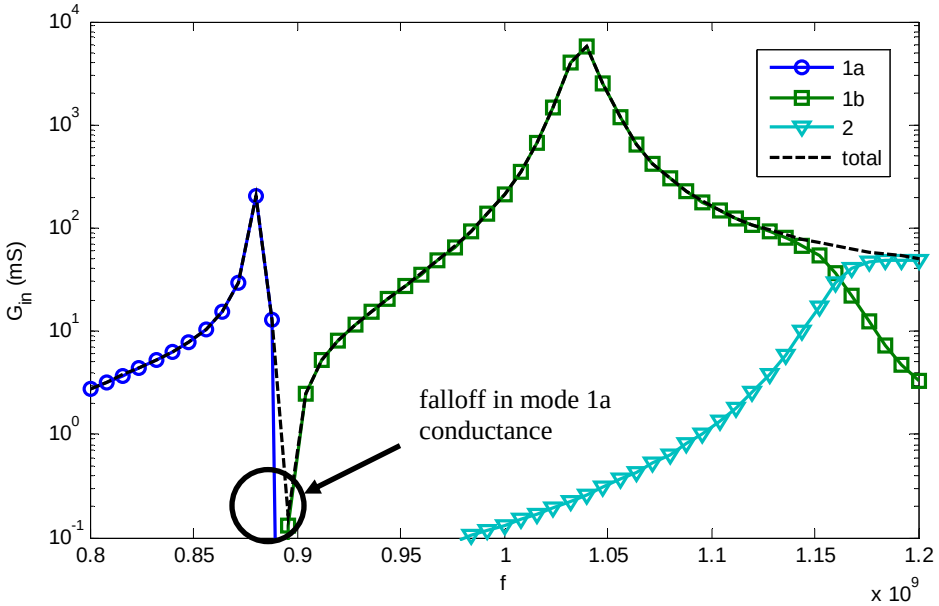

Figure 3: Feed conductance of a two mode, offset pitch antenna showing anomalous falloff of mode 1a conductance.

From Eq. 4, we know that such a drop in the conductance can either come from a large increase in the modal eigenvalue at that frequency or a sharp drop in the feed point current of the mode. In this case, the mode is near resonance and the eigenvalue is actually decreasing. Thus, there must be a drop in the feed point current. Figure 2a shows the currents of mode 1a. There is a notable current null on the feed trace associated with the inactive arm. As frequency increases, the null is observed to move

along the trace toward the center until it reaches the feed point and causes the conductance null. A small current mode exists in the two inactive arms and as the frequency changes, the nulls of this mode move quickly. At a particular electrical length, the null passes the feed point causing a conductance null.

To avoid this current null, the symmetry of the structure is broken up by placing the arms with the same pitch adjacent to each other, rather than across from each other. This eliminates the current null and allows both modes 1a and 1b to be excited as seen in Figure 4.

However, as can also be seen from the figure, the RACR is still much too high for multiresonant operation when the modes are far apart (Figure 4a). While the conductance peaks are fundamental to the mode and difficult to change, the antiresonance can often be adjusted to some extent as shown in [15]. If the modes were closer together, their conductance curves might cross at a higher value and result in a higher antiresonance conductance minimum.

Figure 4b shows the conductance response when the pitches p_a and p_b are closer together. However, the effect is not as intended; the modes move closer together but mode 1a deteriorates as it moves close to 1b. As the pitches move even closer, mode 1a continues to deteriorate, eventually collapsing into the single TM_{10}-like mode that appears when the pitches are the same. In order to operate the antenna at multiple resonances, a different set of modes, which have either a lower resonant conductance or a higher antiresonant conductance must be found.

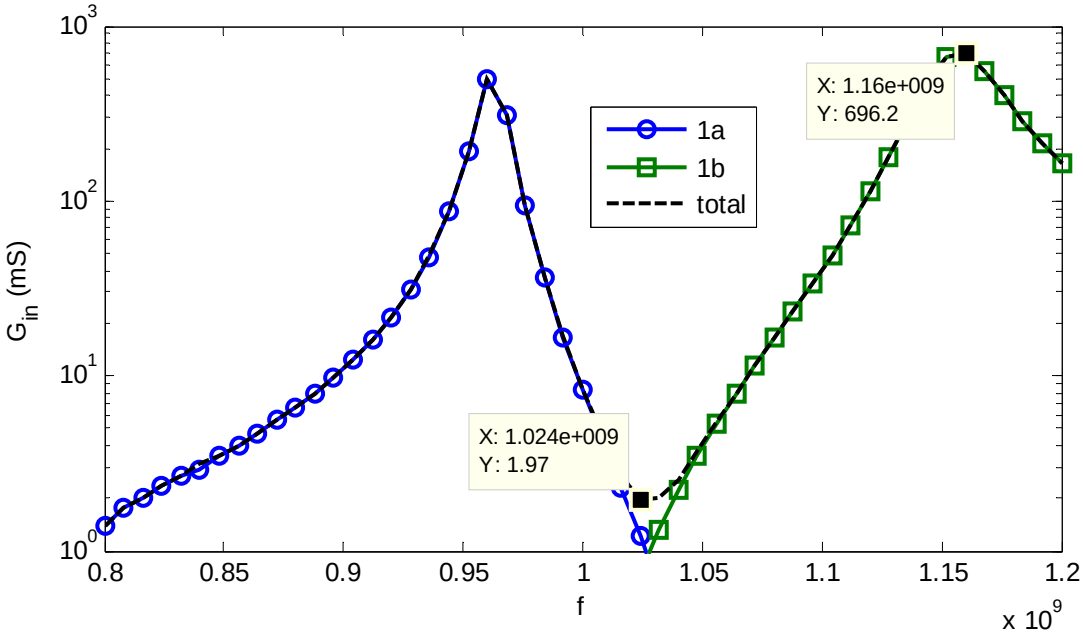

(a)

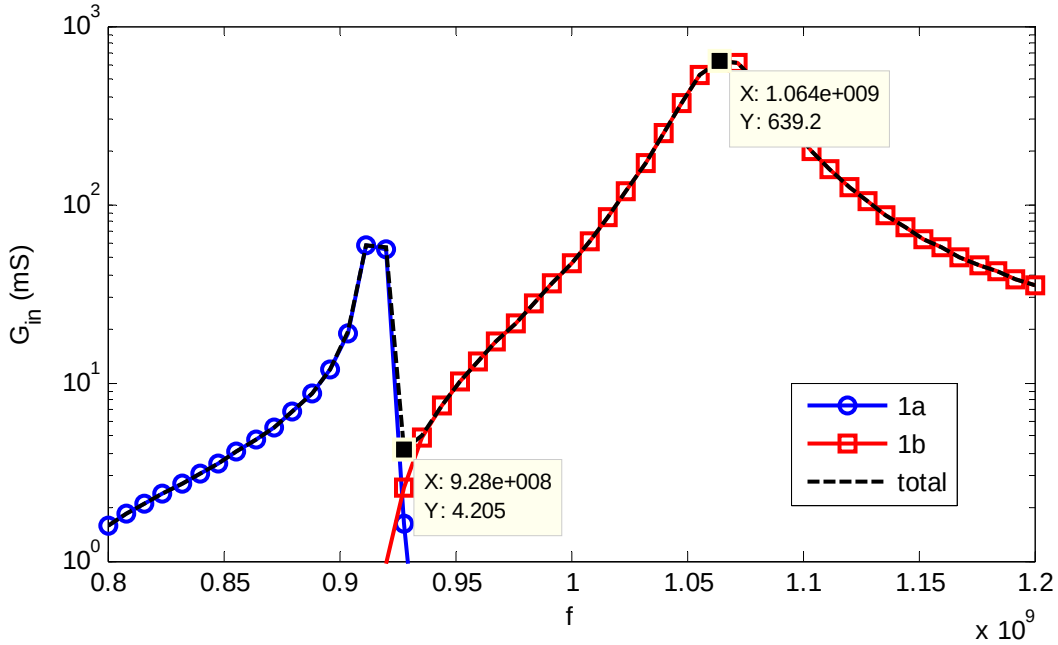

(b)

Figure 4: Conductance plots for two mode asymmetric antenna with (a) p_a = 3.0 mm, p_b = 9.5 mm and (b) p_a = 3.5 mm, p_b = 4.5 mm. Both designs are on a 0.050" Duroid 6002 substrate and have b = 21 mm, r_H = 2.5 mm, w_a = w_b = 2 mm, and wire diameter of .2 mm.

7. Multiresonant behavior using higher order characteristic modes

Combining the two first order modes to yield a multiresonant structure seems impossible because of the very high RACR that is found. However, higher order modes can also be excited in the structure in the electrically small region. When the pitches are equal, the next highest order mode excited after mode 1 has large currents flowing along the feed traces. This mode, which we call mode 2, is shown in Figure 5.

In [15] we observed that this mode could be moved to adjust the antiresonant conductance between modes 1 and 2 to tune the antenna without an external network. For example, Figure 6 shows modes 1 and 2 when the substrate dielectric constant (ε_r) is changed. Mode 2's resonance is seen to decrease greatly when ε_r increases while the Mode 1 resonance hardly moves. As this happens, the minimum conductance increases and the RACR decreases.

As these modes get closer together, they do not degenerate into one as was observed with the low order modes. Because the conductance minimum changes so greatly, the combination of mode 1 and mode 2 can be made to have a much smaller RACR than the two low order modes. To further reduce the RACR, we found that a substrate with large dielectric constant, more helical arms, and wider feed traces should be used. Furthermore, these two modes have very similar radiation patterns which resemble a monopole pattern, so the pattern remains consistent across the band and cross-polarization is very low.

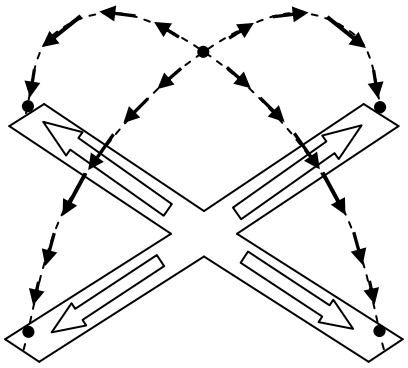

Figure 5: Schematic illustrating the currents of characteristic mode 2.

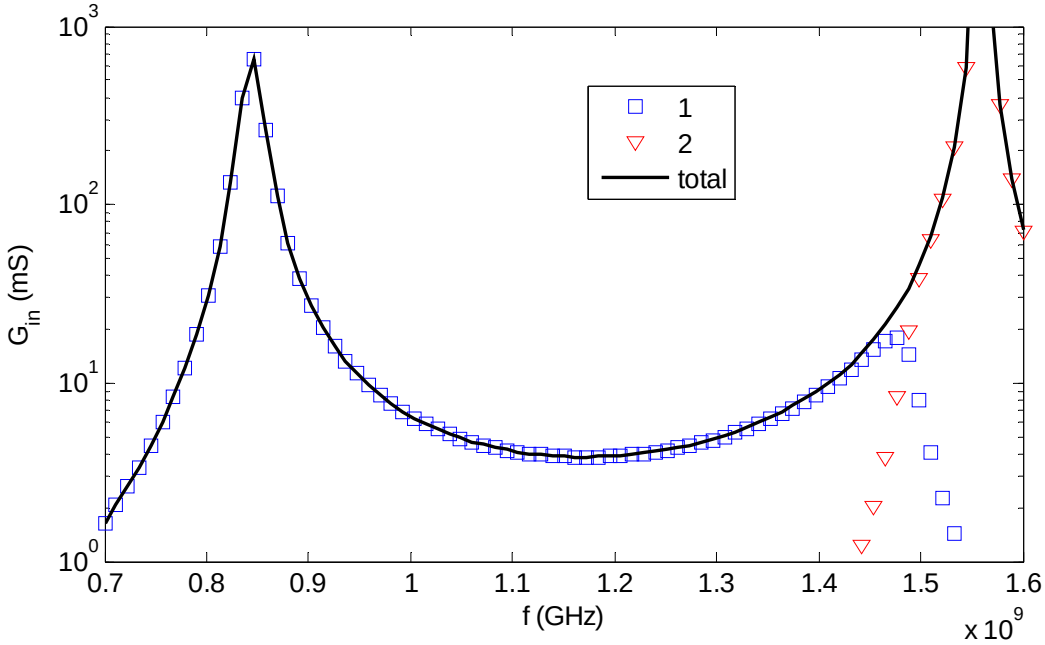

(a)

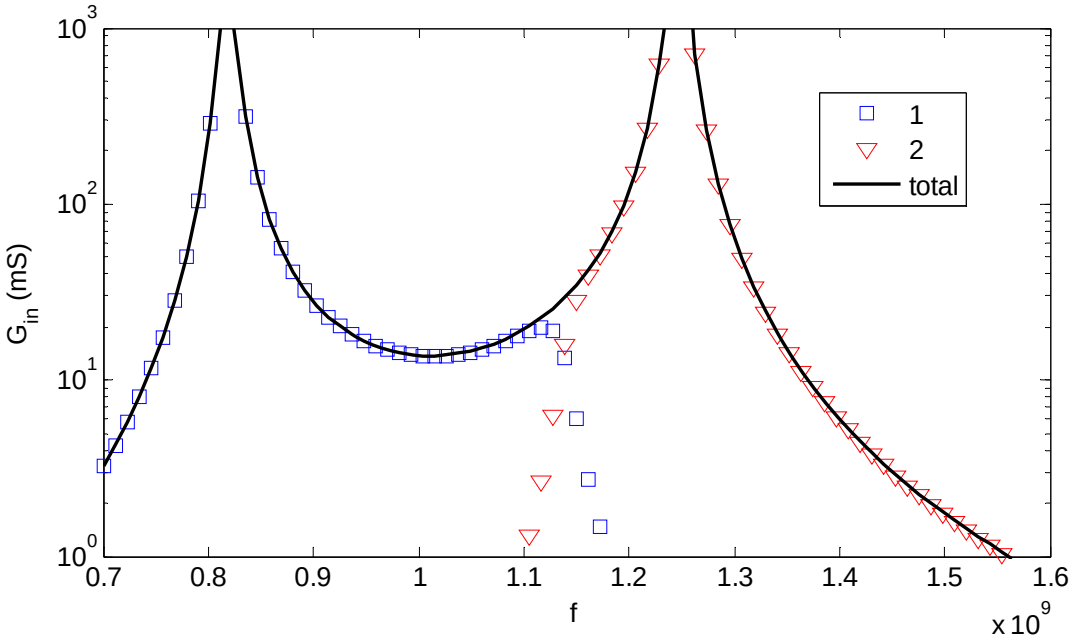

(b)

Figure 6: Conductance plots for higher order mode antenna with b = 21 mm, p = 2.85 mm, w = 2 mm, r_H = 2.5 mm and wires with .1 mm diameter. Two different substrates are used a) ε_r = 2.94 and b) ε_r = 6.

8. Multiresonant antenna with matching network

An 8 arm antenna on 0.050" Duroid 6010 was designed with the following parameters, b = 21 mm, p = 2.0 mm, w = 6 mm, r_H = 2.5 mm, and wire diameter = .6 mm. The antenna will need to be tuned to match well to the system impedance. A simple shunt capacitor connected to a variable system impedance serves as the matching network.

The antenna has a small RACR of approximately 12 as seen in Figure; however it has a large inductive susceptance. The susceptance was matched out with a 43 pF shunt capacitor and attached to a 21 Ω transmission line. The antenna's impedance after the matching network is attached is shown in Figure 7.

Figure 8 shows a VSWR plot of the antenna using this matching network. Centered at approximately 1050 MHz, the antenna has 120 MHz of 2:1 VSWR bandwidth, which is about 11.4%. The antenna's electrical size, from the bottom of the substrate to the outer radius of the furthest helix, is $ka = 0.54$. Using Chu's limit to estimate the bandwidth of a singly resonant antenna at this electrical size, we find that this antenna's fractional bandwidth is about 31% larger than that achievable with a single resonance *in the ideal case*. Compared to the more practical limit derived by Thal [7], our antenna has 96% greater bandwidth than an ideal singly resonant antenna. It is important to note that this does not violate Chu's fundamental principle, which is a constraint only on the Q of an antenna. Instead we use the fact that the Q-bandwidth relationship no longer holds for closely spaced resonances [8].

9. Conclusion

Our understanding of the characteristic modes of the electrically small TM_{10} antenna has allowed us to identify modes which are candidates for multiresonant operation and eliminate those which are not. As a general design approach the RACR must be kept to a minimum for multiresonant operation. Because of large conductance and large susceptance, if we choose to design a small multiresonant antenna, we must typically be prepared to match to very low resistances.

By superimposing a first order and higher order characteristic mode with a small RACR, an electrically small multiresonant antenna ($ka \approx 0.54$) was designed with half-power bandwidth greater than that of an ideal singly resonant antenna according to Chu's limit by 31% and to Thal's limit by 96%.

In future work, the matching network will be investigated in more detail, especially the effects of losses and more optimal designs for the network. The possibility of further increasing the bandwidth by combining more modes will also be investigated.

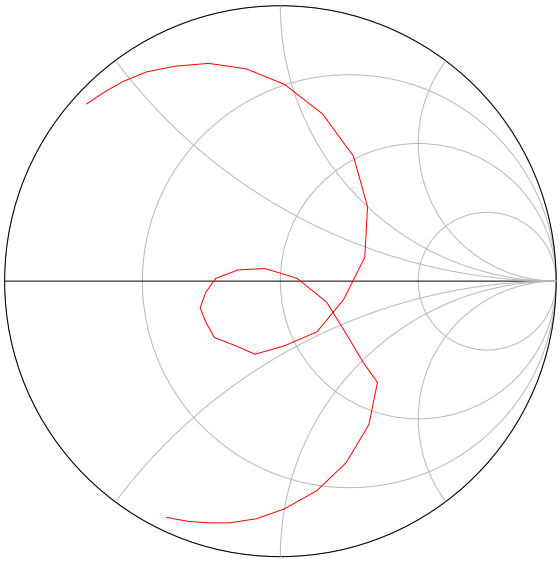

Figure 7: Impedance (normalized to 21 Ω) of multiresonant antenna matched with a 43 pF shunt capacitor.

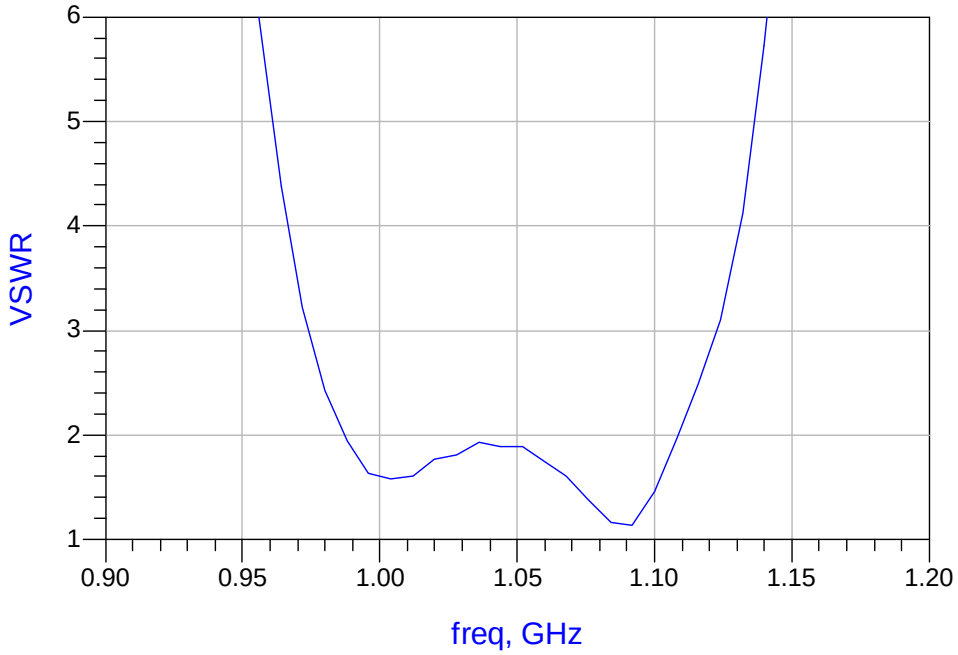

Figure 8: VSWR of multiresonant antenna connected to a 21 Ω transmission line with 43 pF shunt capacitor.

Acknowledgments

This work is supported under a National Science Foundation Graduate Research Fellowship.

References

[1] A. D. Yaghjian and S. R. Best, “Impedance, bandwidth, and *Q* of antennas,” *IEEE Trans. Antennas Propagat.*, vol. 53, no. 4, pp. 1298–1324, April 2005.
[2] L. J. Chu, “Physical limitations of omni-directional antennas,” *J. Appl. Phys.*, vol. 19, no. 12, pp. 1163–1175, Dec. 1948.
[3] J. S. McLean, “A re-examination of the fundamental limits on the radiation *Q* of electrically small antennas,” *IEEE Trans. Antennas Propagat.*, vol. 44, no. 5, pp. 672–676, May 1996.
[4] H. D. Foltz and J. S. McLean, “Limits on the radiation *Q* of electrically small antennas restricted to oblong bounding regions,” in *Proc. 1999 IEEE Antennas and Propagatation Int. Symp.*, pp. 2702–2705.
[5] J. J. Adams and J. T. Bernhard, “A class of electrically small spherical antennas with near-minimum Q," in *Proc. 2008 Antenna Appl. Symp.*, pp. 165-175, Monticello, IL.
[6] J. J. Adams and J. T. Bernhard, “Tuning method for a new electrically small antenna with low Q," *IEEE Antennas Wireless Propagat. Lett.*, vol. 8, pp. 303-306, 2009.
[7] H. L. Thal, “New radiation *Q* limits for spherical wire antennas,” *IEEE Trans. Antennas Propagat.*, vol. 54, no. 10, pp. 2757–2763, Oct. 2006.
[8] H. R. Stuart, S. R. Best, A. D. Yaghjian, “Limitations in relating quality factor to bandwidth in a double resonance small antenna,” *IEEE Antennas Wirel. Propagat. Lett.*, vol. 6, pp. 460-463 , 2007.
[9] R. J. Garbacz and R. H. Turpin, “A generalized expansion for radiated and scattered fields,” *IEEE Trans. Antennas Propagat.*, vol. 19, no. 3, pp. 348–358, May 1971.
[10] R. F. Harrington and J. R. Mautz, “Theory of characteristic modes for conducting bodies,” *IEEE Trans. Antennas Propagat.*, vol. 19, no. 5, pp. 622–628, September 1971.
[11] ——, “Computation of characteristic modes for conducting bodies,” *IEEE Trans. Antennas Propagat.*, vol. 19, no. 5, pp. 629–639, September 1971.
[12] M. Cabedo-Fabres, E. Antonino-Daviu, A. Valero-Nogueira, and M. Ferrando Bataller, “The theory of characteristic modes revisited: a contribution to the design of antennas for modern applications,” *IEEE Antenna Propagat. Mag.*, vol. 49, no. 5, pp. 52-68, Oct. 2007.
[13] EM Software and Systems, *FEKO Suite 5.5*. Stellenbosch, South Africa, 2009.
[14] A. O. Yee and R. J. Garbacz, “Self- and mutual-admittances of wire antennas in terms of characteristic modes," *IEEE Trans. Antennas Propagat.*, vol. 21, no. 6, pp. 868-871, November 1973.
[15] J. J. Adams and J. T. Bernhard, “Characteristic mode analysis of a TM_{10} electrically small spherical antenna," presented at *2009 URSI National Radio Science Meeting*, Boulder, CO.

[16] H. R. Stuart and C. Tran, “Small spherical antennas using arrays of electromagnetically coupled planar elements,” *IEEE Antennas Wireless Propagat. Lett.*, vol. 6, pp. 7–10, 2007.
[17] H. R. Stuart and S. R. Best, “A small wideband multimode antenna”, in *Proc. 2008 IEEE Antennas Propagat. Int. Symp*, San Diego, CA.
[18] S. R. Best, “The state-of-the-art in small wideband antenna design”, in *Proc. 2008 Antenna Appl. Symp.*, Monticello, IL.

TOWARDS THE DEVELOPMENT OF ELECTRICALLY SMALL ANTENNA MEASUREMENTS SYSTEMS TECHNOLOGY

Nathan Clow, Ivor L. Morrow
Security Sciences Department, DSTL, Fort Halstead, Kent, UK
Department of Aerospace and Sensors, DCMT, Cranfield University, UK

The measurement of the radiation efficiency of Electrically Small Antenna (ESA) has been of interest for some decades. This paper introduces a new form of measurement technique based on the Wheeler Cap method, that uses electro-optic devices to isolate the ESA from the measurement system. The reflection coefficient can then be measured with the isolated ESA inside the Wheeler Cap and in freespace to determine the antennas efficiency. The measurement system can also be used in the measurement of far-field radiation of an ESA.

I. INTRODUCTION

ONE of the most important defining characteristic relating to the performance of an ESA is its radiation efficiency. The radiation efficiency is a figure of merit relating to the antenna's ability to radiate the electromagnetic energy delivered to its input terminal. The accurate measurement of the radiation efficiency of ESA is notoriously difficult and has been the focus of much study since the introduction, by Harold Wheeler, of the now well-known Wheeler Cap method [1]. Subsequently, this method has been investigated [2–4], adapted [5] and improved upon [6, 7]. Alternative methods of measuring the efficiency of ESA is indicative of the level of interest in this area for mobile communication systems and bodyworn antennas [8–15]. This paper discusses the progression of the Wheeler Cap method, the benefits and limitations of each stage of its development and then introduces a modified method which incorporates the use of novel fibre-optic system to attempt overcoming some of the limitations discussed.

II. BACKGROUND

THE measurement of the Q of an ESA is made difficult by the presence of ohmic losses which are often of the same order as the radiation losses. Therefore, it is not possible to accurately determine the Q simply from a measurement of the input impedance of the antenna when the antenna is in an anechoic environment. A method for experimentally determining the radiation Q of ESA was developed by Wheeler [1]. This method has been further investigated by Newman [9] and Pozar [3]. In this method, the antenna is placed in a conducting sphere or hemisphere with the antenna placed on a ground plane. The sphere is known as a "Wheeler Cap" and is used to prevent radiation by ensuring that all the radiated energy is stored in the static field, the measured impedance is then due to conductor and material losses.

A review of literature has revealed that there are nine methods of measuring the radiation efficiency of an ESA, each having its own merits.

- Pattern integration [9]
- Q factor method [9]
- Resistance comparison method [8]
- Reflection method [12, 13]
- Radiometric method [11, 16]
- Random field measurement [10, 17, 18]
- Calorimetric method [15, 19]
- Reverberation chamber method [14, 20]
- Wheeler cap method [1, 7]

The pattern integration method although being the most precise is convoluted, time consuming and difficult to implement in practice at frequencies below $500MHz$ [2, 9]. The Q factor and resistance comparison methods assume that the form of current distribution on the antenna remains unchanged when a change is made in the antenna or its surroundings [8, 9]. The reflection method is an extension to the Wheeler Cap method which although being more complicated, takes account of non-simple antenna structures. The radiometric method is based on the principle that a lossy antenna directed at an area of low noise will generate more noise power than a lossless antenna directed at the same area. The loss in the antenna can be seen as a noise source at the ambient temperature. The method is suitable for high-gain antennas with pencil-beam type radiation patterns. The measurement system requires high-quality system components adding to the expense [11]. Furthermore, the

antenna must be impedance matched to the source to avoid increasing system noise [3]. The random field measurement method places the antenna in close proximity to a human body. It is more time consuming than other conventional methods [10, 17, 18]. The calorimetric method is based on the measurement of the power dissipated rather than the power radiated. It is reported to be a low-cost alternative to the pattern integration and a replacement of the Wheeler cap method [15, 19]. However, the measurement procedure is more complicated and the set-up equipment more expensive than the Wheeler cap method. The reverberation chamber method is stated to be a less expensive alternative to the pattern integration method. Mode and platform stirring is used to set-up a multi-path environment inside a metallic chamber. Statistical analysis is then used to determine the radiation efficiency of an antenna. The modes inside the chamber are modulated by a metallic paddle which is rotated at a constant and know velocity. To obtain improved measurement accuracy the antenna under test, also referred to as the platform, is also rotated. The method is based on the premise that the average received power in a reverberation chamber is proportional to the radiation efficiency of the test antenna [20].

The concept of a radiation shield in the form of a conducting shell the size of a radian sphere originates from 1959 [1], in which Wheeler he states that, for an ESA , the radiation shield enables a separate measurement of radiation resistance and loss resistance. This method of measuring the radiation efficiency is now known as the classic Wheeler Cap method [2] and is widely used, as it is easy to implement in practice, requiring only two measurements of the input impedance. The Wheeler Cap method is modelled on an equivalent series RLC circuit, which may not be the case for all antennas such as microstrip antennas [21]. Consequently, a modified Wheeler Cap method was presented [7], which approximates the input impedance of an antenna near resonance with either a series or parallel RLC circuit model.

III. Hybrid Fibre-Optic RF Reflection Measurement System (HRS)

ANTENNAS that are embedded in compact hosts, such as mobile communication handsets, are generally electrically small making them sensitive to the surrounding environment and vulnerable to detuning which results in loss of signal and poor quality of service. The detuning occurs because the host is in the antenna's reactive near-field or its radiating near-field, thus modifying

the current distribution on the antenna's surface. Furthermore, a measurement system placed close to the antenna has the same effect and can act as a parasitic element becoming part of the antenna that can then contribute to the antenna's far-field radiation pattern, in a constructive or destructive manner [22]. The ground plane of an ESA also tends to be electrically small and plays a vital part in the overall efficiency and impedance bandwidth of the antenna. Interest in quantifying and mitigating ground plane effects has been the subject of recent research [23, 24].

In this paper a novel method is described for isolating the ESA from the measurement system to enable accurate characterisation of the antenna and to examine ground plane effects by measuring the antenna's efficiency and impedance bandwidth.

The initial challenge is to measure the forward and reverse antenna transfer characteristics without compromising the RF properties of antenna. This is done by effectively isolating the measurement system from the antenna, thus preventing the measurement system from becoming part of the antenna.

The Hybrid Fibre-Optic RF Reflection Measurement System (HRS)[1] and RF to fibre optic system have been developed and characterised to measure the forward and reverse signals while isolating the antenna from the RF components of the measurement system. This system was then used to measure the radiation pattern and reflection coefficient of different types of antennas. The advantage of using this system over conventional measurement systems is that the ESA is isolated from the measurement system.

The HRS and RF over fibre optic system have been integrated into the Wheeler Cap and measurements on several different types of antennas have been undertaken. These types of measurement have not been previously reported in literature. The measurements show that the integration of the measurement system into the Wheeler Cap is possible, providing a new technique for measuring the efficiency of host-embedded antennas.

A. Flow Chart Analysis of the HRS

SIGNAL flow network analysis is used to obtain the system's scattering parameters, [25, 26].

The HRS consists of four modules as shown in Figure 1; each module is a two-port network represented by a block which has two input ports and two

[1] The HRS combines the fibre optic data link with the Dual Directional Coupler.

output ports. The ports associated with each module are:

- The Radio Frequency (RF) to Optical module
  - a_1 Input incident signal node
  - a_2 Output reflected signal node
  - b_1 Input reflected signal node
  - b_2 Output incident signal node
- The Optical to RF module
  - a_3 Input incident signal node
  - a_4 Output reflected signal node
  - b_3 Input reflected signal node
  - b_4 Output incident signal node
- The Dual-Directional Coupler RF (DDC (RF)) module
  - a_5 Input incident signal node
  - a_6 Output reflected signal node
  - b_5 Input reflected signal node
  - b_6 Output incident signal node
- The Dual-Directional Coupler A/D converter (DDC (A/D)) module
  - b_8 Input incident signal node
  - a_9 Output reflected signal node
  - b_8 Input reflected signal node
  - b_9 Output incident signal node

The source V_s, is connected to the RF to Optical module and has a characteristic impedance and reflection coefficient Z_s and Γ_s, respectively. The antenna is connected to the DDC (RF) module and has a characteristic impedance and reflection coefficient Z_A and Γ_A, respectively. The DDC (A/D) converts the measured signals received from the DDC (RF) to a digital stream, prepared to be transmitted over an optical fibre. The DDC (A/D) is assumed to be perfectly matched to the DDC (RF) as the paths a_5 to b_8 and b_8 to a_6 are optical signals and the paths are isolated from the RF modules. Therefore the DDC (A/D) component is not required to determine the scattering parameters of the HRS. This simplifies the system network, as shown in Figure 2. The optical interface between the RF to Optical module and the Optical to RF module is assumed to be matched by the line impedance Z_{opt}. The interface between the Optical to RF module and the DDC (RF) is also assumed to be matched by the line impedance Z_{rf}. Referring to the signal flow chart in Figure 3, the scattering parameters for the RF to Optical module, Optical to RF module and the DDC

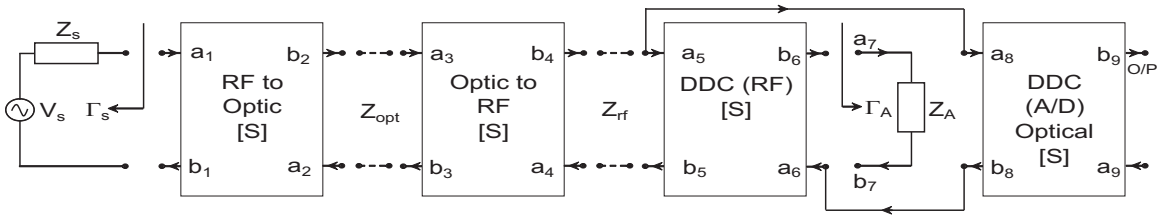

Figure 1. HRS system network diagram.

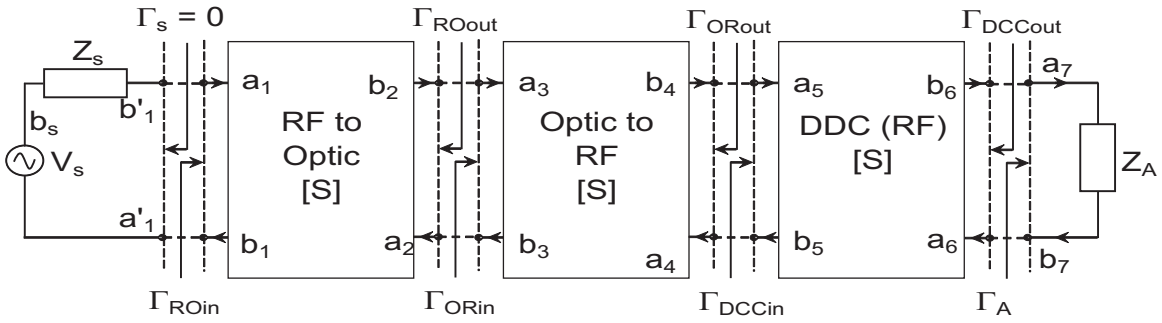

Figure 2. HRS simplified system network diagram.

(RF) module are denoted by ζ, ρ and υ, respectively. Two additional nodes, $a_1^{'}$ and $b_1^{'}$, and a number of loss less connections are introduced into the signal flow chart to aid with the mathematical analysis.

The signal flow chart can be reduced by process of repetitive decomposition to determine the signal delivered to the input of the HRS (a_1) as a function the entire network scattering parameters and the input source signal V_s. One can assume that the path taken by the optical signal cannot produce RF reflections, therefore $\Gamma_{ROout} = \Gamma_{ORin} = 0$. From these assumption the input reflection co-

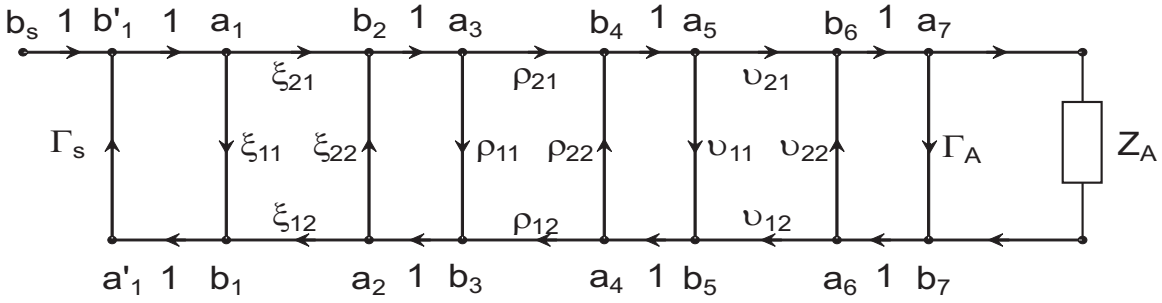

Figure 3. HRS signal flow chart diagram.

efficient of the HRS is Eqn. 1.

$$\begin{aligned}\Gamma_{HRSin} &= \frac{b_1}{a_1} \\ &= \zeta_{11} + \\ &\quad \zeta_{21}\zeta_{12}\frac{\rho_{21}\rho_{12}\left\{\upsilon_{11} + \dfrac{\upsilon_{21}\upsilon_{12}}{1-\upsilon_{22}\Gamma_A}\right\}}{1-\rho_{22}\left\{\upsilon_{11} + \dfrac{\upsilon_{21}\upsilon_{12}}{1-\upsilon_{22}\Gamma_A}\right\}}\end{aligned} \tag{1}$$

IV. Characterisation of the HRS

THE input port, $P_{in} \equiv P_1$, shown in Figure 4, was connected to the HP8645A signal generator[2] and the output port, $P_{out} \equiv P_2$, was connected to the input port of an E4404B spectrum analyser. The digital data was transferred to the PC via a fibre-optic cable. The forward and reverse power, and reflection coefficient are each represented by an integer. In theory the HRS is a reciprocal device, however a small amount of asymmetry was found. The ports were chosen to give the best impedance match at the port that is connected to the antenna.

The measurements were done at five discrete frequencies: $250MHz$, $300MHz$, $350MHz$, $400MHz$ and $450MHz$. The linearity of the output data to the input power for both the forward and reverse direction were measured at each frequency. The data is used in a lookup table to determine the power travelling into either P_1 or P_2. It is important to know the amount of power travelling into both P_1 and P_2; the power delivered to the antenna can be determined[3] from the power travelling into P_1 and the reflected power from the antenna can be determined from the power travelling into P_2.

A network analyser was used to characterise its scattering parameters. At $350MHz$ the scattering parameters are: $S_{11}(-19.8dB)(58\Omega)$, $S_{21}(-0.86dB)$, $S_{21}(-0.86dB)$ and $S_{22}(-23.19dB)(52\Omega)$. The HRS has a good match at both ports and an acceptable insertion loss of less than $1dB$.

[2] The HP8645A was calibrated to take account of the losses in the cable
[3] The power delivered to the antenna takes into account the insertion loss of the HRS

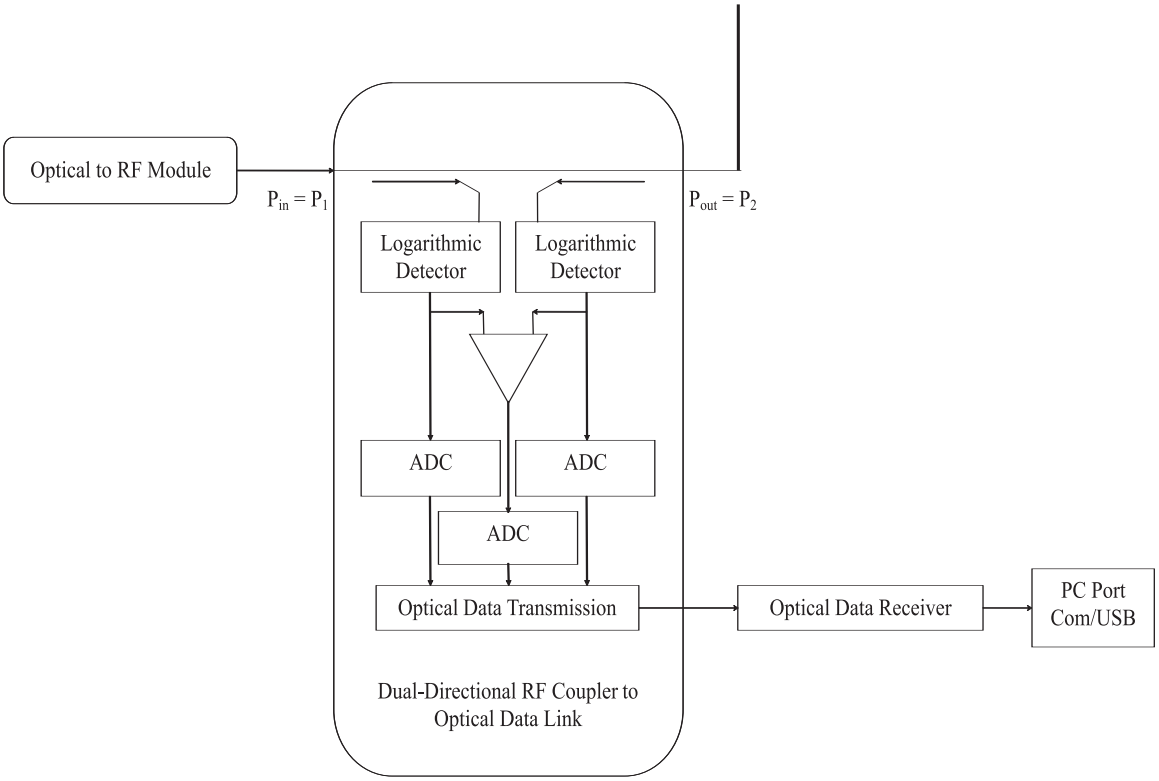

Figure 4. System diagram of the HRS.

V. Characterisation of the HRS combined with the Fibre Optic to RF Module.

THE HRS and the Fibre Optic to RF Module were both mounted inside a die-cast box to isolate the two modules from external effects and enables the calibration of the combined modules. The HRS was set-up in the normal mode of operation with power being delivered to P_1 and received at P_2. To characterise the whole measurement system[4] the RF input power to the RF to Fibre-Optic Module and the corresponding RF and digital data form the HRS must be know. The equipment set-up for calibrating P_1 is shown in Figure 5. The RF to Fibre Optic Module converts the RF power received at its input port, P_A, to an optical signal which is transmitted to the Fibre Optic to RF module, which converts the optical signal to RF before transmitting it to the HRS. The output at P_2 of the HRS is measured by the E4404B spectrum analyser and the corresponding numerical values are recorded on a PC. This calibration was also done with the HRS set-up in the reverse mode with power being delivered to P_2 and received at P_1. The calibrated data were then used in a lookup table

[4] The whole measurement system includes the HRS, the Fibre-Optic to RF Module and the RF over fibre module.

to determine the measured input and reflected power in dBm. The reason for calibrating the HRS in reverse mode was to obtain calibration data for the reflected power from the output port, P_2, as this is the port that is connected to the antenna.

The Fibre-Optic to RF Module is operated in saturation to generate the maximum output power of $10dBm$ at $350MHz$. The output port of this module is connected directly to the HRS input port, P_1. The HRS has a nominal insertion loss of $1.2dB$, thus $8.8dBm$ is presented at its output port, P_2. This agrees with the scattering parameter measurements of the HRS, which were obtained using the network analyser, and gives a degree of confidence in the calibration process.

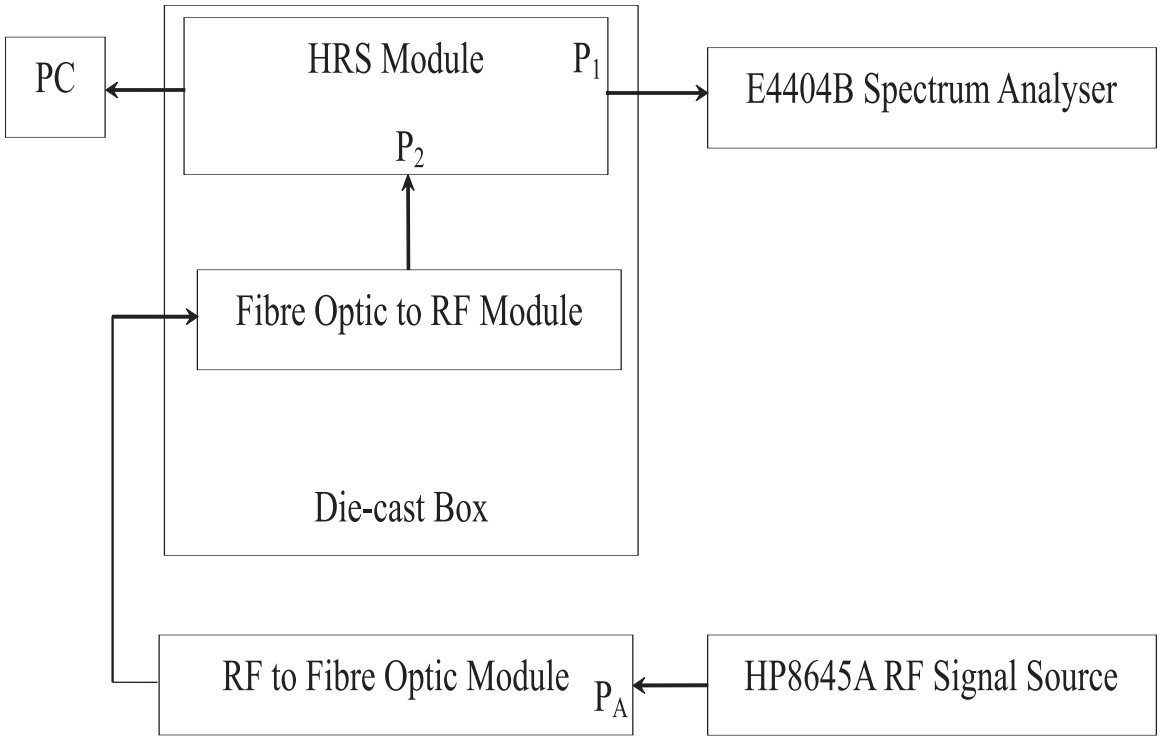

Figure 5. Power linearity calibration set-up for HRS and FO RF module.

VI. Calibrating the HRS to measure return loss.

THE HRS requires calibration to ensure that the measured reflected power from the antenna, which is received at P_2 of the HRS, is calibrated against a know return loss. This was done by measuring the return loss of several calibrated attenuators using the HRS, as shown in Figure 6. The attenuators range from $1dB$ to $20dB$, enabling calibration measurements covering the dynamic

range of the HRS. The reflection coefficients of the attenuators are shown in

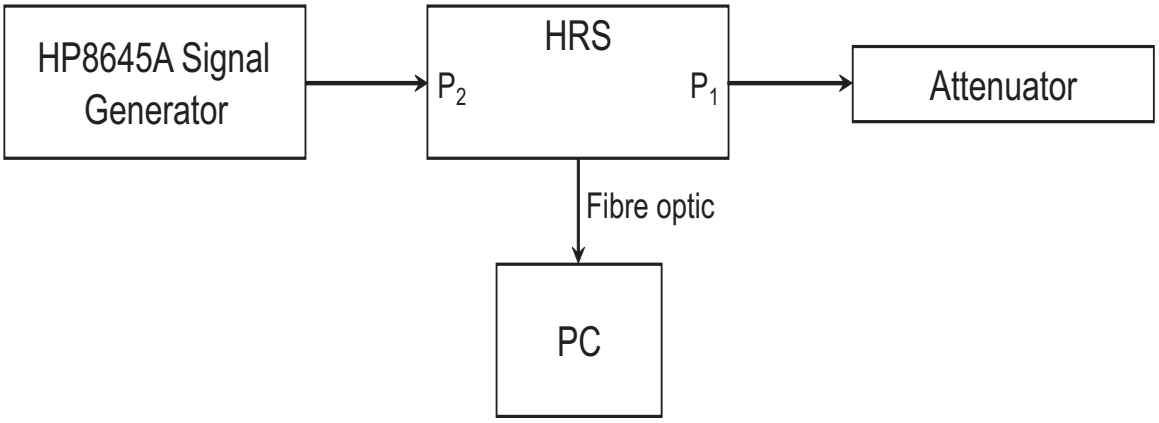

Figure 6. HRS calibration set-up for Port 1.

Table I. The measured digital data were then used in a lookup table to determine the return loss of an antenna. The calibration was done both with and without the Fibre Optic to RF Module. Therefore, where it is not convenient to use an optical feed to the HRS, calibrated S_{11} measurements can be taken with a RF cable connected directly to the HRS.

Attenuator	$S_{11}(dB)$
A	-1.55
B	-1.65
C	-4.35
D	-4.95
E	-7.64
F	-8.22
G	-10.82
H	-11.74
I	-15.04
J	-19.36
K	-22.01
L	-41.43

TABLE I
CALIBRATED S11 DATA FOR THE ATTENUATORS, AT $350MHz$

The reflection coefficient can be measured to $-22dB$ when using the HRS alone. This figure deteriorates to $-17dB$ when the HRS is combined with the Fibre-Optic to RF Module. This is thought to be due to the mismatch between the two modules. The two modules are connected together by a short

wire connection. At this stage no attempt was made to impedance match the connection as the level of measured reflection coefficient is acceptable as it is within the typical refection coefficient values for electrically small antennas that are at best $-10dB$.

VII. The HRS integrated into an antenna radiation measurements system

THE HRS was integrated into a measurement system which is used to plot the radiation pattern of an antenna. When measuring the radiation pattern of an ESA, where the impedance match is known to be very poor, most of the RF energy delivered to the antenna is reflected along the outer shielding of the cable, and a small percentage of energy is radiated from the antenna. The reflected energy is then radiated over the length of the cable and is detected by the receive antenna. This adverse effect is eliminated by incorporating the RF over fibre module into the measurement system.

Referring to the measurement system set-up as shown in Figure 7, the RF signal from the signal generator travels through the RF to Fibre Optic Module which converts it into an optical signal. The optical signal is then delivered to the host via a fibre optic cable where the Fibre Optic to RF Module converts it to RF. The function of the HRS module is to measure and transmit the RF signal to the antenna, Transmit (Tx); and measure the reflected RF signal from Tx; convert these RF signals to a digital stream before transmitting them to to a Personal Computer (PC) over a fibre-optic data cable. The RF energy radiated from the antenna is received by a calibrated log-periodic antenna, Receive (Rx).

VIII. Antenna radiation measurements using the HRS and Fibre Optic to RF Module.

SEVERAL antennas were measured using the HRS to ensure that the measurements were consistent and not specific to a particular type of antenna. These measurements enable the investigation of cable and ground effects on antenna performance, and how best to mitigated the adverse effects which may arise from the near-field environment. Five antennas were measured:

1. Calibrated dipole
2. Monopole 1 (M1)
3. Monopole 2 (M2)
4. Monopole 3 (M3)

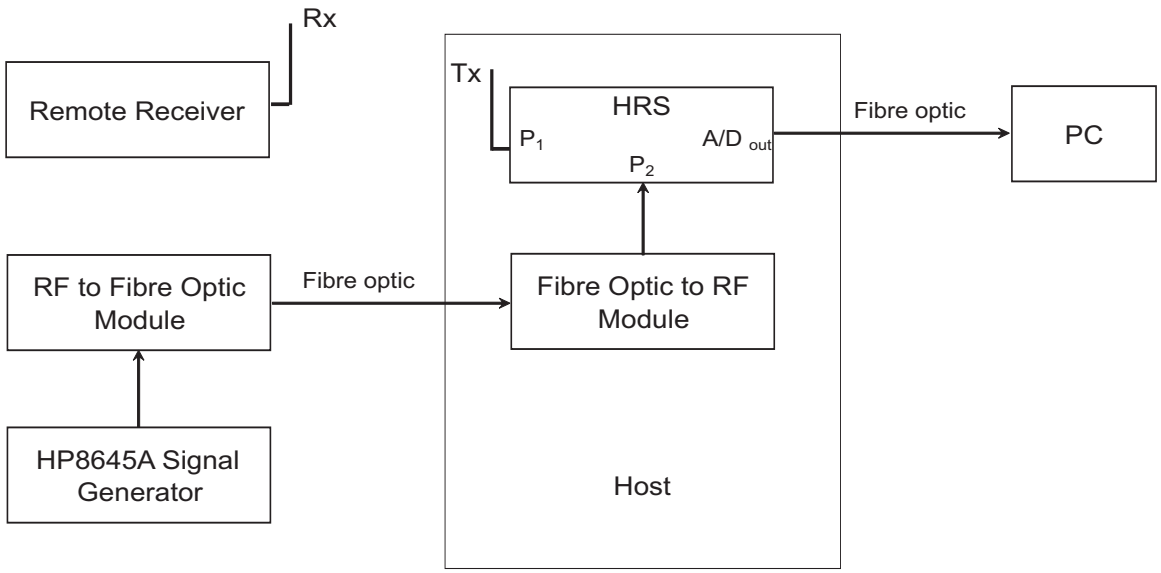

Figure 7. Antenna polar radiation measurement set-up.

5. Electrically Small Patch (ESP)

Each antenna was measured in the conventional manner with a RF cable connected directly to the antenna and then by using the HRS. In this paper the results from the calibrated dipole and M1 are discussed.

A. Calibrated dipole

THE calibrated dipole is used as a reference antenna as it has a well understood radiation pattern. The dipole was tuned to $350MHz$ (S_{11}= $-18dB$) and the radiation pattern of the vertically polarised dipole was then measured using a far-field antenna range. There are two radiation patterns shown in Figure 8, one for the dipole connected directly to the RF cable and the other for the dipole connected to the HRS. The radiation patterns show that for a well tuned antenna the RF over fibre-optic system is not required as very little RF energy is reflected back to the source. The RF energy reflected along the cable from the dipole is just 1.6% of the RF energy delivered to it. The power delivered to the antenna is $8.5dBm$, therefore the reflected power is -0.5dBm.

B. Monopole M1

MONOPOLE 1 is a monopole set parallel to a ground-plane. M1 has a reasonable match at $350MHz$ of S_{11}= $-12.5dB$ and was used to assess the performance of HRS when measuring sidelobe levels.

The radiation plot for M1 is shown in Figure 9; little effect is observed on

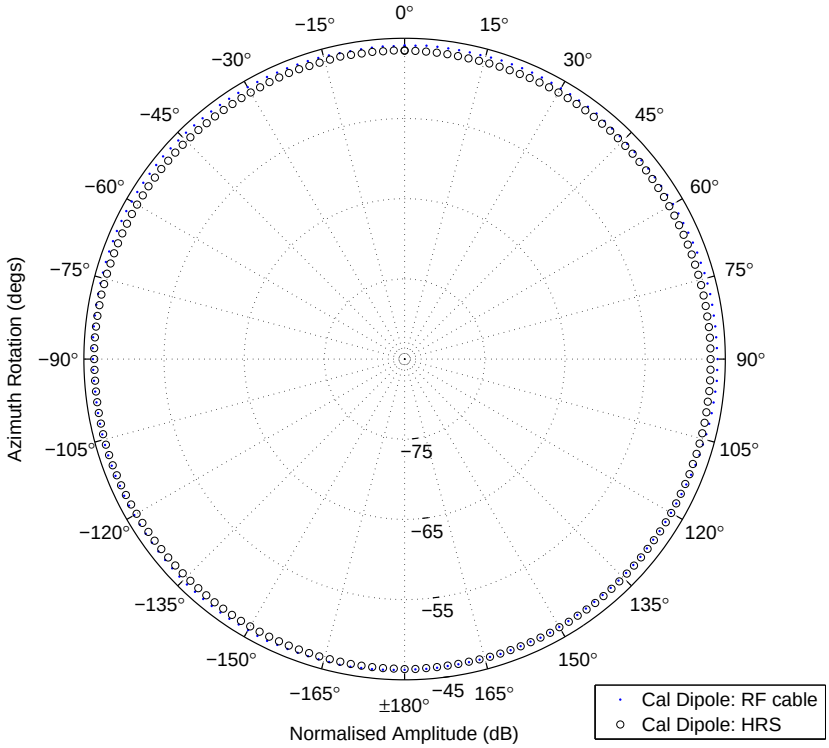

Figure 8. Calibrated dipole polar radiation.

the radiation pattern when the antenna is connected to a vertically orientated RF cable or when the HRS is placed behind the ground-plane (HRS unconnected). This is expected as the antenna is tuned to the operating frequency and the HRS module simply becomes part of the ground plane. The RF energy reflected back to the antenna is 5.6%, $(-4dBm)$, of the RF energy delivered to it. Therefore a small amount of this reflected energy will be radiated by the cable. An improvement is seen in the fidelity of the sidelobes when the RF cable is set horizontal to the antenna. This shows that the RF radiation from the cable contributes to the far-field radiation pattern of the antenna and that its influence can be somewhat mitigated by positioning the cable orthogonal to the polarisation of the antenna; in this case the antenna is polarised vertically and the cable horizontally. Further improvement is seen when the HRS is used to isolate the antenna from the RF source. Isolating the antenna in this way significantly reduces systematic measurement error and ensures that the measured far-field radiation pattern is that of the antenna and not the measurement system.

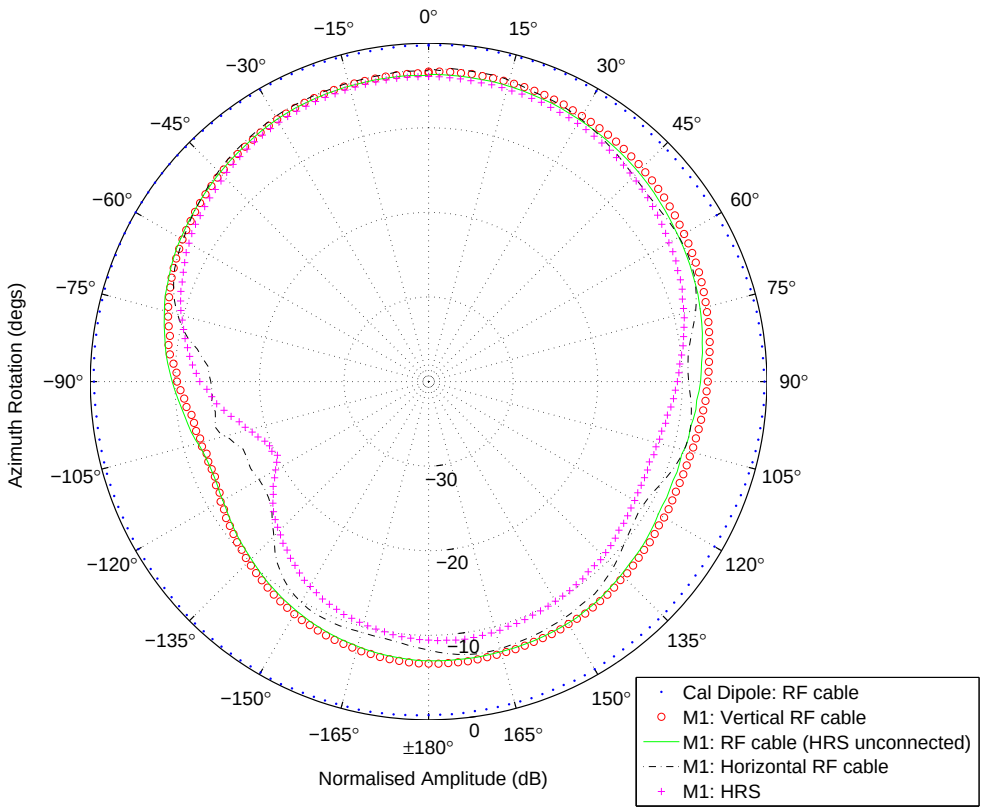

Figure 9. Radiation plot for Monopole 1

IX. Integrating the HRS and Fibre Optic to RF Module in to the Wheeler Cap.

In this section the HRS is used to measure the reflection coefficient and efficiency of an ESA. The reason for integrating the HRS and Fibre Optic to RF Module in to the Wheeler Cap is to enable repeatable efficiency measurements of host-embedded antennas and provide a benchmark for antennas developed in the future.

The HRS and Fibre Optic to RF Module are integrated into the Wheeler Cap to determine the efficiency of the antenna.

The integrated set-up is shown in Figure 10. Fibre optic cables are used to interface with the Wheeler Cap. The RF signal is generated from within the Wheeler Cap, thus isolating the Wheeler Cap from the external RF source.

To calculate the efficiency of an ESA both the freespace and shielded complex reflection coefficients must be measured. At this stage only the magnitude of the reflection coefficient is capable of being measured with the HRS.

The S_{11} of M1, was taken in freespace with and without a RF feed-cable.

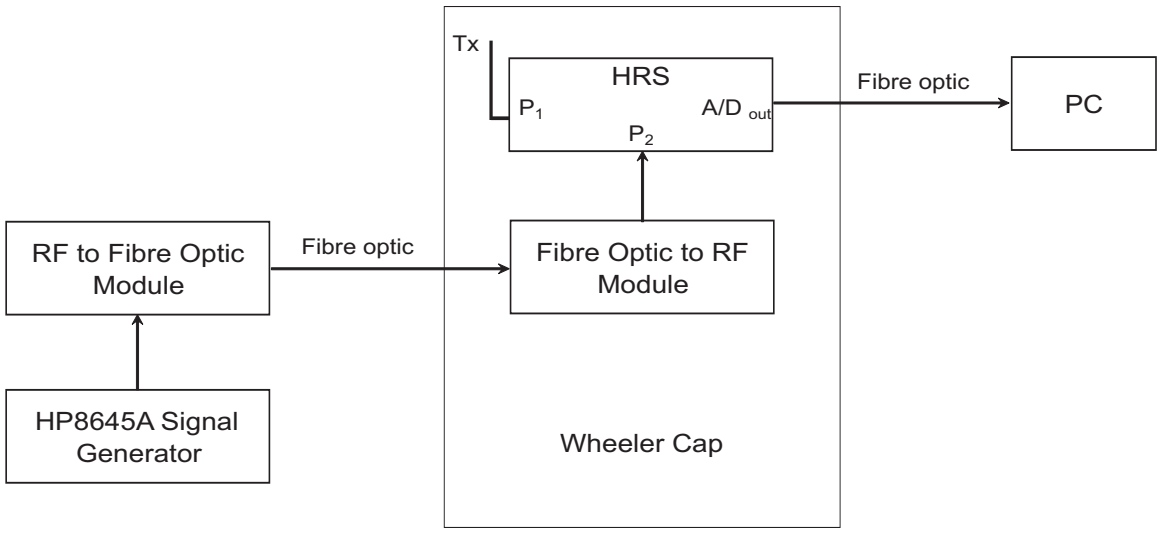

Figure 10. RF and fibre optic integrated antenna efficiency measurement system.

The feed-cable, which is $61cm$ in length, positions the antenna in the centre of the Wheeler Cap; without it the antenna would be placed against the top surface, which would act as a ground plane and possibly give rise to spurious readings. Although the operating frequency is $350MHz$ it is beneficial to know what happens to the resonant frequency over a wider bandwidth. Therefore the measurements were taken form $345MHz$ to $355MHz$.

Two separate measurements were undertaken and the results compared; one using the Vector Network Analyser (VNA) and the other using the HRS. In both cases, the measurements were undertaken with the antennas in freespace and then placed in the Wheeler Cap. A lookup table is used to calculate the S_{11} measurements from the HRS. A linear gradient calibration factor is used to calibrate the HRS to the specific antenna.

The Fibre Optic to RF Module is used to effectively isolate the antenna from the RF source. The effects of this isolation on the match of the antenna have hitherto not been reported in literature. The HRS is used to measure the reflection coefficient of the antenna, revealing the impact made on the performance of the antenna.

The reflection coefficient measurements for M1 when placed in freespace is shown in Figure 12 and Figure 13. The reflection coefficient measurements for M1 when placed in the Wheeler Cap are shown in Figure 14 and Figure 15.

The HRS measures the magnitude of the reflection coefficient, therefore the phase was reconstructed by differentiating the magnitude with respect to frequency. The phase reconstruction error was determined by applying the pro-

cess to the measured VNA reflection coefficient for each antenna. This was then used as the correction factor for the HRS measurements. The reflection coefficient magnitude and reconstructed phase was then used to determine the complex input impedance, Z_A, of the antenna. The efficiency of the antenna was then determined by substituting the real part of the impedance from the freespace and Wheeler Cap measurements using Eqn. 2. The efficiency of M1 is shown in Figure 11.

$$\eta = \frac{R_r}{(R_r + R_l)} = 1 - \frac{R_{cap}}{R_{fs}} \tag{2}$$

where, R_r is the radiation resistance and R_l is the loss resistance. The real part of the antenna input impedance is the quantity R_r+R_l, which can be measured using a VNA.

M1 is a narrow-band resonant antenna, which has a bandwidth of 0.2%, however, the bandwidth is increased to 0.5% by isolating the antenna and measuring the S_{11} using the HRS as shown in Figure 12. The polar radiation patterns over a wider bandwidth were not undertaken to establish the effects on radiation pattern. Modes adjacent to the resonant mode are observed using the HRS and requires further investigation. When the antenna is placed in the Wheeler Cap, the influence of the feed-cable is clearly seen. Therefore, when measuring ESA's it is essential to ensure that the Wheeler Cap is isolated from the measurement system.

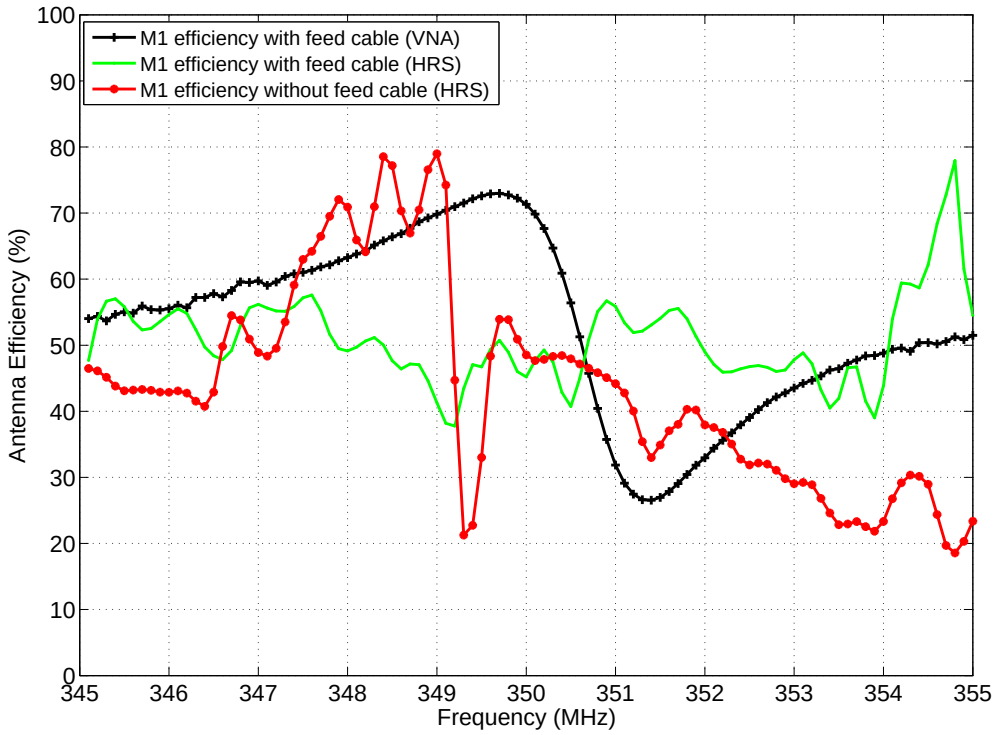

Figure 11. Efficiency for antenna M1.

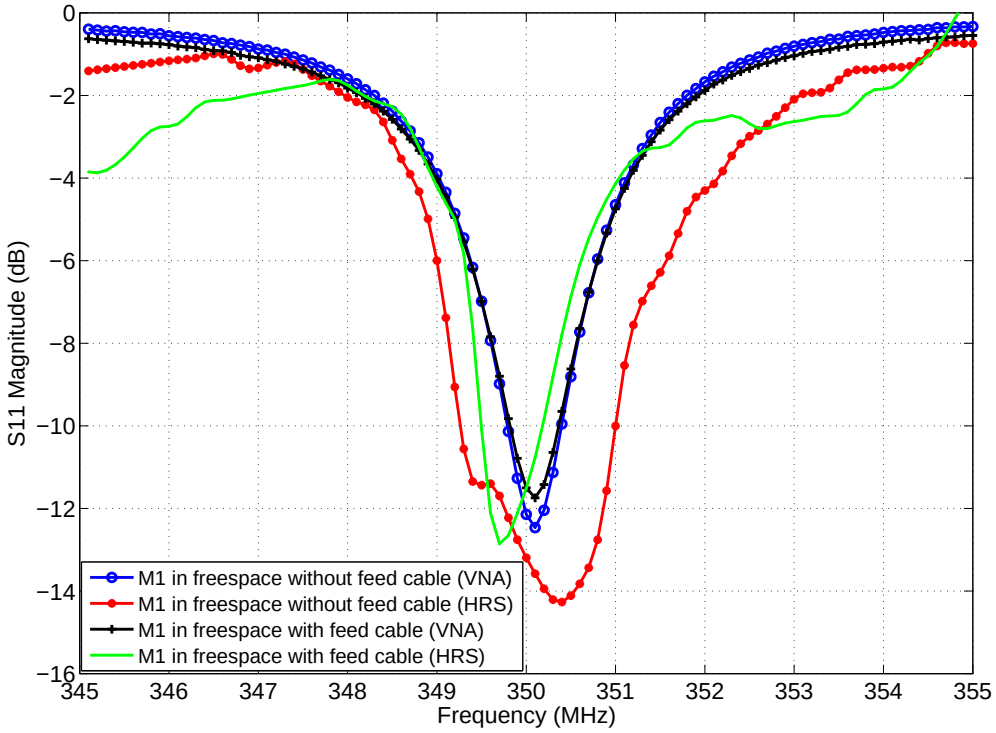

Figure 12. M1: Freespace S11 magnitude.

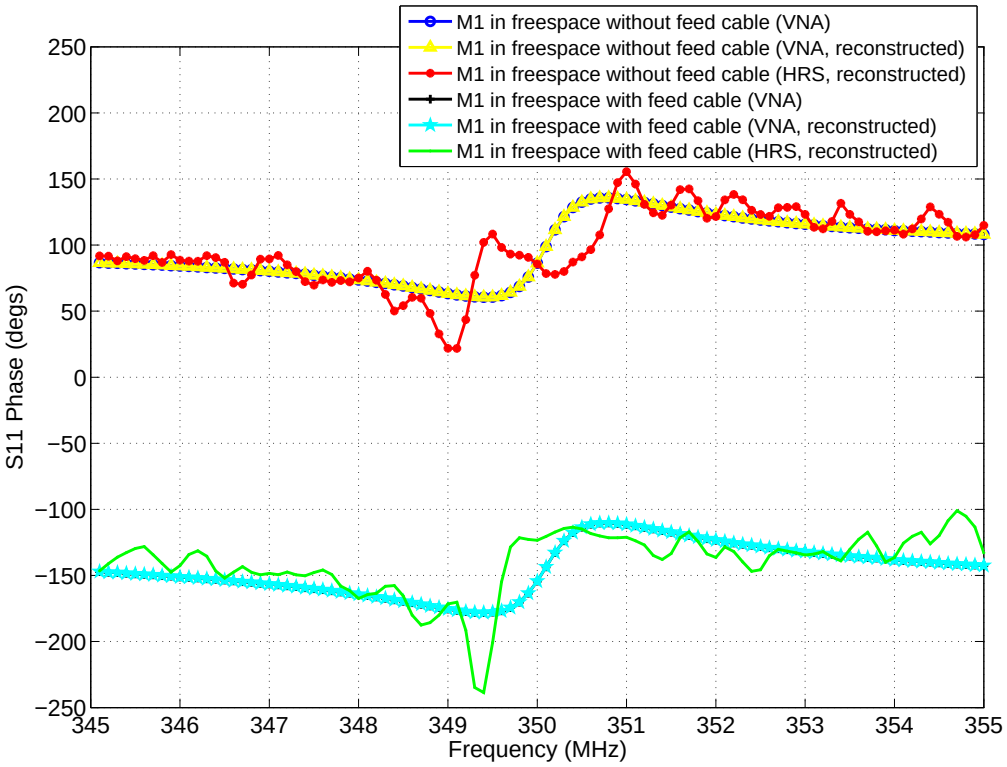

Figure 13. M1: Freespace S11 phase.

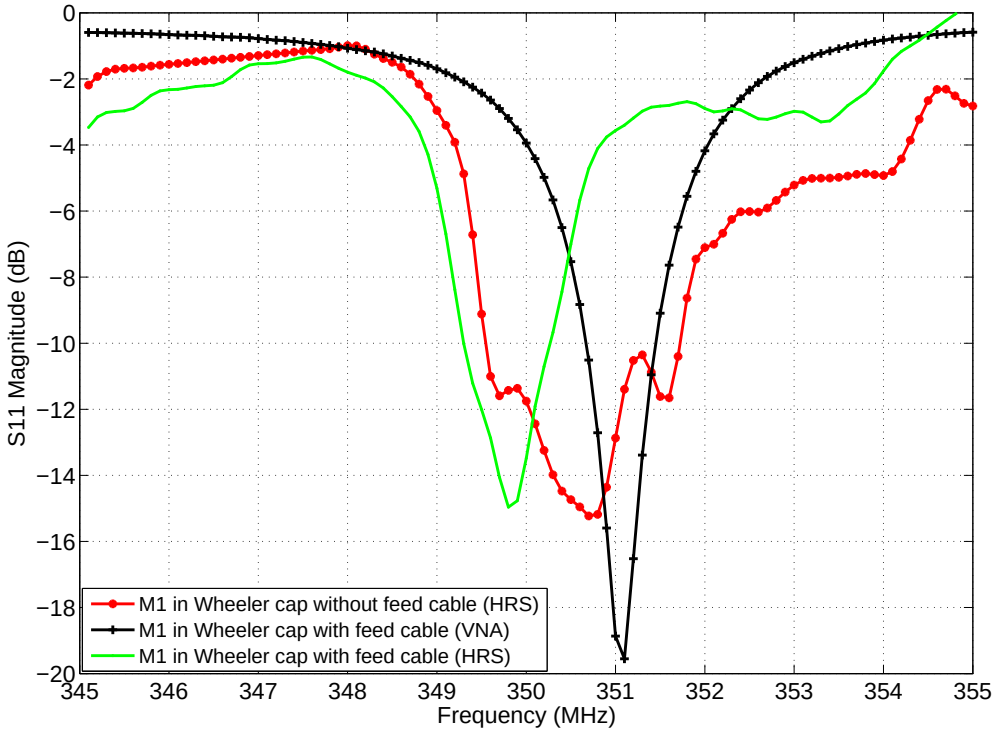

Figure 14. M1: Wheeler cap S11 magnitude.

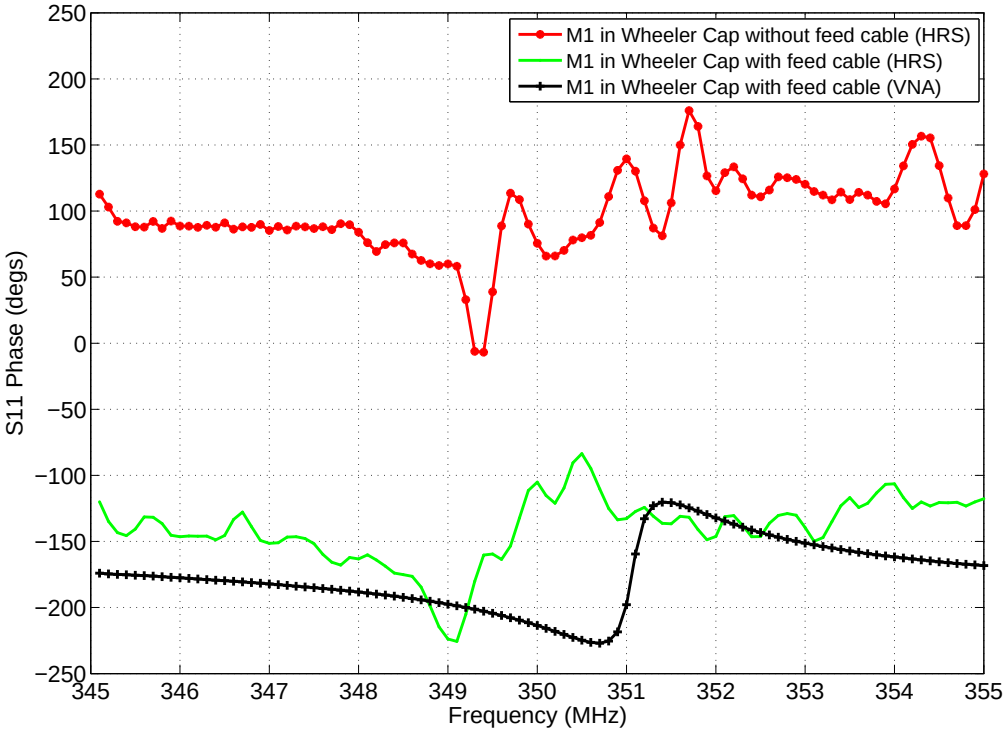

Figure 15. M1: Wheeler cap S11 phase.

X. Conclusions

THESE measurements have shown that the HRS can be integrated with the RF over fibre optic measurement system to improve the sensitivity of ESA radiation pattern measurements. The measurements provide a baseline for reflection coefficient measurements of host-embedded antennas using the HRS. The measurement system effectively isolates the antenna from the RF source while enabling the measurement of its reflection coefficient. Consequently, the radiation from the antenna rather than from the RF cable and the antenna is measured. The discrepancy becomes significant when measuring ultra-wideband antennas or narrowband antennas with truncated ground plane.

A new technique for isolating a ESA from the measurement system has been developed and integrated into the Wheeler Cap to characterise the efficiency of ESA and to explore the effects of ground plane on the efficiency of an ESA.

The signal flow through the measurement system has been analysed using flow chart analysis to gain the transfer function of the system and derive its full scattering parameters.

Measurements have been undertaken of the radiation pattern, reflection coefficient and radiation efficiency of several antennas. In this paper the measurements of Monopole 1 have been discussed. These measurements have revealed the importance of isolating the ESA from measurement system for radiation pattern and radiation efficiency measurements.

The radiation pattern measurements show that radiation from the common mode current on the feed cable contributes significantly to the far-field pattern of the antenna. This biases the measurements toward the antenna having a higher gain. Thus the gain of the ESA is dominated by the RF measurement technique used in characterising it. Isolating the ESA from the RF measurement system by using the HRS system reveals these effects and measures the gain of the ESA, which tends to be significantly less than when measured in the conventional manner.

XI. Acknowledgements

This work was done over a number of years by the Defence Science Technology Laboratory (DSTL) Security Sciences Department (formerly Electronics Department based in Malvern, UK) and was funded by the Ministry of Defence. The author wishes to thank all members of staff in the department for their past and continued contributions to this work.

REFERENCES

[1] H. Wheeler, "The radiansphere around a small antenna," *Proceedings IREE Australia*, vol. 47, pp. 1325–1331, Aug 1959.

[2] G. S. Smith, "An analysis of the wheeler method for measuring the radiating efficiency of antennas," *IEEE Transactions on Antennas and Propagation*, vol. 25, pp. 552–556, Jul 1977.

[3] D. M. Pozar and B. Kaufman, "Comparison of three methods for the measurement of printed antenna efficiency," *IEEE Transactions on Antennas and Propagation*, vol. 36, pp. 136–139, Jan 1988.

[4] H. Choo, R. Rogers, and H. Ling, "On the wheeler cap measurement of the efficiency of microstrip antennas," *IEEE Transactions on Antennas and Propagation*, vol. 53, pp. 2328–2332, Jul 2005.

[5] M. Geissler, O. Litschke, D. Heberling, P. Waldow, and I. Wolff, "An improved method for measuring the radiation efficiency of mobile devices," *IEEE Antennas and Propagation Society International Symposium*, vol. 4, pp. 743–746, June 2003.

[6] R. H. Johnston and J. G. McRory, "An improved small antenna radiation-efficiency measurement method," *IEEE Antennas and Propagation Magazine*, vol. 40, pp. 40–48, Oct 1998.

[7] W. E. McKinzie, "A modified wheeler cap method for measuring antenna efficiency," *IEEE Antennas and Propagation Society International Symposium*, vol. 4, pp. 542–545, Jul 1997.

[8] T. H. Crowley, "Measurement of antenna efficiency by using metals with different surface resistivities," *Technical Report No.478-21*, 1953.

[9] E. H. Newman, P. Bohley, and C. H. Walter, "Two methods for the measurement of antenna efficiency," *IEEE Transactions on Antennas and Propagation*, vol. 23, pp. 457–461, Jul 1975.

[10] J. B. Andersen and F. Hansen, "Antennas for vhf/uhf personal radio: A theoretical and experimental study of characteristics and performance," *IEEE Transactions on Vehicular Technology*, vol. 26, pp. 349–356, Nov 1977.

[11] J. Ashkenazy, E. Levine, and D. Treves, "Radiometric measurement of antenna efficiency," *Electronics Letters*, vol. 21, pp. 111–112, Jan 1985.

[12] R. H. Johnston, J. G. McRory, and L. Ager, "A new small antenna efficiency measurement method," *IEEE Antennas and Propagation Society International Symposium*, vol. 1, pp. 176–179, Jul 1996.

[13] R. H. Johnston and J. G. McRory, "Small antenna efficiency by the reflection and the Q measurement methods," *IEEE Antennas and Propagation Society International Symposium*, vol. 3, pp. 1810–1813, Aug 1999.

[14] K. Rosengren, P.-S. Kildal, J. Carlsson, and O. Lunden, "A new method to measure radiation efficiency of terminal antennas," *Antennas and Propagation for Wireless Communications Conference*, vol. 1, pp. 5–8, Nov 2000.

[15] W. L. Schroeder and D. Gapski, "Direct calorimetric measurement of small antenna radiation efficiency," *Antennas and Propagation Society International Symposium*, vol. 2b, pp. 744–747, Jul 2005.

[16] N. J. McEwan, R. A. Abd-Alhameed, M. Nasir, and Z. Abidin, "A modified radiometric method for measuring antenna radiation efficiency," *IEEE Transactions on Antennas and Propagation*, vol. 51, pp. 2099–2105, Aug 2003.

[17] T. Maeda and T. Morooka, "Radiation efficiency measurement method for electrically small antennas using radio wave scatterers," *IEEE Antennas and Propagation Society International Symposium*, vol. 1, pp. 324–327, Jun 1988.

[18] M. Murase, Y. Tanaka, and H. Arai, "Propagation and antenna measurements using antenna switching and random field measurements," *IEEE Transactions on Vehicular Technology*, vol. 43, pp. 537–541, Aug 1994.

[19] W. L. Schroeder and D. Gapski, "Direct measurement of small antenna radiation efficiency by calorimetric method," *IEEE Transactions on Antennas and Propagation*, vol. 54, pp. 2646–2656, Sept 2006.

[20] K. Rosengren, P.-S. Kildal, J. Carlsson, and J. Carlsson, "Characterization of antennas for mobile and wireless terminals by using reverberation chambers: improved accuracy by platform stirring," *Microwave and Optical Technology Letters*, vol. 30, pp. 391–397, Jul 2001.

[21] K. R. Carver and J. W. Mink, "Microstrip antenna technology," *IEEE Transactions on Antennas and Propagation*, vol. 29, pp. 2–24, Jan 1981.

[22] R. Johnson, *Antenna Engineering Handbook*. McGraw-Hill, Inc, 1993.

[23] R. Urban and C. Peixeiro, "Ground plane size effects on a microstrip patch antenna for small handsets," *International Conference on Microwaves, Radar and Wireless Communications*, vol. 2, pp. 521–524, May 2004.

[24] M. John, J. A. Evans, M. J. Ammann, and J. C. Modro, "Reduction of ground-plane-dependent effects on microstrip-fed printed rectangular monopoles," *IET Microwaves, Antennas and Propagation*, vol. 2, pp. 42–47, Feb 2008.

[25] K. Kurokawa, "Power waves and the scattering matrix," *IEEE Transactions on Microwave Theory and Techniques*, vol. 13, pp. 194–202, Mar 1965.

[26] R. Ludwig and P. Bretchko, *RF Circuit Design, Theory and Applications*. Prentice-Hall, 1 ed., 2000.

MEASUREMENT OF ELECTRICALLY SMALL ANTENNAS

Suhail Barot, Paul E. Mayes, Paul W. Klock and Jennifer T. Bernhard
Electromagnetics Laboratory, University of Illinois at Urbana-Champaign

ABSTRACT: Measuring and biasing electrically small antennas presents several challenges due to the small impedances and high mismatches of the antennas. When these antennas are fed, however, the mismatch results in currents on the feed cable. These currents radiate, and their effect can be seen in the radiation resistance and radiation pattern. This paper examines the effects of cable radiation on electrically small antennas – specifically center loaded dipoles. We observed cable radiation, and showed that the radiation could be suppressed by use of baluns and ferrites. However our most noteworthy result was that currents on the feed cable diminished without any intervention at the resonant point of the antennas.

INTRODUCTION

Electrically small antennas are those that fit within a sphere having diameter less than half a wavelength at the frequency of operation. This class of antennas is of great interest, given the continual drive to miniaturize communication systems, especially for handheld consumer devices. One of the simplest antenna classes in existence is the linear half-wavelength dipole antenna, and antennas derived from it. This is a balanced antenna class and feeding such antennas is the focus of this paper.

Electrically small antennas can be derived from the half-wavelength dipole by inductive loading. If loads and feeds are placed on the structure consistent with its symmetry, the antenna will remain a balanced structure. The challenge with this technique is the reduction in radiation resistance and bandwidth of the antenna. We have shown several techniques to inductively load linear antennas, and/or combine them to utilize multiple resonances, so as to achieve increased radiation resistances or bandwidths [1].

Coaxial transmission lines are a common unbalanced line used in feeding antennas. However, when feeding balanced lines, we expect that currents to flow onto the shield and radiate. This effect distorts the shape of the radiation pattern and introduces cross-polarization. Additionally, when measuring antennas, the cable radiation makes it difficult to extract the true properties of the antenna. These difficulties are amplified when dealing with electrically small antennas, because the large mismatch with the cable increases shield currents, while the antenna radiation is suppressed due to the small size.

In this study, we examine the effects of feeding symmetric, loaded dipoles with a coaxial transmission line. We seek to better understand the effect of this feed method on the antennas and learn how to reduce the expected cable radiation.

The linear antennas used in the study all have cross sections of 1.25 mm by 1 mm and had two loads placed 5 mm offset from the center of the antenna. The frequency band of interest is 100 MHz to 500 MHz, though smaller bands may be shown for clarity. All results in this paper have been generated using Ansoft HFSS® [2].

EFFECT OF COAXIAL FEEDS

In Fig. 1, we simulate a 300 mm dipole, with a simple lumped excitation, and obtain a family of curves for different loads. The unloaded antenna shows the conventional dipole result with the curves moving to the left, and becoming less continuous with loading. This shows the expected reduction in radiation resistance and bandwidth with loading. Also as we move off-resonance, we can see that the more heavily loaded antennas trace out impedance curves further to the outside of the Smith chart.

In Fig. 2, we simulate the same antenna, with the same loads, but fed with a 500 mm coaxial transmission line. We then perform a phase rotation within HFSS to de-embed the transmission line and obtain the impedance at the antenna terminals. The coaxial cable used has outer diameter 2.3 mm, and has characteristic impedance of 50 Ω.

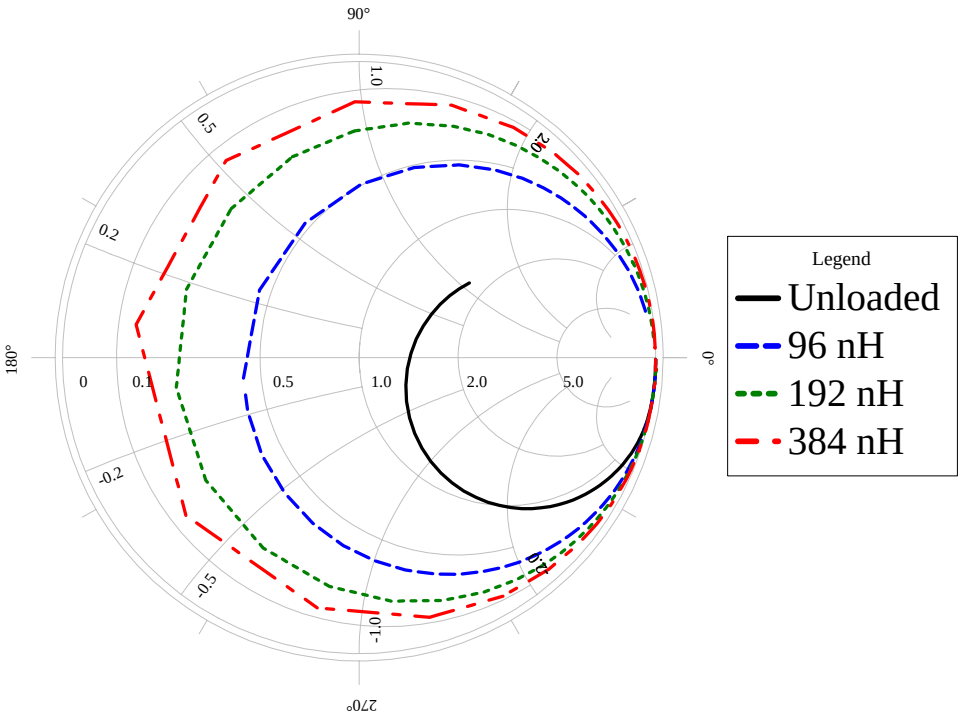

Fig. 1. 300 mm loaded dipole antenna with lumped port feed.

When the two figures are compared, we see that the curves appear very similar, especially at resonance. In Table 1, we can see a comparison of impedances and resonant frequencies for different cases, from the two simulations. We see very good agreement for all the loaded cases. When off-resonance however, we can see that the cable-fed

simulations reflect less power back to the source, probably due to radiation by the feed cable. This suggests that cable radiation is being suppressed at resonance.

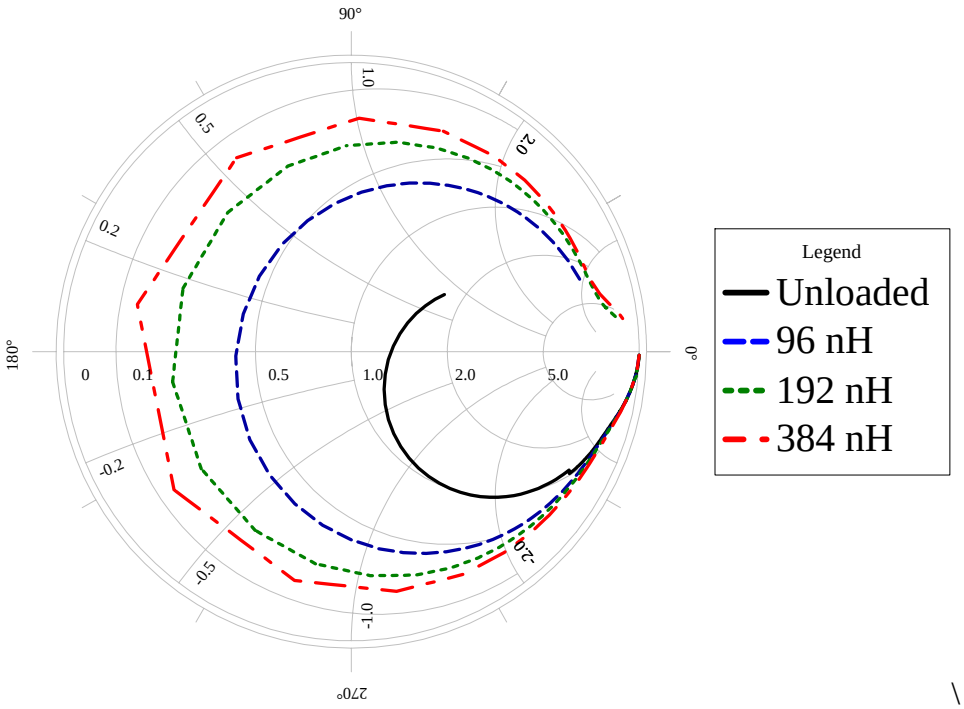

Fig. 2. 300 mm loaded dipole antenna with coaxial transmission line feed.

Loading	Lumped port feed		Coaxial line feed	
	Frequency of Resonance	Resistance at Resonance	Frequency of Resonance	Resistance at Resonance
Unloaded	471 MHz	70.17 Ω	474 MHz	65.82 Ω
96 nH	301 MHz	22.02 Ω	300 MHz	21.34 Ω
192 nH	237 MHz	11.77 Ω	237 MHz	11.60 Ω
384 nH	178 MHz	6.86 Ω	178 MHz	6.86 Ω

Table 1. Frequency and Resistance comparison for 300mm loaded dipole antenna having a lumped port feed vs. a coaxial feed

Fig. 3 and Fig. 4 show results for simulations of a 150 mm antenna configured equivalently to the above. The same off-resonance radiation from the cable simulation is seen. However, the curves again match up well at resonance, as displayed in Table 2. As the antenna is smaller, it radiates less, and the effects of the cable are more pronounced.

The unloaded case can barely be made out, as it does not resonate over the band simulated.

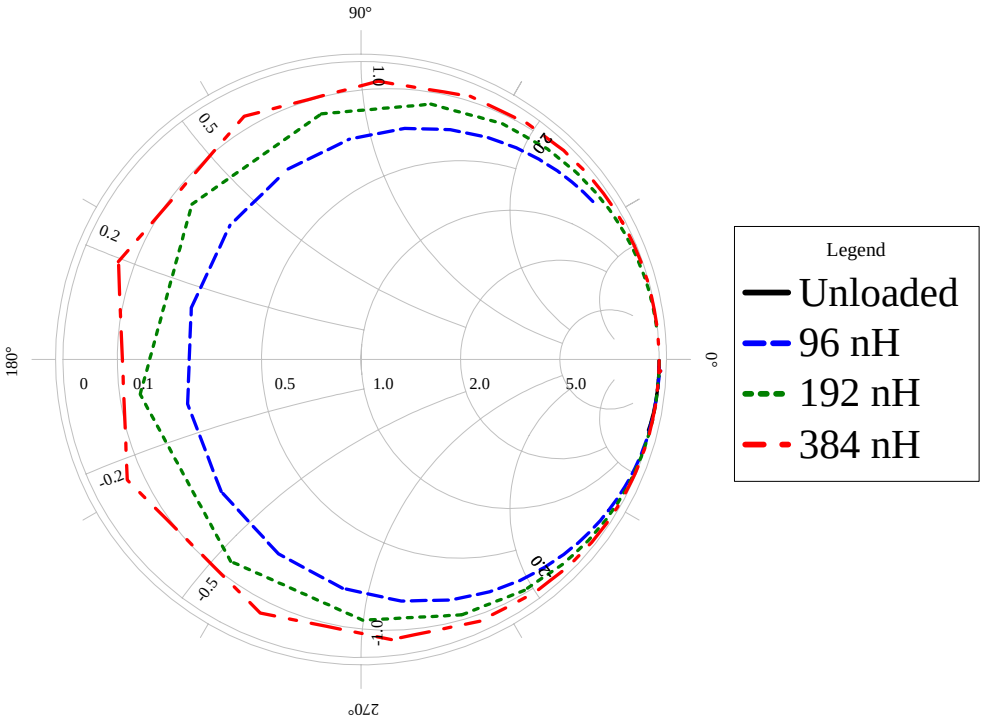

Fig. 3. 150 mm loaded dipole antenna with lumped port feed.

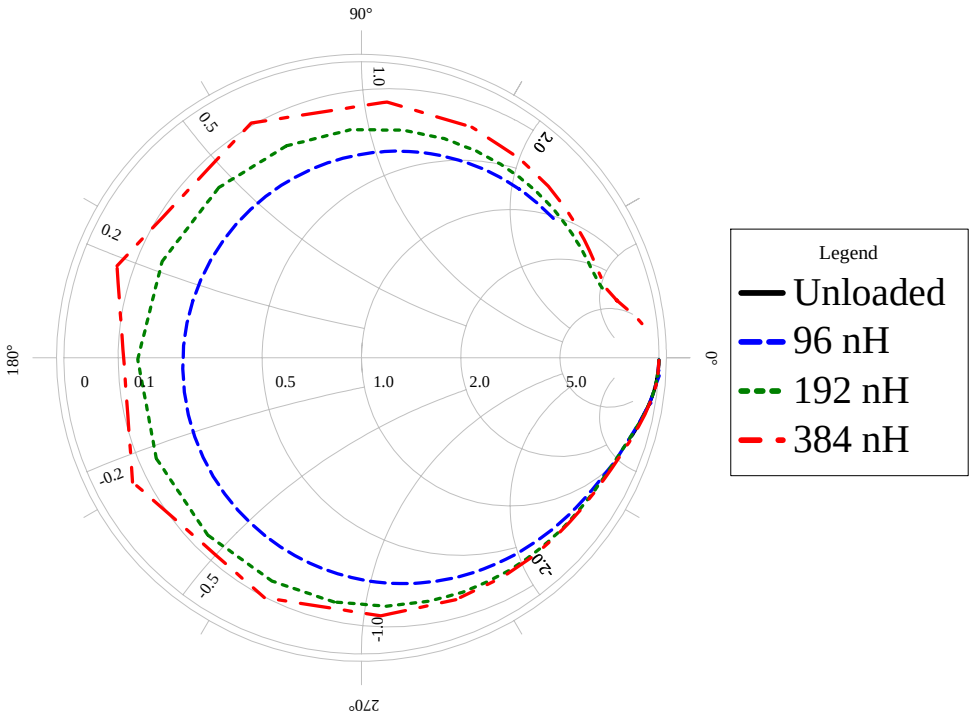

Fig. 4. 150 mm loaded dipole antenna with coaxial transmission line feed.

Loading	Lumped port feed		Coaxial line feed	
	Frequency of Resonance	Resistance at Resonance	Frequency of Resonance	Resistance at Resonance
96 nH	450 MHz	12.80 Ω	450 MHz	12.50 Ω
192 nH	337 MHz	7.23 Ω	334 MHz	7.09 Ω
384 nH	245 MHz	3.34 Ω	246 MHz	3.53 Ω

Table 2. Frequency and Resistance comparison for 150 mm loaded dipole antenna having lumped port vs. coaxial feeds

DETAILED CASE STUDY

We now focus in on the case of the 150 mm antenna with 384 nH loading. In Fig. 5, impedances for both the lumped feed case and the transmission line case are displayed on the same chart. We can clearly see that the impedance trace for the antenna with the coaxial feed is squeezed toward the center when off-resonance. Fig. 6 displays the same information, in the form of the magnitude of the reflection coefficient. This shows the effect of cable radiation, reducing the power reflected back to the source, when off-resonance.

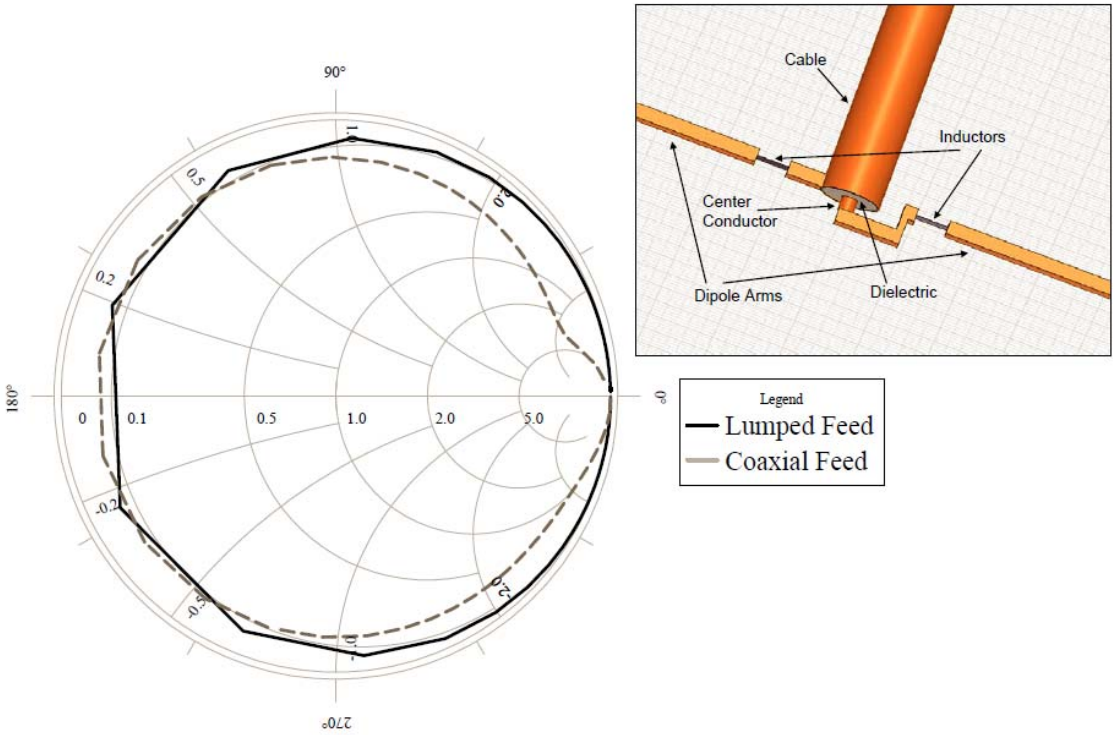

Fig. 5. 150 mm antenna with 384 nH loading, showing effects of off-resonance cable radiation. Inset figure shows antenna feed structure.

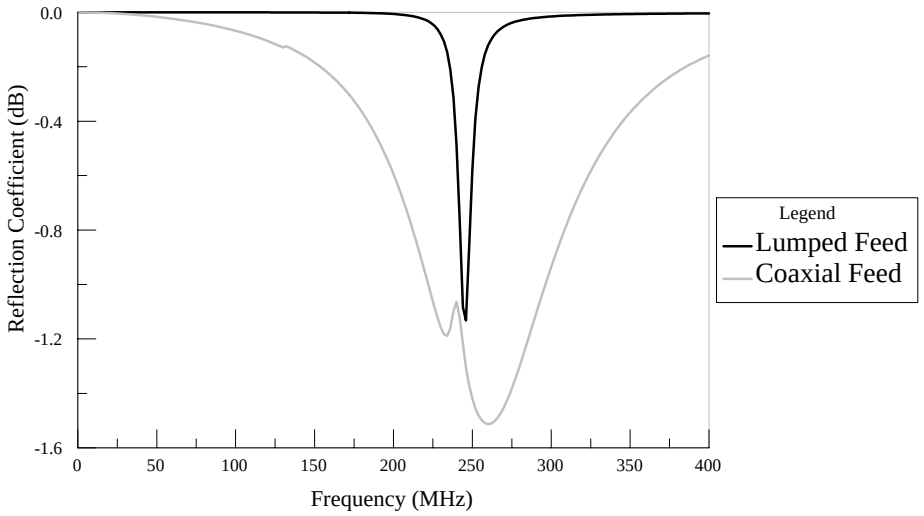

Fig. 6. 150 mm antenna with 384 nH loading, showing effects of off-resonance cable radiation vs. frequency.

In Fig. 7 and Fig. 8, we show the radiation patterns of the antenna at 246 MHz (resonance) and 300 MHz (off-resonance), in the plane containing the antenna, and perpendicular to the cable. The cable and antenna both sustain linear currents and produce dipole patterns, but are perpendicular to each other. Thus we can attribute the electric field component in the plane to the antenna and the perpendicular component to the cable. We can see that the antenna dominates at resonance but that the cable radiates much more strongly off-resonance.

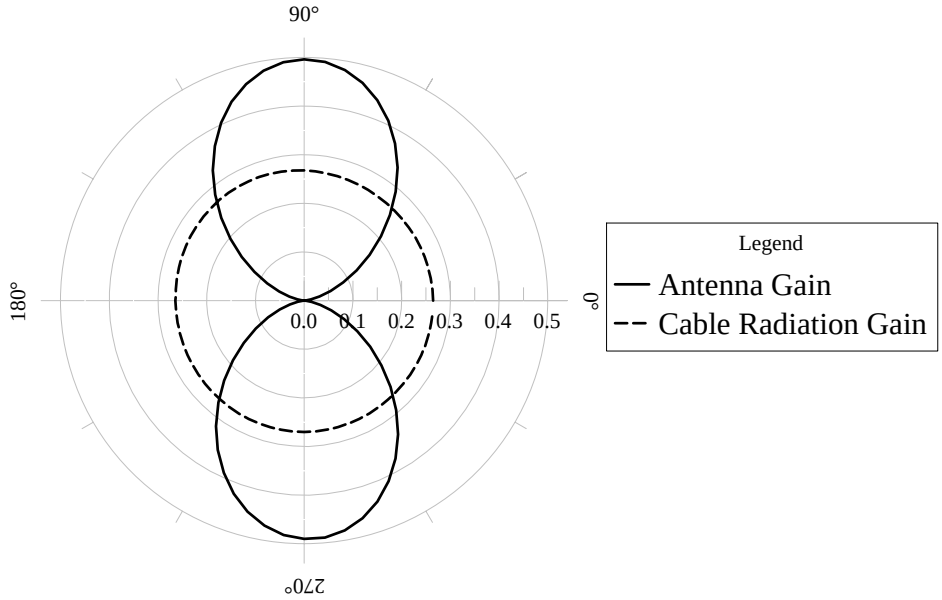

Fig. 7. Radiation Pattern for 150 mm antenna with 384 nH loading, at 246 MHz (resonance).

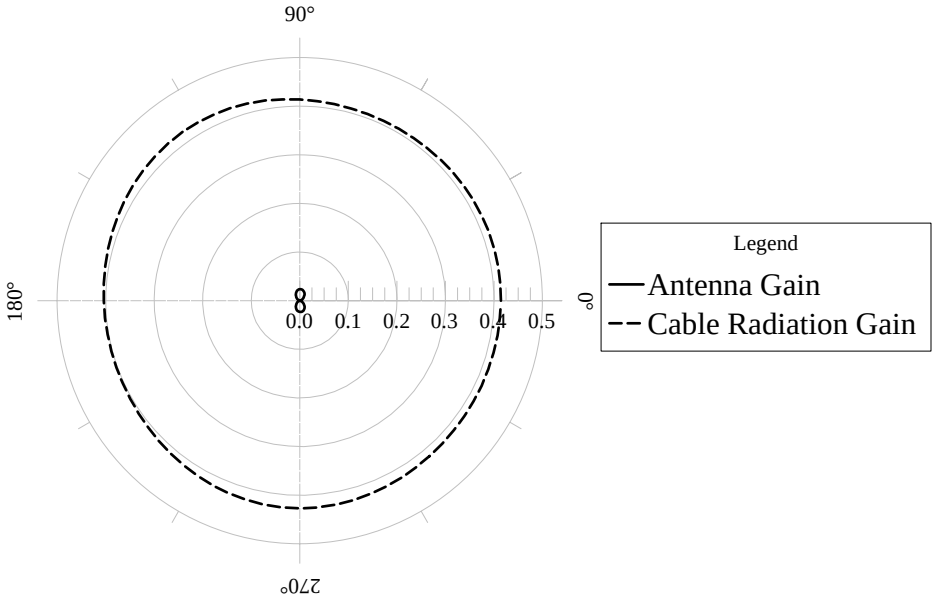

Fig. 8. Radiation Pattern for 150 mm antenna with 384 nH loading, at 300 MHz.

Since the current suppression at resonance was unexpected, we were concerned that it might be a quirk of the simulator, caused by some strange interaction between the cable and the problem boundary. This was tested in Fig. 9 by taking the lumped port feed case and adding a large solid metal artifact to act as a dummy cable.

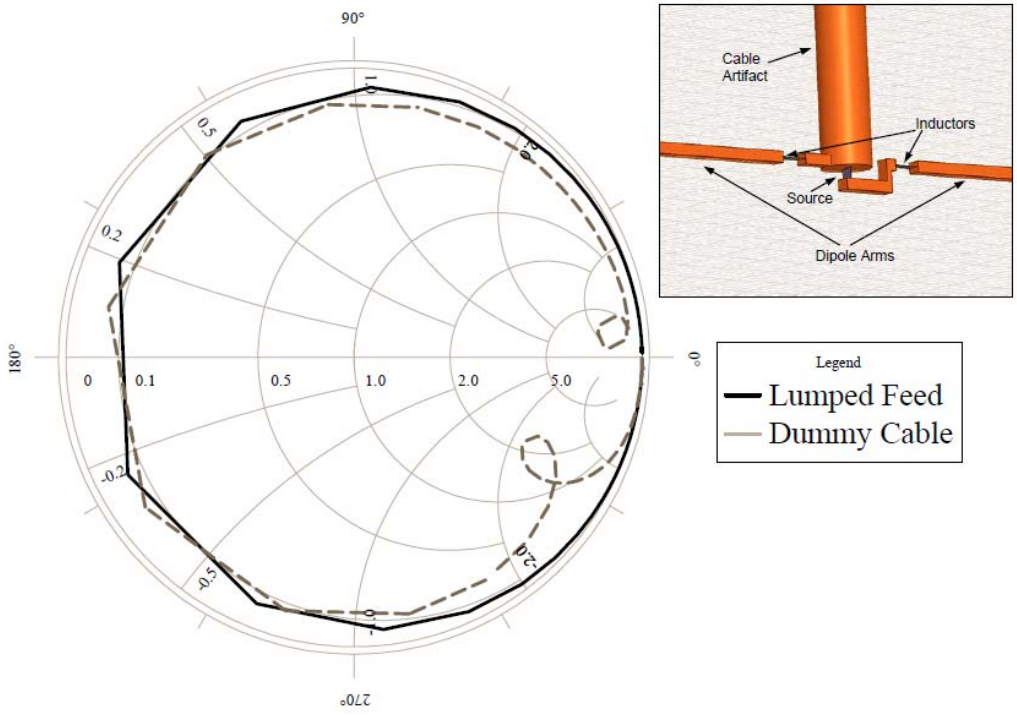

Fig. 9. 150 mm antenna with 384 nH loading, showing effects of dummy cable. Inset figure shows the cable artifact placement.

What we see is that while the presence of the artifact introduces off-resonance loops in the impedance plot, the resonant behavior completely follows the simple lumped feed case. The resonant frequency is shifted by only 1 MHz. This suggests that the artifact (or feed cable) does not carry significant current at resonance.

A common technique used in suppressing cable radiation is the use of a ferrite choke - a hollow cylinder of a high permeability material slipped over the feed cable, that acts as an inductive load, to decrease current flowing on the feed cable. We performed such a simulation with a 2 cm length choke having a $\mu_r = 125$, placed 1cm from the antenna terminals. The results, shown in Fig. 10, are that the choke is effective at suppressing cable radiation, but has no effect at resonance. This appears to confirm the hypothesis of having no feed cable current at resonance, leaving nothing to be suppressed by the choke.

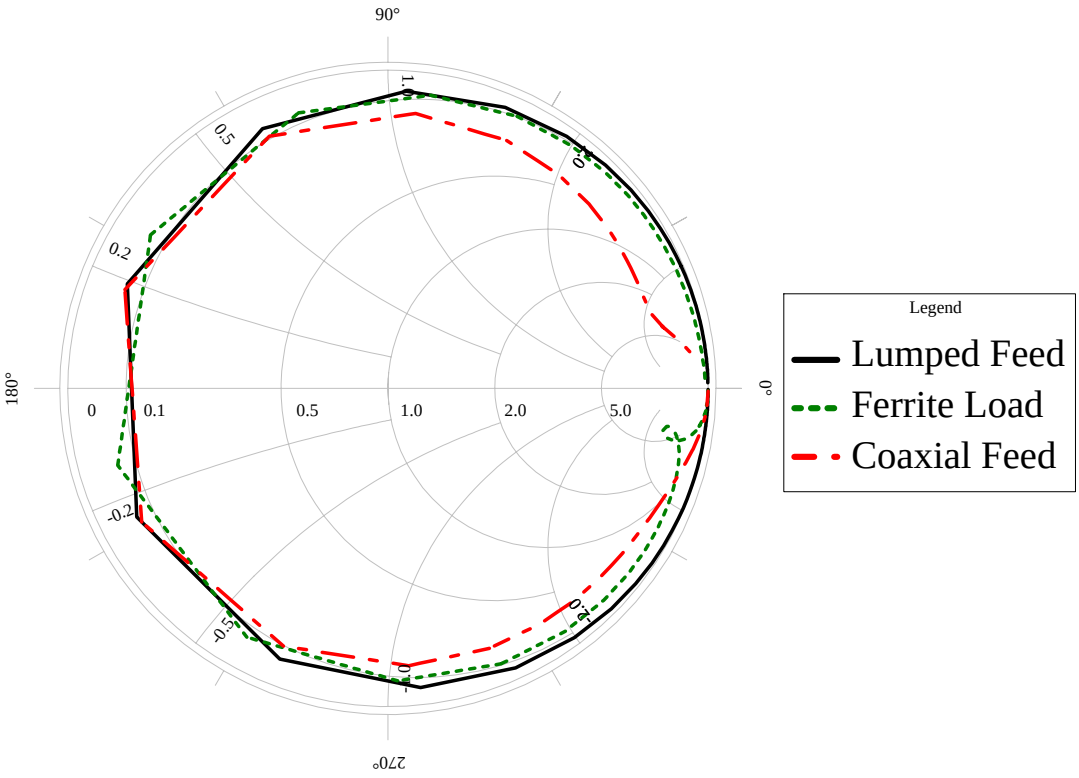

Fig. 10. 150mm antenna with 384 nH loading, showing effects of a ferrite choke.

CURRENT DISTRIBUTIONS

To better understand this behavior, we examine the current distributions in Fig. 11-14. In these figures, we see the currents on the antenna and a small portion of the feed cable, at four frequencies – 150 MHz, 200 MHz, 250 MHz and 300 MHz. The currents on the antenna cable are displayed on a log scale. Please see the electronic version of this paper for color plots, which are easier to interpret.

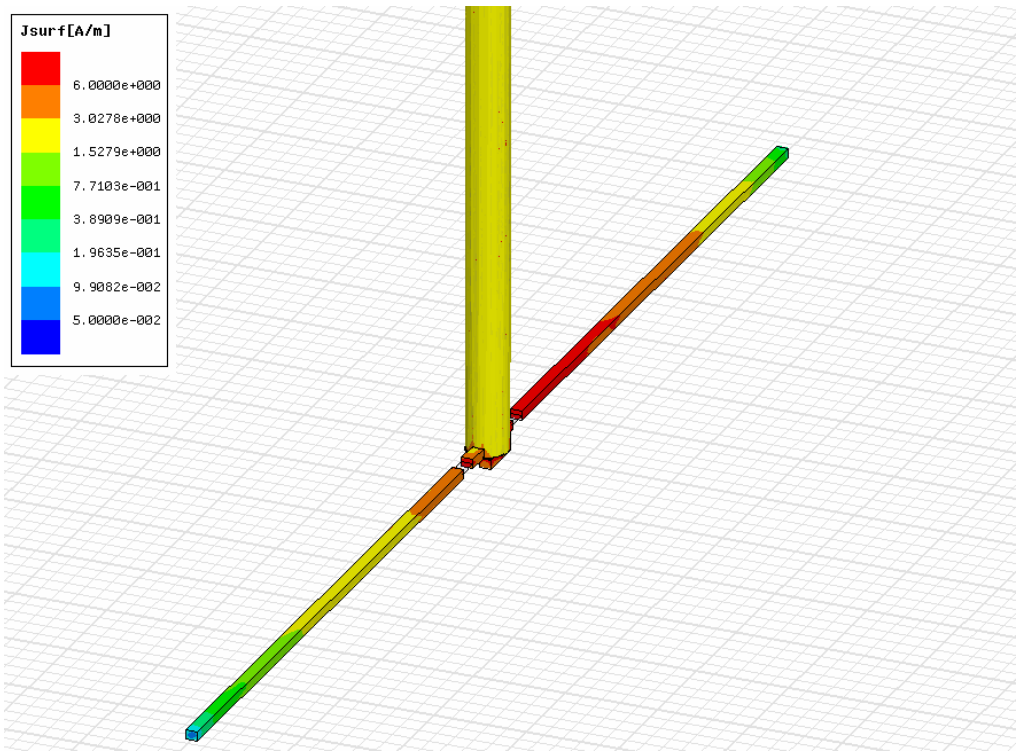

Fig. 11. Current distribution of 150 mm antenna with 384 nH loading for f = 200 MHz.

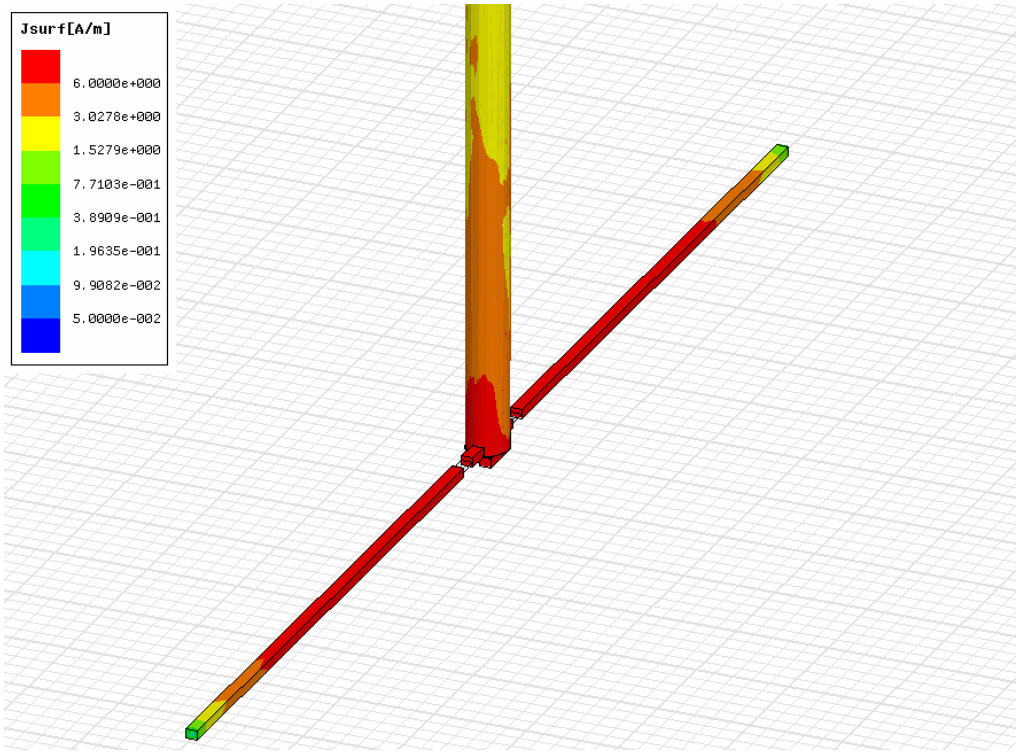

Fig. 12. Current distribution of 150 mm antenna with 384 nH loading for f = 250 MHz (resonance).

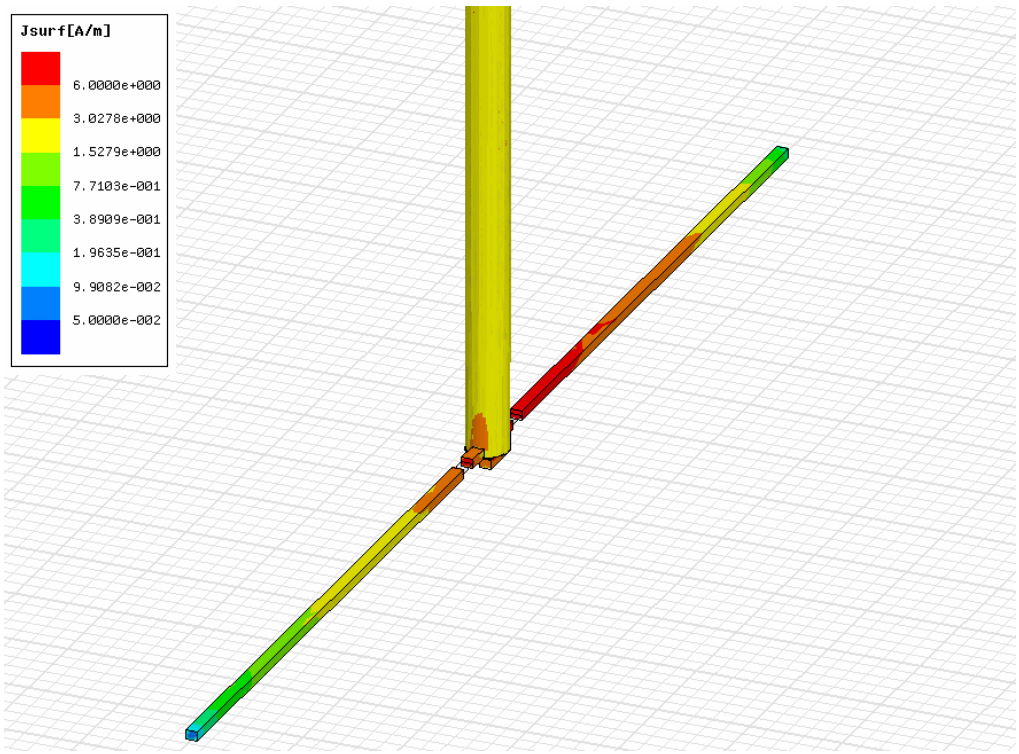

Fig. 13. Current distribution of 150 mm antenna with 384 nH loading for f = 300 MHz.

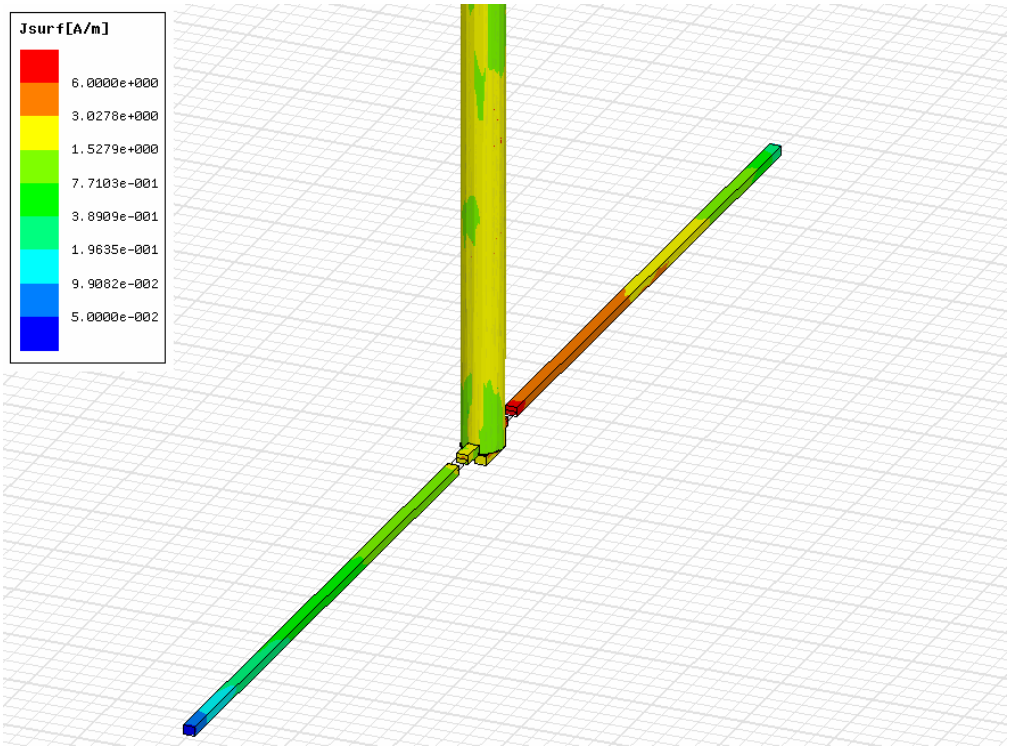

Fig. 14. Current distribution of 150 mm antenna with 384 nH loading for f = 350 MHz.

What we notice is that the current distribution on the antenna is generally unbalanced, despite the symmetric structure of the antenna. This is because of the presence of the cable, which unbalances the system. Thus the arm connected to the center conductor has more current than the arm connected to cable shield, resulting in balancing currents flowing onto the shield. However, the currents on both arms at resonance are equivalent. This means that currents do not need to flow onto the shield, and we see that the shield currents are sub-dominant to the arm currents in this case. This gives us the results seen in the Smith charts.

CONCLUSION

We see that when feeding and measuring electrically small symmetric linear antennas at resonance, we can use a simple coaxial feed, without suffering ill-effects. While narrow-band in nature, this cable radiation suppression effect appears to be sufficient to avoid the use of baluns and chokes over the operating band. Given that those devices would add to the antennas electrical size, this is helpful in simplifying and miniaturizing the antennas system. More work is needed to explore this effect in asymmetric linear antennas, and with other unbalanced transmission lines.

REFERENCES

[1] P. E. Mayes, P W. Klock and S. Barot, "Using Series Resonators in Parallel To Achieve Broadband Performance in Inductively Loaded Antennas," *2008 Antenna Applications Symposium*, Allerton Park, IL, September 2008.

[2] "Ansoft HFSS, Version 9.2.1," Ansoft Corporation, Pittsburgh, PA.

REDUCED-SIZE LINEAR ANTENNA ELEMENTS

Paul E. Mayes, Paul W. Klock and Suhail Barot
Electromagnetics Laboratory
University of Illinois at Urbana-Champaign

Abstract: Loading with inductive reactances has long been used as a method to produce a series resonance in short lengths of linear conductor, and thus to produce a small antenna. However, problems occur with conventional methods of using this idea. Sometimes, it is difficult to transfer power from a short element to a practical line or load because of the relatively small value of real input impedance at resonance. Even though the short antenna may have a small value (difficult to match) real impedance when fed at its center, the impedance can be increased to a practical value by feeding the resonator at a point closer to the end. Inductors near the end of a resonator can also be used to increase the real part of the input impedance by maintaining near-constant current over an appreciable part of the element length.

Although the above procedures can be used to produce a reasonable match to a shortened linear radiator, the input impedance may change rapidly with frequency so that the operating bandwidth will be small. The introduction of complexity into the element so that multiple resonances are made to occur provides a way to increase the bandwidth of operation.

1. Introduction

Many electronic devices are getting smaller, why not antennas? There are several problems that remain to be solved before we can say that antennas have been reduced in size in a manner similar to that which has occurred with many other electronic devices. The argument is often made that antennas that are small compared to the wavelength will be so small that they will not radiate. What this really means is that the input resistance at resonance of such a small antenna is likely to be small compared to the characteristic resistance of conventional transmission lines, or small compared to the resistance of the generator that is producing the signal to be radiated. While this proposition is generally correct, it ignores the fact that there are ways of solving the impedance-matching problem.. When the system has been designed so that all of the power available has been delivered to the antenna, then the best has been achieved. The job of "impedance matching" is to make sure that the impedance at the antenna terminals is equal to the complex conjugate of the impedance seen in the connecting circuitry.

For years it has been recognized that the problem of achieving impedance match in a small antenna is simplified by operating the antenna and accompanying matching circuitry as a resonant device near the frequency of resonance. There are many examples of resonant antennas that have values of input impedance that depend upon the location of the point of connection. This point is a matter of choice and therefore becomes a

matter for design. The frequency of resonance is not greatly affected by changing the location of the feed, but the value of the impedance may be quite different.

As usual, Mother Nature may be expected to extract some compensation for her willingness to cooperate to some extent in the design of small antennas. While the solution of the impedance-matching problem may be possible, it does not follow that it is necessarily easy or without cost. For example, the level of the input resistance of an antenna depends not only upon the radiation from the antenna, but also upon the conversion of the input power into other forms such as heat. A small antenna must be carefully designed so that the power lost in conversion to heat is kept small. Otherwise, the efficiency of the small antenna will be reduced, an undesirable effect. Another consequence of making the antenna small is the rapid variation with frequency of the amount of energy that is stored in the immediate vicinity of the antenna. A popular way of evaluating this effect is to define a bandwidth at which the antenna reactance (due to the stored energy) is equal to or less than the antenna resistance (due to irretrievable energy conversion). While there are ways of minimizing the power lost in heat, a much bigger improvement in bandwidth can be achieved by making the system resonant at more than one frequency, carefully selected with respect to one another. The achievement of wide match bandwidth has been the principal focus of preceding papers in this series.

Much time and effort has gone into the solution of the problem of making small antennas and this effort is continuing. In this, and preceding papers in this series, [1], [2], we are trying to discuss some of the recent work that seems to be pointing the way to achieving practical results.

2. Self-matched, tuned radiating resonators

The case of a linear antenna element is one of the simplest examples that can be used to introduce the idea of matching a small antenna. Suppose we first make the antenna resonant at a length that is smaller than usual. That is to say, the antenna is resonant at a frequency for which the wavelength is much less than the length of the element. This can be done by adding inductive elements distributed along the axis of the conductor that forms the radiator. In the past, this has often been done by placing the inductive element near the feed point, near the base of a monopole version of the element. The argument can be made that the frequency of resonance will indeed be reduced by so placing an inductor, since the impedance of the antenna element itself will be capacitive when the element is less than one quarter wavelength in length. Although the presence of the inductor near the base, in series with the feed point, will shift the resonant frequency down, as desired, it does not counter the tendency of the resistance observed at the feed point to decrease in magnitude as the element length is reduced. However, it is also well known that the input impedance observed at the feed point of a linear (straight-wire) antenna can be made to assume almost any value simply by changing the location of the feed point. This result is observed to occur regardless of the value of the resonant frequency. The resonant frequency is determined by the size of any loading inductors and the length of the wire and is not greatly changed by changing the location of the feed point.

3. Center-fed blade dipole

The validity of the above statements is readily established by observing the computed (or measured) values of the input impedance under the presumed conditions. Figure 1 shows the input impedance as it is calculated for a blade antenna by the computer code LFMoM (low-frequency method of moments) [3]. Figure 1 is a plot of the computed current along the axis at a frequency that is near resonance. Note that the tip-to-tip length of the blade is 15 cm, which is one-half wavelength at 1 GHz. However, the resonant frequency (Fig. 2) is only approximately 490 MHz when a 191.8 nH inductor is placed on the same central patch as the source. Whereas the axial current would be expected to be sinusoidal on an unloaded element, the computed axial current at resonance is observed to be more nearly triangular. This is a consequence of the reduced length of the element, the sinusoidal function being nearly linear when observed at the necessarily small arguments that locate points on the small antenna.

4. Off-center inductances, off-center fed blade dipole

Now let us suppose that the load inductors are moved from the center (feed point) of the antenna to patches that are near the ends [4]. Figure 3 shows the axial current on the dipole when lumped inductors are placed on the fourth patch from each end of an antenna that is 21 cm in length (z from -9.375 to 6.375 cm). The feed point on this antenna is located at the center of the sixth patch from the upper end (z = 4.875 cm). By comparing Figs. 1 and 3, it is apparent that the current moment is greater for the latter case.

Not only does the increased current moment produce a larger value for the input resistance at resonance, but the resistance at resonance can be altered by changing the parameters of the antenna. Figure 4 shows the computed input impedance for the set of parameters that are given in the figure. Figure 5 shows how the input resistance at resonance for an antenna with the same geometric parameters can be made to pass through the center of the chart, the point of perfect match to the attached cable, by changing the value of the inductors.

Similar results can be obtained for other antennas. Figure 6 shows the computed input impedance for two antennas, one of full length and the other loaded with a central inductor. Figure 7 shows the computed current distribution near resonance for this linear (blade) antenna. Figures 8 and 9 show the results for the same length of conductor but the resonance has been lowered by a greater amount by applying the loads near the ends. The center load is appropriate for light values of loading whereas the location of the source on the sloping part of the current distribution works for more heavily loaded cases.

5. Conclusions and future work

The results described here all apply to linear elements that have a pair of terminals. The input impedance shows the characteristics of a series resonance. As such, several such circuits with appropriate different values of resonance can be used in parallel to increase the match bandwidth of the antenna [5]. It has already been shown that direct connection of particular series resonators will produce multi-band response whereas reversal of the

leads will result in wideband response. It is planned to compute, and also to build and test, several examples,

.

Figures

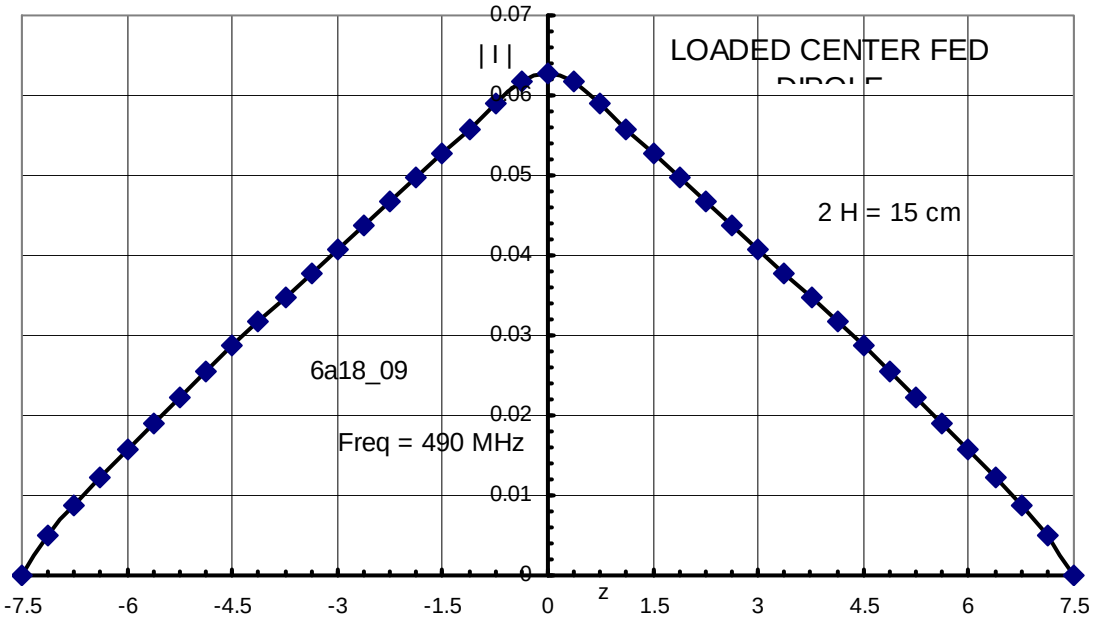

Figure 1. Computed values of the near-resonance current along the axis of a blade dipole that is loaded (in the same central patch as the source) with a 191.8 nH inductor.

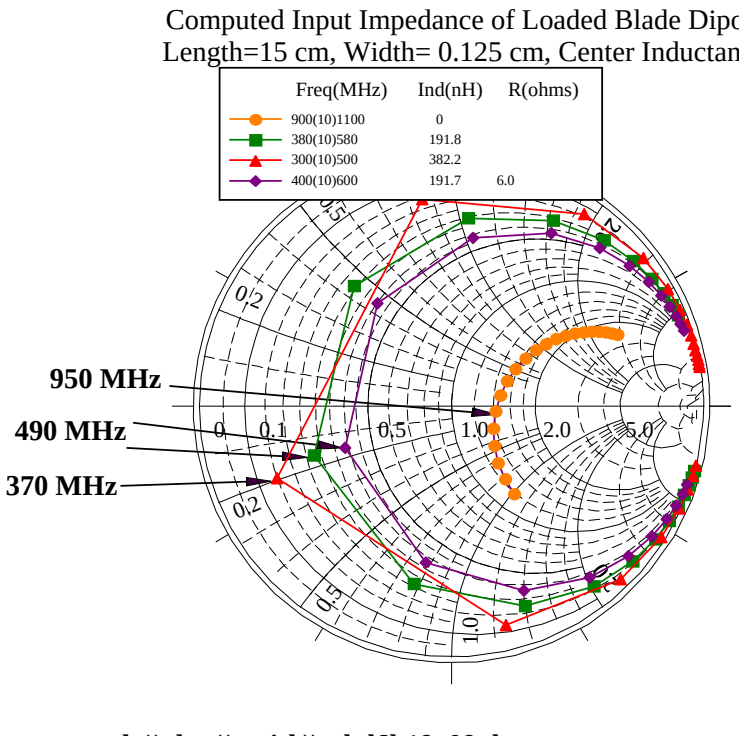

Figure 2. Computed input impedance for center-loaded blade dipoles showing the effect of various loads.

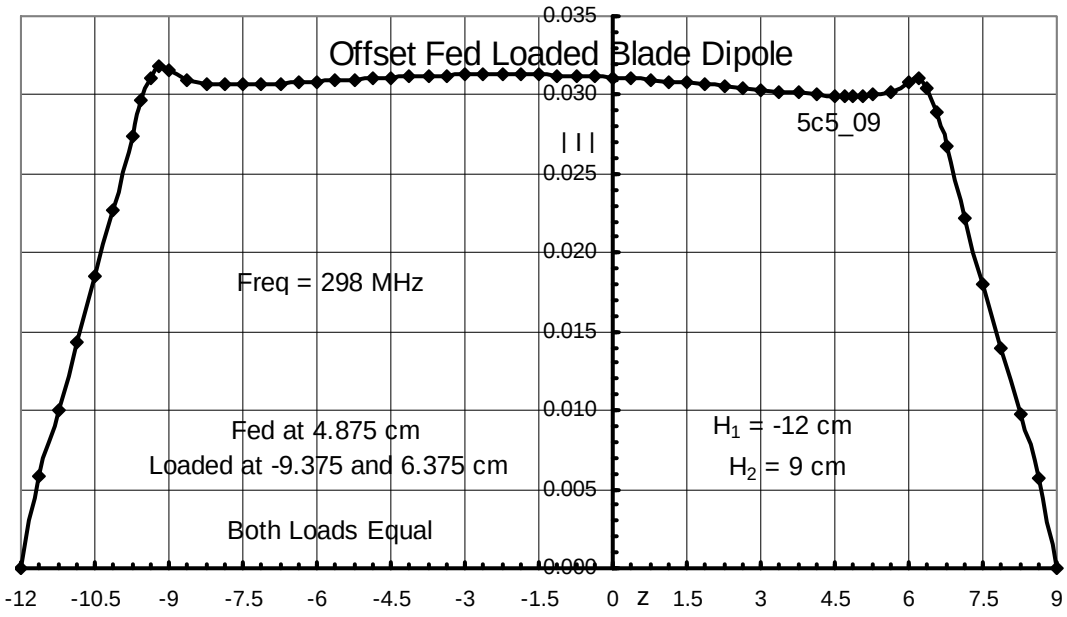

Figure 3. Computed current distribution on a blade dipole of 21 cm length that is loaded near each end and fed at the sixth patch from the upper end. In this case the source is located between the two loads.

Computed Input Impedance of Rectangular Blade Antenna
Length=21 cm, Width=0.125 cm, Feed: z=3.375 cm
Chokel:z1=-9.375 cm, Chokeu:z3=6.375 cm

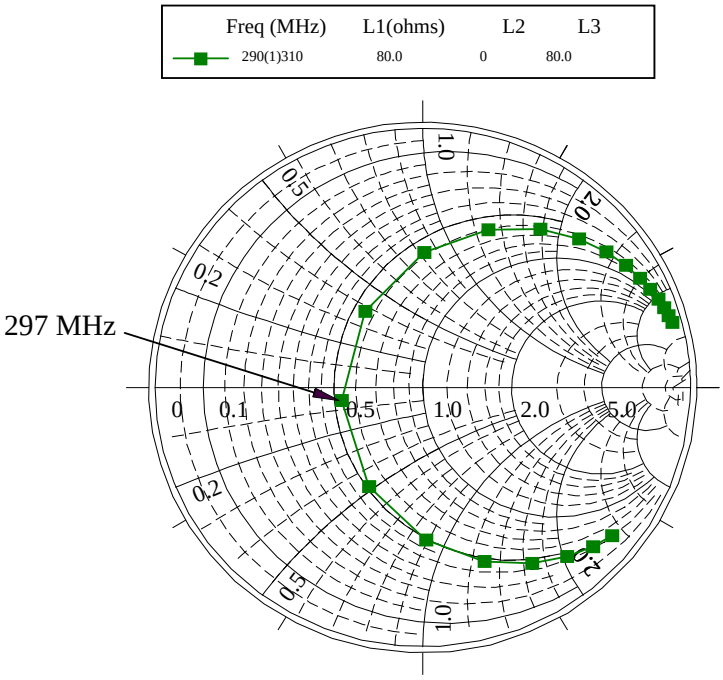

Figure 4. Computed input impedance of blade dipole with two series inductors near the ends of the dipole.

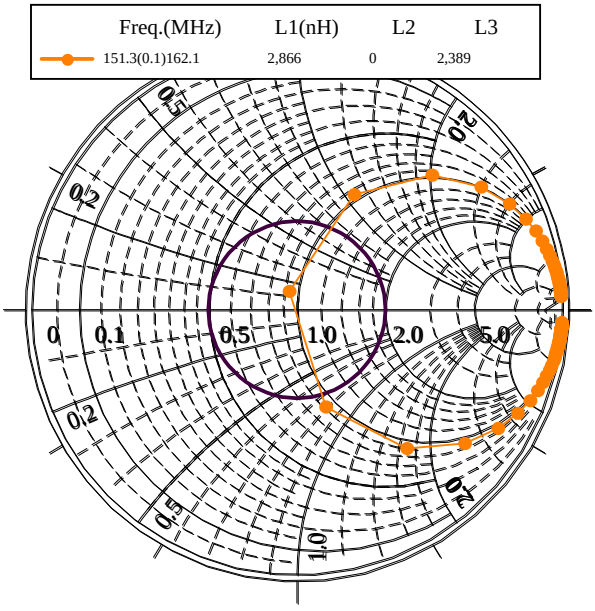

Figure 5. Same as Figure 4 but with inductors adjusted to produce almost perfect match at resonance.

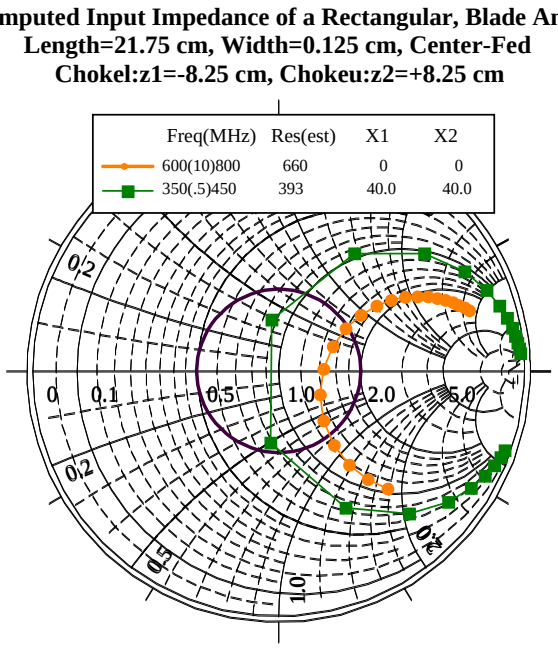

Figure 6. Case of lightly loaded, center-fed blade dipole compared to case where no load is present.

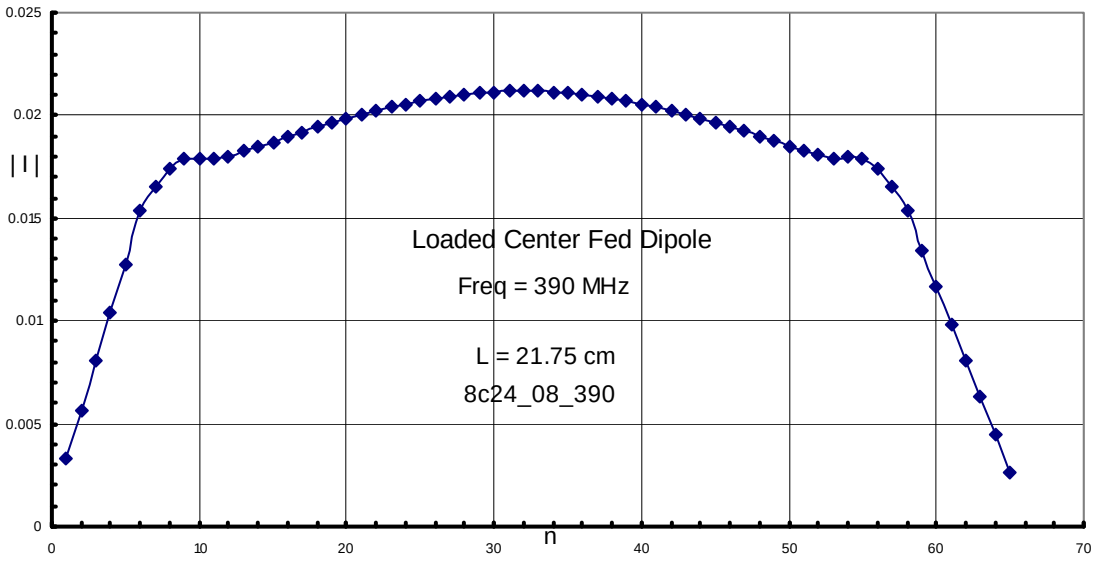

Figure 7. Current distribution computed near resonance for a center-fed blade dipole that is 21.75 cm long, 0.175 cm wide, loaded with inductors at fourth patch from left end (slight asymmetry is due to error in number of patches on right).

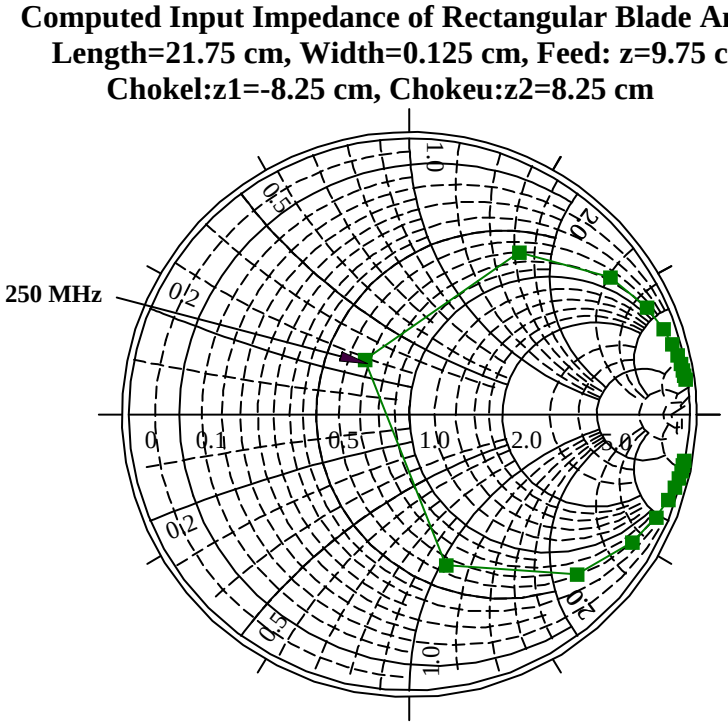

Figure 8. Computed input impedance of more heavily loaded blade dipole where resonant frequency has been lowered to just under 250 MHz and yet input impedance is still within the SWR=2.0 circle. (This is an example of the source being between a choke and the end.)

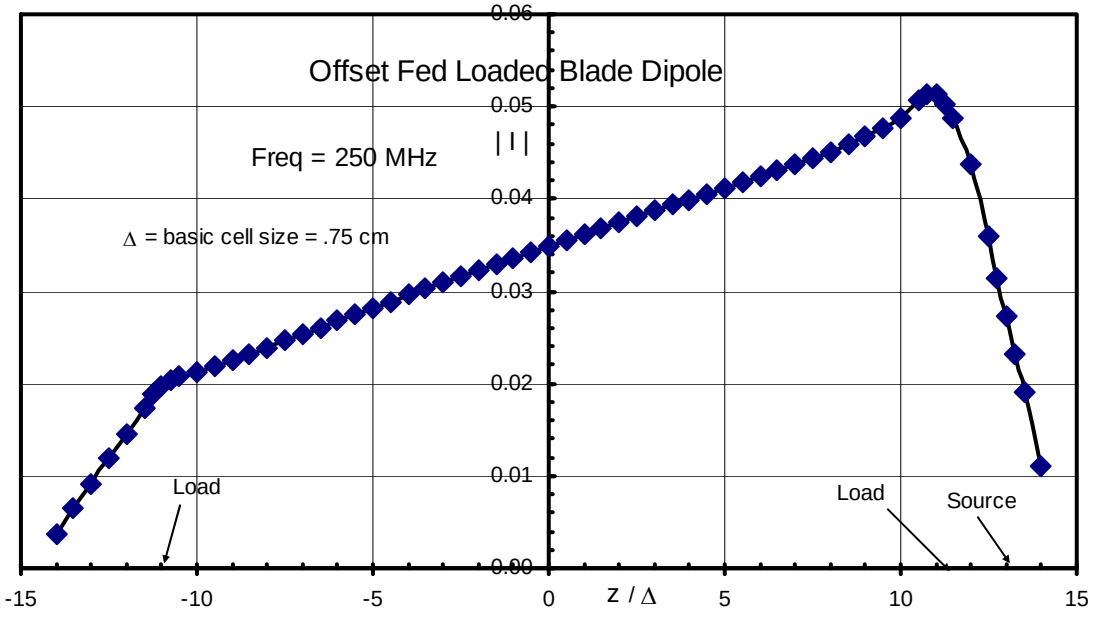

Figure 9. Current distribution computed near resonance for a blade dipole where the source is located between a choke (load) and the end of the dipole.

References

1. P. E. Mayes and P. W. Klock, “Impedance and Gain Bandwidths of Broadband, Electrically Small, Stacked Conical Radiating Resonators,” Proc. Antenna Applications Symposium, 2003, Allerton Park, Illinois.
2. P. E. Mayes and P. W. Klock, “Log-Periodic Networks of Resonant Circuits: Models for Multiband, Electrically Small Antennas,” Proc. Antenna Applications Symposium, 2004, Allerton Park, Illinois.
3. J-S. Zhao, W. C. Chew and P. E. Mayes, “Accurate Analysis of Electrically Small Conical Antennas,” Proc. Antenna Applications Symposium, 2001, Allerton Park, Illinois.
4. Hanson, R. C., “Electrically Small, Superdirective, and Superconducting Antennas,” Hoboken, N. J., John Wiley & Sons, 2006.
5. P. E. Mayes, P. W. Klock and S. Barot, “Using Series Resonators in Parallel to Achieve Broadband Performance in Inductively Loaded Antennas,” Proc. Antenna Applications Symposium, 2008, Allerton Park, Illinois.

Low-Profile Monopole Antenna with Integrated EBG Reflector and Director

Ivor L. Morrow and Ryan W. Davies

Department of Informatics and Sensors,

Cranfield University, SN6 8LA, UK

This paper presents a wire monopole antenna integrated with electromagnetic band-gap (EBG) surfaces that enhance the realized gain of the monopole to 15 dBi. The antenna is sandwiched between an electromagnetic band-gap superstrate that behaves as a frequency selective surface (FSS) and a Sievenpiper type high impedance substrate. The substrate and superstrate wave reflection and transmission phase properties permit very close integration of the monopole antenna while each surface provides a reflective and directive radiated gain, respectively. Integration of the EBG superstrate and substrate with the monopole antenna is examined and design trade-offs in operating frequency, bandwidth and realized gain are evaluated using numerical calculations. Measurements on constructed EBG surfaces and EBG surfaces integrated with the antenna demonstrate good agreement with calculations.

I. Introduction

Recent years have seen an upsurge of interest in the properties and application of radio frequency electromagnetic bandgap (EBG) surfaces. EBG surfaces are periodic metallic, dielectric or metallo-dielectric arrangements and resemble electrically small frequency selec-

tive surfaces (FSS) and volumes. These structures, like FSSs may block or allow the passage of electromagnetic radiation or guided waves [1]. The reflection phase in a perfect electric conductor (PEC) exhibits a frequency invariant π phase change close to the surface while an EBG surface may behave like a perfect magnetic conductor (PMC) with a reflection phase varying from π to $-\pi$ with changing frequency [2].

Much research effort has focussed on using EBGs with small antennas to enhance their radiation or impedance matched properties. Various antenna, such as patch, wire and non-resonant antennas have used EBG substrates to reduce their electrical thickness [3] [4] and eliminate surfaces waves or reject multi-path propagation [1] [5]. EBGs have also been used as superstrates to antenna providing increased radiation efficiency and gain [6] [7] [8] [9].

In this paper we present a probe monopole antenna integrated with different EBG host surfaces to form a small box enclosure with a high gain radiating aperture. The floor and walls of the box consist of via-less Sievenpiper type high impedance surfaces. The wire antenna is flush mounted adjacent to the floor thus increasing its radiation efficiency and directivity. Via-less Sievenpiper scattering element were chosen to facilitate printed fabrication and compactness; since for a given frequency a smaller element size and periodicity is possible [10] [11] [12].

On the cover face of the box an EBG superstrate was used which we call the Filter-Antenna-Filter (FAF). The FAF has spectral and polarization filtering performance similar to a multiple stacked FSS [13]. A drawback with conventional multi-layer FSSs is that a separation of $\lambda/4$ is required between adjacent layers resulting in an electrically thick radome. Also deleterious coupling between the antenna and radome (FSSs) effects antenna impedance and restricts antenna proximity in an installation [14] [15]. On the other hand, the FAF are composed of thin multi-layers, ($\approx \lambda/6$) and have an EBG reflective wave phase [16] property

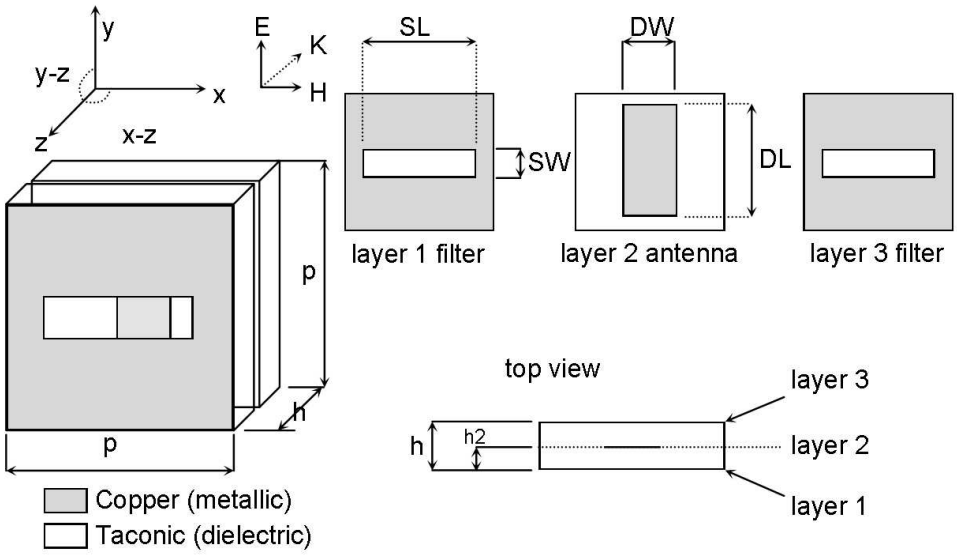

Figure 1. Geometry and dimensions of a unit cell of the FAF. Dimensions are; $p = 10mm$, $h = 3.1mm$, $h2 = 1.55mm$, $SW = 2mm$, $SL = 9mm$, $DW = 4mm$, $DL = 9mm$ (Legend shows the co-ordinate frame and incident wave field vector).

near the surface. Antenna radome coupling is ameliorated and close integration is feasible.

This paper describes the design and analysis of the FAF and its performance is compared with EBG and conventional FSS surfaces. An investigation of element size, geometry and periodicity effects on frequency, bandwidth and wave reflective and transmissive phase is undertaken. Various integration issues and design trade-offs are critically discussed when assembling the FAF superstrate, integrating the radiating antenna and via-less Sievenpiper reflector surfaces. The EBG host antenna is constructed and measurements of input impedance, radiation pattern and realized gain confirm the antenna properties.

II. Assembling The Filter-Antenna-Filter (FAF)

Fig. 1 illustrates the geometry and dimensions of a unit cell of the FAF composed of planar dipole and slot arrays. The electromagnetic transmission response for individual layers and the stacked FAF was calculated using the full-wave commercial simulation software CST [17]. Fig. 2 show the results of simulations for transmission versus frequency at normal

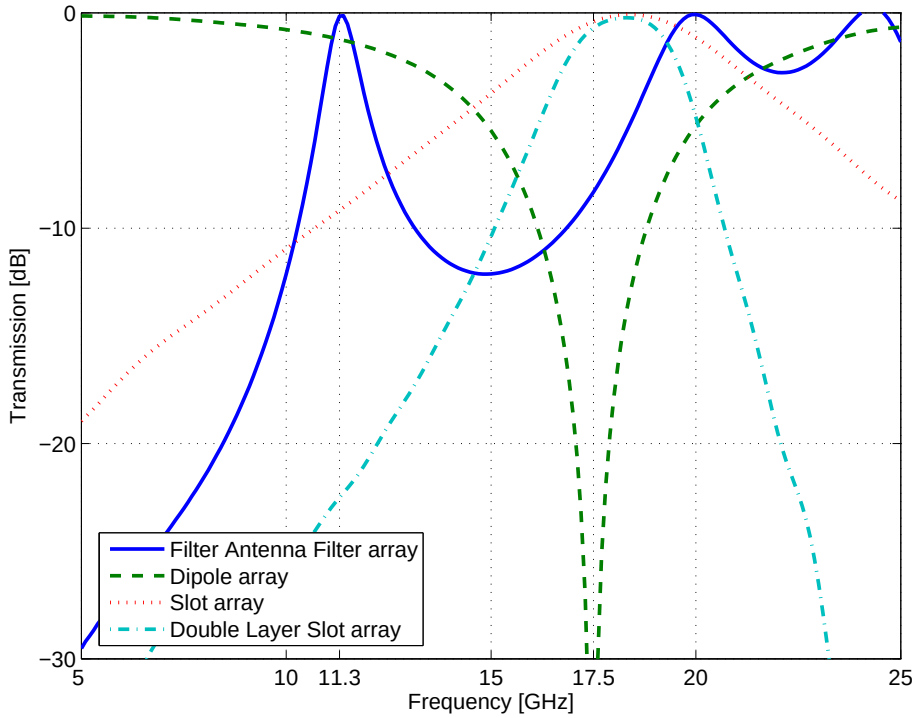

Figure 2. Transmission response of assembled FAF and its constituent arrays.

incidence on the (i) dipole array, (ii) the slot array, (iii) double layer slot array and (iv) the assembled FAF. As expected the single layer slot and dipole arrays have complementary band-pass and band-stop responses. The double layer slot array makes the band-pass more narrowbanded. Insertion of the dipole array between the double layer slot array causes the principal transmission mode to lower in frequency. The mode is supported in the band-stop of the double layer slot filter and may be thought of as a defect mode similar to that introduced in the band-stop of a photonic crystal [18] [19]. The transmission mode at 20 GHz (Fig 2) is also propagating within the band-gap and would also normally exist in transmission through the single dipole array.

A study was undertaken using CST [17] to understand how geometric dimensions such as dipole length and width and slot length and width effected the plane wave transmission

through the FAF. The focus of the numerical experiments were on the two modes supported over the frequency of the forbidden band-gap. An element of the FAF was simulated in a waveguide unit cell with periodic boundary conditions applied. The geometry and dimensions of the FAF is shown in Fig. 1 and consists of printed copper dipoles or etched slots on a substrate of dielectric constant $\epsilon_r = 3.5$ with array periodicity p = 10 mm and dielectric layer separations h = 3.1 mm and h2 = 1.55 mm.

Figs. 3 and 4 show the results of the power transmission simulations from 2-20 GHz. The slot and patch dimensions of the FAF are of fractional wavelength 6 mm ($\lambda/10$) of the transmission mode, at 5 GHz. The resonant frequency of this mode is controlled by the effective dipole length $\lambda_e = \lambda_o/\sqrt{\epsilon_r}$. Larger dipole and slot width increases the bandwidth and causes some lowering of the resonant frequency. A second higher order mode can be made to resonate around 12 GHz. The modal frequency is entirely dependent on the slots length; dipole length or width has little, or no, effect. However, dipole width does determine the third order modal frequency. From Fig. 3 the second and third order modes are made to be nearly co-incident in frequency when the dipole width is reduced to 1 mm.

A. FAF Design and Measured Results

A FAF was constructed with dimensions chosen using the following data from the parametric study (P = 10mm SW = 2mm, SL = 9mm, DW = 4mm, DL = 9mm). A planar metallic patch array was prepared by CNC milling of Taconic circuit board of dielectric constant $\epsilon_r = 3.5$. The FAF constructed was a relatively small planar sample of 6 x 8 periods. The FAF transmission response was measured in a free-space frequency selective surface test rig. Complex power transmission was recorded in both linear planes of polarization on boresight and over a range of incident angles.

Fig. 5 shows the measured and simulated transmission response versus frequency for

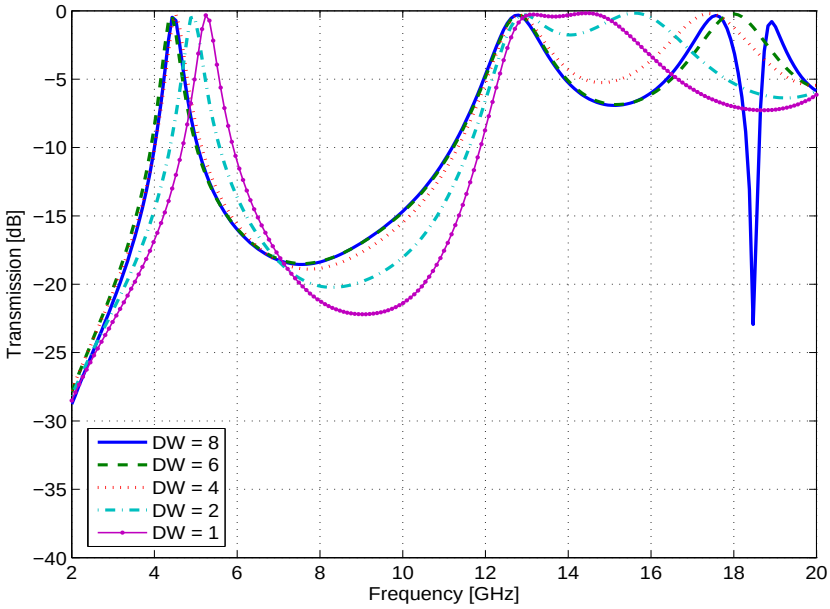

(a)

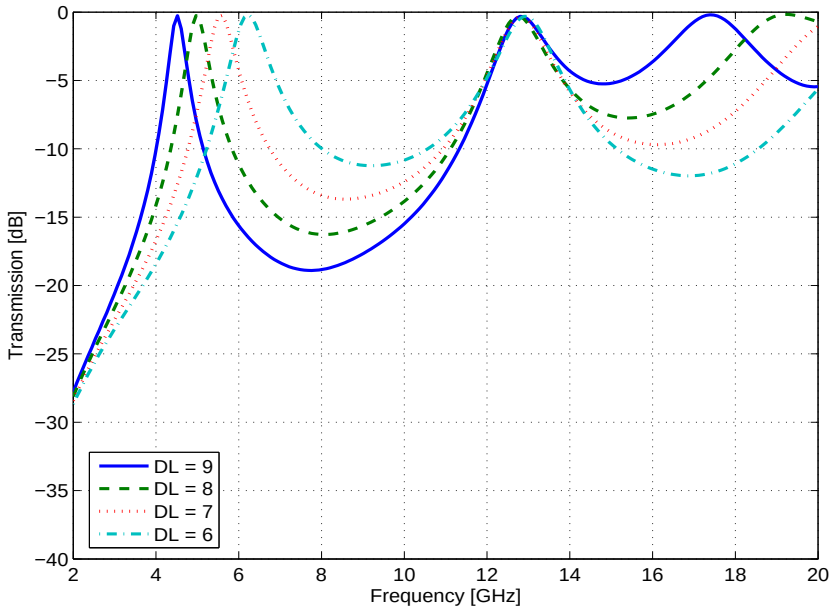

(b)

Figure 3. Simulated transmission response of the FAF for vertical polarized field and variation of dipole dimensions; (a) FAF with dipole width varied DW ($SL = 9mm, SW = 4mm, DL = 9mm$), (b) FAF with dipole length varied DL ($SL = 9mm, SW = 4mm, DW = 4mm$).

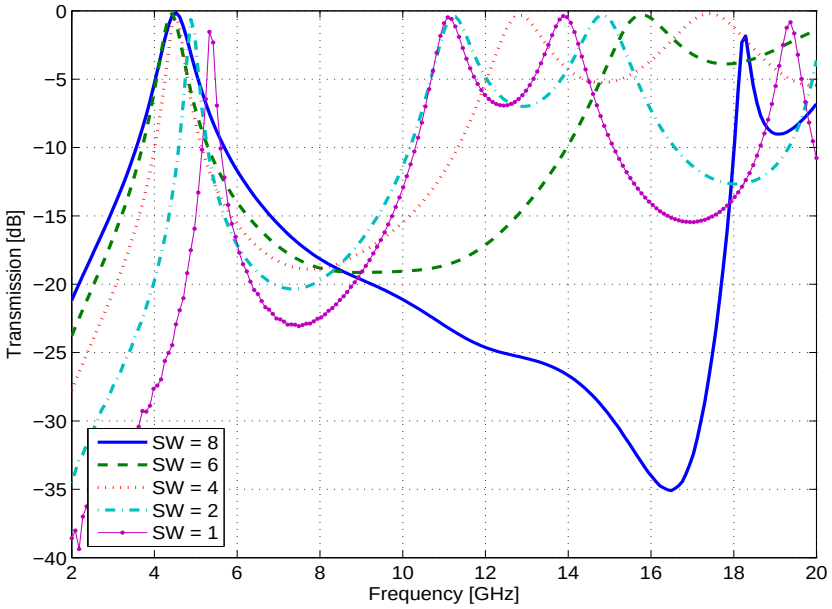

(a)

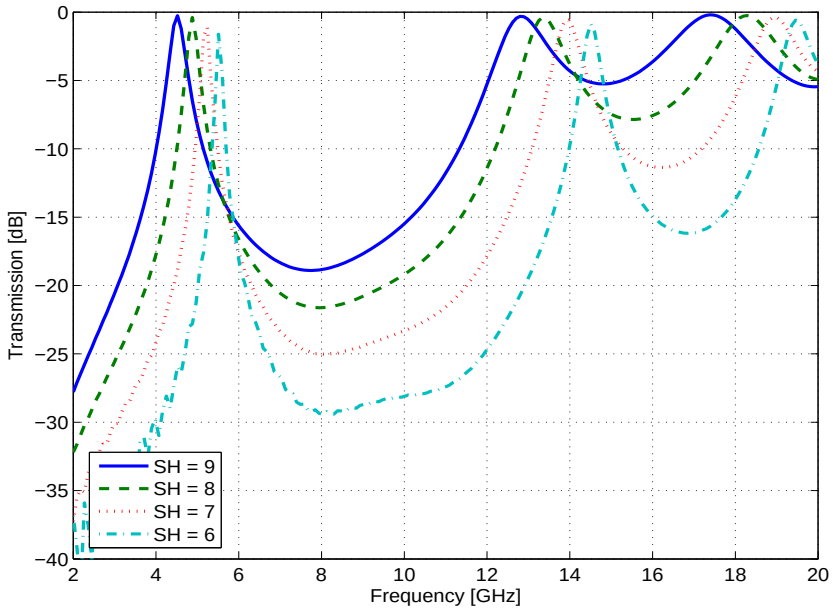

(b)

Figure 4. Simulated transmission response of FAF for vertical polarized field and variation of slot dimensions; (a) Simulation of FAF with slot width varied SW ($SH = 4mm, DW = 4mm, DL = 9mm$), (b) Simulation of FAF with slot height varied SH ($SW = 9mm, DW = 4mm, DL = 9mm$).

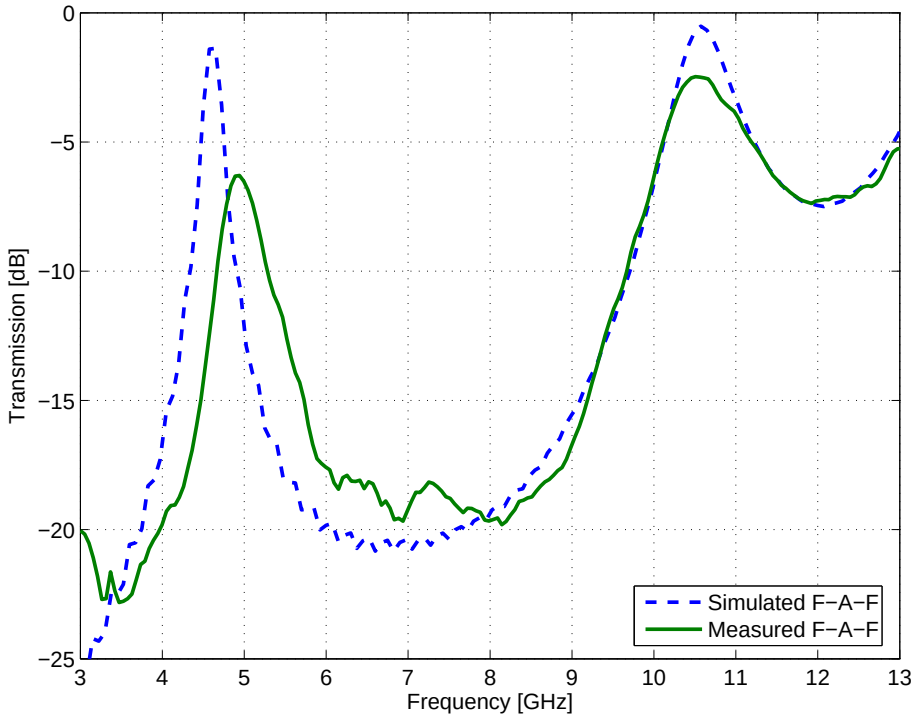

Figure 5. Comparison of measured and simulated bore-sight transmission performance of FAF with dimensions ($P = 10mm$, $SW = 2mm$, $SL = 9mm$, $DW = 4mm$, $DL = 9mm$.)

a plane wave normal incidence and electric field polarized perpendicular to the slot, (i.e. TM polarized). Measured and computed results compare well but some losses are present in both the simulated and measured transmission mode. The small loss in the simulated result is attributed to the dielectric loss tangent of the Taconic circuit board (specified as $\tan\,\delta = 0.0025$ at 10 GHz). The higher losses in the measured result are experimental in origin and due to lateral wave leakage from the sample in the test rig.

Fig. 6 shows the measured power transmission of the FAF at various angles in both the TE (see Fig. 1 co-ordinate frame) and TM planes of polarization. Note the FAF here spatially filters in one polarization only since the configuration of dipole and slot is single linearly polarized [20]. Inspection of Fig. 6 shows the first transmission mode at 5 GHz

is stable with respect to angle of incidence and is narrow bandpass ($\approx$ 5% 3dB BW). The transmission response in the TM plane of polarization has marginally wider bandwidth than the TE. This response is similar to that reported with conventional resonant bandpass FSSs [13].

The second higher order mode of the FAF shown in Fig. 6 at 10.5 GHz is broader band (approx 7.5% 3dB BW) and the resonance is unstable w.r.t angle of incidence in both TM and TE planes. The transmission frequency decreases with increased grazing angle in the TM plane and behaves conversely in the TE plane. The transmission window around 10.5 GHz and its narrow angular dependence make it attractive for enhancing the directionality of an isotropic source.

B. Integration of FAF Superstrate and Monopole Antenna

A prototype monopole antenna was located below the FAF superstrate and its length tuned to the frequency of the mode identified previously for directivity enhancement. The principal H-plane radiation pattern of the integrated monopole and FAF was measured in the anechoic chamber and compared with an identical isolated monopole[†]. The field patterns were measured with the FAF at increasing distances d = 10 mm and d = 20 mm below the monopole. It was found that the proximity of the FAF had little effect on the monopole impedance. However, the radiated field pattern increased directivity with increasing d, as shown in Fig. 7. At horizonal some field leakage is apparent where a gap exists between the FAF and monopole and this was also seen in simulations. Field patterns were normalized for comparison and the measured realized gains for the integrated FAF and monopole are 7 dB and 7.5 dB at d= 10 mm and d = 20 mm respectively. This is 3 dB more gain than for the isolated monopole. Optimum gain occurred at 10.5 GHz with an antenna-FAF spacing

[†] All antennas were measured in the receive mode and reciprocity is assumed.

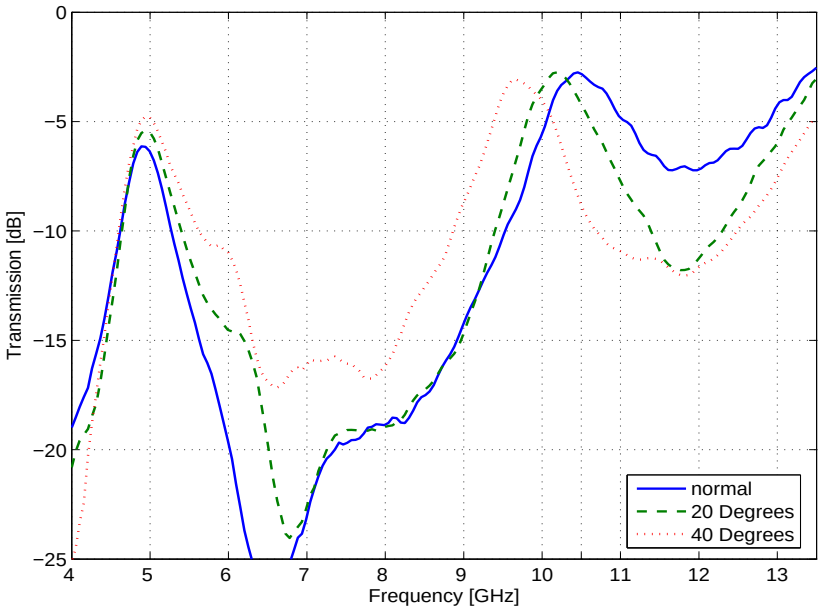

(a)

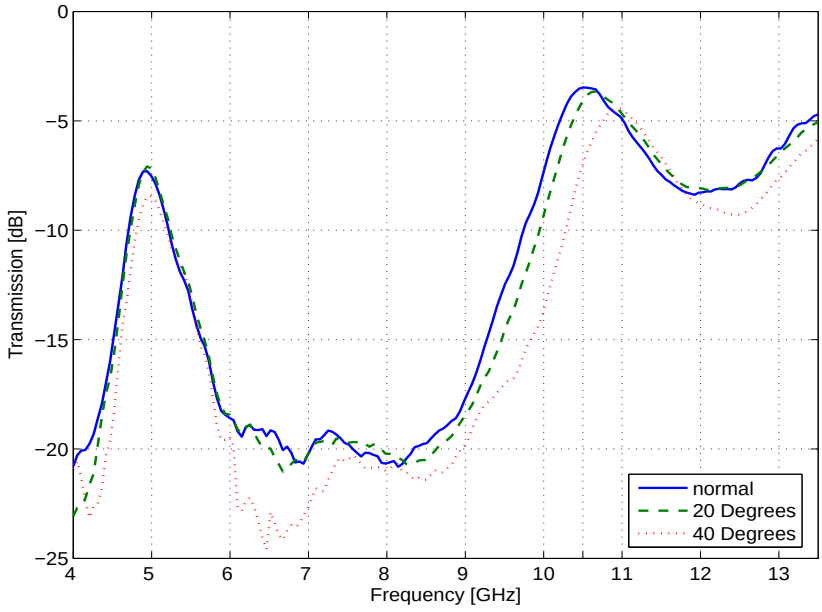

(b)

Figure 6. Measured transmission through FAF at various angles of incidence. (a) Angular variation in TM plane of incidence, (b) Angular variation in TE plane of incidence.

of 20 mm. Some field pattern ripples are also present and this is attributed to fields creeping around the edges of the FAF structure.

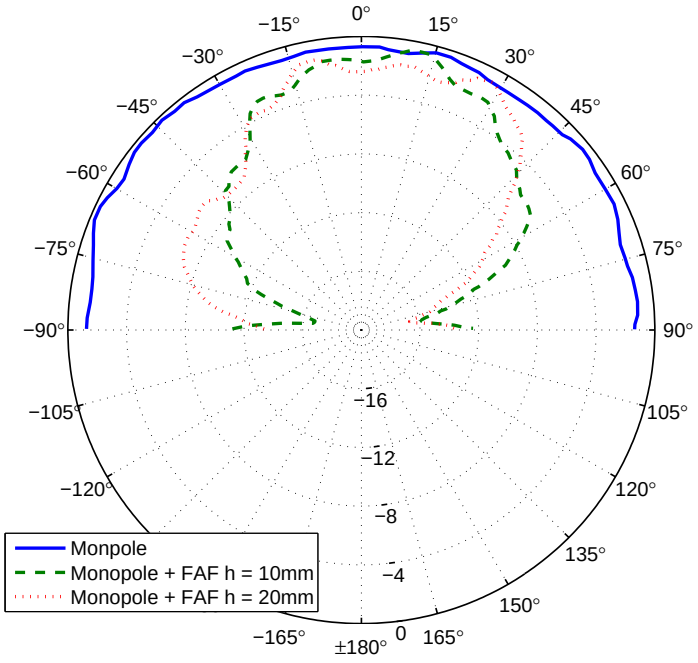

Figure 7. H-plane patterns of monopole antenna in anechoic chamber without and with an FAF superstrate placed in front of the antenna at distances $h = 10mm$ and $20mm$.

III. Compact High Gain Antenna Design

A. Design of EBG Reflector Surfaces

To further increase the radiated gain of the monopole antenna an EBG Sievenpiper surface was designed and integrated with the FAF and monopole antenna. The reflection phase properties of the EBG reflector allows the antenna to be placed near its surface thus retaining a thin planar structure while enhancing the impedance match of the source/antenna [2][21].

Via-less square patch EBG elements were used but it is noted that other geometric shapes can be used and provide more bandwidth. The EBG consisted of a 4x4 array of

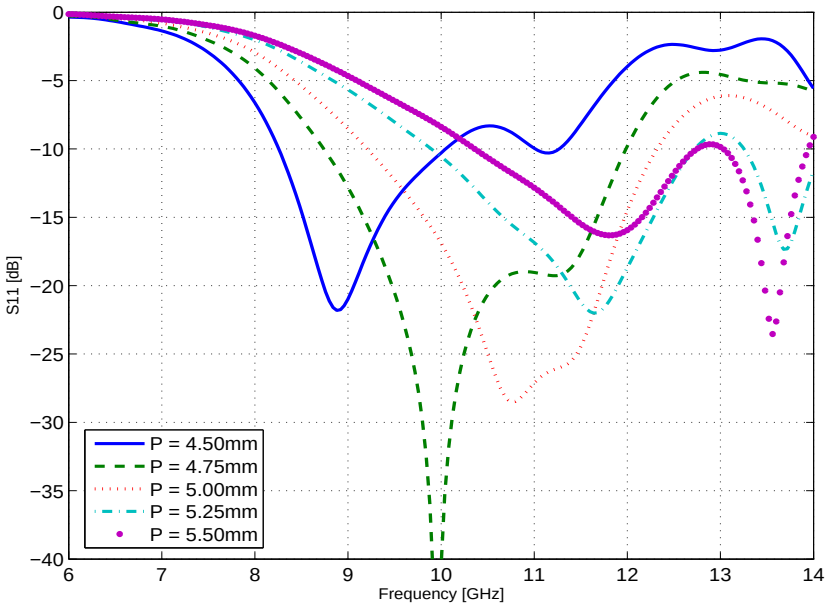

(a)

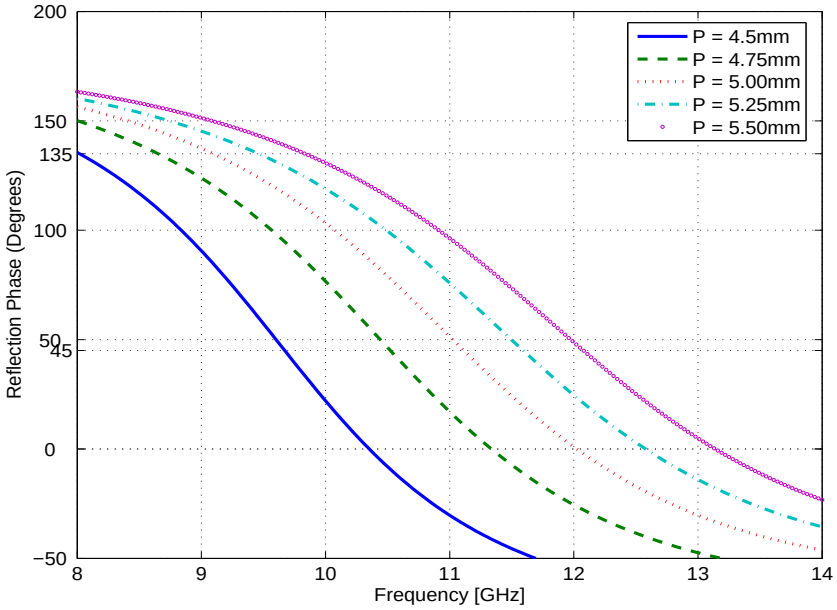

(b)

Figure 8. Return loss and reflection phase for various EBG periodicity; (a) Insertion loss of antenna near EBG surface with varying P = periodicity, (b) Reflection phase of EBG surfaces with varying P = periodicity.

elements which is relatively small in contrast to other EBG reflector surfaces reported in the literature.

The EBG substrate consisted of 1.55mm thick Taconic circuit board of dielectric constant $\epsilon_r = 3.5$. The design goal was to obtain a monopole antenna insertion loss of $S_{11} \leq 10$ dB over the transmission mode with the EBG reflector integrated. The metal patch size was fixed at 4 mm square and the array periodicity was initially set to 4.5 mm. The EBG reflector in close proximity to the monopole (1 mm) did not effect antenna impedance match but it did perturb the resonance frequency. The monopole length was shortened from 7.50 mm to 5.55 mm to maintain resonance at 10.5 GHz. Parametric simulations shown in Fig 8 examined the effect on monopole input impedance and the reflection phase of the EBG array while varying the periodicity from 4.5 to 5.5 mm in steps of 0.25 mm. The insertion loss of the monopole was found to be sensitive to small changes in array periodicity. Increasing the array periodicity results in a reflection phase response higher in frequency and of more gradual slope. The region $90^\circ \pm 45^\circ$ is marked on the reflection phase graph and the frequency range for each array periodicity that lies within this region corresponds with a monopole insertion loss ≤ -10 dB.

Fig. 9(a) illustrates the monopole/reflector configurations and Fig. 9(b) shows the EBG simulated and measured input impedance results. For comparison the input impedance of a monopole antenna with a metallic reflector at the ideal distance of $\lambda/4$ ($h = 7.5mm$) is also shown.

The measured and simulated results for monopole integrated with the EBG reflector demonstrated good insertion loss from 9-12 GHz. The results suggest that good phase reflection properties are achievable even with a small 4 x 4 element reflector. The broadband frequency response of the monopole does allow for further fine-tuning if required.

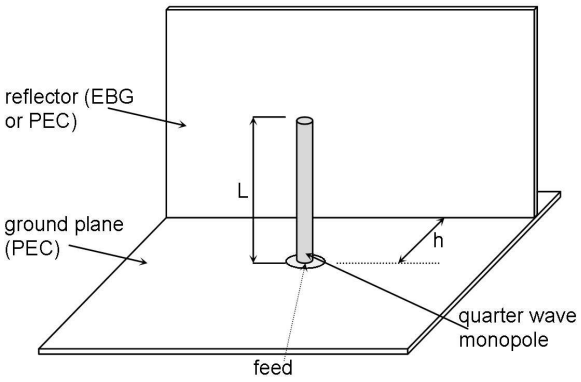

(a)

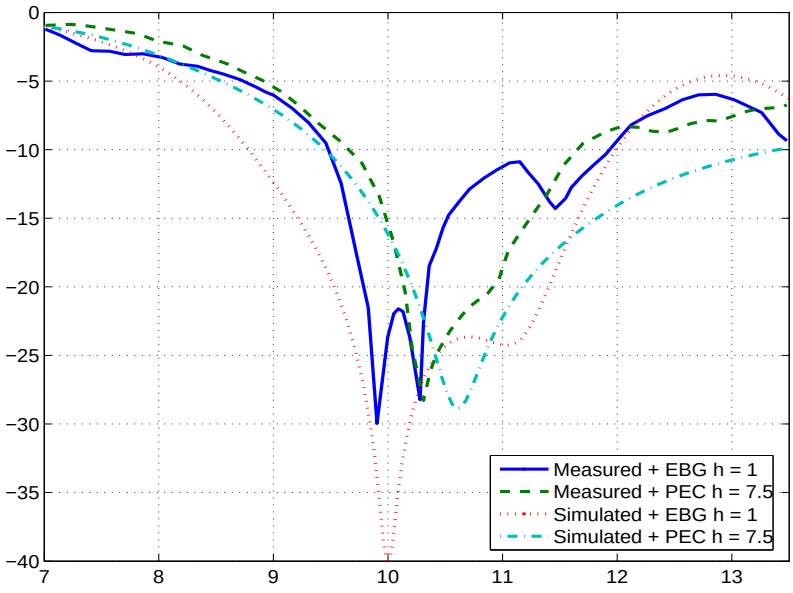

(b)

Figure 9. (a) Monopole design with layout of ground plane and reflector; $L = 5.5mm$ and h is varied for different designs depending on the use of EBGs or PECs. (b) Simulated and measured return loss of monopole antenna $L = 5.5mm$ with PEC reflector $h = 7.5mm$ and EBG reflector $h = 1mm$.

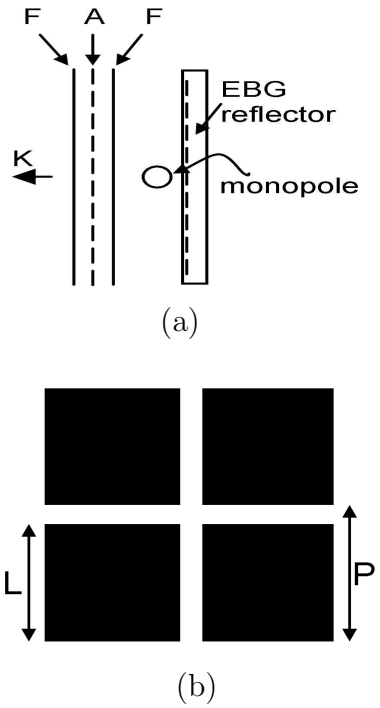

Figure 10. (a) Schematic diagram of FAF superstrate, monopole and EBG substrate, (b) Optimum EBG reflector dimensions L = 4mm P = 4.85mm (K = propagation direction).

B. Integrated FAF Superstrate and EBG Reflector with Antenna

The monopole was sandwiched between the FAF and EBG reflector as shown in Fig. 10(a). The antenna was positioned 2.5 mm from the EBG reflector and 4 mm from the FAF. Fig. 10(b) shows the final optimum via-less EBG geometry and periodicity.

One drawback with the configuration is unwanted radiation spill from the open sides of the parallel structure. To eliminate this problem the three open sides are closed with EBG reflector walls to form a small box. The remaining open face forms a radiating aperture that can be covered by the FAF superstrate. Similar dimension via-less EBG elements are used for the box sides and top. Fig. 11 illustrates the monopole antenna encapsulated in EBG materials.

The effect of the side walls was to introduce some loss in antenna gain and the length of

the monopole had to be re-tuned. Simulations indicated that without the FAF cover a 12.8 dB gain is achieved at 10.5 GHz.

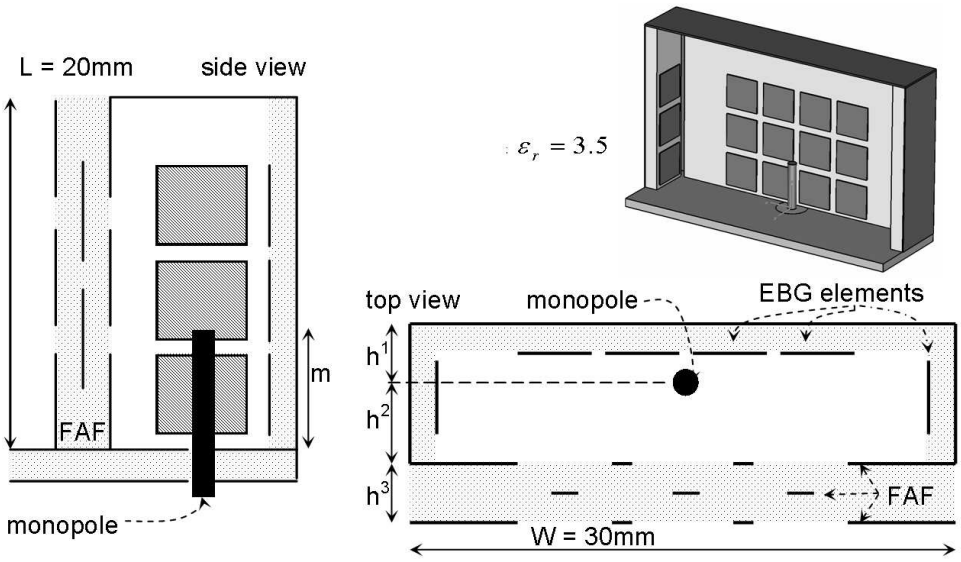

Figure 11. Schematic of monopole antenna with EBG reflectors located on the back, sides and top faces. The FAF superstrate is located on the front face $h^1 = 2.5mm$, $h^2 = 4mm$, $h^3 = 3.1mm$, m = 5.5, L = 20mm

To further increase the antenna gain the FAF cover was placed over the aperture. Measured and simulated insertion loss results for the antenna (i) with and (ii) without the FAF superstrate are shown in Fig. 12. The measured and simulated S_{11} of the antenna with an open aperture has a -10 dB bandwidth of 3.5 GHz simulated and $>$ 4 GHz measured. When the FAF is inserted in the aperture the mode at 10.5 GHz is, as expected, still present. The antenna is well matched with a -15 dB insertion loss but the bandwidth has considerably narrowed.

The final constructed FAF superstrate contained 3 x 2 array of elements and the dimensions of the box were 30 mm x 20 mm with a depth of 10 mm. The normalized simulated and measured field patterns of the encapsulated monopole antenna without FAF superstrate and with FAF superstrate, are shown in Fig. 13. It is seen that the ripples in the field pattern have been alleviated. The antenna radiation efficiency of the radiating box at 10.5

GHz was simulated using CST and found to be $\geq 98\%$ and measured experimentally using the Wheeler cap technique to be $\geq 95 \pm 2\%$. The simulated and measured antenna gain results are summarized in Table I. The FAF superstrate has increased the antenna gain by 3 dB and the EBG reflector by about 9.0 dB.

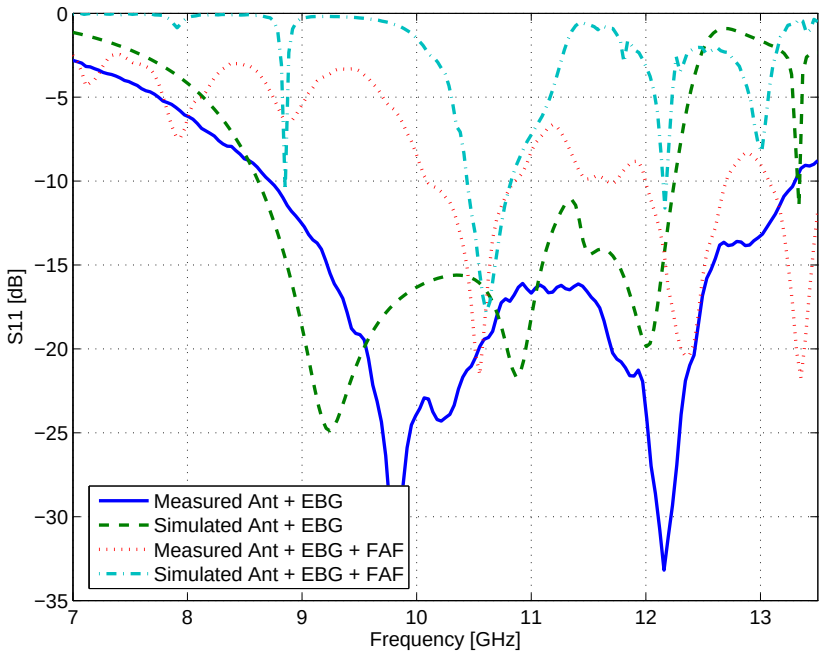

Figure 12. Simulated and measured insertion loss of monopole antenna encapsulated in EBG and (i) with FAF superstrate and (ii) without FAF superstrate.

	Simulated Gain [dB]	Measured Gain [dB] ±0.5 dB
Mpole	4.0	3.5
Mpole + FAF	7.5	7.0
Mpole + Enclosed EBG	12.8	12.6
Mpole + Enclosed EBG + FAF	16.0	15.1

TABLE I

Comparison of Gains for EBG encapsulated monopole antennas at 10.5 GHz. (Mpole = Monopole, EBG = via-less Sievenpiper reflector, FAF = Filter antenna filter superstrate.)

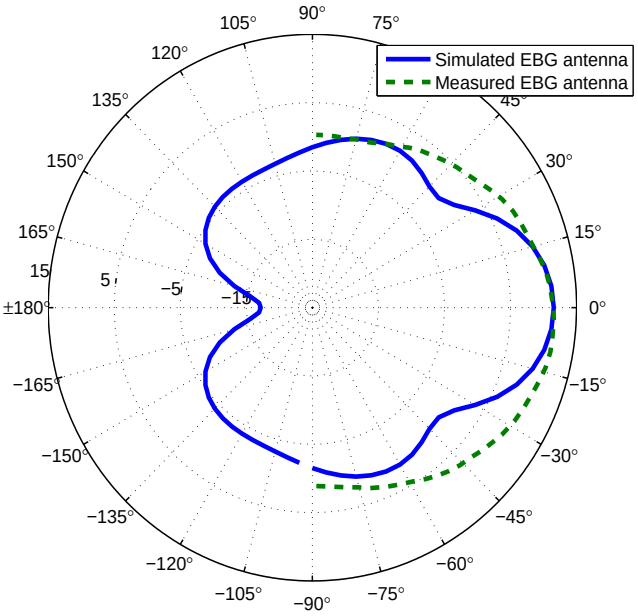

(a)

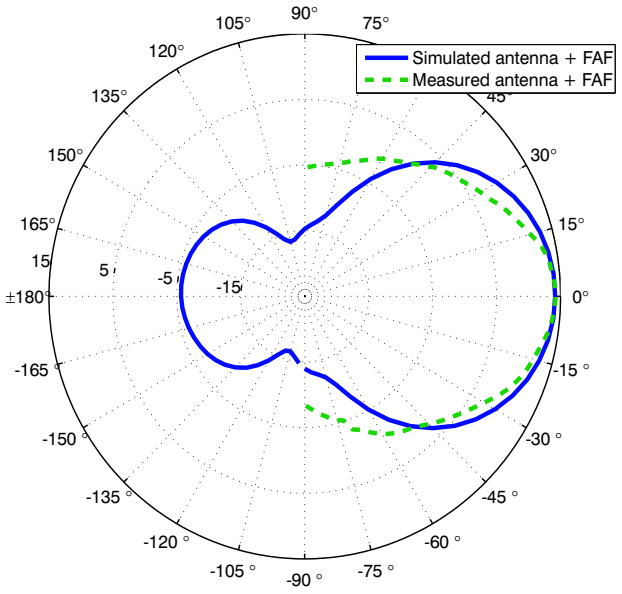

(b)

Figure 13. Simulated and measured H plane patterns of EBG enclosed antenna at 10.5 GHz (a) without FAF superstrate, (b) with FAF superstrate.

IV. Conclusion

A new form of high gain conformal antenna consisting of a monopole antenna encapsulated with EBG superstrate and substrate has been described. Results from computer simulation and measurement have been presented that demonstrate its performance and identify the important design parameters. A novel EBG superstrate called the FAF (filter-antenna-filter) was used to provide an electrically thin planar director to the antenna. Computer simulations and laboratory measurements were used to examine the design trade-offs in antenna impedance, bandwidth, radiation pattern and gain. The antenna realized gain has been significantly improved. At resonance the EBG substrate and walls increase measured antenna gain from 3.5 dB to 12.6 dB and the FAF further increases the gain to 15.1 dB. This is close to but does not exceed the maximum gain of 18.3 dB for an aperture antenna of equivalent radiating area.

V. Acknowledgements

The authors would like to thank the DSTL UK for funding the earlier part of Mr. Davies PhD studies. Thanks are also due to Miss Stacy Paget for CNC milling and assembly of the electrically small FSSs and Mr. Chris Ransom for the design and construction of the FSS sample holders.

References

[1] D. Sievenpiper, "High impedance electromagnetic surface with a forbidden frequency band," *IEEE Trans. on Antennas and Propagat.*, vol. 47, pp. 2059–2072, November 1999.

[2] F. Yang and Y. Rahmat-Samii, "Reflection phase characterizations of the EBG ground plane for low profile wire antenna applications," *IEEE Trans. on Ants. and Propagat.*, vol. 51, pp. 2691–2703, October 2003.

[3] J. M. Bell and M. F. Iskander, "A low-profile archimedean spiral antenna using an EBG ground plane," *IEEE Ant. and Wireless Prop. Letters*, vol. 3, pp. 223–226, 2004.

[4] H. Nakano, M. Ikeda, K. Hitosugi, J. Yamauchi, and K. Hirose, "A spiral antenna backed by an electromagnetic band-gap material," *IEEE International Workshop on Antenna Technology*, pp. 482–485, 2003.

[5] M. Qiu and S. He, "High directivity patch antenna with both photonic band gap substrate and photonic band gap cover," *Microw. and Optic. Technol. Letts.*, vol. 1, pp. 41–44, July 2001.

[6] M. Diblane, E. Rodes, E. Arnaud, M. Thevenot, T. Monediere, and B. Jecko, "Circularly polarized metallic EBG antenna," *IEEE Microwave and Wireless Components Letters.*, vol. 15, pp. 638–640, October 2005.

[7] L. Leger, T. Monediere, and B. Jecko, "Enhancement of gain and radiation bandwidth for a planar 1D EBG antenna," *IEEE Microwave and Wireless Components Letters.*, vol. 15, pp. 573–575, September 2005.

[8] Y. J. Lee, J. Yeo, R. Mittra, and W. S. Park, "Thin frequency selective surface (FSS) superstrate with different periodicities for dual-band directivity enhancement," *IEEE International Workshop on Antenna Technology*, pp. 275–278, 2005.

[9] H. Boutayeb, T. A. Denidni, A. R. Sebek, and L. Talbi, "Design of elliptical electromagnetic bandgap structures for directive antennas," *IEEE Ant. and Wireless Prop. Letters*, vol. 4, pp. 93–96, 2005.

[10] H. Nakano, Y. Asano, and J. Yamauchi, "A wire inverted F antenna on a finite-sized EBG material," *IEEE International Workshop on Antenna Technology*, pp. 13–16, 2005.

[11] P. Salonen, F. Yang, Y. Rahmat-Samii, and M. Kivikosi, "WEBGA - wearable electromagnetic band-gap antenna," *IEEE Ants. and Propagat.*, pp. 451–454, 2004.

[12] A. P. Feresidis, G. Goussetis, and J. C. Vardaxoglou, "Metallodielectric arrays without vias as artificial magnetic conductors and electromagnetic band gap surfaces," *IEEE Ants. and Propagat.*, pp. 1159–1162, 2004.

[13] B. A. Munk, *Frequency Selective Surfaces: Theory and Design.* New York: John Wiley and Sons, 2000.

[14] E. A. Parker, B. Philips, and R. J. Langley, "Analysis of coupling between a curved fss and an enclosed planar dipole array," *IEEE Microw. and Guided Wave Letts.*, vol. vol. 5, pp. 38–40, 10 1995.

[15] V. Prakash, N. Huang, and R. Mittra, "Accurate analysis of interaction between microwave antennas and frequency selective surface (FSS) radomes," *IEE Intern. Conf. on Ants and Propagat.*, pp. 319–323, 2003.

[16] A. Monorchio, G. Manara, and L. Lanuzza, "Synthesis of artificial magnetic conductors by using multilayered frequency selective surfaces," *IEEE Ant. and Wireless Prop. Letters*, vol. 1, pp. 196–199, 2002.

[17] *Computer Simulation Technology.* CST©, 1998-2003.

[18] A. R. Weily, K. Esselle, B. C. Sanders, and T. S. Bird, "Antennas based on 2D and 3D electromagnetic bandgap materials," *IEEE International Workshop on Antenna Tech-*

nology, pp. 847–850, 2003.

[19] Y. J. Lee, J. Yeo, R. Mittra, and W. S. Park, "Application of electromagnetic bandgap (EBG) superstrates with controllable defects for a class of patch antennas as spatial angular filters," *IEEE Trans. on Ants. and Propagat.*, vol. 53, pp. 224–235, January 2005.

[20] R. W. Davies and I. L. Morrow, "Wideband compact monopole antenna with EBG reflector and superstrate.," *IASTED Proc. Antennas, Radar and Wave Propag.*, pp. 23–26, July 2006.

[21] M. P. K. G. S. Smith and J. G. Maloney, "Dipole antennas used with all-dielectric, woodpile photonic band gap reflectors: Gain, field patterns and input impedance," *Microw. and Optic. Technol. Letts.*, vol. 21, pp. 191–196, May 1999.

18-110GHz Integrated Planar Log-Periodic Antennas

Joseph R. Mruk, Yuya Saito, and Dejan S. Filipović
Department of Electrical, Computer, and Energy Engineering
University of Colorado, Boulder, CO 80309-0425
{mruk, saito, dejan}@colorado.edu

Abstract: Multi-octave bandwidth antennas are used in systems ranging from communication and electronic warfare to interferometers, radiometers, etc. Fabrication of front-ends that can operate consistently at frequencies ranging from Ku- to W-band will allow for the development of advanced broadband military and commercial systems. Planar log-periodic antennas belong to the class of frequency independent radiators with bandwidths that depend on the overall size of the aperture and the finesse of the feed region. In this paper, the development of a planar log-periodic antenna with an integrated feed is studied using two different transmission line technologies. Specifically, a log-periodic designed on a dielectric substrate with an integrated microstrip line impedance transformer is compared to an air-loaded embodiment fed with an integrated micro-coaxial impedance transformer. The two structures are contrasted to develop theoretical and practical foundations that will guide their future development, and be used throughout the millimeter and sub-millimeter wave frequencies.

1. Introduction

Frequency independent planar log-periodic antennas were first introduced by DuHamel and Isbell in 1957 [1]. It is shown that they can achieve multiple decade bandwidths with logarithmically periodic performance characteristics. The bandwidth of operation is limited by the dimensions of the radiator. Specifically, the lowest frequency of operation is determined by the overall footprint size while the highest frequency of operation is limited to the finite size and precision of the feed region. Log-periodics have been used in communications, electronic warfare systems, remote sensing, radio astronomy, and many other applications up to Ku-band. Broadband front-ends operating up to W-band can take advantage of higher seldom used frequency bands and thus play a major role in the development of new systems for military and commercial users.

Over the past two decades, log-periodics have been demonstrated up to terahertz frequencies [2]. However, antennas fabricated for terahertz applications use bolometers and/or diodes to detect RF power and convert it to a DC current. It is, however, often desirable to have directly RF fed antennas particularly when the signal being received or transmitted is encoded with meaningful information. The characteristics and technology of the transmission lines chosen have detrimental effects on the performance of the RF

front-end at high frequencies. Losses, coupling, dispersion, radiation, the ability to integrate multiple components, and manufacturability are only a few important issues that must be considered.

In this paper, two transmission line technology candidates able to fabricate wideband Ku- to W-band log-periodic antennas are studied and compared. Microstrip is a well known and widely used planar transmission line that can be fabricated on a variety of different dielectrics with different dielectric constants. The upper frequency is determined by the structural parameters including trace and dielectric dimensions. Surface and higher order modes can severely degrade performance and should be avoided. The other technology is the recently introduced surface micromachined process [3] which allows for an antenna to be integrated with a micro-coaxial transmission line. These lines have low loss and dispersion and have been shown to operate in excess of 450GHz without overmoding [4]. The findings presented here will enable better understanding of the limitations of the two technologies and their future use for wideband millimeter and sub-millimeter wave front ends.

2. Microstrip Feed Line Design Considerations

Microstrip transmission lines can be used to cover a broad range of frequencies. Care must be taken due to the fact that these lines are quasi-TEM and dispersive. A theoretical study on how the impedance of the lines change as a function of frequency was performed to better understand the effects of dispersion. Three dielectric constants (ε_r = 12.9, 6.5, and 2.2) and three different substrate thicknesses (t = 0.010", 0.004", and 0.002") are selected. The lowest and highest characteristic impedances studied are 50Ω and 104Ω, respectively. These values are chosen because they represent the highest and lowest impedances required to match a 160Ω load to a 50Ω system. With ε_r = 2.2, the nominal impedance of the self-complementary antenna is approximately 160Ω.

Obtained results are shown in Table 1. The data includes the computed line width needed to realize the desired impedance at the specified frequency for different dielectric constants and dielectric thicknesses. As seen, the frequency increase from 18 to 110GHz for the 10mil substrate has a profound effect. This effect magnifies when a high dielectric constant material is used clearly indicating that substrates with a thickness of 10mil would perform inadequately for this frequency range. Another point of interest is that low dielectric constant materials with thin substrate thicknesses are shown to have small variations in the change of the line widths.

The substrate chosen to be best suited for this application was RT/duroid 5880. This substrate has a dielectric constant of 2.2, a loss tangent measured at 10GHz of 0.0009, and W-band components have already been demonstrated for 5mil thicknesses [5]. A 5-step impedance transformer was designed to match 160Ω to 50Ω and operate from 18 to 110 GHz. The values of the impedances used in the transformer are 104Ω, 89Ω, 75Ω, 63Ω, and 55Ω. The layout of the transformer is shown in Fig 1. The full-wave design was

carried out using Ansoft's HFSS and it is compared to a design created in CST's Microwave Studio. The higher order mode of the 50Ω line will occur above 200GHz and surface modes are excited at higher frequencies. The impedance transformer simulation results are shown in Fig. 2.

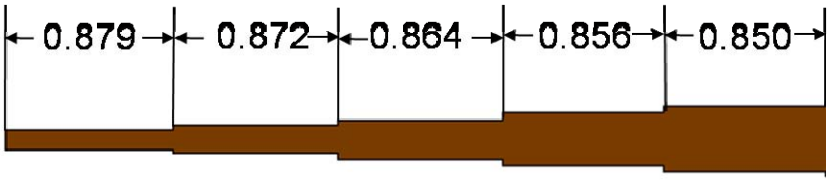

Fig. 1. Microstrip layout of impedance transformer (dimensions in millimeters).

		104Ω			50Ω		
ε_r	Freq	10 mil	4 mil	2 mil	10 mil	4 mil	2 mil
12.9	18 GHz	16.52	6.28	2.963	186.8	73.73	36.70
12.9	110 GHz	78.72	7.30	2.81	326.3	83.06	37.10
6.5	18 GHz	58.07	22.74	11.11	357.3	142.0	70.84
6.5	110 GHz	107.0	24.26	10.97	478.4	149.8	71.07
2.2	18 GHz	206.7	81.97	40.58	783.2	312.4	156
2.2	110 GHz	254.9	83.92	40.41	895.8	318.9	156

Table 1. Variation in the line width required to achieve 104Ω and 50Ω lines on different dielectric materials and dielectric thicknesses (dimensions in micrometers).

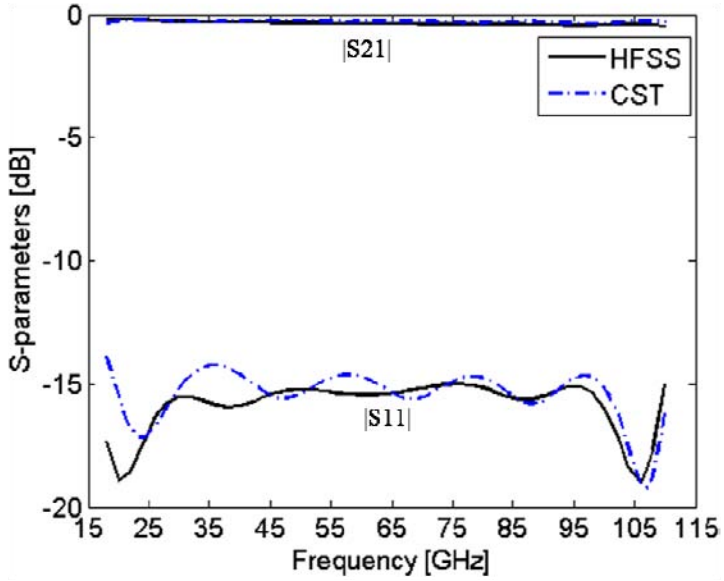

Fig. 2. Computed S-parameters of the designed transformer.

3. Rectangular Micro-Coaxial Feed Line Design Considerations

PolyStrata™ is a photolithographic process that is able to produce micro-coaxial transmission lines that operate up to sub-millimeter wave frequencies [4]. These transmission lines have ultra-low loss, cross-talk, and dispersion [6]. The process allows for the realization of extremely small features that are essential to the high frequency performance of frequency independent antennas. Because the PolyStrata™ process can produce micron-sized components, it is ideal for the fabrication of an extremely small feed region of the antenna.

A five step impedance transformer using the same impedances as the microstrip transformer in the previous section was designed using rectangular micro-coaxial (recta-coax) lines. The cross-sections corresponding to the impedances required of the recta-coax lines were computed using HFSS. The results are compared to those of the microstrip impedance transformer, and are shown in Fig. 3. In both cases, the transformers are matching 50Ω to 160Ω. As seen, the recta-coax line has loss similar to that of the microstrip line.

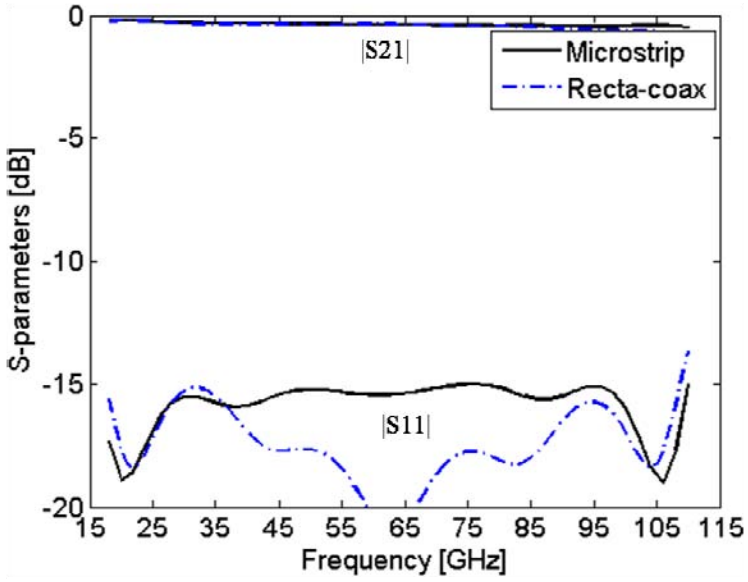

Fig. 3. HFSS simulation comparing the microstrip and recta-coax tranformers.

The realizations of higher impedance lines require that the top half of the recta-coax line is removed. By doing this, the capacitance of the line is decreased which increases the characteristic impedance of the line. In general, higher impedance lines can be made by making the inner conductor thinner, however, the choice of strata heights and aspect ratio are limiting factors. The design in this paper has a strata configuration that was pre-determined by the foundry. The strata stack-up from the silicon wafer up used in the transformer design is {50, 120, 20, 100, 50, 50, 100, 50, 125}μm, respectively. These dimensions correspond to the overall height of the recta-coax line of 665 μm. The inner

conductor of the coax is on layers 5 and 6, which are each 50μm thick. The strata configuration is shown in Fig 4. Strata 1 is the bottom and strata 9 is the top of the coaxial line. Strata 2 to 8 are used to construct the outer wall and form the interior of the line. Strata 5 and 6 are used to construct the inner conductor of the line.

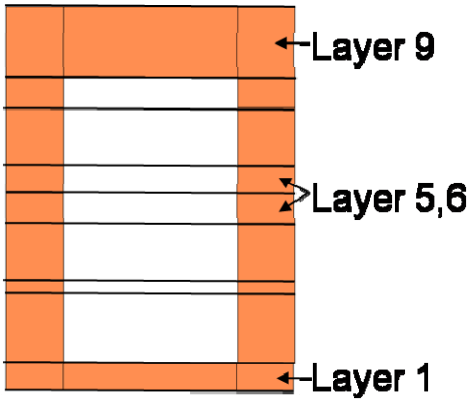

Fig. 4. The stack up of the recta-coax line with the heights of the layers from 1 to 9 being {50, 120, 20, 100, 50, 50, 100, 50, 125}μm, respectively. Layers 5 and 6 are used to construct the inner conductor of the line.

4. Log-Periodic Antenna Design

A planar log-periodic antenna with curved teeth is designed to operate from 18 to 110GHz. The angles that describe the antenna geometry are shown in Fig. 5. The antenna is designed to be self complimentary with $\alpha = 45°$, $\beta = 135°$, and $\chi^2 = \tau$. A slot configuration is chosen to enable the release from the wafer. The large α angle is used to allow for the feed line to enter the center of the antenna.

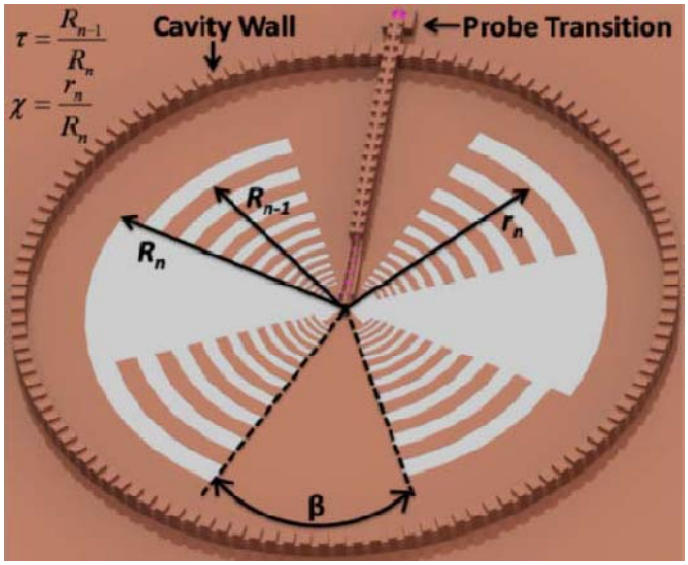

Fig. 5. Layout of the 10-50 GHz recta-coax antenna and the associated parameters.

Two prototypes of this antenna have been fabricated to validate the computational models. The first is a microstrip antenna with integrated band rejection at 6GHz operating from 1.8 to 11GHz [7]. This antenna was simulated on a 0.508mm thick RT/Duroid 6002 substrate. A four step microstrip impedance transformer is integrated onto the back side of the antenna. The impedances of the transformer are 126Ω, 104Ω, 86Ω, and 61Ω, respectively. The microstrip feed line is fed from the outside of the antenna, using the metallization of the aperture as the ground plane. A via is used to connect the feed line to the antenna aperture.

This prototype has the ninth tooth removed from the center to achieve band rejection. The measured VSWR of the antenna in the pass bands is below 2.0:1. The measured VSWR at the rejection frequency is greater than 13:1. The simulated co-polarized and cross-polarized realized gain is compared to the measured data and is shown in Fig 6., along with a photo of the front side of the radiator. Excellent agreement is shown between the measured and simulated data. The broadside gain is shown to be stable in the pass bands of the antenna.

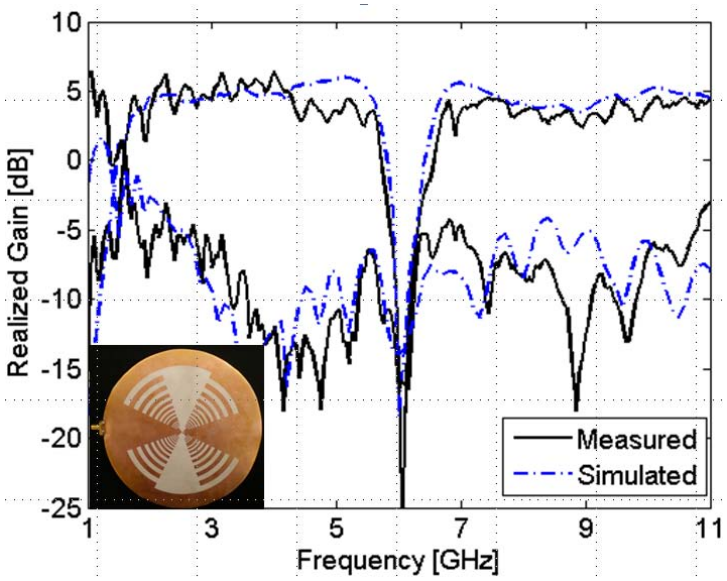

Fig. 6. Measured and HFSS simulated broadside gains of the low-frequency prototype.

The second article is fabricated in the PolyStrata™ process and operates from 10 to 50GHz. This antenna uses a three cascaded quarter wavelength lines, at 30 GHz. The impedances used in this transformer are 108Ω, 86Ω, and 60Ω. The upper limit of the realizable impedances that can be manufactured is set by the fabrication process. For this fabrication run, the design was limited to a maximum impedance of 108Ω. The simulated and measured VSWR of this antenna are also shown in Fig. 7. As seen, there is excellent agreement between computational model and measured data. Good performance is obtained for both test cases.

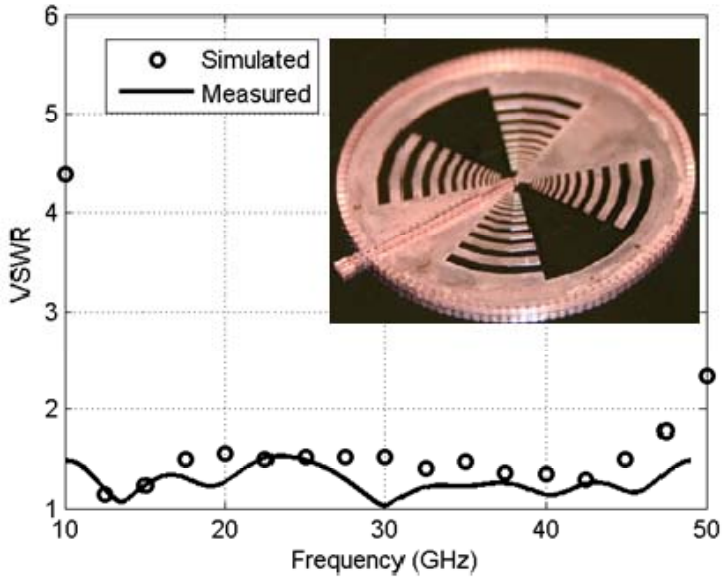

Fig. 7. Measured and HFSS simulated VSWR of Ku through V band antenna.

An 18 to 110GHz log-periodic antenna in free-space is designed and simulated using FEKO. The first antenna simulated had an edge length of the mesh specified to be 250μm. This simulation lead to an interesting result when the antenna pattern was studied at 102GHz. Based on previous simulations and measurement results, the pattern shown at 102GHz looked like a computational error rather than the physical pattern. Shown in Fig 8. is the 3-dimensional far-field plot. Notice how the field looks extremely deformed at 102GHz when compared to the field pattern at 18GHz.

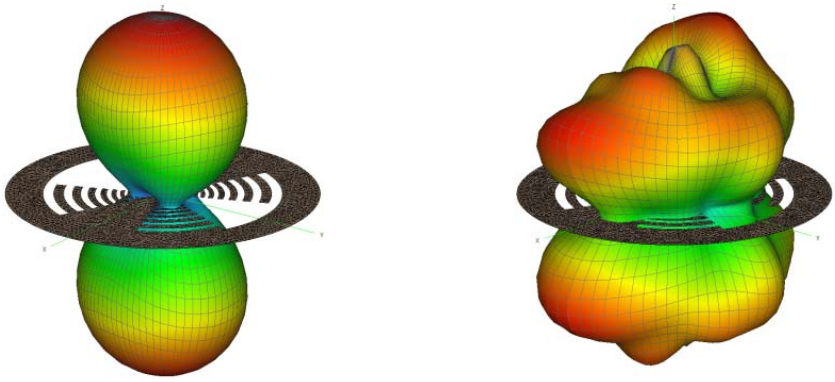

Fig 8. Simulated antenna patterns at 18 GHz (left) and 102 GHz (right).

To get a better understanding of what exactly happened in this simulation, the current distribution on the radiator was analyzed to see if there was anything irregular in regards to the structure. As shown in Fig. 9, the current distribution is plotted near the feed region of the antenna. The high current density, shown to be red, is the radiation region at 102GHz. It can be seen that the mesh is set to be smaller in the feed region of the antenna. After this region is passed, the mesh makes some triangles that are very narrow

and long. These have an undesirable aspect ratio and can lead to inaccuracies in the model. The log-periodic antenna is a symmetric device, and there is a large discrepancy between the two arms of the antenna in terms of meshing symmetry which could lessen the accuracy of the solution.

The antenna was meshed with a specified length of 200μm to allow for smaller triangles to fit in the regions where the triangle with the high aspect ratios were found. The model was ran at 102GHz to see if this change would correct the performance of the antenna at that frequency. Shown in Fig. 9 is the modified mesh and current distribution due to changes in mesh size. The current distribution shows that the antenna is radiating in the same region of the antenna at 102GHz as expected. Also, the antenna pattern is compared to the pattern at 18GHz and a great degree of pattern stability is observed, as shown in Fig. 10.

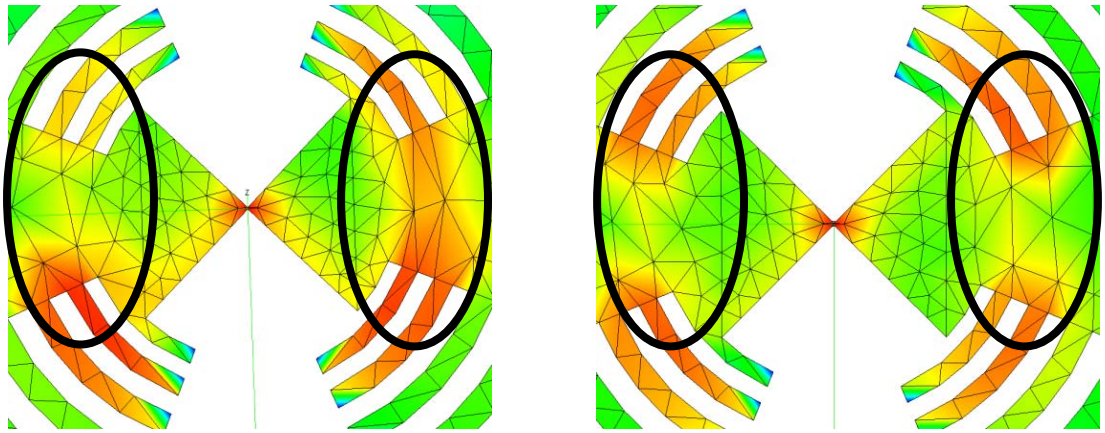

Fig. 9. Current distribution and the mesh with an edge length of 250μm (left) and 200μm (right).

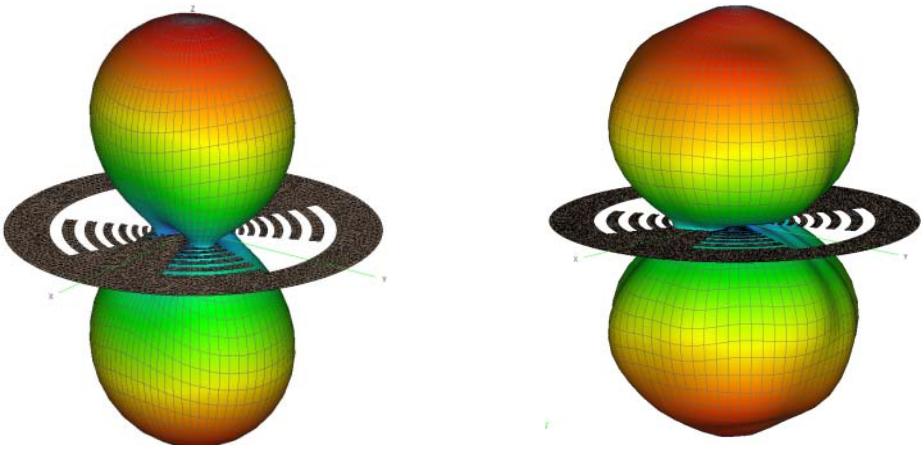

Fig. 10. Far-field antenna patters at 18GHz (left) and 102GHz (right) with an edge length of 200μm.

The stability of a CEMsolution can often be described by the matrix condition number. A desiredcondition number for a system matrix is 1, and it is shown that it typically increases as the rank of the matrix increase. The condition number is negatively affected by a poor discretization which could also lead to inaccurate results. Note that the size of the system matrix is dependent on the discretization of the problem. The condition numbers for 250μm and 200μm discretizations, inherent to the internal method of moment formulation within FEKO, were found to be 44,587 and 27,734, respectively. As discussed, the condition number of a matrix typically increases as the size of the matrix increases. Since the mesh segment length was decreased, one would expect that the solution matrix would become more unstable, or become larger. This was not the case. The finer mesh resulted in a higher degree of mesh symmetry. A higher degree of symmetry in the segmentation of the model resulted in a more accurate solution. For this problem, the condition number of 27,734 resulted in a solution that was expected. This number seems high in relationship to the ideal condition number. However, an example discussed by Garg describes a study that resulted in a stable solution even when the condition number of the matrix was on the order of 10^8 [8]. In this case, it appears that a condition number of 27,734 produces the expected result, whereas a value such as 44,587 produces a non-physical result.

5. Discussion

There are trade-offs to consider when deciding which process to use. For microstrip, the first design constraint is the excitation of higher order modes. If impedances lower than 50Ω are desired, which may be required if a filter or mulitplexer were to be integrated with the feed line, the cut-off frequency for higher order modes will reduce [9]. Secondly, the ability to precisely manufacture small lines and line gaps is crucial for the proper performance at millimeter waves. For the antenna designed on a dielectric of 2.2, the smallest tooth of the antenna has a width of approximately 2.3mils. Tight tolerances must be enforced to ensure that the structure of the antenna remains self-complimentary.

The tolerances of the PolyStrata™ technology allow for very delicate structures to be fabricated. Shown in Fig. 11 and 12 are the fabricated 18 to 110GHz log-periodic antenna with an integrated impedance transformer. The structure shown has features on the order of 50μm, such as the feed gap in the center of the SEM. The coaxial line feeding the center of the antenna has the upper half of the outer conductor removed to decrease the capacitance of the line, similar to the 10 to 50GHz prototype. The post that is connecting the antenna to the recta-coax feeder line has a diameter of 130μm. The 250μm long gaps in the outer conductor are used to allow the photoresist to exit the coaxial line. It is seen that these holes have little effect on the performance of the line.

These TEM lines can also achieve low impedances useful in filter design. The process allows for filters to be fabricated directly on the antenna aperture. Other types of devices such as diplexers, hybrids, and power dividers can be monolithically integrated in this

process. This allows for the complete integration of arrays and feed lines into on process. The capability of achieving low impedance lines for beamformers is a fundamental problem for microstrip antenna realizations with integrated feed lines that operate at, or above, 110GHz. Fig. 12 shows an integrated filter with one shorted stub on a planar log-periodic antenna in this process.

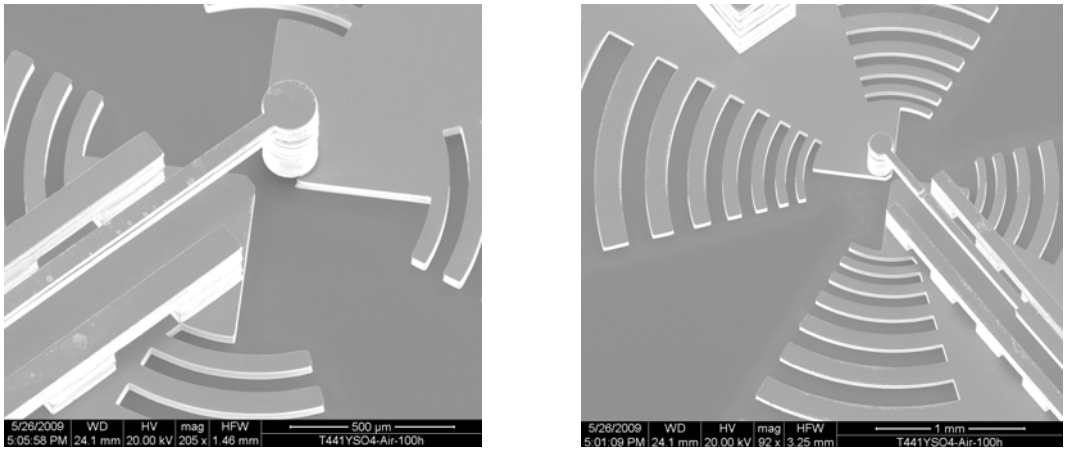

Fig. 11. Fabricated 18-110GHz recta-coax log-periodic. SEMs are of the feed region.

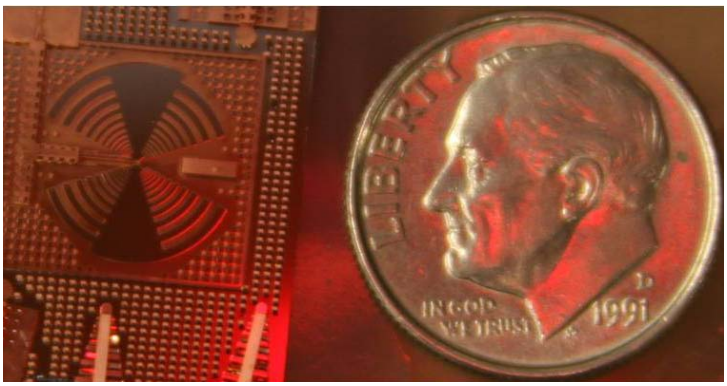

Fig 12. Photograph of a recta-coax log-periodic with integrated filter.

A log-periodic antenna is shown to perform well computationally when designed on a microstrip substrate or using the PolyStrata™ process, and the results are shown in Fig. 13, 14, and 15. The co- and cross-polarized gains are very similar in both cases. The gain also follows very closely to the simulations of the 1.8 to 11GHz prototypes shown in Fig. 3. The VSWR of both antennas are very similar, both being less than 2.0:1 through the pass band. Both realizations show that they would operate effectively up to 110 GHz. The PolyStrata™ antennas have the added benefit of being TEM and able to be manufactured to have lower impedances at higher frequencies than that of the microstrip lines, whereas the microstrip antenna has a smaller overall footprint due to the dielectric loading. Additionally, the recta-coax antennas can be more easily scaled to operate at higher frequencies. The fabrication cost between the two technologies are comparable for high quantities.

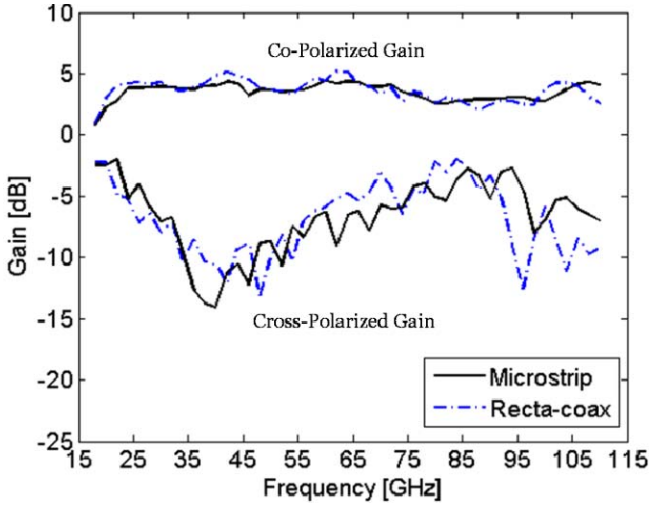

Fig 13. Broadside gains for two log-periodic antenna realizations.

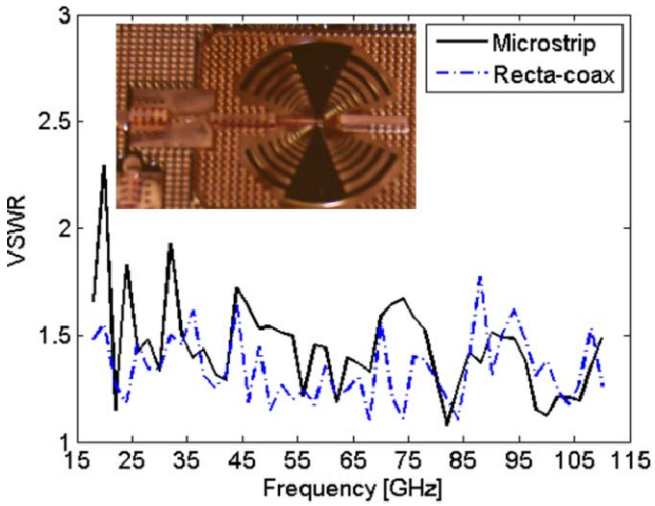

Fig 14. VSWR for two log-periodic antenna realizations. Shown in the inset is a photograph of the fabricated 18-110GHz recta-coax antenna.

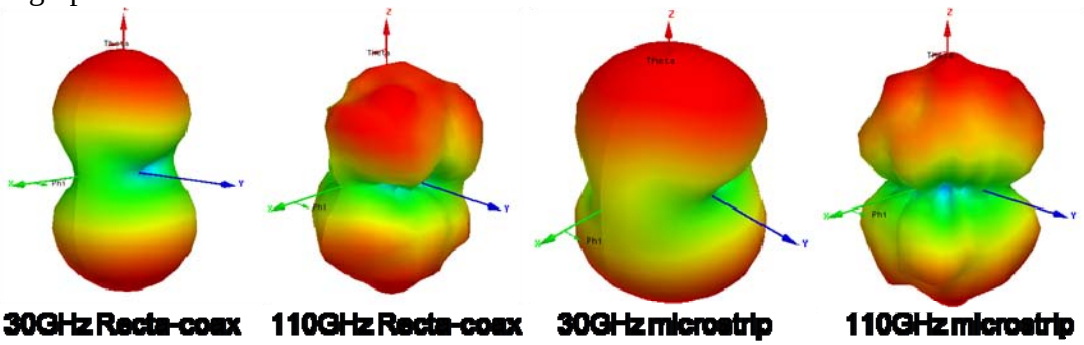

Fig 15. Radiation patterns at 30GHz and 110GHz for the recta-coax antenna (left) and microstrip (right).

7. Conclusions

Microstrip realizations of antennas operating up to W-band with integrated feed lines are feasible using thin dielectrics with low dielectric constants. Miniature recta-coaxial line and microstrip line impedance transformers are shown to operate with similar performance from 18 to 110GHz. Mesh symmetry is shown to be an important factor on the accuracy of the simulations. Two antennas were simulated using the different technologies and similar far-field performance and input impedance was shown. Recta-coax lines have the advantages of easier scaling to submillimeter-wave frequencies and the ability to achieve lower impedance values which are of use for any integration with feed networks.

6. Acknowledgements

This work is sponsored by the Office of Naval Research grant #N00014-07-1-1161. The authors would like to thank Dr. Peter Craig from the Office of Naval Research and W. Neill Kefauver from the University of Colorado.

7. References

[1] R. H. DuHamel, and D. Isbell, "Broadband logarithmically periodic antenna structures," *IRE Internation convention,* vol. 5, pp. 119-129, Mar 1957.

[2] K. M. P. Aghdam, R. Faraji-Dana, and J. Rashed-Mohassel, "Compact dual-polarisation planar log-periodic antenna with integrated feed circuit," *Proc. IEE Microw. Antennas and Propag.,* vol. 152, no. 5, Oct 2005.

[3] D. Sherrer and J. Fisher, "Coaxial waveguide microstructures and the method of formation thereof," U.S. Patent 7012489, Mar. 14, 2006.

[4] M. Lukic, S. Rondineau, Z. Popovic, and D. Filipovic, "Modeling of realistic rectangular μ-coaxial lines," *IEEE Trans. on Micro. Theory and Tech.,* vol. 54, no. 5, May 2006.

[5] M. Madjar, M. Muzia, "Low loss low cost microstrip millimeter wave mixers at 94 GHZ," *Convention of Electrical and Electronic Engineers in Israel,* pp. 1-5, March 1995.

[6] Y. Saito and D. S. Filipovic, "Analysis and design of monolithic rectangular coaxial lines for minimum coupling," *IEEE Trans. on Micro. Theory and Tech.,* vol. 55, no. 6, Dec. 2007.

[7] J. Mruk, W.N. Kefauver, and D.S. Filipovic, "Band rejection and feeder effects on the far-field purity of log-periodic antennas," *Antenna Measurements and Techniques Association 2008,* pp.1-6, Nov. 2008

[8] R. Garg, *Analytical and Computational Methods in Electromagnetics,* Boston, Massachusetts: Artech House, 2009, pp. 227.

[9] K.C. Gupta, R. Garg, I. Bahl, and P. Bhartia, *Microstrip Lines and Slot Line,* Boston, Massachusetts: Artech House, 1996, pp. 112-113

A Decoupling Technique for Compact Antenna Arrays in Handheld Terminals

Lap K. Yeung and Yuanxun E. Wang
Electrical Eng. Dept., Univ. of California at Los Angeles, CA 90095, USA

Abstract

In this paper, a practical method for decoupling small-form two- and four-element antenna arrays is discussed. This method is generic in the sense that it works on any types of antenna elements as long as they are identical and symmetrically arranged. The basic principle is to use a passive multi-port network to separate out various orthogonal radiation modes of a highly-coupled array for transmission and reception. In other words, the array as a whole, rather than each element, is treated as a single radiation entity. As these mutually orthogonal modes are uncorrelated and have no real energy exchange among them, the network ports corresponding to these modes are well isolated from each other. Therefore, problems associated with impedance matching and signal correlation due to close spacing of elements in traditional compact arrays can be avoided completely. Practical implementation issues of the mode decoupling networks for two- and four-element cases are the major concerns of this work. In addition, experimental prototype arrays with approximately 0.1λ element-to-element separation have been fabricated and tested to demonstrate the practicability of the method. Measurement results obtained are in good agreement with expectations, showing promising potential of the proposed mode-based decoupling approach for miniaturized arrays in handheld terminals.

1.0 Introduction

In recent years, miniaturization techniques for antenna arrays have drawn a great amount of attention owing to the ever-increasing interest in the multiple-input-multiple-output (MIMO) wireless communication architecture [1], which promises significant improvements on both capacity and diversity, for compact handheld terminals. At the same time, traditional smart antenna systems are continuing in demand of array modules with lower costs in smaller and lighter formats. However, the major limitation for conventional arrays used in these systems of multi-antenna architecture is that the element spacing is usually around 0.5λ to avoid mutual coupling. Hence, there is a

serious size concern which prevents these systems from being implemented in nowadays small-size handheld devices with wireless communication capability.

Traditionally, the design of compact antenna arrays is complicated due to the fact that array elements are not independent of each other. Instead, they interact electromagnetically through what is called mutual coupling. In fact, under strong coupling environment, elements in a closely-spaced array can sometimes be dramatically different from their isolated counterparts in terms of operating frequency, bandwidth, and radiation pattern. A considerable amount of research has been devoted in the past to study the impacts of mutual coupling on multi-antenna systems, especially for MIMO-based systems [2,3]. In general, it is found that the resulting impacts can be undesirable, such as reduction in capacity due to signal correlation or in gain due to impedance mismatch.

To overcome this problem, researchers have proposed different approaches [4]-[6] to decouple closely-spaced arrays. Recently, a mode-based technique [7]-[9] has been proposed for both beamforming and MIMO applications. The major advantage of this particular technique is that both wideband and element-independent decoupling can potentially be achieved. This paper focuses on mode-based decoupling for compact arrays with only two or four elements. Specifically, practical implementation issues for the mode decomposition networks (MDNs) using two typical package technologies are discussed. While presenting the basic theoretical background, experimental results from fabricated prototypes are also presented to demonstrate the practical aspects of the approach.

2.0 Theory

2.1 Orthogonal Radiation Modes

In essence, the number of orthogonal radiation modes associated with an antenna array equals to its number of radiation elements. Any radiation patterns originated from the array can be represented by linear combinations of these modes with different complex-valued weights. To understand this concept mathematically, conventional multi-port circuit analysis can be used. Without loss of generality, a four-element circular array with identical elements is considered. The scattering matrix of this array has the form of

$$\mathbf{S}_{\mathrm{a}} = \begin{pmatrix} s_{11} & s_{12} & s_{13} & s_{12} \\ s_{12} & s_{11} & s_{12} & s_{13} \\ s_{13} & s_{12} & s_{11} & s_{12} \\ s_{12} & s_{13} & s_{12} & s_{11} \end{pmatrix}, \quad \text{with } \mathbf{b} = \mathbf{S}_{\mathrm{a}}\mathbf{a} \tag{1}$$

where **a** and **b** are vectors of power waves going into and coming out from the antenna ports. By performing the eigenvalue decomposition on the matrix, it can be written as

$$\mathbf{S}_a = \mathbf{X}\mathbf{D}\mathbf{X}^{-1} \tag{2}$$

where **D** is a diagonal matrix containing all eigenvalues of $\mathbf{S}_a$, **X** is an orthonormal matrix consisting of the corresponding eigenvectors and $\mathbf{X}^{-1}$ is the matrix inverse of **X**. Due to the unique symmetry of $\mathbf{S}_a$, the orthonormal matrix is real and is given by

$$\mathbf{X} = \begin{pmatrix} +1/2 & -1/2 & -1/2 & +1/2 \\ +1/2 & -1/2 & +1/2 & -1/2 \\ +1/2 & +1/2 & -1/2 & -1/2 \\ +1/2 & +1/2 & +1/2 & +1/2 \end{pmatrix}, \quad \text{and } \mathbf{X}^{-1} = \mathbf{X}^{\mathrm{T}}. \tag{3}$$

Now, if we define a new in-coming power wave vector as $\mathbf{a}_{\text{new}} = \mathbf{X}^{\mathrm{T}}\mathbf{a}$, and a new out-going power wave vector as $\mathbf{b}_{\text{new}} = \mathbf{X}^{\mathrm{T}}\mathbf{b}$, we can rewrite (1) as

$$\mathbf{b}_{\text{new}} = \mathbf{D}\mathbf{a}_{\text{new}}. \tag{4}$$

According to (4), it is seen that the array is decoupled in the sense that the four newly defined excitation modes, or eigenmodes (given by $\mathbf{a}_{\text{new}} = (1, 0, 0, 0)^{\mathrm{T}}$, $\mathbf{a}_{\text{new}} = (0, 1, 0, 0)^{\mathrm{T}}$, $\mathbf{a}_{\text{new}} = (0, 0, 1, 0)^{\mathrm{T}}$ and $\mathbf{a}_{\text{new}} = (0, 0, 0, 1)^{\mathrm{T}}$), do not interfere with each other because of the diagonal feature of **D**. This is also true for their radiation patterns.

2.2 Mode Decomposition Networks

From the previous analysis, it is clear that we can "diagonalize" an array by having a passive multi-port network which plays the same role as that of **X**. For two-element symmetrical arrays, it can be achieved by simply using a single 180-degree coupler. When the two antennas are connected to its IN and ISO ports, the even- and odd-mode can then be accessed through its Σ and Δ ports. Since the two ports are well isolated, independent matching to each mode becomes possible. For four-element arrays, four 180-degree couplers connecting in the way shown in Fig. 1 is required. It should be mentioned that there are more than one way to construct the so called mode decomposition networks (MDNs). As an example, Fig. 3b shows an alternative configuration for the four-element case. Here, 90-degree couplers (branch-line or coupled-line) with additional transmission lines are used. The advantage for this specific arrangement is the possibility of uniplanar or miniaturized realization.

Viability of this mode-based technique depends heavily on the correct implementation of MDNs. Various packaging technologies are available for this purpose including multilayered printed circuit board (PCB) and low temperature co-fired ceramic (LTCC). Traditional multilayered PCBs have the low cost advantage due to the use of FR4 as their substrate material. Even though they are relatively lossy at radio frequency (RF) and their vertical layering configuration is generally less flexible, they are nevertheless a good choice for realization of MDNs for applications at the lower-end RF spectrum. On the other hand, LTCC can be used to obtain better loss performance and

further miniaturized in size. There are already many successful examples of using this technology to completely integrate a RF front-end into a single and yet small-size volume of substrate. Thanks to the flexible multilayer architecture of LTCC, various innovative passive structures and compact integration of many components become possible. Figs. 2a and 3a show examples of PCB-based and LTCC-based MDN designs respectively.

3.0 Design Examples and Results

3.1 A Scanning Array Module

A compact electronically scanning array based on the proposed technique has been designed. It operates at 2.4 GHz and is suitable for WLAN applications. The prototype consists of four $\lambda/4$ monopole antennas with 0.1λ spacing. Moreover, the MDN and matching networks are fabricated on a two-layer PCB with the monopoles soldered on it separately. Fig. 2a depicts its layout and the actual prototype mounted on a 128 mm × 128 mm ground plane. It is seen that the MDN is implemented by four 90-degree hybrids to facilitate for a uniplanar implementation since no cross-over is needed. However, in order to provide the missing 90-degree phase-shift, each hybrid requires a 90-degree transmission-line connected at one of its ports.

From the measured results, a 13-dB return loss for each of the signal ports (except Port 3 which is not used) and a 16-dB port-to-port isolation at the operating frequency has been obtained. Hence, the orthogonal modes of this four-monopole array can be independently accessed. By combining these modes with suitable power weightings, a high-gain pattern with full 360-degree scanning capability can be achieved. Fig. 2b shows the measured high-gain (5 dBi) pattern scanned from $\varphi = 90°$ to $\varphi = 180°$ in four steps. Details of the module can be found on [9].

To reduce the size of the MDN, a modified LTCC version has been designed. In this version, coupled-line couplers instead of branch-line couplers are used. Its schematic and metal printings on different LTCC substrate layers are depicted on Figs. 3a and 3b. The overall size is 6.1 mm × 6.1 mm, a significant size reduction as compared with the uniplanar counterpart. Notice, however, that the 180-degree transmission-line (as shown in the schematic) is not implemented in this case as balanced-type antennas are intended to be used. Furthermore, integrated matching networks are also deliberately left out so that flexible external matching can be done. Nevertheless, all these components can be easily integrated into the substrate by simply adding only two to three more layers without increasing its size. From the full-wave simulation results shown in Fig. 3c, it is seen that the amplitude balance between every pair of antenna ports is within 1 dB and the isolation between every pair of signal ports is more than 15 dB.

3.2 A Low-profile MIMO Module

Another potential application of the technique is in low-profile MIMO arrays for Digital Video Broadcasting – Handheld (DVB-H) terminals. DVB-H operating frequency is allocated at the UHF band from 470 MHz (channel 21) to 862 MHz (channel 69) but is usually limited to 702 MHz (channel 49) for interoperability consideration with GSM-900 systems. Nevertheless, the relative operating bandwidth required for this radio is about 40% which makes the use of antenna-specific decoupling techniques very difficult if not impossible.

Since wideband 180-degree couplers are available, MDNs covering the whole DVB-H band are possible. Fig. 4 shows an example of such wideband couplers. This particular configuration is similar to the traditional rat-race ring but with the 270-degree transmission-line section being replaced by a diagonally shorted coupled-line pair. However, the required level of coupling is usually too strong for a single pair of edge-coupled microstrips to achieve. Therefore, a multi-line coupling configuration should be used (see Fig. 4). With this specific design, a wideband MDN for four-element arrays can be realized by following the schematic shown in Fig.1. In order to have the network fitted on a PCB of size 50 mm × 110 mm (a typical size for handheld terminals), multilayer PCB technology is used. Fig. 5 depicts the PCB layout design consisting of six printed metal layers. Whereas layers 2, 4, and 6 serve as RF grounds and are completely filled with metal, the four couplers are implemented on layers 3 and 5 in stripline format for good isolation. Buried vias are then used to connect these couplers together. From the measured results shown in Fig. 6, it is seen that an isolation of more than approximately 20 dB over the whole DVB-H band is achieved between any two signal ports when all antenna ports are terminated by 50-Ω loads.

To form a complete MIMO array, four spiral antennas suspending by 12-mm thick foam below layer 6 are connected to the MDN. At the same time, lumped matching components are used on the top side (layer 1) to individually match the four orthogonal modes associated with the array. The fabricated prototype is shown in Fig. 7 and its measured s-parameter is shown in Fig. 8. It is seen that an isolation of more than 15 dB is achieved between any pair of signal ports over 410 MHz to 702 MHz. Without the MDN, coupling among any two antennas would be much stronger. However, as fixed matching networks (matched at 610 MHz) are used in this work, the 10-dB return loss bandwidth for each mode cannot cover the whole DVB-H band. Therefore, tunable matching will be required for the future versions of the module. It should also be mentioned that the isolation is generally poor around the matched frequency because of the undesired phase-shifts from the via-hole connections inside the PCB. In addition, the four hand-made antenna elements are not completely identical.

5.0 Conclusion

A practical mode-based decoupling approach for compact arrays has been demonstrated. In this approach, orthogonal radiation modes, or eigenmodes, of highly-coupled arrays are utilized as independent radiation mechanisms to avoid mutual coupling and correlation. Comparing with traditional arrays, mode-based arrays can be much smaller in size and be more readily integrated into miniaturized handheld terminals. Two example applications, namely, 2.4-GHz pattern scanning and DVB-H MIMO modules have been designed using either multilayer PCB or LTCC packaging technologies. The corresponding PCB-based prototypes have been fabricated and tested. Measured results indicate that at least 15-dB port-to-port isolation has been achieved even for an element-to-element separation of less than 0.1λ. These results suggest the practicability of the technique.

References

1. M. A. Jensen and J. W. Wallace, "A Review of Antennas and Propagation for MIMO Wireless Communications," *IEEE Trans. Antennas Propag.*, vol. **52**, no. 11, pp. 2810-2824, November 2004.
2. J. W. Wallace and M. A. Jensen, "Mutual coupling in MIMO wireless systems: a rigorous network theory analysis," *IEEE Trans. Wireless Comm.*, vol. **3**, no. 4, pp. 1317-1325, July 2004.
3. T. Svantesson and A. Ranheim, "Mutual coupling effects on the capacity of multielement antenna systems," in *Proc. IEEE ICASSP*, May 2001, vol. **4**, pp. 2485-2488.
4. J. B. Andersen and H. H. Rasmussen, "Decoupling and descattering networks for antennas," *IEEE Trans. Antennas Propag.*, vol. **24**, no. 6, pp. 841-846, November 1976.
5. H. J. Chaloupka and X. Wang, "Novel approach for diversity and MIMO antennas at small mobile platform," in *Proc. IEEE PIMRC*, Sept. 2004, vol. **1**, pp. 637-642.
6. H. J. Chaloupka, X. Wang, and J. C. Coetzee, "A superdirective 3-element array for adaptive beamforming," *Microwave Optical Tech. lett.*, vol. **36**, no. 6, pp. 425-430, March 2003.
7. T. I. Lee and Y. E. Wang, "A planar multipolar antenna for MIMO applications," in *Proc. IEEE Antennas Propag. Symp.*, June 2007, vol. **1**, pp. 2429-2432.
8. T. I. Lee and Y. E. Wang, "Mode-based information channels in closely coupled dipole pairs," *IEEE Trans. Antennas Propag.*, vol. **56**, no. 12, pp. 3804-3811, Dec. 2008.
9. L. K. Yeung and Y. E. Wang, "Mode-based beamforming arrays for miniaturized platforms," *IEEE Trans. Microwave Theory Tech.*, vol. **57**, no. 1, pp. 45-52, Jan. 2009.

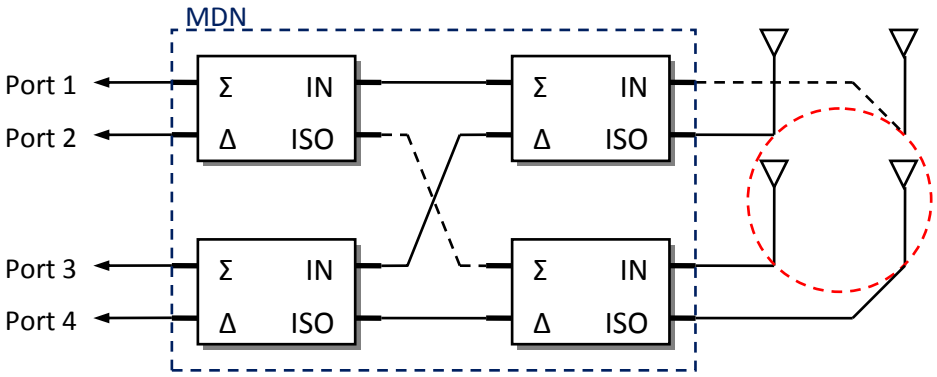

Fig. 1. A mode decomposition network for four-element arrays.

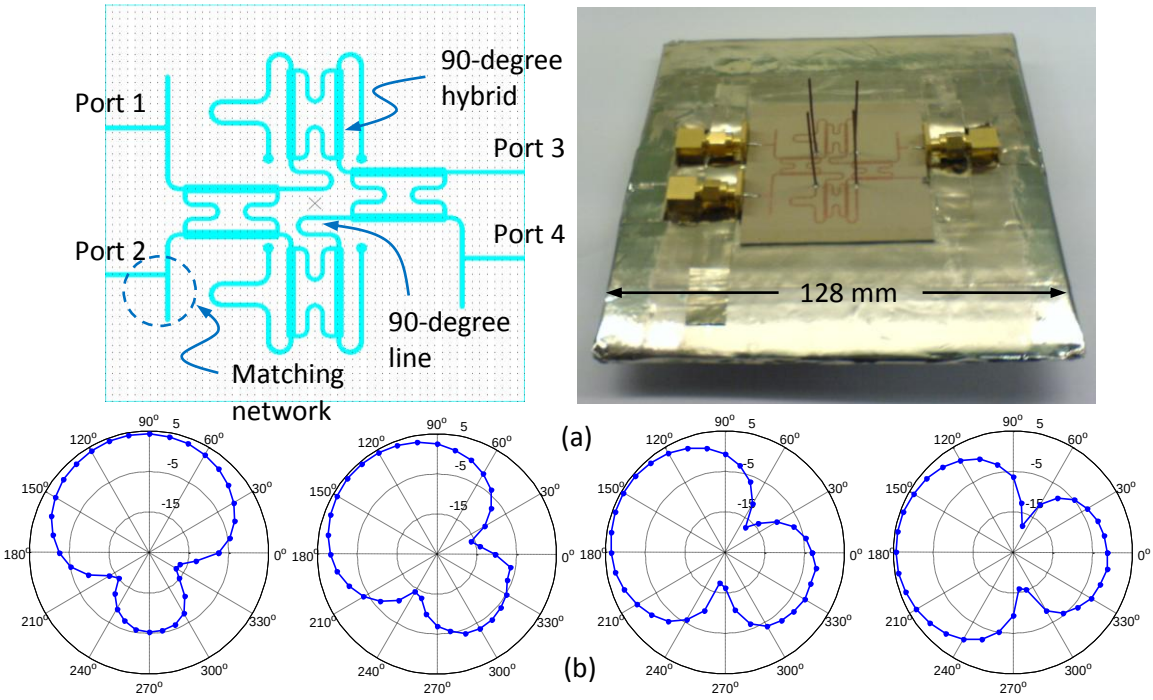

Fig. 2. A 2.4-GHz electronically scanning array module (a) layout; and its (b) measured scanning gain patterns.

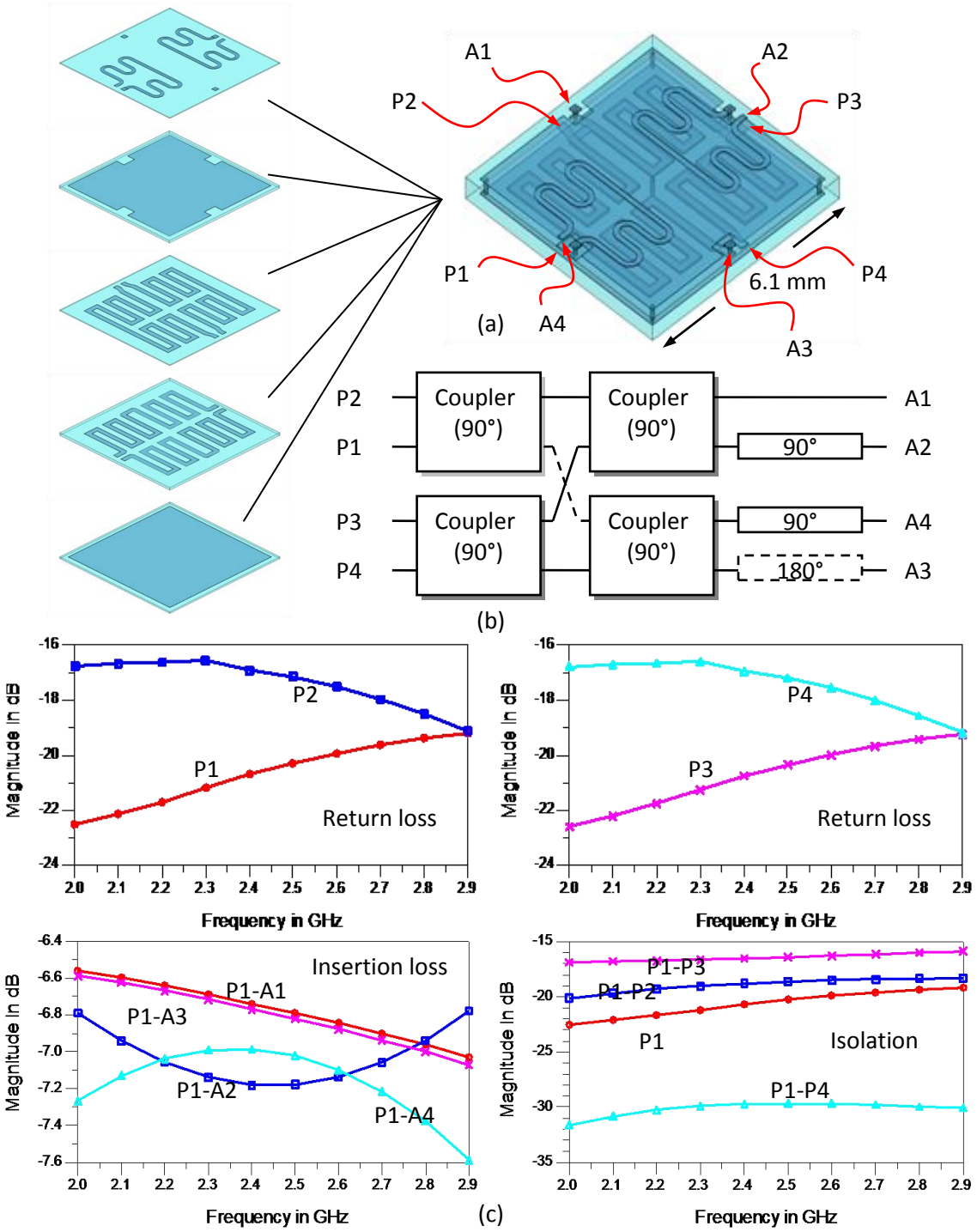

Fig. 3. A miniaturized 2.4-GHz LTCC-based MDN (a) layout and (b) schematic; and its (c) full-wave simulated scattering parameters.

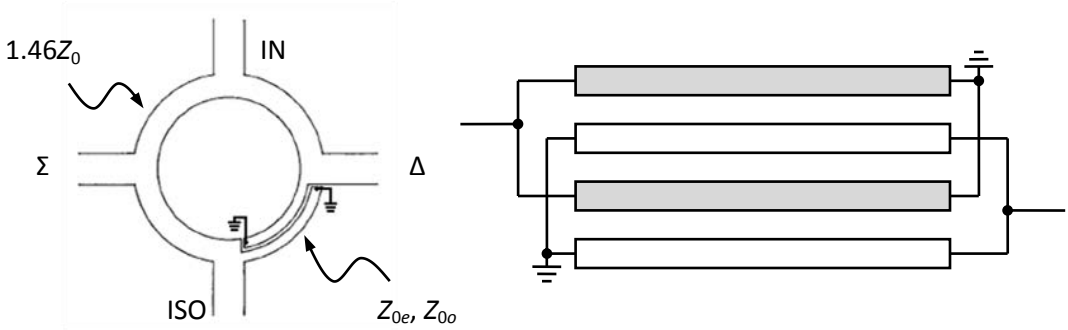

Fig. 4. A wideband 180-degree hybrid ring and a multi-line coupling section.

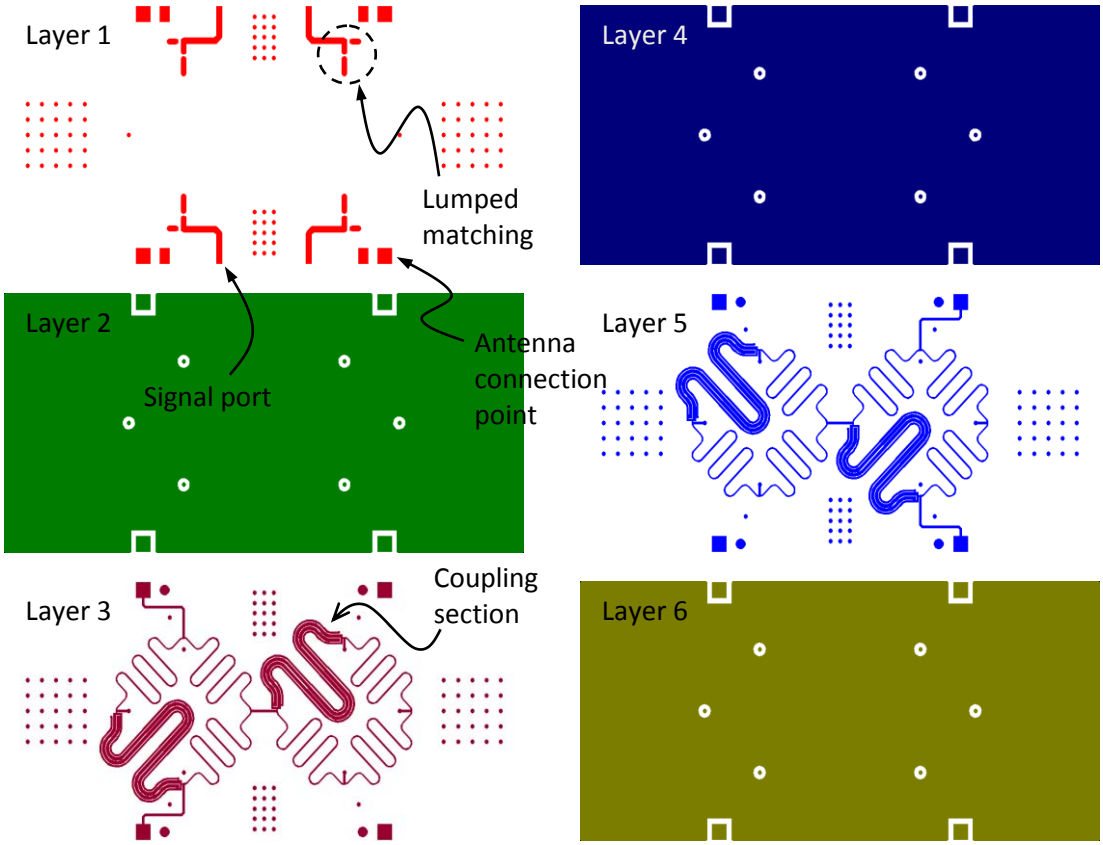

Fig. 5. The PCB layout of a wideband MDN for DVB-H applications.

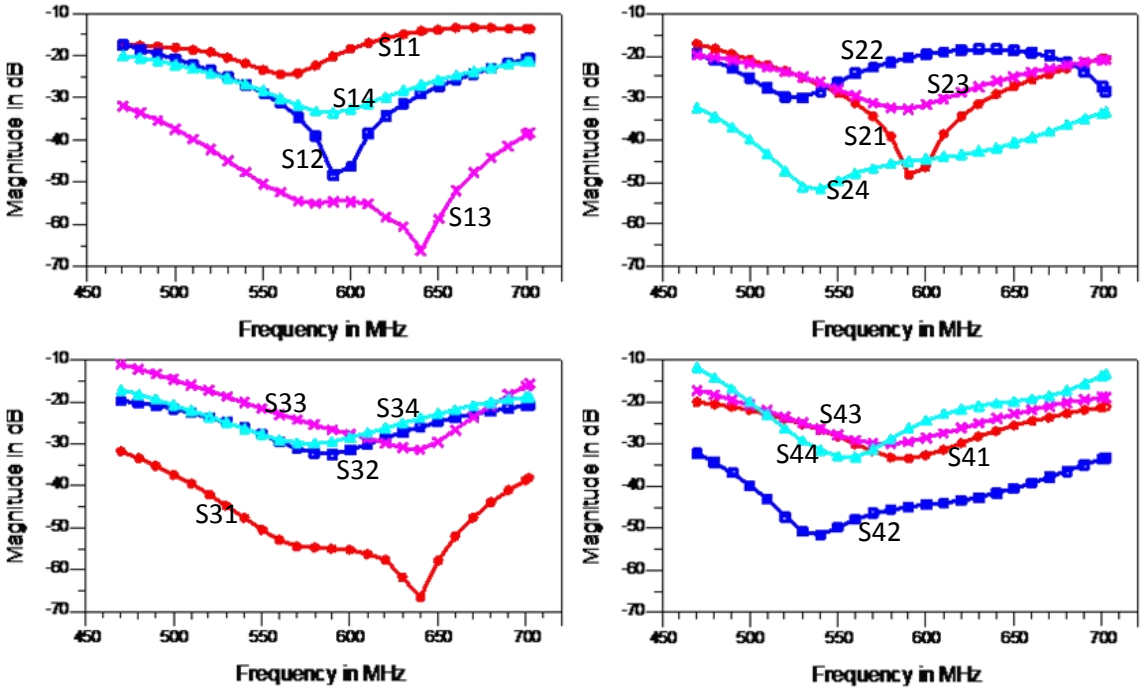

Fig. 6. Measured scattering parameters for the DVB-H band MDN with 50-Ω terminations at the antenna ports.

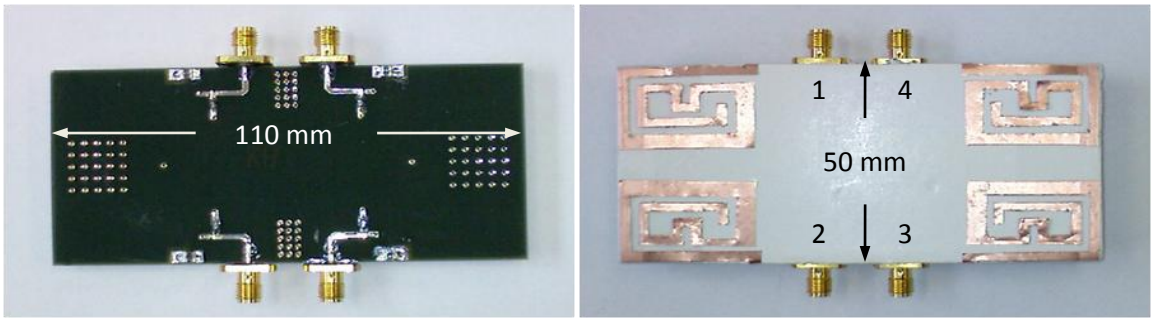

Fig. 7. The fabricated prototype DVB-H MIMO array module.

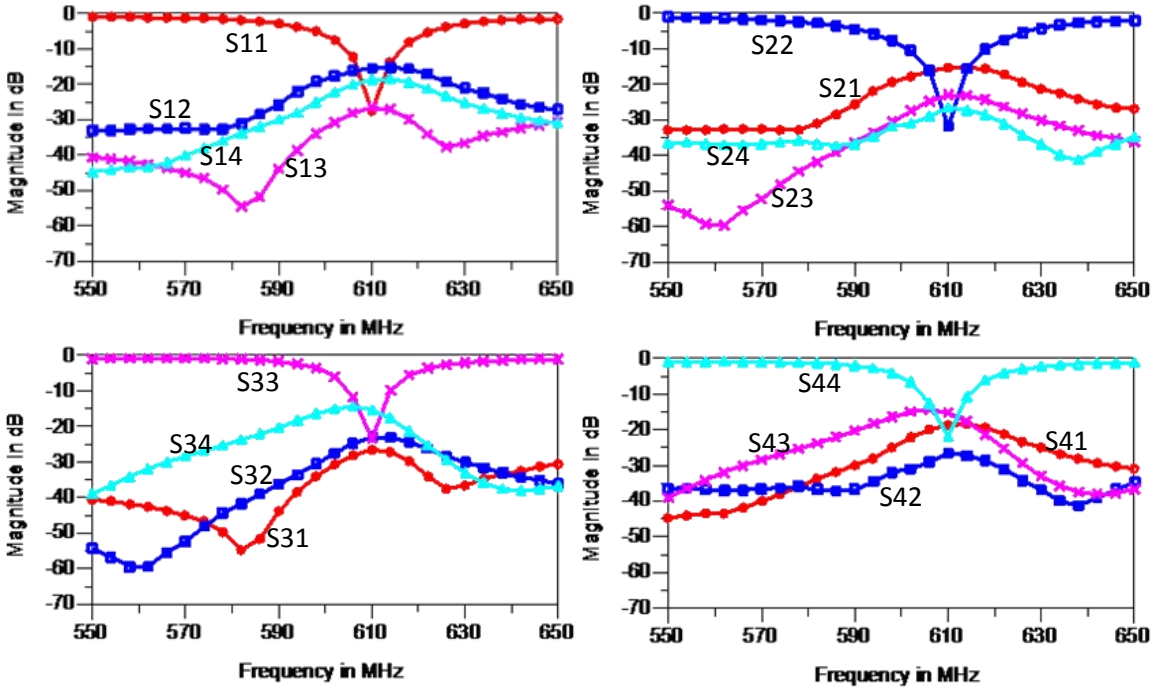

Fig. 8. Measured scattering parameters for the complete DVB-H MIMO array with fixed matching at 610 MHz.

A New Modular Wideband Array Topology

S. S. Holland, M. N. Vouvakis, D. H. Schaubert

Center for Advanced Sensor and Communication Antennas
Department of Electrical and Computer Engineering
University of Massachusetts, Amherst, MA 01003
{sholland, vouvakis, schaubert}@ecs.umass.edu

This paper introduces the Banyan Tree Antenna (BTA) array which offers wide-band, wide-scan operation with modular, low-cost fabrication and assembly. More importantly, the new array is directly fed by unbalanced transmission lines (via standard RF interfaces), eliminating the use of external baluns or hybrids. At the present development stage, the array has demonstrated approximately two octaves of bandwidth in infinite array simulations for both single- and dual-polarized arrangements. BTA array elements are made of two flared conducting fins that are not connected to neighboring array elements, similar to bunny-ear or balanced antipodal Vivaldi antenna (BAVA) designs. When fed with unbalanced feeds, such two-conductor designs are known to develop severe mid-band impedance anomalies due to a common (monopole) mode. The key advantage of BTA over these designs is the elimination of that common mode through the use of shorting posts at each element fin. This enables performance similar to balanced fed modular designs, but without external baluns.

1. Introduction

Wideband phased arrays will be the central RF-front-end component in future multi-functional communications/sensing/countermeasure systems. In such systems multiple antennas are replaced by one or two phased array systems each with stringent electrical and manufacturing specifications. Typical array electrical specifications require:

- wideband and wide-scan performance,
- multi-beam ability,
- polarization agility,

while manufacturing/maintenance specifications require:

- low cost and frequency-scalable fabrication,
- modular assembly,
- direct connection to standard RF interfaces, and
- low profile.

Over the years, a lot research effort has focused on meeting both electrical and manufacturing requirements with various levels of success.

Some designs, like the tapered slot (Vivaldi) arrays [1],[2], have successfully met all electrical requirements, but are relatively expensive to build in dual-polarized arrangements or at higher frequencies due to their non-modular, vertically-integrated

fabrication. In addition, wideband Vivaldi arrays use long end-fire elements that increase weight and size and can degrade polarization purity (at D-plane scans) and scattering signature (at grazing angles). Various other Vivaldi-like designs such as the body-of-revolution (BOR) Vivaldi arrays [3] have been proposed that eliminate the need for connected fins but, as shown in their publication, a machined back-plate that spans the entire array is needed.

In search of modular and low-profile arrays Elsallal and Schaubert [4, 5], and later Otter et al. [6], used the Antipodal Vivaldi Antenna (AVA) [7] and Balanced Antipodal Vivaldi Antenna (BAVA) [8] as array elements. These designs, under appropriate feeding conditions, can achieve multi-octave bandwidths, and are modular and low-profile. Elsallal showed that a naive arrangement of BAVA elements in a two-dimensional array led to severe mid-band impedance anomalies due to the development of a common-mode. In the same work, a novel technique based on the mirroring of every other element in both E and H planes was proposed to eliminate the common-mode [9]. The Doubly-Mirrored BAVA (Dm-BAVA) has demonstrated bandwidths up to 5:1, and is modular and low profile, but it requires a non-trivial feeding mechanism. Namely, to recover the proper aperture-field distribution, mirrored elements must be fed 180º out-of-phase. For narrowband designs this is easily done, but in a wideband setting it is equivalent to using external wideband baluns or hybrids, thus limiting the array's ability to directly connect to standard RF-interfaces.

Along the same lines, Lee et al. [10] proposed a bunny ear element to design modular wideband arrays. The element consists of a dielectric slab with a tapered slotline printed on each side that transitions from a narrow slot at the ground plane to a wide slot at the radiating aperture. The ground plane of the slotline is shaped into fins, with a narrow fin at the ground plane and a wide fin at the aperture. The element achieves wide bandwidth, and is low profile and modular, but it also requires a balun at the base of the element.

Several other low-profile wideband array technologies i.e. Current Sheet Array (CSA) [11] and Fragmented Aperture Array (FAA) [12], have proposed the use of planar printed elements. Although wideband, both of these designs are not modular and require elaborate feeding mechanisms that involve feed organizers and external baluns.

The insistence on eliminating external baluns is not merely a matter of taste. In practice, external baluns have inherent phase and amplitude imbalances and finite common-mode rejection ratios (CMRR) [13] that can weakly excite the catastrophic common-mode in the array. In addition, passive baluns with more than 4:1 bandwidth, although bi-directional, are large, leading to increased array profile, and have high insertion loss. On the contrary, active baluns are small, wideband and have gain, but are limited to receive-only arrays due to power handling and thermal sensitivity considerations [13].

From the above discussion it is apparent that, to date, no array technology has met both electrical and manufacturing specifications for multi-functional arrays. The present paper

introduces the Banyan Tree Antenna (BTA) array that meets all electrical and manufacturing specifications for bandwidths up to two octaves. The BTA array is made of elements that have two distinct tapered fins that are not connected to neighboring elements, thus leading to modular construction. Unlike bunny-ear or BAVA arrays, the BTA array eliminates the mid-band common-mode by modifying the element topology, through the addition of shorting posts at each fin. These posts shift the common-mode out-of-band, without significantly affecting the in-band performance. BTA arrays are low-profile (approximately half-wavelength at the highest frequency), can be manufactured with various low-cost technologies (e.g. printed circuit board etching), and are directly connected to standard RF-interfaces (SMA, GPO, GPPO, etc) or unbalanced transmission lines. BTA arrays have demonstrated in simulations approximately 4:1 bandwidths in both single- and dual-polarized arrangements, with good scanning performance out to 45-degrees in all planes.

The remainder of the paper is organized as follows. Section 2 will identify and study the problem of the common-mode on arrays that use elements with more than two conductors in a unit cell. Section 3 describes the BTA array topology. In section 4, the means of controlling the common-mode on-set in BTA arrays is given. Sections 5 through 7 document the impedance performance of various BTA embodiments in single- and dual-polarized arrangements, for broadside and scan excitation. The paper concludes in section 8.

2. The Common-Mode Problem

Consider the element shown in Figure 1(A), which consists of two vertical dipole-like fins. The fins are fed unbalanced, with one fin excited by a signal source below the ground plane and the other fin connected to ground (note: parameters are identical to the element described in Figures 3 and 4, except without the shorting posts). These elements behave similarly to a BAVA or AVA element, exhibiting end-fire radiation and wideband impedance behavior when used as large isolated elements, but are also plagued by severe bandwidth-limiting impedance anomalies when arranged in planar rectangular grid arrays. This particular element shows good performance over two separated frequency bands, the first from 1.7GHz and 5GHz and again from 6.8GHz and 8GHz, shown in Figure 1(A). While dual band applications do exist, this element is not useful for true wideband systems. Studies of the fields and currents on the structure reveal differential current modes on the fins throughout both operating bands, and strong common mode (monopole) currents at frequencies in between the operating bands which cause the VSWR anomaly.

In recent years, Elsallal [9] has found that by mirroring the elements and properly phasing them, as shown in Figure1(B), the common mode anomaly can be suppressed and moved completely out of the operating band. This method has very good VSWR performance, achieving a large continuous bandwidth from below 2GHz to over 8GHz

and is modular, low-profile construction, but requires an external balun/hybrid in the feed network.

Further study of this problem has led to the development of the Banyan Tree Antenna, shown in Figure 1(C), where the elements are no longer mirrored but now include additional vertical metal posts shorting each of the fins to the ground plane. The shorting posts allow the frequency of the common mode to be controlled, as discussed in section 5, and can be used to increase the common mode frequency sufficiently to move it out of the operating band. This configuration shows good VSWR performance from 2GHz up through 8GHz of continuous bandwidth. While this topology attains bandwidth slightly less than the mirrored configuration, there is no balun or hybrid required to feed the elements, thus making this solution robust and economical.

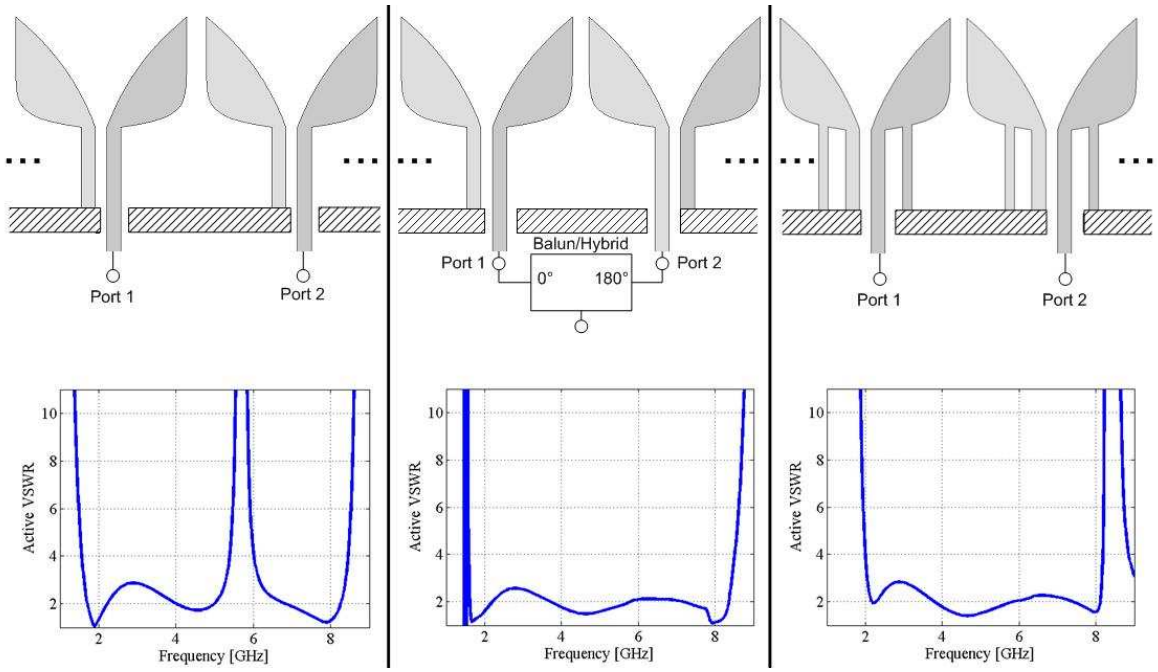

Figure 1 – Methods of controlling the common mode anomaly in planar arrays of tapered fin elements. Comparison of infinite planar array VSWR (broadside beam) of single-polarized, planar arrays for (A) exponentially flared element, (B) mirrored exponentially flared elements and (C) the Banyan Tree Antenna. (Design parameters are kept the same in all three cases).

3. Banyan Tree Antenna (BTA) Topology

The Banyan Tree Antenna array, shown in a modular single-polarized arrangement in Figure 2, is an array of vertically integrated fins which flare from a narrow feed line at the ground plane to arms with exponential tapers on the interior and exterior edges with taper rates R_i and R_o respectively, as shown in Figure 3. The fins are approximately λ/4

in height at the middle of the operating band. Two feed lines extend from the ground plane to the tapered arms, with one line connected directly to ground and the other excited directly with an unbalanced generator or transmission line, for example, the inner conductor of a coaxial probe. The tapered fins act as an impedance transformer to match the high impedance presented at the top of the array's flared arms to the 50Ω RF interface at the ground plane. In addition to the tapered fins, metal posts of width W_s are placed a distance d from the feed stem connecting each of the fins directly to the ground plane. These shorts are critical to the array's wideband operation, and resemble the root system of its namesake, the Banyan tree. Spacing in the E and H-plane of the array is chosen to be less than $\lambda/2$ at the highest frequency in the operating band to avoid grating lobes, and the element width is typically close to the element spacing. This allows the capacitive coupling between elements to be large, which is one of the tuning mechanisms that allows for high bandwidth operation.

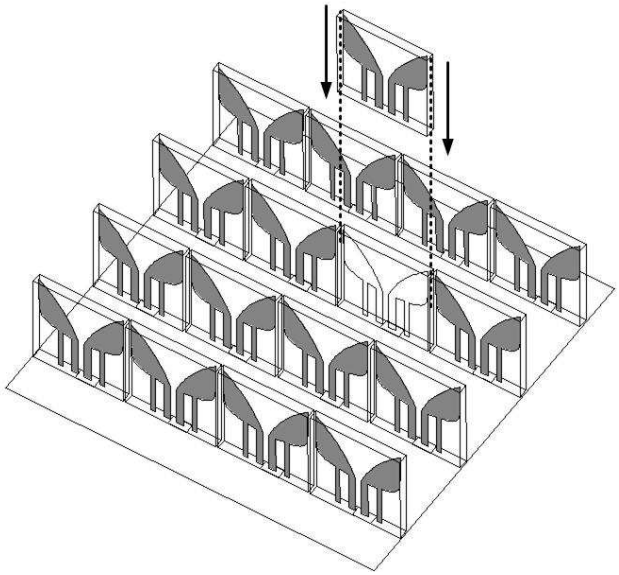

Figure 2 - Single-polarized Banyan Tree Antenna array. Modular BTA elements are directly connected to unbalanced transmission lines.

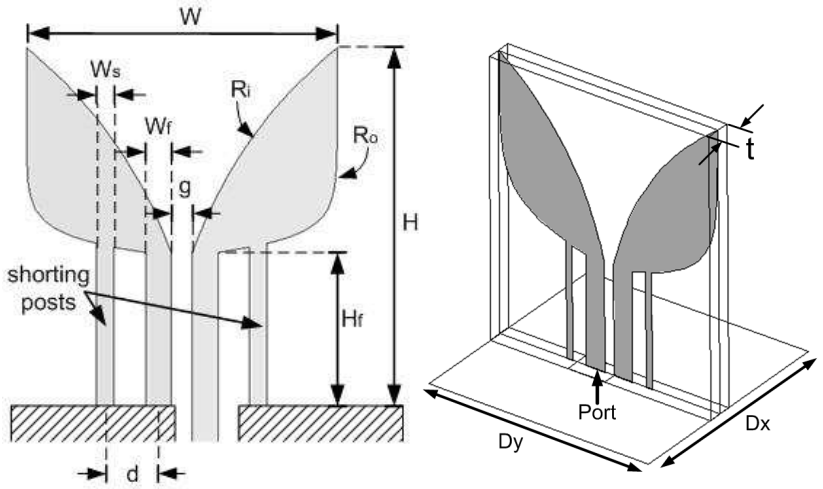

(A) (B)

Figure 3 - Banyan Tree Antenna element. (A) Element side view along with the geometrical design parameters used in this study, (B) element isometric view.

4. Control of the Common Mode in BTA

The shorting posts of the Banyan Tree Antenna allow control over the frequency at which the common mode anomaly occurs through the location of the shorting posts. The single-polarized element shown in Figure 3 is placed in an infinite planar array and the effect of the shorting posts is investigated. The solid curve in Figure 4(A) shows the broadside active VSWR of the baseline structure without shorting posts. In this geometry a catastrophic anomaly appears at 5.6GHz, leading to reduced bandwidth.

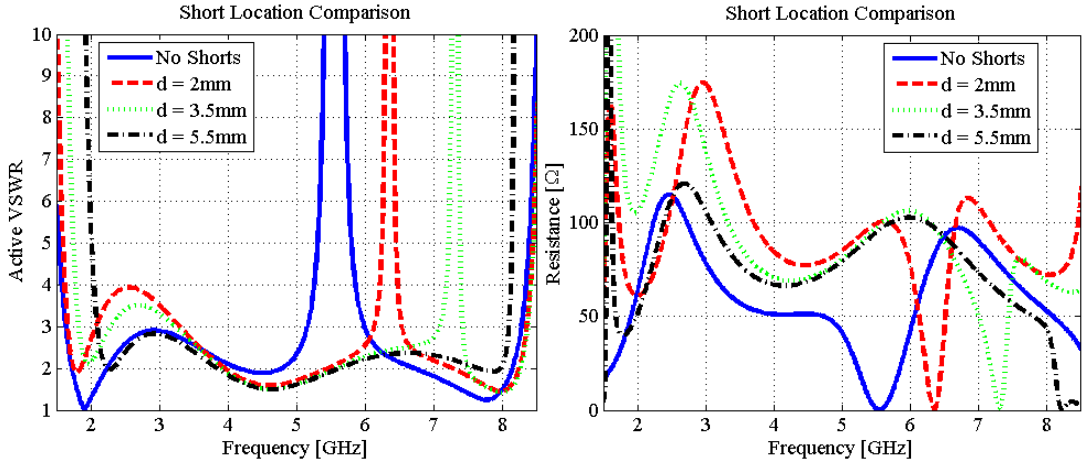

(A) (B)

Figure 4 – Shorting post position effects on the broadside operation of the single-polarized Banyan Tree Antenna. (A) Effects on VSWR and (B) effects on the input resistance. Geometric parameters: W_f = 1.6mm, W_s = 0.25mm, H_f = 8mm, R_i = 0.1mm^{-1}, R_o = -0.33mm^{-1}, W = 19.5mm, H = 21.25mm, g = 0.6mm, t = 2mm, D_x = 1.5cm, D_y = 2cm. Z_o = 50Ω, ε_r=2.2 (Rogers RT/Duroid 5880)

.
Figure 4(B) shows that this VSWR anomaly corresponds to a resonance with zero resistance, caused by the common mode (monopole mode) that forms on the fins. Previous studies by Elsallal [9] showed that the anomaly frequency was sensitive to the unit cell size, where smaller unit cell sizes showed an increase in anomaly frequency, and therefore the separation between the vertical feed stems dictates the frequency of the anomaly. This observation has led us to study in detail the fields in the array unit cell. At approximately the frequency whe the common mode appears, an approximately cosine half wave variation in the E_z component (z is normal to ground plane) between the narrow feed stems. This half wavelength variation corresponds approximately to the frequency of the common mode anomaly. To suppress this vertical field dominated mode, the shorting posts were added to the fin topology. In the Banyan Tree Antenna, the shorting posts are similar to mode-suppression vias used in circuit board design, where the vias are strategically placed to move resonances of the geometry out of the operating band of interest. In this case, the shorting posts decrease the length of the half wave variation by forcing the E_z fields to go to zero, thereby increasing the frequency at which the common mode occurs.

The placement of the shorts very close to the feed stems, shown by the d = 2mm curve, moves the anomaly frequency to above 6GHz. Moving the shorting posts further away (increasing d) from the feed stems moves the anomaly to higher frequencies. Finally, at d = 5.5mm, the anomaly is moved completely out of the operating band. The shorting posts alter the impedance at the low end of the frequency band, with the impact on the lowest usable frequency becoming more substantial with increased shorting post spacing d, which indicates that d should be tuned to the minimum separation required to move the common mode frequency out of band.

5. Single-Polarized BTA Array Performance

The predicted broadside active VSWR performance for a single-polarized infinite planar Banyan Tree Antenna array is shown in Figure 5, with and without shorting posts (the Bunny ear antenna). All results have been obtained with Ansoft HFSS infinite Floquet cell analysis, PML absorbing boundary condition, and a realistic wave port for excitation. Other commercial and in-house software has also been used to verify some of the following results. The E-plane spacing is D_y=2cm, which corresponds to a grating lobe onset frequency of f_g = 7.5GHz, and the bandwidth is defined with f_g as the upper frequency of operating band (typically the array bandwidth is designed to extend past this frequency). The H plane spacing is Dx=1.5cm. The element without shorts (Bunny ear element) has a bandwidth of 3.3:1 with VSWR less than 3, and the Banyan Tree Antenna is shown to move the anomaly frequency completely out of the operating band, thereby improving the bandwidth from 3.3:1 to 3.75:1 with a VSWR below 3. The low frequency limit of the operating band increases from 1.6GHz to approximately 2GHz, but the topology allows a wider bandwidth and operation up to the grating lobe onset frequency.

It is noted that no attempt to optimize one design over the other was done in order to have a fair comparison.

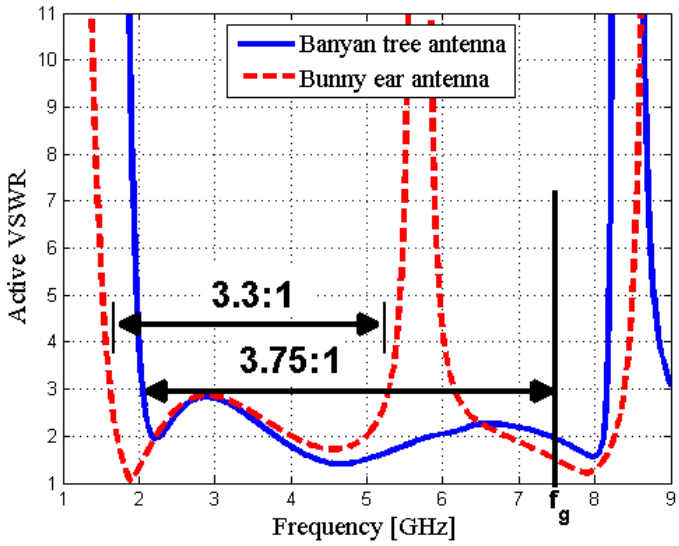

Figure 5 – Single-polarized Banyan Tree Antenna array. Broadside VSWR comparison between a Banyan Tree Antenna and a bunny-ear antenna array. Geometry parameters: W_f = 1.6mm, W_s = 0.25mm, H_f = 8mm, R_i = 0.1mm^{-1}, R_o = -0.33mm^{-1}, W = 19.5mm, H = 21.25mm, g = 0.6mm, t = 2mm, D_x = 1.5cm, D_y = 2cm d = 5.5mm. Z_o = 50Ω. ε_r=2.2 (Rogers RT/Duroid 5880).

The scan performance of this element is shown in Figure 6 for E-plane, D-plane, and H-plane scans out to θ = 45°. All three planes show good VSWR performance, with the common mode anomaly staying out of band for all scan angles. The H-plane shows a large VSWR hump occurring near 3GHz that increases to a VSWR greater than 4 for θ = 45°, but this H-plane performance is typical of elements of tapered arms, including typical Vivaldi or BAVA elements, and is not a result of the shorting posts.

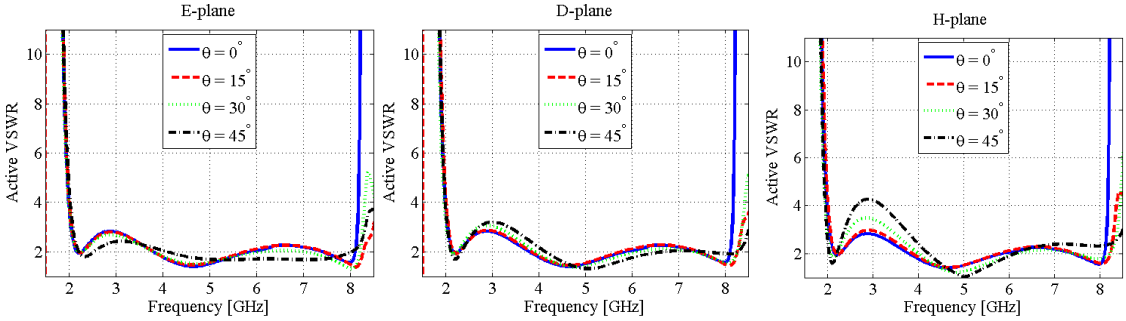

Figure 6 – Scan performance of the single-polarized Banyan Tree Antenna. (A) E-plane (B) D-plane, and (C) H-plane. Geometry parameters: W_f = 1.6mm, W_s = 0.25mm, H_f = 8mm, R_i = 0.1mm^{-1}, R_o = -0.33mm^{-1}, W = 19.5mm, H = 21.25mm, g = 0.6mm, t = 2mm, D_x = 1.5cm, D_y = 2cm d = 5.5mm. Z_o = 50Ω. ε_r=2.2 (Rogers RT/Duroid 5880).

6. Single-Polarized Balanced Antipodal BTA Array

A variation on the Banyan Tree Antenna is a balanced antipodal (stripline) topology, shown in Figure 7(A) and Figure 7(B). This structure is a three-layer structure with two outer grounded fins and one central excited fin. Shorting posts connect all three fins to the ground.

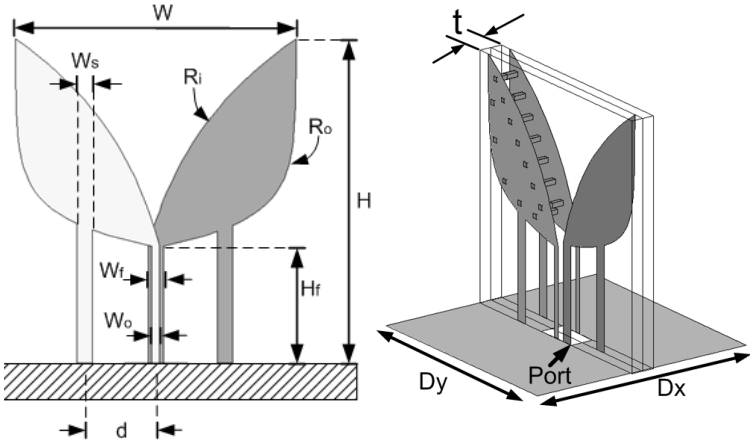

(A) (B)

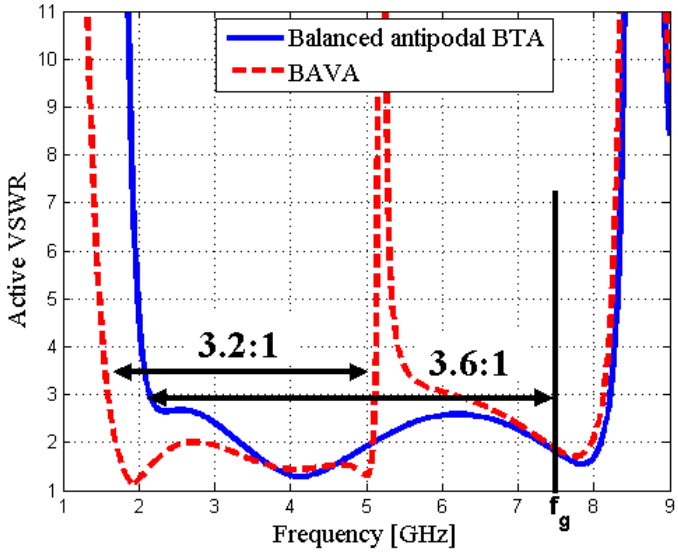

(C)

Figure 7 – Single-polarized Balanced antipodal Banyan Tree Antenna element. (A) Element side view along with the geometrical design parameters used in this study, (B) element isometric view, (C) broadside VSWR comparison of the balanced antipodal BTA and a BAVA infinite array. Geometric parameters: D_x = 15mm, D_y =20mm, W = 18mm, d = 6mm, W_f = 1mm, W_o = 1mm, W_s = 1mm, H = 20.75mm, H_f = 7.5mm, R_i = -0.55mm^{-1}, R_i = 0.125mm^{-1}, t = 2mm. Z_o = 50Ω. ε_r=2.2 (Rogers RT/Duroid 5880).

The balanced antipodal Banyan Tree Antenna performance is compared to that of a traditional un-mirrored BAVA. The predicted broadside VSWR performance for a single-polarized array of the BAVA elements with E plane spacing of 2cm and H plane spacing of 1.5cm is shown in Figure 7(C), where f_g = 7.5GHz. The BAVA is shown to have a bandwidth of 3.2:1 for VSWR less than 3, while the balanced antipodal Banyan Tree Antenna embodiment increases the bandwidth to 3.6:1 for VSWR less than 3 by moving the anomaly frequency well above the onset of the grating lobe.

7. Dual-Polarized BTA Array Performance

The Banyan Tree Antenna can also be arranged in dual-polarized planar arrays. The predicted broadside VSWR performance for a dual-polarized infinite planar array of the single layer Banyan Tree Antenna is shown in Figure 8, where the element spacing in the H and E planes is 2cm. The BTA bandwidth for VSWR <3 is 4.1:1 (two octaves).

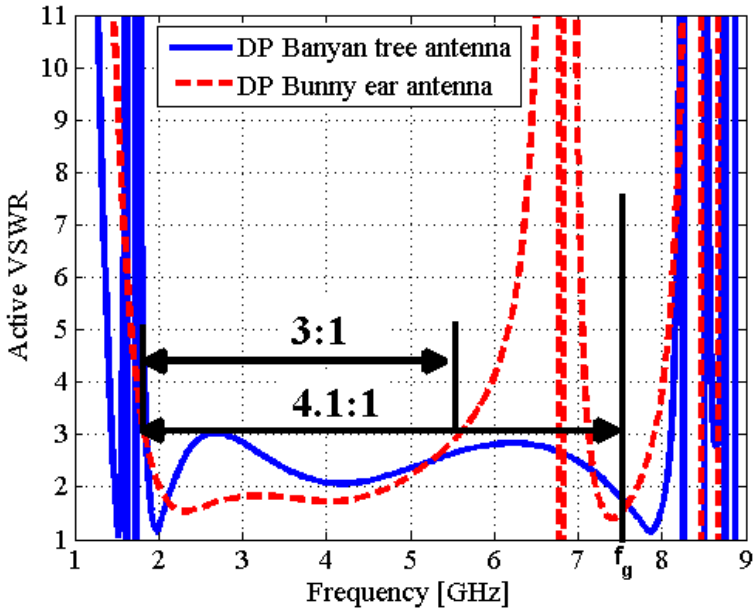

Figure 8 – Dual-polarized Banyan Tree Antenna array. Broadside active (CP polarization) VSWR comparison between the Banyan Tree Antenna and the bunny-ear antenna array. Geometry parameters: W_f = 1.6mm, W_s = 0.25mm, H_f = 8mm, R_i = 0.1mm^{-1}, R_o = -0.33mm^{-1}, W = 19.5mm, H = 21.25mm, g = 0.6mm, t = 2mm, D_x = 1.5cm, D_y = 2cm d = 5.5mm. Z_o = 50Ω. ε_r=2.2 (Rogers RT/Duroid 5880).

8. Conclusions

A new array topology is presented that can simultaneously achieve wideband performance, low-cost modular fabrication and low-profile, and direct feeding from standard RF interfaces (no external balun). At the present stage in its development, this new element has deomonstrated, via infinite array simulations, a 3.75:1 bandwidth in a

single-polarized array, and up to 4.1:1 bandwidth (two octaves) for dual-polarized designs. The use of shorting posts to control the monopole (common) mode frequency allows the elements to be fed directly without additional balun/hybrid circuitry. This initial proof-of-concept study did not attempt any extensive design optimization of the BTA parameters. Further studies are needed to better understand the behavior and to optimize matching to achieve VSWR<2 for scan out to 45-degrees. Dual-polarized designs must be further evaluated in terms of polarization purity at scanning.

10. Acknowledgements

This work was funded by the US Naval Research Laboratory under contract N00173-08-1-G033.

11. References

[1] T.H. Chio and D.H. Schaubert, "Parameter Study and Design of Wide-Band Widescan Dual-Polarized Tapered Slot Antenna Arrays," *IEEE Transactions on Antennas and Propagation,* vol.48, no.6, pp.879-886, Jun. 2000.

[2] M. Kragalott, W. R. Pickles and M.S. Kluskens, "Design of a 5:1 Bandwidth Stripline Notch Array from FDTD Analysis," *IEEE Transactions on Antennas and Propagation,* vol. 48, no. 11, pp.1733-1741, Nov. 2000.

[3] H. Holter, "Dual-Polarized Broadband Array Antenna With BOR-Elements, Mechanical Design and Measurements," *IEEE Transactions on Antennas and Propagation*, vol. 55, no. 2, Feb. 2007.

[4] M. W. Elsallal and D. H. Schaubert, "Parameter Study of Single Isolated Element and Infinite Arrays of Balanced Antipodal Vivaldi Antennas," 2004 Antenna Applications Symposium, Allerton Park, Monticello, IL., pp.45-69, 15-17 September, 2004.

[5] M. W. Elsallal and D. H. Schaubert, "Reduced-Height Array of Balanced Antipodal Vivaldi Antennas (BAVA) with Greater than Octave Bandwidth," Antenna Applications Symposium, Allerton Park, Monticello, Ill., pp. 226-242, 21-23 Sep., 2005.

[6] W. J. Otter, B.P. Pirollo, R.I. Henderson and R.A. Lewis, "Multi-Octave BAVA Radiating Elements for use in Modular Phased Array Antennas," *3rd European Conference on Antennas and Propagation (EuCAP) 2009,* pp. 1324-1328, 23-27 March, 2009.

[7] E. Gazit, "Improved design of the Vivaldi antenna," *IEE Proceedings H Microwaves, Antennas and Propagation,* vol. 135, pt.H, pp. 89–92, Apr. 1988.

[8] J. D. S. Langley, P. S. Hall and P. Newham, "Balanced Antipodal Vivaldi Antenna for Wide Bandwidth Phased Arrays," *IEE Proceedings -Microwaves, Antennas and Propagation,* vol. 143, no. 2, pp. 97-102, April 1996.

[9] M.W. Elsallal, "Doubly-Mirrored Balanced Antipodal Vivaldi Antenna (DmBAVA) for High Performance Arrays of Electrically Short, Modular Elements," PhD dissertation, Electrical and Computer Engineering, Univ. of Massachusetts, February 2008.

[10] J. J. Lee, S. Livingston, R. Koenig, "Performance of a Wideband (3-14GHz) Dual-Pol Array," *IEEE Antennas and Propagation Society International Symposium*, vol. 1, pp. 551-554, 20-35 June 2004.

[11] B. Munk, R. Taylor, T. Durharn, W. Croswell, B. Pigon, R. Boozer, S. Brown, M. Jones, J. Pryor, S. Ortiz, J. Rawnick, K. Krebs, M. Vanstrum, G. Gothard, D. Wiebelt, "A Low-Profile Broadband Phased Array Antenna," *IEEE Antennas and Propagation Society International Symposium,* vol.2, pp. 448 451, 22-27 June 2003.

[12] J. G. Maloney, M. P. Kesler, P. H. Harms and G. S. Smith, "Fragmented Aperture Antennas and Broadband Antenna Ground Planes," U. S. Patent 6,323,809, May 26th, 2000.

[13] B. Gondara and A. Fabre, "A Highly Compact Active Wideband Balun With Impedance Transformation in SiGe BiCMOS," *IEEE Transactions on Microwave Theory and Techniques*, vol. 56, no.1, pp. 22-30, Jan. 2000.

A NOVEL NON-SYMMETRIC TIGHTLY COUPLED ELEMENT FOR WIDEBAND PHASED ARRAY APERTURES

Justin A. Kasemodel, Chi-Chih Chen, John L. Volakis
ElectroScience Laboratory
Department of Electrical and Computer Engineering
The Ohio State University, Columbus, OH 43220
kasemodel.1@osu.edu

Abstract: A novel non-symmetric element is proposed for wideband phased array apertures. The antenna is based on a infinite periodic array of tightly coupled dipoles which are modified to provide an increase in the design degree of freedoms. Specifically, each arm on the dipole is different than the other, or non-symmetric, enabling one to control inductance and capacitance independently. In this case, the arms are similar near the center feed portion, but change shape towards the end of the dipole, forming a ball-and-cup. The non-symmetric qualities can be manipulated for improved UWB performance or operation over a specific bandwidth. A design example for the latter is developed at X-band, specifically 7.75-13.25GHz. Equally important is the balun and matching network, as such, we propose a small feed printed behind the ground plane using twin wire interconnects between the array aperture and balun circuity. The non-symmetric arms can be used to create radically different designs than symmetric ones currently found in literature.

1 Introduction

With space at a premium, there is strong interest to develop a single ultra wideband (UWB) phased array aperture capable of supporting multiple communication, electronic warfare and radar functions simultaneously. Furthermore, recent focus on conformal designs is challenging the established wideband antennas and arrays dating back to the 60s and 70s. It is not therefore surprising that recently introduced designs based on electromagnetic bandgap ground planes (EBGs) have attracted considerable attention. However, EBGs and other periodic ground planes are narrowband and therefore not suited for wideband applications. It is therefore desirable to design an aperture which is concurrently broadband and low-profile for conformal installations.

The infinite current sheet concept proposed by Wheeler [1], was not realized until recently when Munk [2, 3] emulated it using a tightly coupled dipole array (TCDA). In his design, the strong coupling among adjacent dipoles reduces stored energy and allows propagation to neighboring elements to realize an infinite current sheet. An important aspect of TCDAs is the capacitive coupling mechanism, which serves to enable the following benefits; allows current to pass between elements maintaining its sinusoidal representation across the array with a strong DC component, maintains resonance for electrically short

dipoles and cancels the inductive ground plane loading, yielding an ultra wideband low-profile phased array aperture. The latter is critical for retaining the aperture's wideband behavior under conformal installations.

Traditional phased array design involves designing an antenna in isolation and optimizing it for the desired performance such as impedance bandwidth, polarization and radiation pattern. It is well understood that mutual coupling in an array can cause undesirable changes in performance such as element impedance variations, polarization degradation and undesirable radiation patterns. In fact, mutual coupling is responsible for one of the more difficult aspects of phased array design, scan impedance. A fundamentally different approach to array design has been developed by Munk [2], were a planar antenna is designed in the array environment and uses mutual coupling to lower the operational frequency leading to ultra wideband designs. This approach is similar to frequency selective surface (FSS) design which are also highly coupled periodic structures [4]. Another important aspect when designing wideband phased arrays is the element type. Using the tradition approach, an UWB array would be required to employ UWB elements such as TEM-horn [5], bunney-ear [6], tapered slot or Vivaldi [7] and the body-of-revolution (BOR) element [8]. All elements are three-dimensional and require a large dimension normal to the aperture surface, typically with a depth of $0.5\lambda_L$, where λ_L is the wavelength at the low end of the operational band. Due to the 3-D nature of said elements, they are are often costly and difficult to fabricate. Furthermore, depending on the element width, arraying the elements close together to avoid grating lobes (commonly $<0.5\lambda_H$ where λ_H is the wavelength at the high end of the band) poses significant challenges.

The planar two-dimensional apertures presented herein provide several advantages; (a) inherently low-profile, (b) allows conformal flush mounting on platforms where the ground plane is used for impedance tuning and increased bandwidth, (c) simple element geometry allows for quick electromagnetic simulations, (d) enables significant opportunity for cost reduction by use of traditional planar PCB fabrication technology and simplified layered assembly procedures.

This paper first develops a understanding of how tightly coupled dipole arrays operate and why capacitive mutual coupling is beneficial using equivalent circuits. The next section introduces a novel non-symmetric element, details important parameters and studies their effect on performance and miniaturization. A feed providing impedance matching and balanced to unbalanced conversion (while maintaining the arrays low-profile) is designed and integrated with the array aperture. Finally, the design is optimized and its scan impedance investigated.

2 Understanding the TCDA

A current sheet can be emulated by a tightly coupled dipole array, where strong coupling reduces the stored energy and allows the current to propagate to adjacent elements.

An important aspect of said arrays is the coupling mechanism, in this case capacitive. For the TCDAs discussed here, each element is capacitively coupled to the neighboring elements. The motivating factor for capacitive versus inductive coupling is shown below in Fig. 1.

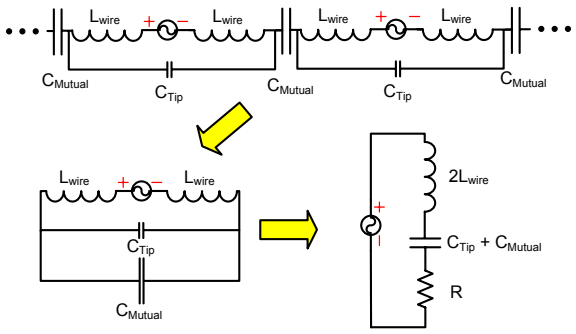

Figure 1: Tightly coupled dipole array equivalent circuit for array in free space.

The mutual capacitance (C_{Mutual}) is parallel to the dipole self tip-to-tip (C_{Tip}) capacitance. As the equivalent capacitance forms a serial RLC network, it can be used to maintain resonance for low frequencies where the dipole wire self inductance (L_{wire}) is small. In addition, the capacitive coupling allows current to pass between elements and can be used to partially cancel the inductive ground plane reactance.

To illustrate the array-ground plane impedance canceling capabilities, a simple "ideal" numerical example is presented using a ground plane backed array equivalent circuit. To explain the equivalent circuit formulation an array in free space was first examined, see Fig. 2. An ideal array is assumed to operate in free space, meeting all the criteria in which the equivalent circuit is valid; elements are electrically small, no grading lobes, scanned only in principal planes [2]. The infinite planar 2D periodic array is positioned between two free space half planes. Each half plane can be represented as a infinite transmission line with characteristic impedance $2R_{Ao}$. The input impedance of the array in free space (denoted by the subscript $_o$), is defined as $Z_a = R_{Ao} + jX_{Ao}$. It is calculated by the parallel combination of each half space transmission line in series with the array reactance X_{Ao} as shown in Fig. 2.

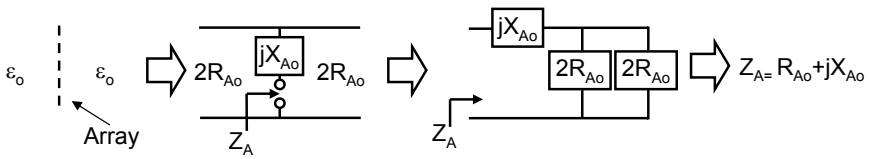

Figure 2: Equivalent circuit for infinite array in free space.

The equivalent circuit in Fig. 2 was extended to include a ground plane. Specifically, the array is positioned a distance (d) above the ground plane as shown in Fig. 3 and the free space array resistance (R_{Ao}) is assumed to be a constant 200Ω from 1-16GHz. The free space array reactance (X_{Ao}) is assumed to vary linearly from -400j to +400j over the respective frequency range. The array impedance is an idealized case used for illustrative purposes; however, for tightly coupled dipole arrays the assumption of constant resistance and a capacitive to inductive impedance variation is reasonable. The array is positioned λ/4 above the ground plane at the center frequency (d=8.8mm at 8.5GHz). The ground plane impedance is calculated using the traditional short circuit transmission line equation, then moved a distance, d, through a transmission line with characteristic impedance, $2R_{Ao}$, to the array plane (Z_{gp}) becoming parallel to twice the array resistance ($2R_{Ao}$). The array reactance (X_{Ao}) is then added in series to obtain the final ground plane compensated impedance. The ground plane inductive reactance partially cancel the dipole capacitive reactance for frequencies below the center frequency. While for higher frequencies, the capacitive ground plane partially cancel the array inductive reactance. The resultant impedance is effectively compressed and forms three resonances compared to the single free space resonance. The return loss bandwidth improvement is also illustrated in Fig. 4(b). The array with ground plane has a 4:1 bandwidth compared to the free space array band width of 1.8:1.

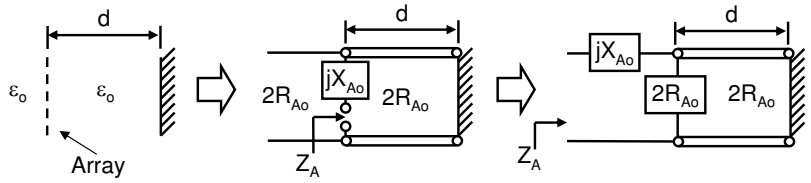

Figure 3: Equivalent circuit for ground plane backed infinite array.

To verify the equivalent circuit and ground plane impedance compensation effectiveness, a physically realizable TCDA was examined [9] . To construct the equivalent circuit, the free space array input impedance was first found using a full wave 3D finite element solver, HFSS v10, for the unit cell dipole geometry (see Fig. 5). The unit cell was used with periodic boundary conditions to model an infinite array. The element to element spacing was 11.5mm ($\lambda/2$ at 13GHz), and the dipole length was 11.25mm, yielding a 0.125mm gap between adjacent dipoles. The array was then positioned over a ground plane and simulated while the separation distance was varied from 4 to 10mm (in 2mm steps). The simulated conformal array impedance was then compared to the equivalent circuit calculated impedance. As seen in Fig. 5(b), the equivalent circuit impedance curves are in good agreement with full wave simulations (for all ground plane heights). The calculated resistance is typically lower than that of full wave simulation and agrees better for lower frequencies where the element is electrically small. This comparison provides the reader

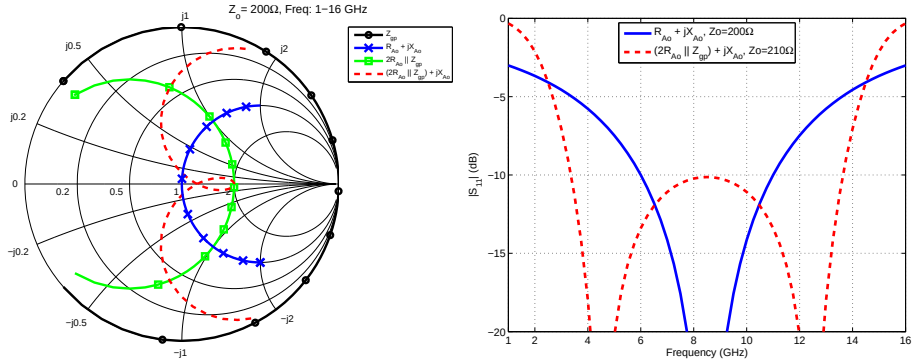

(a) (b)

Figure 4: (a) Array impedance transformation for equivalent circuit. (b) Return loss comparison for the ideal array in free space and with ground plane.

with an intuitive feel for ground plane spacing effects and verifies the equivalent circuit which was introduced to demonstrate impedance cancelation ability of capacitive coupled dipole arrays above a ground plane.

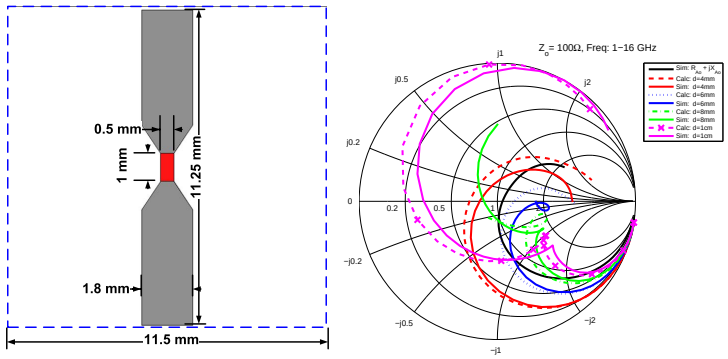

(a) (b)

Figure 5: (a) Periodic unit cell dipole geometry. (b) Full wave array simulation vs. equivalent circuit for different ground plane heights.

3 Non-Symmetric Element

To further improve TCDA performance, a increase in the design degree of freedoms is proposed by introducing asymmetry. Specifically, each dipole arm is different than the other or non-symmetric. This allows one to control the inductance and capacitance independently. A non-symmetric TCDA element was parameterized with the following five variables; t1 (cup width), t2 (ball width), t3 (arm width), g (element separation gap) and α (cup opening angle), see Fig. 6(a). The element was positioned 8mm above a ground plane. The corresponding baseline input impedance is displayed in Fig. 6(b). The scan

element pattern (SEP) for E and H-planes are shown in Fig. 7. The SEP includes the element pattern and all mutual coupling effects. The overall array pattern is the product of the scan element pattern and the corresponding array factor where the array factor incorporates the effects of array lattice and size. For the infinite arrays considered herein, the array quantities of importance are the scan impedance and SEP. The E-plane SEP is similar to the H-plane pattern for $-45^\circ \leq \theta \leq 45^\circ$ and fairly constant over a broad range. For low elevation angles there are sharp nulls in the E-plane, however, the gain does not go to zero at horizon as is the case for H-plane. The pattern null is caused by the ground plane image dipole current canceling radiation at $\theta = \pm 90^\circ$.

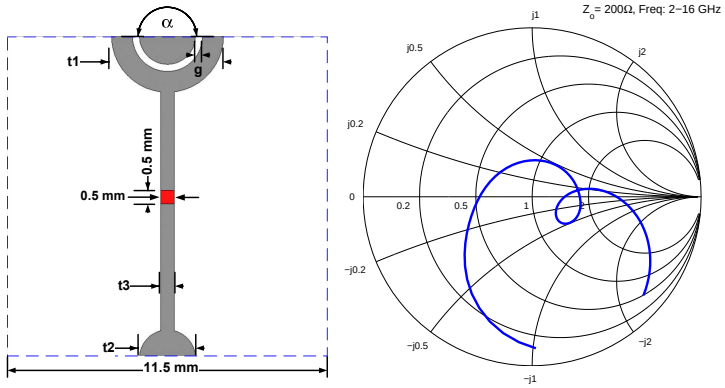

(a) (b)

Figure 6: (a) Baseline non-symmetric TCDA unit cell for parameter study. (b) Input impedance with t1=2mm, t2=1mm, t3=0.5mm, g=10mil, $\alpha = 180^\circ$ scanned to $\theta_o = 0^\circ$.

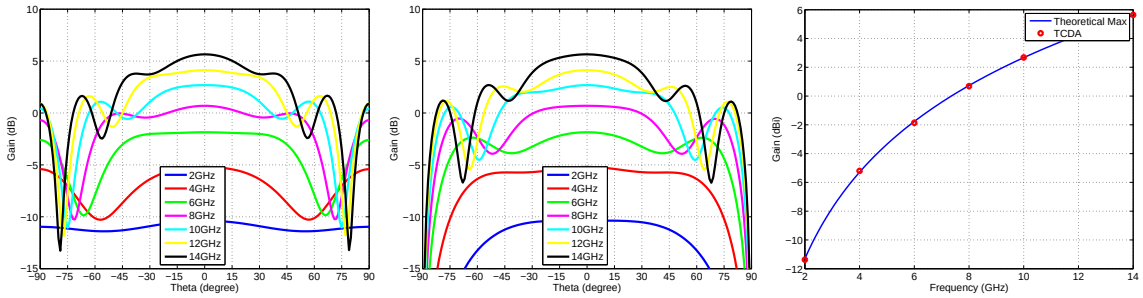

(a) (b) (c)

Figure 7: (a) Baseline TCDA E-plane scan element pattern. (b) Baseline TCDA H-plane scan element pattern. (c) Simulated TCDA and calculated unit cell directivity.

Comparing the boresight SEP to the maximum directivity possible for the given unit cell size (Eq. 1), good agreement is observed, implying 100% unit cell aperture efficiency, see Fig. 7(c). For all parameter sweeps studied, the SEP remains constant (within 2dB of Fig. 7) and thus are omitted. It is therefore necessary only to study the input or scan impedance of each non-symmetric TCDA design.

$$D = \frac{4\pi A}{\lambda^2} \tag{1}$$

The first parameter studied was t1 or cup width. As t1 is increased, the resistance is significantly reduced, while the low frequency reactance is reduced. Furthermore, the high frequency reactance increases, effectively shifting the input impedance on the smith chart and increasing the loop diameter, Fig. 8. This is due to an increased tip-to-tip capacitance formed by the large cup size. Frequencies below 5GHz are minimally effected.

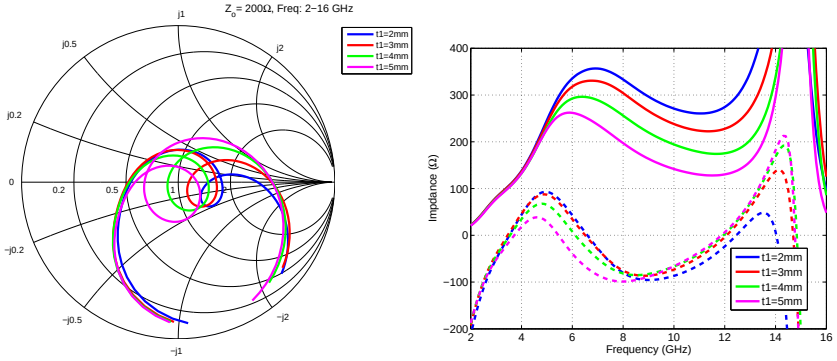

(a) (b)

Figure 8: (a) TCDA impedance and (b) corresponding resistance (solid) and reactance (dash) with t1 varied, t2=1mm, t3=0.5mm, g=10mil, $\alpha = 180^\circ$, scanned to $\theta_o = 0^\circ$.

To facilitate sweeping t2, while not shorting the element to it's neighbor, t1 had to also increase accordingly. In an effort to separate the effects, t1 was increased to maintain the same cup trace width, namely, 0.25mm for all values of t2. As t2 increases, the resistance increases over the entire frequency range see Fig. 9. In a similar fashion, the reactance is reduced for low frequencies becoming less capacitive. For a small ball width (t2=0.25mm) the first resonance occurs at 12GHz, but for larger sizes the first resonance occurs much lower, for example 2.2GHz when t2=3mm. When t2 is increased, the element is effectively miniaturized, a result of increased mutual coupling. For larger t2 values, the ball and cup capacitive junction area increases, resulting in a larger mutual and tip-to-tip capacitance. As a result significant miniaturization is achieved.

The next parameter studied was the arm width or t3. To accommodate large t3 values, t1 and t2 had to be increased to 3mm and 2mm respectively, otherwise the element would be electrically connected to is neighbor. As t3 increases, the loop size on the smith chart also increases and shifts to the left, implying a reduction of resistance and a larger reactance variation over the band, see Fig. 10. Below 5GHz the resistance is constant while for higher frequencies the resistance is halved when increasing t3 to 3mm from 0.5mm. The decrease in resistance is attributed to a reduction of the wire inductance shown by a

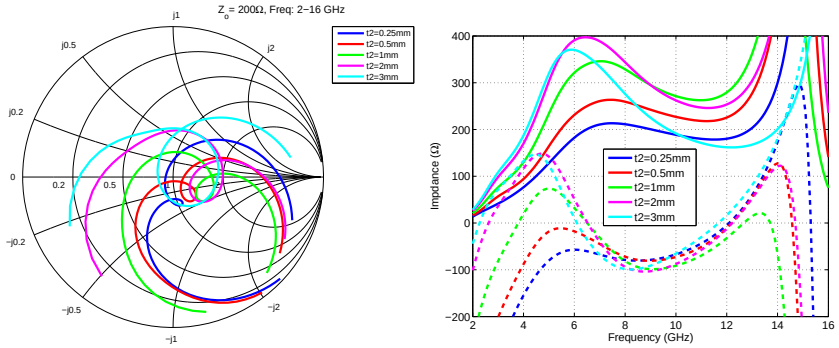

(a) (b)

Figure 9: (a) TCDA impedance and (b) corresponding resistance (solid) and reactance (dash) with t1=t2+g+0.25mm, t2 varied, t3=0.5mm, g=10mil, $\alpha = 180^\circ$, scanned to $\theta_o = 0^\circ$.

increased capacitive reactance over the entire frequency range.

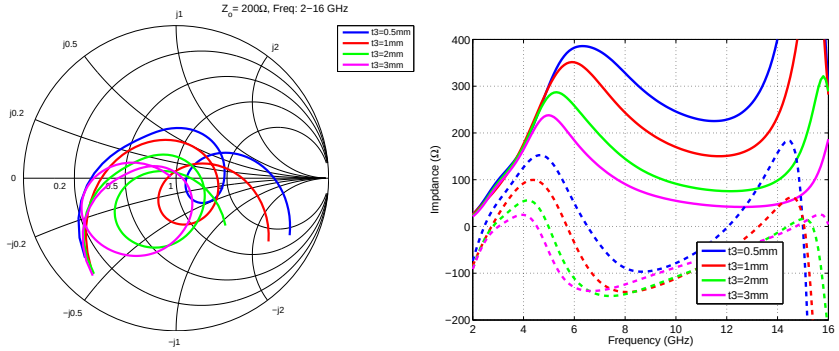

(a) (b)

Figure 10: (a) TCDA impedance and (b) corresponding resistance (solid) and reactance (dash) with t1=2mm, t2=1mm, t3 varied, g=10mil, $\alpha = 180^\circ$, scanned to $\theta_o = 0^\circ$.

The next parameter of interest is the gap separating the ball and cup, g. When the separation gap is small, a significant increase in mutual coupling effectively miniaturizes the antenna. This is observed by a resistance increase for all frequencies, while simultaneously decreasing the low frequency capacitive reactance and high frequency inductance, see Fig. 11. The gap separation should be small as possible (within manufacturing tolerances) to ensure strong mutual coupling, enabling the array to operate to lower frequencies.

The final parameter investigated is the cup opening angle α. The values studied were $45 - 275^\circ$ in 60° steps. The corresponding geometries are displayed in Fig. 12(a). As α is reduced, the amount of mutual coupling increases due to a larger capacitive area. For all cases the anti-resonance point (6.5GHz) remains the same, while the first resonance point is miniaturized up to 100% when α decreases from 275° to 45°, Fig. 12(c).

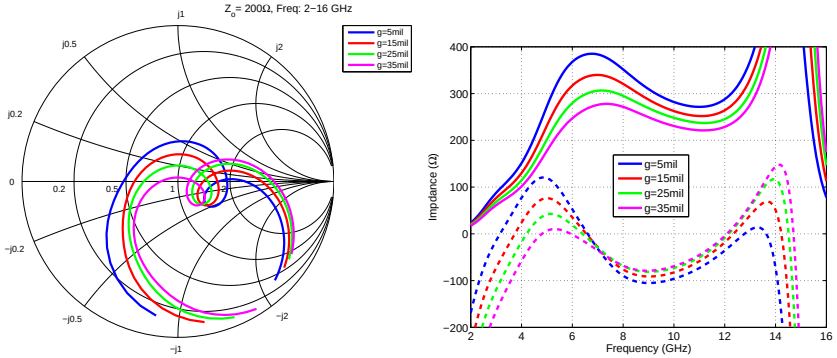

(a) (b)

Figure 11: (a) TCDA impedance and (b) corresponding resistance (solid) and reactance (dash) with t1=2mm, t2=1mm, t3=0.5mm, g varied, $\alpha = 180^\circ$, scanned to $\theta_o = 0^\circ$.

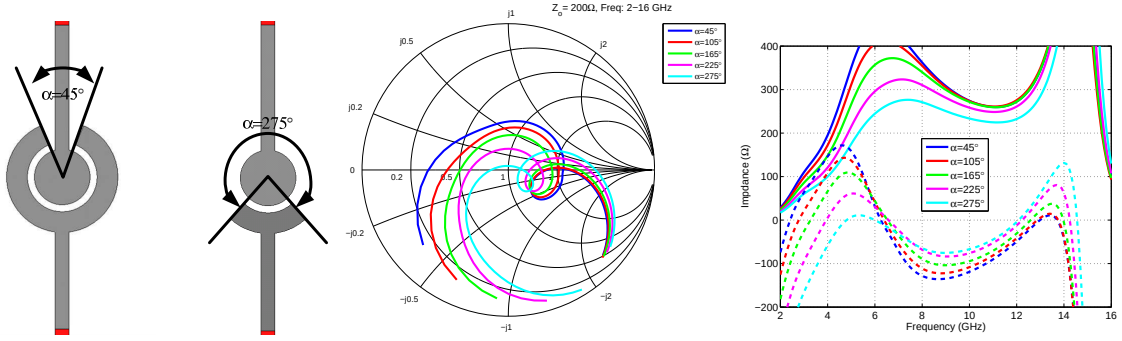

(a) (b) (c)

Figure 12: (a) TCDA with $\alpha = 45^\circ$ and 275°, t1=2mm, t2=1mm, t3=0.5mm, g=10mil. (b) TCDA impedance and (c) corresponding resistance (solid) and reactance (dash), scanned to $\theta_o = 0^\circ$.

4 Balun circuity and matching network

A wideband ring hybrid based on coupled microstrip lines [10], was designed to operate from 8-12.5GHz. The hybrid was optimized to provide a input (S_{11}) return loss <-10dB from 7.5-13GHz or <-15dB from 9-12.8GHz, with a balanced output transmission (S_{21}) >-0.75dB from 8-12.5GHz. For balun functionality, the ring hybrid is operated in difference mode. Difference mode is excited using a 50Ω microstrip input (Port 1) with each output port extending inside the ring, 180° out of phase. As a result, the fields add in series resulting in a 100Ω balanced line which is connected to a twin wire transmission line. A small hole is necessary to allow the twin wire section to pass through the ground plane. See Fig. 13 for the final design layout and performance.

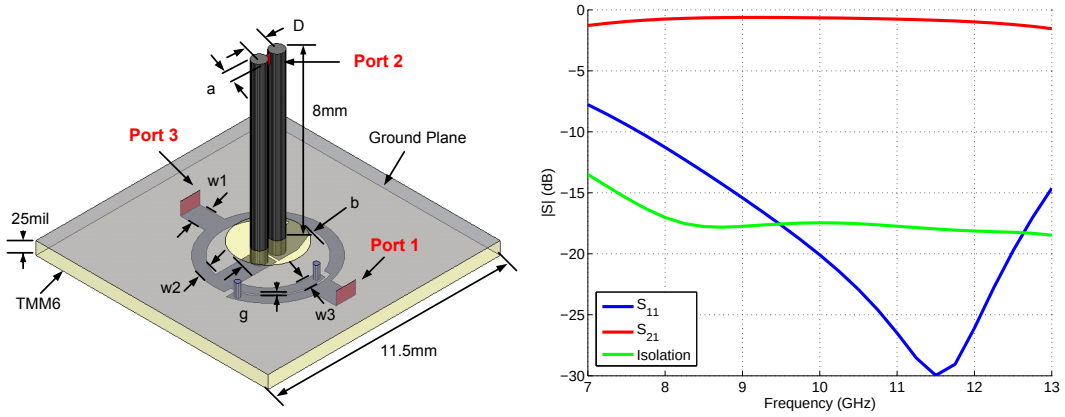

(a) (b)

Figure 13: (a) Wideband ring hybrid printed behind ground plane with balanced twin tire output. (b) S-parameters with a=0.64516mm, D=0.88mm, w1=38mil, w2=20mil, w3=17mil, g=3mil, b=3mm, d=8mm.

Due to the large array input resistance ($Z_a \approx$ 200-300Ω for typical non-symmetric TCDAs), the element cannot be directly optimized for a 100Ω input impedance (Z_{in}) required for the proposed feed. As a result, a matching circuit must be used. Specifically, the antenna is connected to a small transmission line of length, l_m, with characteristic impedance Z_m. The matching impedance is bound by the following relationship, $Z_{in} < Z_m < Z_a$. Concurrently, to maintain the arrays inherent low-profile, the matching circuit length should equal the array ground plane separation distance, d. This is critical, as the feed circuit is printed behind the ground plane. That is, interconnects between the TCDA surface and the balun circuitry are necessary.

5 TCDA with Feed Network

A non-symmetric TCDA was feed using the optimized wideband ring hybrid from Fig. 13(a). The twin wire diameter and spacing was increased to 0.8128mm (20 gauge) and

1.6mm, respectfully, yielding a 155Ω characteristic impedance for matching. To facilitate a wider grating lobe free scanning range the unit cell was reduced to 8.5mm. Applying the non-symmetric TCDA geometry-impedance relationships discussed in Section 3, a TCDA element was designed with a boresight return loss <-10dB from 7.75-13.25GHz, Fig. 14(b).

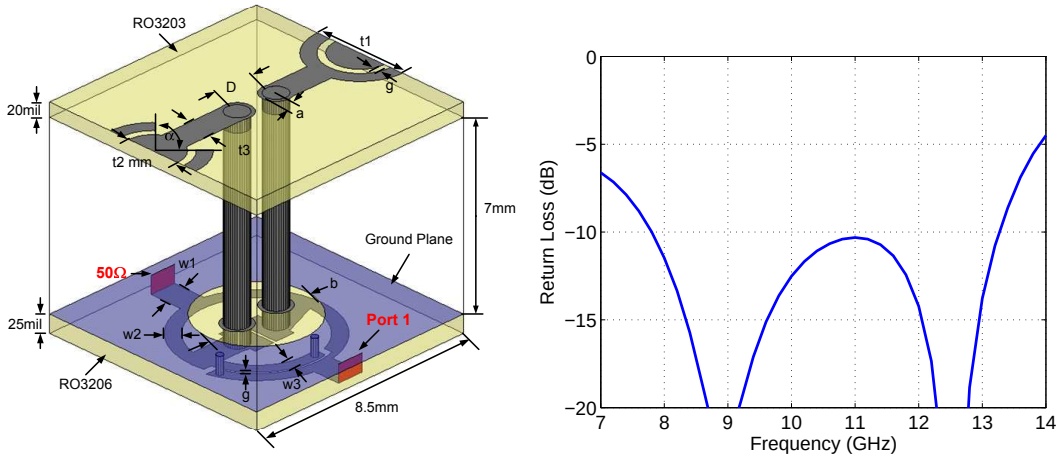

(a) (b)

Figure 14: (a) Non-symmetric TCDA geometry and (b) return loss at antenna terminals and ideal matching network, t1=1.75mm, t2=1mm, t3=1mm, g=10mil, $\alpha = 85°$, a=0.8128mm, D=1.6mm, w1=38mil, w2=20mil, w3=17mil, g=10mil, b=4mm scanned to $\theta_o = 0°$.

After the element design was finalized (with a return loss criteria of <-10dB from 8-12.5GHz) the radiation characteristics were investigated. This is necessary as the wideband ring hybrid uses a 50Ω isolation resistor, where a acceptable return loss does not guarantee effective radiation. The boresight directivity and realized gain is shown in Fig. 15(a), where good agreement is observed. The realized gain approaches the directivity at 9GHz and 12.75GHz which corresponds to minimum return loss. Furthermore, the realized gain is within 0.7dB of directivity over the desired 8-12.5GHz band. The radiation efficiency was also calculated to be maximum at 9GHz (98%) and minimum at either band edge (92%). The TCDA array was then scanned off boresight, specifically to 30° and 45° in both E and H planes, see Fig. 15(b).

For E and H-plane scanning up to 30°, the VSWR is less than 2 over the desired 8-12.5GHz band. For wider scanning the E-plane mid-band VSWR increases above 2, while H-plane scan impedance deteriorates quickly below 9GHz. The first E-plane resonance point at 8.75GHz remains stable while scanning, whereas the H-plane second resonance at 12.75GHz remains constant.

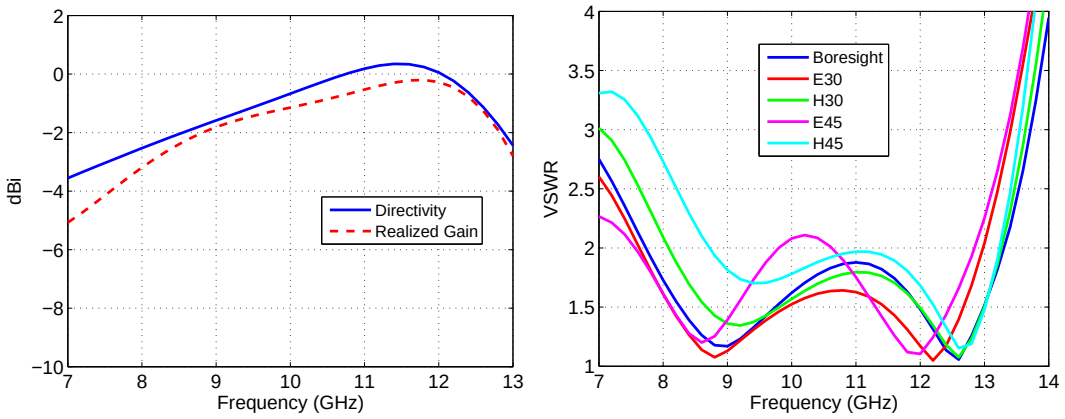

(a) (b)

Figure 15: (a) Unit cell boresight directivity and realized gain. (b) Scanning VSWR.

6 Conclusion

A non-symmetric tightly coupled dipole array with balun and matching network was presented for a ground plane backed phased array aperture. Several important geometry parameters were studied by examining their effect on the array input impedance. A non-symmetric element forming an interlocking ball-and-cup joint was designed with a boresight return loss <-10dB from 7.75-13.25GHz. A wideband ring hybrid was employed for unbalanced to balanced conversion and is printed directly under the element behind the ground plane, maintaining the arrays low-profile height (0.18λ at 7.75GHz). A 155Ω twin wire transmission line connects the aperture and feed while concurrently providing impedance matching. The array is capable of scanning up to 45° in the E-plane and 30° in the H-plane with a VSWR <2.25 from 7.75-13.25GHz. Further work includes improving the E and H-plane wide angle scanning capability to 60° using a dielectric superstrate. Subsequently, a test coupon will be fabricated and tested in the near future.

References

[1] H. Wheeler, "Simple relations derived fom a phased-array antenna made of an infinite current sheet," vol. 13, no. 4, pp. 506–514, 1965.

[2] B. A. Munk, *Finite Antenna Arrays and FSS*. John Wiley and Sons, 2003.

[3] B. Munk, R. Taylor, T. Durharn, W. Croswell, B. Pigon, R. Boozer, S. Brown, M. Jones, J. Pryor, S. Ortiz, J. Rawnick, K. Krebs, M. Vanstrum, G. Gothard, and D. Wiebelt, "A low-profile broadband phased array antenna," in *Proc. IEEE Antennas and Propagation Society International Symposium*, vol. 2, 22–27 June 2003, pp. 448–451.

[4] B. A. Munk, *Frequency Selective Surfaces: Theory and Design*. John Wiley and Sons, 2000.

[5] E. L. Holzman, "A wide band tem horn array radiator with a novel microstrip feed," in *Proc. IEEE International Conference on Phased Array Systems and Technology*, 21–25 May 2000, pp. 441–444.

[6] J. J. Lee, S. Livingston, and R. Koenig, "A low-profile wide-band (5:1) dual-pol array," vol. 2, pp. 46–49, 2003.

[7] J. Shin and D. H. Schaubert, "A parameter study of stripline-fed vivaldi notch-antenna arrays," vol. 47, no. 5, pp. 879–886, 1999.

[8] H. Holter, "Dual-polarized broadband array antenna with bor-elements, mechanical design and measurements," vol. 55, no. 2, pp. 305–312, Feb. 2007.

[9] J. A. Kasemodel, C.-C. Chen, and J. L. Volakis, "A miniaturization technique for wideband tightly coupled phased arrays," in *Proc. IEEE Antennas and Propagation Society International Symposium APSURSI '09*, 1–5 June 2009, pp. 1–4.

[10] S. March, "A wideband stripline hybrid ring (correspondence)," vol. 16, no. 6, pp. 361–361, Jun 1968.

DEVELOPMENT OF A RECONFIGURABLE UWB THREE-DIMENSIONAL SEE-THROUGH-WALL RADAR IMAGING SYSTEM

Yazhou Wang, Aly E. Fathy
Min Kao Department of Electrical Engineering and Computer Science
University of Tennessee, Knoxville, TN 37996

Abstract: A reconfigurable ultra-wideband radar for imaging application has been developed. The radar operating frequency can be electronically selected using FPGA circuitry to cover either (2-4 GHz) or (8-10 GHz) UWB bands. The lower UWB band is used for relatively high loss wall material, but the upper band can be utilized to achieve high image resolutions. The developed synthetic aperture radar utilizes an array of wideband tapered slot Vivaldi antennas and covers a wide frequency range, extending over 2-10 GHz; thus covering both regions. The developed beam-forming algorithm includes both near and far field models, and accounts for wall effects. Both the wave refraction and propagation speed changes are accounted for to obtain accurate images of the targets. Real-time experiments have been performed on both static and moving targets to validate the performance of the radar system. The three-dimensional beamforming algorithm and experimental results are presented here. The obtained 3D images precisely localize the targets and accurately recognize the shape of the targets. This capability is essential for see-through-wall human being detections.

1. Introduction

In this paper, we developed a three-dimensional reconfigurable radar system [1] with a switchable operating frequency range extending over the 2-10 GHz to provide operational flexibility. After a brief introduction in section one, we present in section two our efforts to design Vivaldi antenna arrays covering the whole UWB band. In section three, the reconfigurable radar system architecture, as well as the data acquisition and digital control modules, is discussed. In section four, the synthetic aperture beamforming methods are presented, including a simplified model and a near-field algorithm, both accounting for wall effects. In section five, real-time images of both stationary objects and moving targets are demonstrated. Finally, a three-dimensional imaging algorithm is presented, along with the 3D experimental results of the object and the human model targets.

2. 2-10 GHz Compact Tapered Slot Vivaldi Antenna and Array

An ultra-wideband Vivaldi antenna is designed to cover the 2-10 GHz frequency range. The configuration of the proposed antenna is depicted in Fig. 1. A wideband transition, from the slot line to a 100Ω microstrip line, was successfully designed. This has greatly

simplified the design and offered up to one decade bandwidth [2]. Next, a smooth 100Ω to 50Ω transition is utilized to achieve the 50Ω impedance at the feed port. The width of the single tapered slot, *W*, is 30 mm, which is one wavelength at the highest operating frequency (10 GHz) to avoid any grating lobes in the E-plane of the Vivaldi array.

The measured return loss of the wideband Vivaldi antenna matches the simulated one very well, as shown in Fig. 2. Both results indicate a good match over the 2-10 GHz frequency range. Fig. 3 demonstrates satisfactory measured radiation patterns of the Vivaldi antenna over the operating frequency range.

The developed Vivaldi antennas are fed in-phase and form an 8-element E-plane array, as presented in Fig. 4, by using the four-section wideband Wilkinson divider [3]. Some slots are added to separate the antenna elements for better decoupling, which is helpful for matching improvement.

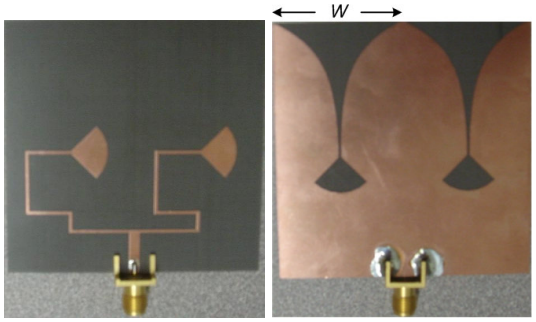

Fig. 1. Configurations of the 2-10 GHz Vivaldi antenna

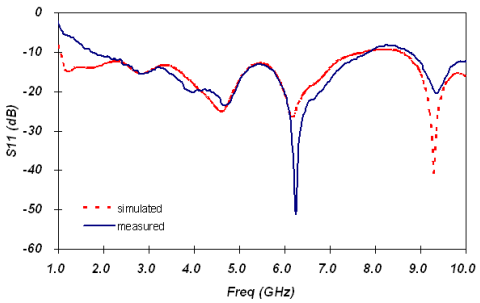

Fig. 2. Simulated and measured return loss

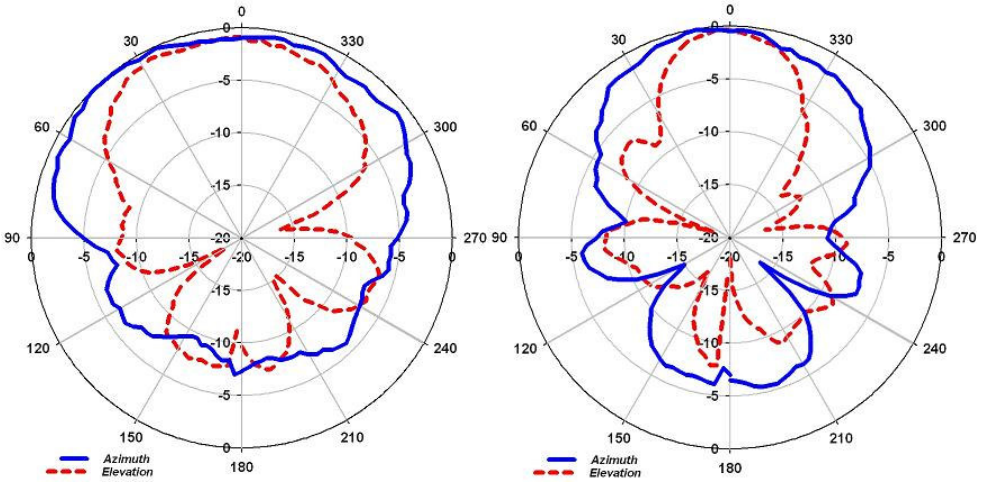

(a) 4 GHz (b) 8 GHz

Fig. 3. Measured radiation pattern versus frequency

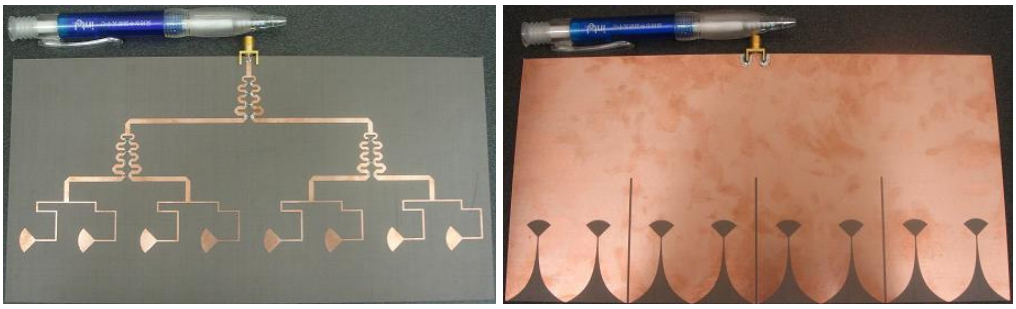

Fig. 4. 2-10 GHz Vivaldi E-plane Array

3. Reconfigurable Radar Imaging System Transceiver

A detailed block diagram of the proposed reconfigurable imaging radar system is outlined in Fig. 5. The aggregate system can be reconfigured to operate at the two frequency bands by using five SPDT switches. A 10 MHz clock (PRF) generated by the FPGA is used to drive a Gaussian pulse generator. The pulse is then modulated by a carrier signal of either 3 GHz (LO1) or 9 GHz (LO2). The modulated signal chosen by the SPDT Switch2 passes through two stages of amplification and is then transmitted via a wideband Vivaldi subarray. At the Rx link, the signal received by the wideband Vivaldi array passes through the SP16T switch and is then amplified by a wideband low noise amplifier (LNA). Next, the signal is selected and band-pass filtered prior to being down-converted into I and Q channels by mixing the same carrier signal with the received signal. Then, the recovered I and Q data are opted, filtered, and amplified before being sent to the analog-to-digital converter for sampling using the equivalent time sampling scheme [4]. Next, all the sampling data are sent to a FPGA circuitry for storage and post-data process. Last, the image is recovered via a microwave beam-forming algorithm implemented by either the FPGA imaging module or a Matlab program [5].

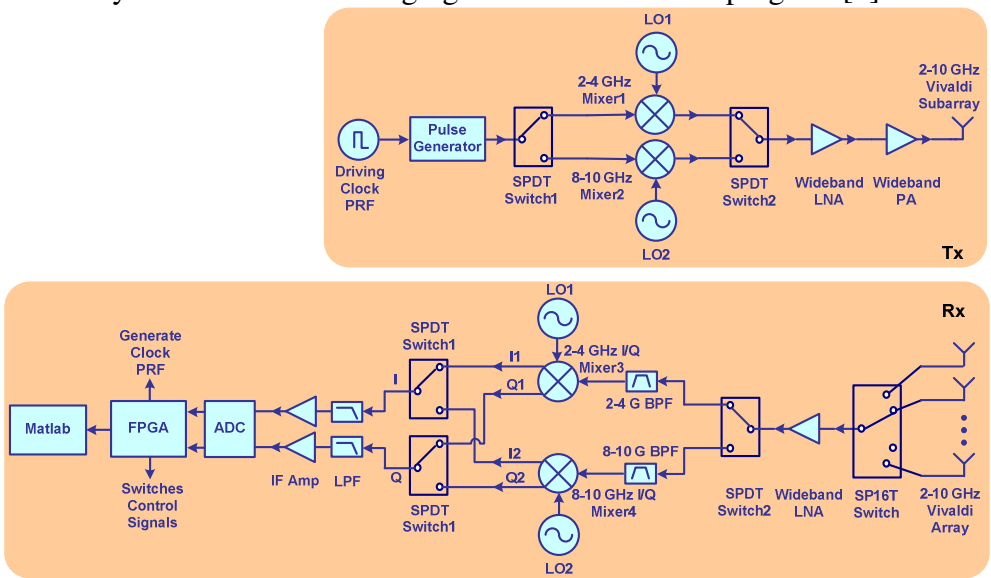

Fig. 5. Detailed block diagram of the reconfigurable imaging radar system

The data acquisition module has been actualized by using an off-the-shelf Avnet Xilinx Virtex-4 FPGA board with a Texas Instrument CDC5801 low-jitter clock multiplier/divider, and two MAX1215 ADC evaluation boards with a 250 MSps conversion rate, as indicated in Fig. 6. The module implements a hybrid sampling scheme (250 MSps real-time rate and 5 GSps equivalent-time rate). The data acquisition module, including the real-time control scheme, is shown in Fig. 7. The Avnet FPGA board, utilizing FPGA-VHDL coding, provides varying sets of logic control signals, such as SAR array switching and system synchronization. The ADC outputs are 12-bit digital differential signals (LVDS), which represent the digitized pulse value. The digitized output is forwarded to, and stored, in the memory of the FPGA board for a real-time imaging processing.

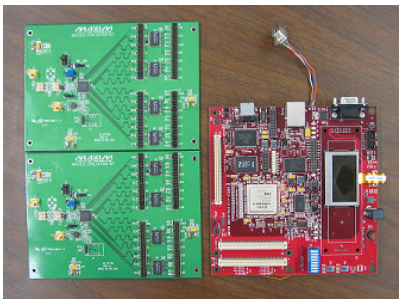

Fig. 6. Avnet FPGA board and MAX ADC boards

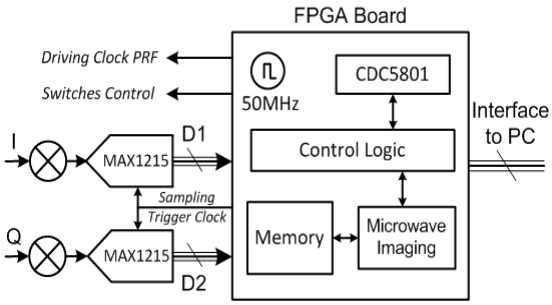

Fig. 7. Diagram of data acquisition and digital control

4. Wideband Synthetic Aperture Radar Beamformers

4.1. Simplified Synthetic Beam-forming Algorithm

The simplified synthetic beam-forming structure is shown in Fig. 8. The reflected signal from the target is assumed to be a plane wave to simplify calculation and implementation. The illustrated simplified method makes it simpler to implement the imaging reconstruction process when using FPGAs. Let $z_i(n)$ be the complex received signal from antenna "i". The output y for direction θ is given by the following relation

$$y_i(n) = \sum_{n=1}^{N} w_i z_i(n) e^{j\varphi_i} \tag{1}$$

where w_i is the correction for scattering signal strength and propagation loss. The phase component φ_i is applied to compensate for the phase difference due to distinct traveling paths. If we assume $\varphi_1 = 0$ and the antenna spacing is 'd', the phase shift for signals from other receiving antennas is gathered to cancel the phase delay, or advance, due to the different traveling lengths as follows

$$\varphi_n = -(n-1)\cdot \beta_0 d \sin\theta \quad (1 \le n \le N) \ . \tag{2}$$

Focusing of the beam in the direction θ implies that the summation of all received signals should produce a maximum value for that particular direction.

4.2. Near-field Synthetic Aperture Beamforming

The simplified synthetic beamformer generates the correct images when the target is at large distance from the detection point, i.e. the target is in the far field. However, the assumption of the reflected plane wave is not completely accurate if the target exists at the near field. A near-field synthetic aperture beamformer [6] is introduced in Fig. 9. Instead of plane waves, the reflected signals from the selected pixel are presumed to propagate from the pixel to the Rx antennas directly. With the near-filed beamformer, Eq. (1) will also be applied to produce the beam output. However, the magnitude correction coefficient w_i alters due to unequal scattering signal or propagation loss. If we still assume $\varphi_1 = 0$, then φ_n is achieved as follows

$$R_n = \sqrt{R_0^{\,2} + (n \cdot d)^2 - 2R_0 (n \cdot d)\sin\theta} \quad (1 \le n \le N), \tag{3}$$

$$\varphi_n = \beta_0 (R_n - R_1) \quad (1 \le n \le N) \ . \tag{4}$$

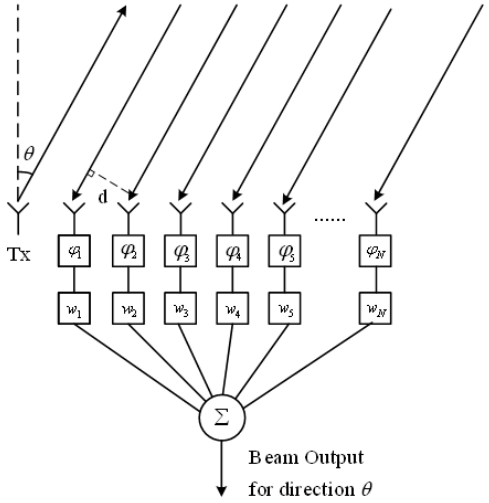

Fig. 8. Simplified beam-forming algorithm

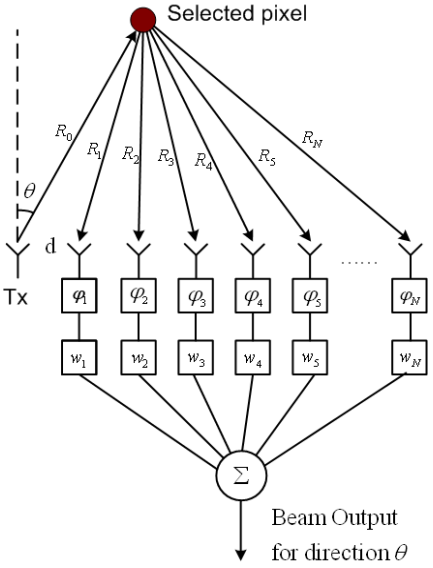

Fig. 9. Near-field synthetic aperture beamformer

4.3. Through-Wall Effects

In a practical situation, the through-wall effects have to be accounted for in order to generate accurate images of the targets. The propagation wave slows down, encounters refraction, and is attenuated as it passes through the wall. If the wall effects are not estimated accordingly, errors may occur in combining the post-data coherently. The through-wall model is presented in Fig. 10. The surveillance space is divided into multiple pixels using range R_0 and angle θ_0. The equivalent electrical length between the selected pixel and observation point is $L = L_1 + \sqrt{\varepsilon_r} L_2 + L_3$. The wall is assumed to be homogeneous and lossless, with a thickness t and a relative permittivity of ε_r. The detection radar has a standoff distance of d from the wall. Then, we can achieve incidence angle θ_1 and refraction angle θ_2 as follows

$$\sin\theta_1 = \sqrt{\varepsilon_r}\sin\theta_2 \ , \tag{5}$$

$$\left(R_0\cos\theta_0 - t - d\right)\tan\theta_1 + t\tan\theta_2 + d\tan\theta_1 = R_0\sin\theta_0 \, . \tag{6}$$

Next, the equivalent electrical length L is acquired by

$$\begin{aligned} L &= L_1 + \sqrt{\varepsilon_r}L_2 + L_3 \\ &= \frac{R_0\cos\theta_0 - t - d}{\cos\theta_1} + \sqrt{\varepsilon_r}\frac{t}{\cos\theta_2} + \frac{d}{\cos\theta_1} \end{aligned} \ . \tag{7}$$

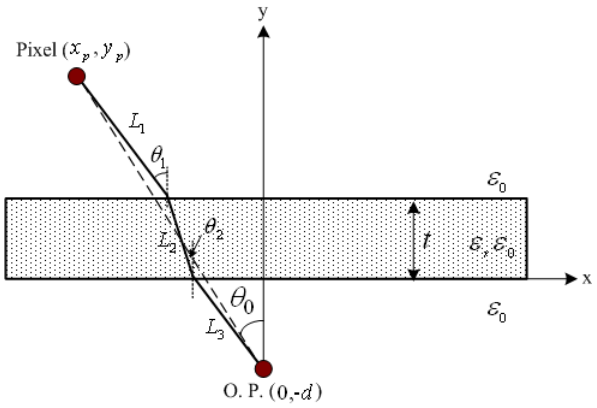

Fig. 10. Through-wall model

Figs. 11 (a) and (b) show the recovered images of the target for two cases: before and after compensating for the wall effects. The drywall utilized in the experiment has a thickness of 4cm and a relative permittivity of 3.0. The real target position is defined in the pictures using a rectangular mark. Comparing figures (a) and (b), the obtained target location is 4cm further from the detection point than its real position if the wall effect is not accounted for.

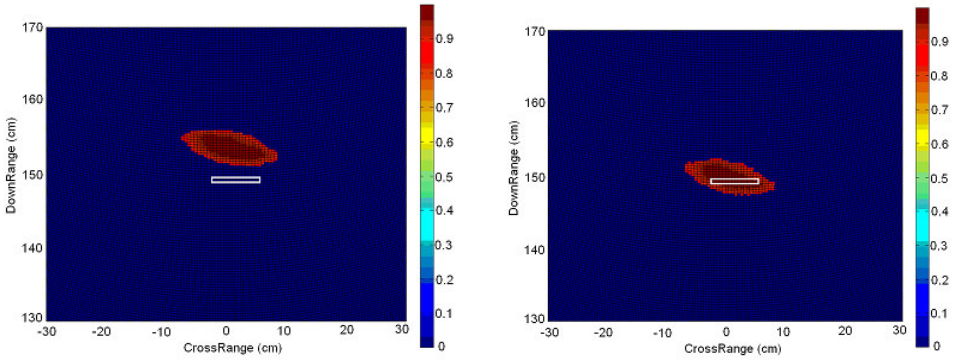

(a) Before compensation for wall effects (b) After compensation for wall effects

Fig. 11. Obtained radar images before and after compensation for wall effects

5. Real-time See-Through-Wall Experiments

5.1. Summary of the System Specifications

The radar imaging system specifications are summarized in Table 1. Typically, a 1ns pulse signal is utilized in our radar imaging system. The minimum pulse width of the signal is 300ps, which is limited by the pulse source and the bandwidth of the Tx/Rx Vivaldi antenna array. The pulse repetition frequency is 10 MHz in the current system and is determined by the reference crystal on the circuit. The image has a refresh rate of 20 Hz in order to track the moving target promptly and accurately.

Table 1. Radar Imaging System Specifications

Modulation Type	Pulse modulated carrier
Pulse Width	1ns (typ.), 300ps (min)
Pulse Repetition Freq.	10 MHz
Center Frequency	3 GHz (min), 9 GHz (max)
Peak Power	0.65 W
Max. Range	12 m
Max. Scan Angle	-40^0 to $+40^0$
Tx / Rx Antenna	2-10 GHz Vivaldi Array
Image Refresh Rate	20 Hertz

5.2. Real-time Images of Stationary Targets

A real-time experiment was performed, as shown in Fig. 12, to investigate the performance of the radar imaging system when detecting static targets. The experiment was performed in a hall of our Engineering building, which occupied an area of approximately 5m by 4m. A 4cm drywall was applied in the experiment. A plate and a cylindrical pipe, both metallic, stand on the floor as the static targets. The images were obtained and displayed on the monitor. The reconstructed image, depicted in Fig. 13, indicates the positions of the metal plate and metal cylinder accurately.

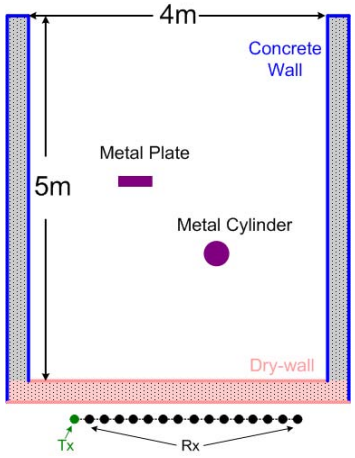

Fig. 12. Experimental setup for stationary targets detection

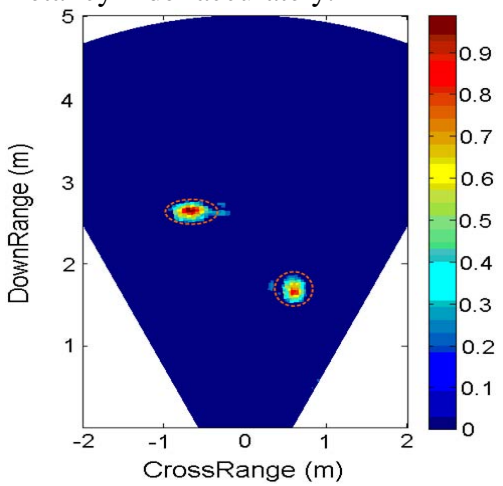

Fig. 13. Real-time image of stationary targets

5.3. Real-time Images of Dynamic Targets

An additional real-time experiment was performed to recover the image of mobile targets, as presented in Fig. 14. A person walks behind the drywall back and forth. The monitor refreshes at a rate of 20 Hz to timely track the location of the moving target. Fig. 15 presents snapshots of the monitor screen in detection of the moving person. The real-time image on the monitor indicates the positions of the person precisely.

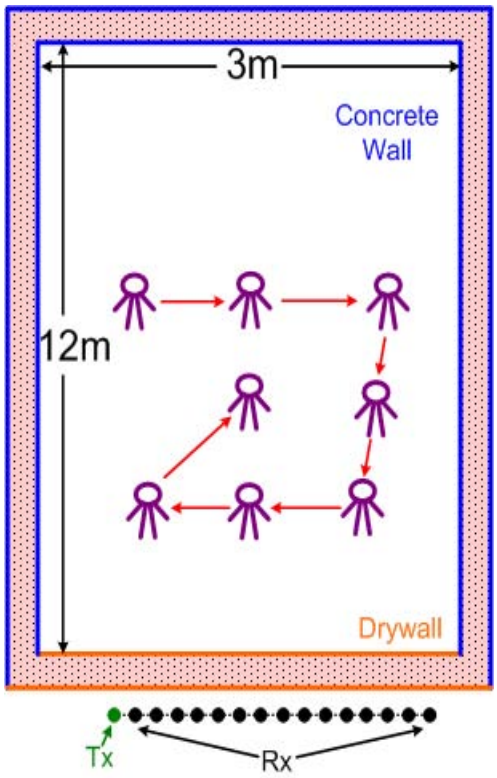

Fig. 14. Experiment detection of a moving person

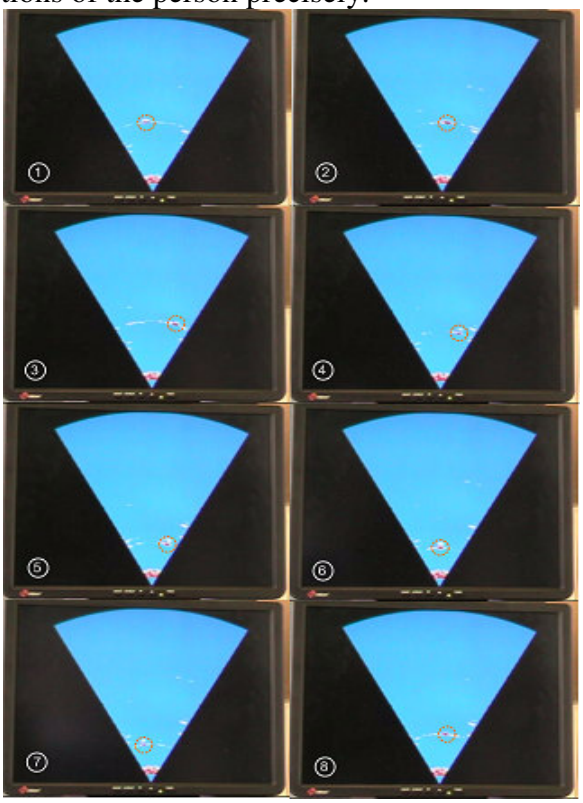

Fig. 15. Real-time image of a dynamic target

6. Three-Dimensional Radar Imaging Experiment

6.1. Three-Dimensional Radar Imaging Beamformer

The three-dimensional radar imaging [7] is investigated, as shown in Fig. 16. A planar Vivaldi array, comprised of the antenna elements in Fig. 1, is required to obtain 3D images. A central element was used for transmitting and additional elements were utilized for receiving. The surveillance space is divided into many voxels in x, y and z axis. Both the near-field synthetic aperture beamformer in Fig. 9 and the through-wall model in Fig. 10 can be applied to capture the 3D images. However, it is not convenient to calculate the transmission or reflection coefficients, or apply Snell's law for the three-dimensional geometry. Next, the coordinate "translator" in [7] was employed to achieve

the same height for the selected antenna and the selected voxel (i.e. $z_a' = z_t'$) in the new coordinate. Therefore, the 3D propagation geometry becomes a 2D model.

Fig. 17 depicts how the coordinate translator works. For a selected antenna at (x_a, y_a, z_a), it becomes (x_a', y_a', z_a') at the new coordinate after the rotation of angle β , where

$$\begin{aligned} x_a' &= x_a \\ y_a' &= y_a \cdot \cos\beta + z_a \cdot \sin\beta \\ z_a' &= -y_a \cdot \sin\beta + z_a \cdot \cos\beta \end{aligned} \tag{9}$$

Similarly, for the selected voxel in the new coordinate

$$\begin{aligned} x_t' &= x_t \\ y_t' &= y_t \cdot \cos\beta + z_t \cdot \sin\beta \\ z_t' &= -y_t \cdot \sin\beta + z_t \cdot \cos\beta \end{aligned} \tag{10}$$

To obtain $z_a' = z_t'$, we get

$$\beta = \arctan\frac{z_t - z_a}{y_t - y_a} \tag{11}$$

The new coordinate, after the transformation, is shown in Fig. 18. The selected antenna and voxel in the new coordinate are at (x_a', y_a') and (x_t', y_t'), respectively. They also have the same height, i.e. $z_a' = z_t'$. Last, all available 2D electromagnetic methods can be applied to analyze this model.

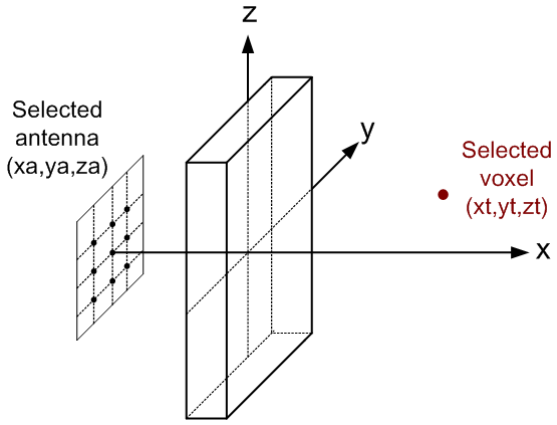

Fig. 16. Diagram of 3D propagation model

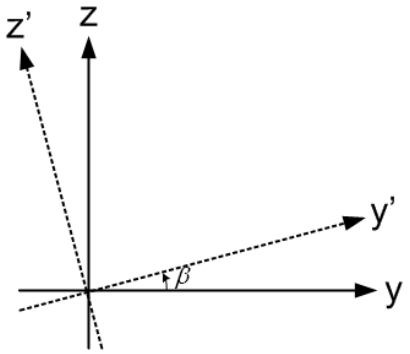

Fig. 17. Coordinate transformer

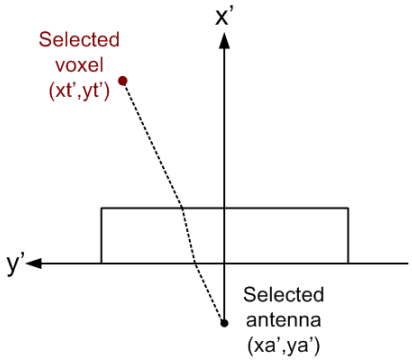

Fig. 18. The new coordinate (x', y', z')

6.2. Three-Dimensional Imaging Experiment

A three-dimensional imaging experiment is performed, as shown in Fig. 19 (a). The transmitting antenna was fixed and a single receiving antenna was moved mechanically to acquire the data at different locations. Fig. 19 (b) presents all the detection positions, with a spacing of λ_0 at its highest operating frequency (10 GHz) in order to achieve the maximum aperture size and avoid the grating lobes. A 2cm thick drywall was utilized and assumed to be homogeneous. A rectangular metal plate with a size of 30cm by 25cm was the detected object.

Fig. 19 (c) presents the obtained 3D image, with the real target position marked. The three-dimensional radar imaging system recognizes the location of the metal plate precisely; with a cross resolution of approximately 10cm. Increasing the number of array elements and the aperture size will further improve the resolution in cross range. The resolution in down range is mainly decided by the pulse width. Using a narrower pulse helps in achieving a better down range resolution.

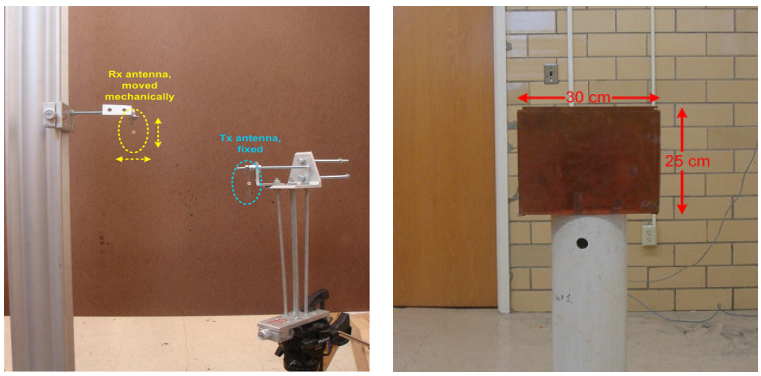

(a) 3D experiment setup

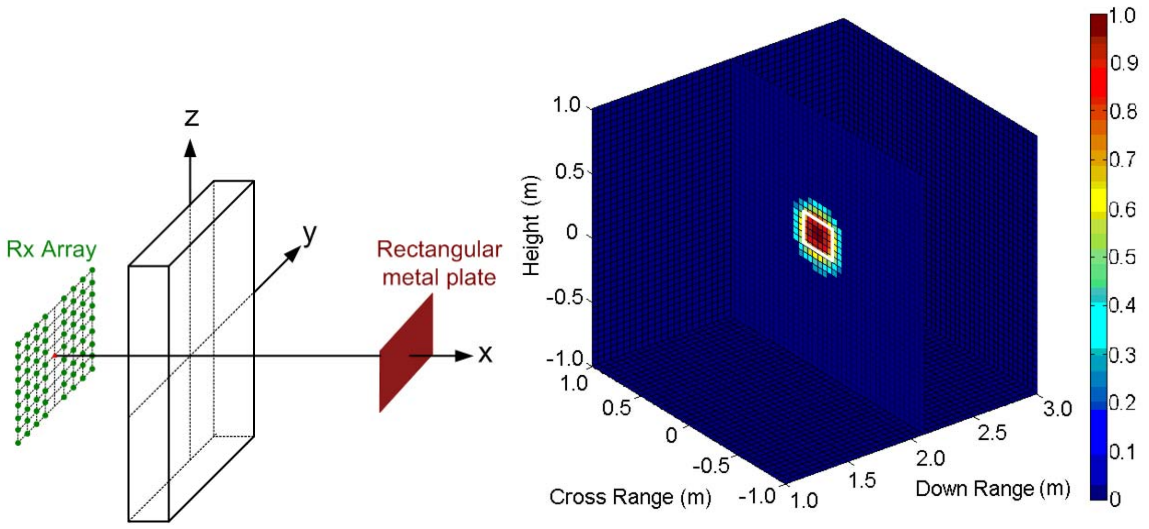

(b) 3D experiment layout (c) Obtained 3D image (x axis – Down range, y axis - Cross range, z axis - Height)

Fig. 19. 3D imaging experiment on a rectangular metal plate
(a) Experiment setup, (b) Experiment layout, (c) Obtained 3D image

A further experiment is employed to recover the three-dimensional image of a human body model behind a 2cm thick drywall, as indicated in Fig. 20 (a). The body model has a height of 1.4 m and a width of 0.6 m. It is located at a down range of 2.2 m. It is clearly seen that the obtained image in Fig. 20 (b) not only localizes the target precisely but also recognizes the outline of the human body accurately. This capability is indispensable for through-wall human being detection, by distinguishing a person from an object successfully.

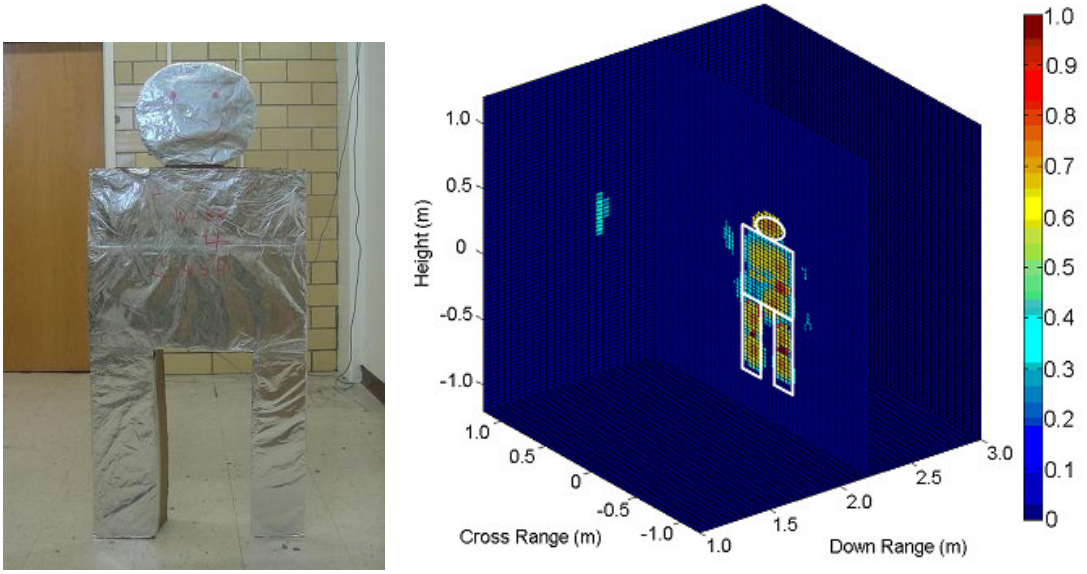

(a) A human body model (b) Obtained 3D image

Fig. 20. 3D imaging experiment on a human body model

7. Conclusion

A reconfigurable radar imaging system is proposed to operate at either the lower UWB band (2-4 GHz) when seeing through the brick or concrete walls to minimize the through-wall attenuation, or the upper UWB band (8-10 GHz) for traveling through drywall (i.e. low loss walls) detection to get the best image resolution. The system is based on utilization of an ultra-wide band antenna design that covers 2 to 10 GHz. The reconfigurable system required only switching of mixers, LOs and BPFs using five switches.

The wideband Vivaldi array design, reconfigurable system transceiver, synthetic aperture beamformers, real-time experiments on static and moving targets, as well as the three-dimensional beamforming algorithm and experimental results, are presented in this paper. Both the near and far field imaging results are very encouraging. These demonstrated results have indicated the capability of accurately locate, track, and image human being objects behind various types of walls.

The parameters of the wall (i.e. thickness and permittivity) in this paper are assumed known. However, in a realistic situation, the wall parameters are unknown. The method in [5] can be applied to simultaneously estimate the wall parameters and obtain accurate images.

References

[1] Y. Wang, Y. Yang and A. E. Fathy, "Reconfigurable ultra-wide band see-through-wall imaging radar system," *2009 IEEE AP-S International Symposium*, June 2009.
[2] M. M. Zinieris et al., "A broadband microstrip-to-slot-line transition," *Microwave and Optical Technology Letters*, Vol. 18, No. 5, Aug. 1998.
[3] S.B. Cohn, "A Class of Broadband Three-Port TEM-Mode Hybrids", *IEEE Trans. Microwave Theory and Tech.*, vol. MTT-16, No. 2, pp. 110-116, Feb. 1968.
[4] Mark Kahrs, "50 Years of RF and Microwave Sampling," *IEEE Trans. Microwave Theory and Tech.*, vol. 51, No. 6, June 2003.
[5] G. Wang, M. G. Amin, and Y. Zhang, "New approach for target locations in the presence of wall ambiguities," *IEEE Trans. Aerospace and Electronics Systems*, vol. 42, issue 1, pp. 301-315, Jan 2006.
[6] F. Ahmad, G. Frazer, S. Kassam and M. G. Amin, "Design and implementation of near-field, wideband synthetic aperture beamformers", *IEEE Trans. Aerospace and Electronics Systems*, vol. 40, NO. 1, Jan 2004.
[7] F. Ahmad, Y. Zhang, and M. G. Amin, "Three-dimensional wideband beamforming for imaging through a single wall", *IEEE Geoscience and remote sensing letters*, VOL. 5, NO. 2, Apr. 2008.

OPERATIONAL PERSPECTIVES OF BIOLOGICALLY INSPIRED CAPILLARY-BASED RECONFIGURATION MECHANISMS IN MICROSTRIP PATCH ANTENNAS

Gregory H. Huff, Sean Goldberger, and S. Andrew Long
Electromagnetics and Microwave Laboratory
Department of Electrical and Computer Engineering
Texas A&M University
College Station, TX 77843-3128

Abstract: Recent work on reconfigurable antennas and smart skins based on biologically inspired mechanisms derived from the cuttlefish has led to several novel architectures for system-level integration. One of the concepts arising from work in this area is the capillary-based reconfiguration/adaptation mechanism utilizing the displacement and/or flow of functionalized nanoparticles dispersions within the substrate of a microstrip patch antenna. Through a pressure-driven system, these capillary structures can be used to reconfigure the impedance bandwidth of the antenna. In addition to this operation, the capillary topology has also demonstrated an ability to provide a self-stimulated, or cognitive, mechanism which can compensate for a localized deformation or bending of the antenna on a flexible substrate via the associated forces from mechanical compression. In both of these cases, the use of a single capillary and series/corporate arrays of capillaries has created the opportunity to investigate some of the fundamental operational perspectives and integration techniques in the design space for microstrip antennas utilizing this reconfiguration/compensation technique. In addition to several small antenna arrays and multi-capillary configurations, an in-depth analysis of the single substrate-embedded capillary will be discussed in this paper and presentation. The resulting design equations and other analytical expressions have been derived using perturbation techniques based on the microstrip antenna's design. These demonstrate many of the limitations and possibilities from different nanoparticle geometries and material compositions as well as different capillary topologies associates with fabrication techniques. Measured, analytical, and simulated results for several antennas in this design space will be discussed to highlight the ongoing work in this area.

1. Introduction

The biological mechanisms of the cuttlefish – specifically the chromatophores in its skin and the coordinated deformation of these color pigment sacs to alter its visual appearance – have inspired the examination of several unique concepts for reconfiguration antennas and reactive loading mechanisms [1]-[2]. The displacement of

magnetodielectric nanoparticles dispersions within strategically located microfluidic mechanisms [3] and/or the performance-governing locations of a given device [4]-[5] are two specific techniques that have precipitated form this biological inspiration. Each of these concepts enables the electromagnetic agility required for reconfiguration by exploiting opportunities to reversibly manipulate the local constitutive material properties to impact the performance of the device. The ability to engineer the desired material composition and physical shape of the nanoparticles and utilize mechanisms to control the volume fraction in these dispersions (e.g., [6]-[10]) add additional dimensions to this design space. The pressure-driven topology also creates opportunities to further capitalize on the use of the materials by reducing the amount of electrically conductive control and/or bias lines close to the aperture and directly perturb the fields of a device.

While these and other operational aspects of these systems provide many different avenues of functional exploration, this increase in functionality come with the trade-offs from the added complexity of a pressure-driven system. The additional need to create high-speed reconfiguration mechanisms from a physically actuated mechanism illuminates additional practical requirements, such that most application will require any new enabling technology to be competitive with current electronically controlled systems (e.g., ferroic materials, RF MEMS, and solid state devices). However, before these operational aspects can be fully translated into performance requirements there are several fundamental operational perspectives that must be attend to. This work focuses on two of these items by: 1) an analytical investigation into the limitations and identifying the capabilities of the substrate-integrated capillary mechanism and 2) benchmarking or exploring its performance experimentally in several configurations through the design and operation of appropriately chosen devices.

This paper begins with a very brief recap on the use of the nanoparticle dispersions as they relate to this work, and the impact of particle geometry on the mixing formulas used to approximate the effective medium properties of the dispersion. An analytical analysis follows this for a linearly polarized microstrip patch antenna with a dispersion-filled substrate-integrated capillary that is aligned with the antenna's H-plane. This single capillary system is then examined as a mechanism to electromagnetically compensate the effects from a physical deformation of the antenna; specifically, a sharp bend located at the center of the resonant length dimension that is coincident with the H-plane and the embedded capillary system – a proof-of-concept design utilizes this mechanism to compensate the bending of a patch antenna up to 90º. Two additional H-plane aligned, substrate-integrated, dispersion-filled capillaries are then utilized with a flat (non-deformed) microstrip patch antennas to facilitate the reconfiguration and the frequency agility of a previously reported single element with the behavior into small arrays; a two-element E-plane and H-plane array are provided to discuss the use of parallel and series capillary networks and the use of miscible fluids in the dispersion. A short summary that recaps the discussion on these items, acknowledgements, and list of referenced work conclude this paper.

2. Effective Medium Properties of the Dispersion

Mixing formulas [11] have an especially important role in the study and implementation of nanoparticle dispersions for reconfigurable antennas and other electromagnetically agile devices derived from these methods. The enabling materials systems can be composed of a great number of particles, which each experience a myriad of length-scale dependant forces that collectively dictate (through multi-body interactions, percolation, etc.) the effective medium properties of the dispersion. Accurately predicting these properties and establishing models that account for the complex interactive behavior at the nano-scale represents a key step in fully utilizing thee systems. This can obviously become quite difficult given the complexity that can arise from these particle interactions and the perceived homogeneity of the mixture. While there is considerable ongoing work in this area (e.g., [12]-[13]), there are several well established mixing formulas that accurately approximate the magnetodielectric properties of the dispersion within the RF and microwave spectra since the ratio of the Mie (resonant) scattering length and nano-scale particle size remains less than unity. The Maxwell-Garnett Formula [14] represents one such method that accurately approximates the complex constitutive parameters; Eq. 1 shows this formula for spherical (e.g., colloidal) particles, or inclusions, where the effective medium property s_{eff} results from the mixing of a liquid s_1 with a volume fraction ϑ of a colloidal materials s_2; the variable s in this expression captures the complex (lossy) properties using $s = s(1 - j\tan\delta)$ and can independently represent ε or μ.

$$s_{eff} = s_1 + 3s_1\vartheta\frac{s_2 - s_1}{s_1 + 2s_2 - \vartheta(s_2 - s_1)} \tag{1}$$

The expression in (1) can be transformed to examine prolate spheroids, multilayered composite particles, and other arrangements that can be mixed into dispersions and displaced within strategically located microfluidic mechanisms and/or the performance-governing locations of a given device. Fig. 1 shows the commonly used example of this flexibility for ellipsoidal geometries with varying aspect ratios [11] – discs, needles, and spheres. Each of these inclusion geometries are assumed to be uniformly sized with a permittivity ε_2 = 1000, randomly orientated in the dispersion, and homogeneously dispersed into a background material with ε_1 = 2.1. This result indicates the impact of material geometry and desire to use less nanoscale inclusions to achieve a greater effect.

This figure also highlights other relevant physical aspects that can impact the use of these formulas by identifying the monodispersed, close-packed filling fraction limit of 74.5% (assuming a face-center cubic lattice similar to the arrangement of pool balls in a triangle). Polydispersity can be used with dispersions of spherical particles to increase ϑ beyond this limit by introducing particles of varying size to the dispersion that can effectively fill the voids between larger spheres (the polydispersity limits for other particle geometries can be obtained but are not included in Fig.1). However, increasing ϑ up to and beyond the monodispersed limit increases the likelihood for particle

interactions (Van der Waals, etc.) and increases the potential for coagulation and other effects than can result in clumping, settling, and adversely high viscosities of the dispersion. This requires an ionic dispersant, or surfactant, to create an electrical double layer and electrostatically-stabilizing the colloids (e.g., coating them in a like-charged, repulsive 'shell'). The ionic loss mechanisms associated with the surfactant are assumed very low for the purpose of this discussion, and are neglected given the very small amount (<1%) of this material that is required.

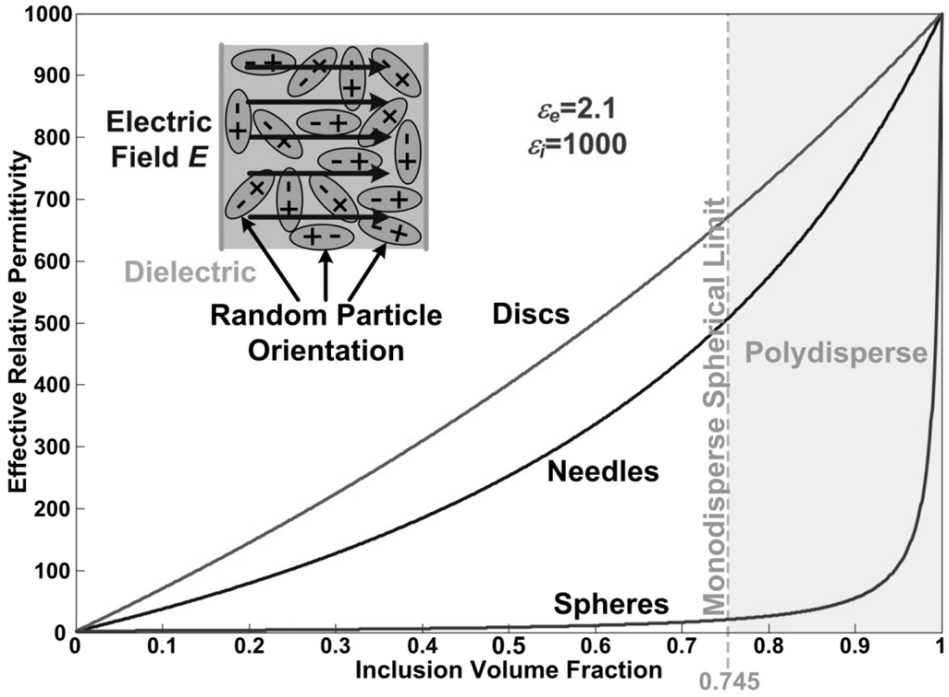

Fig. 1. Calculated effective permittivity ε_{eff} using the Maxwell-Garnett mixing rule for disc, needle, and spherical particle geometries with a permittivity ε_2 = 1000 dispersed into a background permittivity of ε_e ~ 2.1. The monodispersed limit is also shown for spherical particles.

3. Analysis of a Substrate-Integrated Capillary

Fig. 2 shows a diagram of a linearly polarized microstrip patch antenna with a substrate-integrated capillary to contain the nanoparticle dispersions that is aligned with the antenna's H-plane. The pressure-driven operation of the capillary structure is captured by including two immiscible, non-magnetic, lossless dispersions within the capillary. These two dispersions are distinguished by their respective permittivity and role in the antenna, one of which acts as a dispersion with $\varepsilon_{r\text{-}in}$ being pumped into the antenna and an initial dispersion $\varepsilon_{r\text{-}out}$ that is displaced out of the structure from the action of the first. Differences in the dielectric properties of these materials, the permittivity $\varepsilon_{r\text{-}sub}$ of the antenna's substrate and its height h, the displacement volume (related to capillary

dimension and geometry), the location *W'* of the boundary between the two dispersions, and the position *L'* of the capillary (of radius *r*) relative to the electric field distribution under the patch create several degrees of freedom.

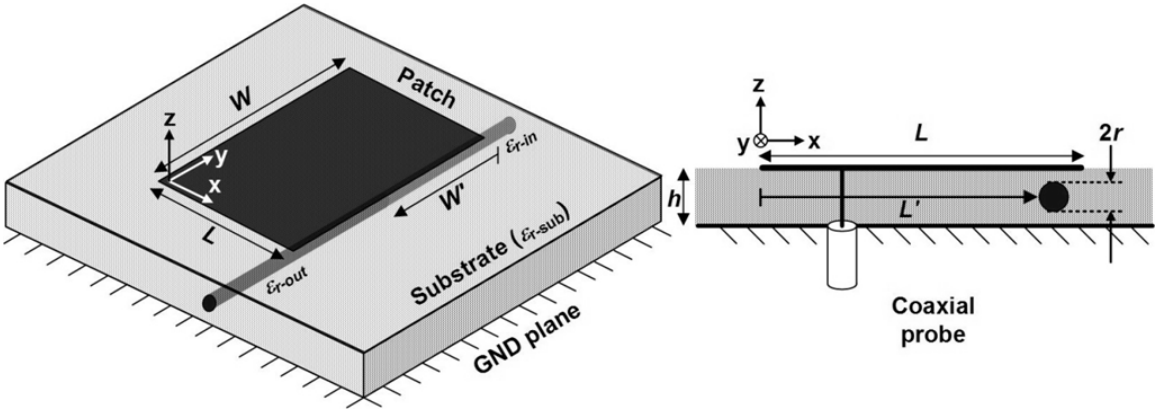

Fig. 2. Diagram of a linearly polarized microstrip patch antenna with a substrate-integrated capillary that is aligned with the antenna's H-plane.

The resonant cavity model of the linearly polarized microstrip patch antenna [15] and perturbation techniques [16] provide the framework for analyzing the topology in Fig. 4 [17]-[18]. The expression in (2) quantifies the change in a cavity's resonant frequency as a result of material perturbation, where $\boldsymbol{E}_o$ and $\boldsymbol{H}_o$ represent the initial electric and magnetic fields within the equivalent rectangular cavity formed by the antenna, and $\boldsymbol{E}$ and $\boldsymbol{H}$ represent the fields after a material displacement; $\Delta\varepsilon$ and $\Delta\mu$ are the respective changes in the cavity material's permittivity and permeability. The fields in the cavity can be approximated as the original fields, and the fields in the capillary (including $\varepsilon_{r\text{-}out}$) can be represented by (3) [16], provided the capillary's cross-section is small with respect to the cavity's cross-section and the electric field is orthogonal to the axis of the capillary.

$$\frac{f - f_o}{f_o} \approx \iiint_{capillary} \left(\Delta\varepsilon\vec{E}\cdot\vec{E}_o + \Delta\mu\vec{H}\cdot\vec{H}_o\right) \Big/ \iiint_{cavity} \left(\varepsilon\vec{E}\cdot\vec{E}_o + \mu\vec{H}\cdot\vec{H}_o\right) \tag{2}$$

$$E_{capillary} = 2E_o\left(1 + {\varepsilon_{r-capillary}}\Big/{\varepsilon_{r-sub}}\right)^{-1} \tag{3}$$

Applying the approximation from (3) into (2) and solving the expression for the geometry shown in Fig. 2 results in Eq. (4). This represents a step towards developing a comprehensive expression that indicates the frequency agility of the antenna with the integrated capillary perturbation. The reconfigurable frequency shift in (4) depends on the materials used, the "visibility" of capillary in the electric field, and the perturbation's volume relative to the cavity. Setting the radius of the capillary to $r = 0.5h$), the amount of fluid pumped into the antenna to $W' = W$, and the location $L' = L$ maximizes the

visibility in the TM_{10} patch mode and reduces (4) to (5). It is important to note that the relationship between the antenna's resonant length L and the initial material parameters $\varepsilon_{r\text{-}in}$, and $\varepsilon_{r\text{-}sub}$ has not been included into (5) – this design relationship provides scaling in (5), which is tied to the ratio of the antennas substrate height to its length. The effect of this perturbation on the impedance match of the antenna is also neglected at this point to abstract the discussion into a study of the cavity's behavior; this represents an important practical consideration that will be discussed in the following sections. Fig. 3 shows three families of curves from (5) obtained by setting $h = 0.1L$ (e.g., a very thick substrate), fixing two of the three material parameters ($\varepsilon_{r\text{-}in}$, $\varepsilon_{r\text{-}out}$, or $\varepsilon_{r\text{-}sub}$), and varying the third continuously over a given range. These material values are given in Table I.

$$\frac{f-f_o}{f_o} \approx \underbrace{\frac{4\varepsilon_{r-sub}\left(\varepsilon_{r-out}-\varepsilon_{r-in}\right)}{\varepsilon_{r-sub}^2+\varepsilon_{r-out}\varepsilon_{r-in}+\varepsilon_{r-sub}\varepsilon_{r-out}+\varepsilon_{r-sub}\varepsilon_{r-in}}}_{\text{Material Properties}} \underbrace{\cos^2\left(\frac{\pi x'}{L}\right)}_{\text{Placement}} \underbrace{\frac{\left(W'\pi r^2\right)}{\left(W\cdot L\cdot h\right)}}_{\text{Dimensions}} \tag{4}$$

$$\frac{f-f_o}{f_o} \approx \frac{4\varepsilon_{r-sub}\left(\varepsilon_{ro}-\varepsilon_{rd}\right)}{\varepsilon_{r-sub}^2+\varepsilon_{r-out}\varepsilon_{r-in}+\varepsilon_{r-sub}\varepsilon_{r-out}+\varepsilon_{r-sub}\varepsilon_{r-in}}\frac{\pi h}{L} \tag{5}$$

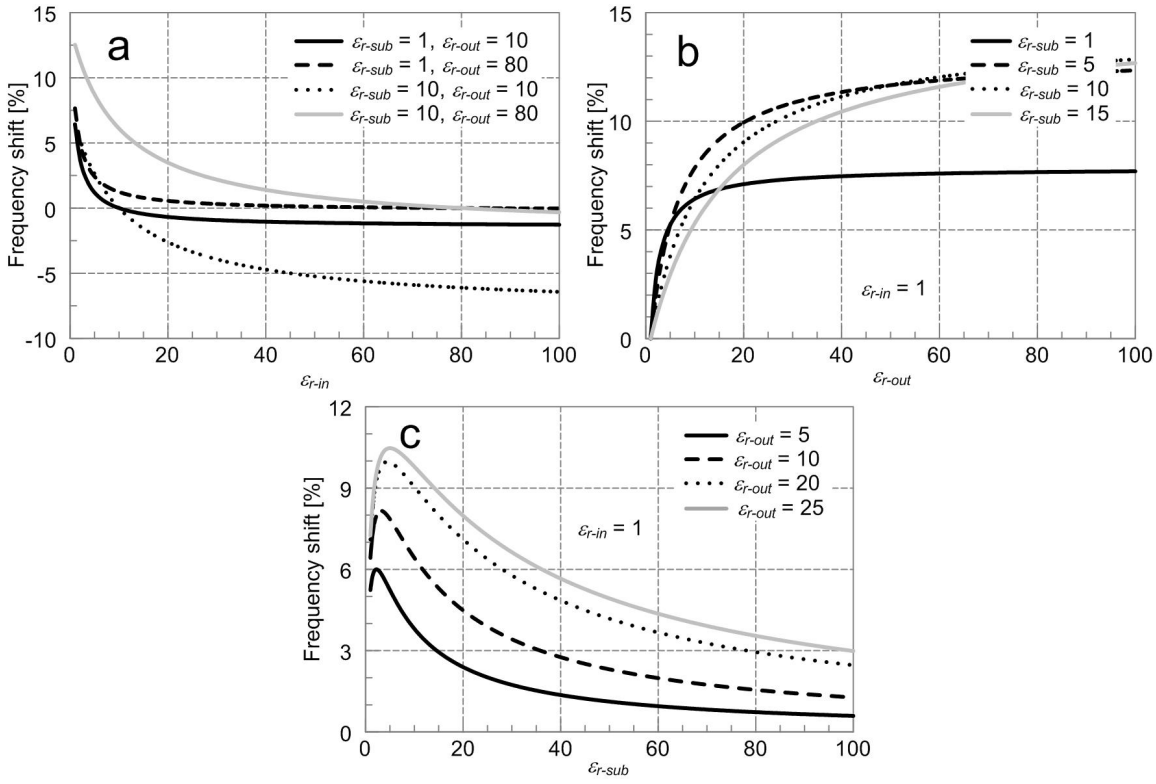

Fig. 3. Families of curves (a, b, and c) from Eq. (5) obtained by fixing two of the three material parameters and varying the third continuously over the ranges shown in Table I.

Table I. Summary of material variations used to calculate the family of curves in Fig. 3.

Plot	Pumped In	Pumped Out	Substrate
3a	$1 \leq \varepsilon_{r\text{-}in} \leq 100$	$\varepsilon_{r\text{-}out}$ 10, 80	$\varepsilon_{r\text{-}sub}$ = 1, 10
3b	$\varepsilon_{r\text{-}in}$ = 1	$1 \leq \varepsilon_{r\text{-}out} \leq 100$	$\varepsilon_{r\text{-}sub}$ = 1, 5, 10, 15
3c	$\varepsilon_{r\text{-}in}$ = 1	$\varepsilon_{r\text{-}out}$ = 5, 10, 20, 25	$1 \leq \varepsilon_{r\text{-}sub} \leq 100$

The rows in Table I provide a summary of the material properties used to obtain the curves in Fig. 3. All available permutations are shown in the respective plots and each of these three curves shows a unique and common trend. Specifically, each set of plots demonstrates the saturating effect derived from the approximation in (3) and the orthogonal orientation of the vertically-directed electric field and the axis of the dielectric-filled capillary. Fig. 4 extends this analysis by including the material-dependant relationship of the resonant length L [15] that was removed in Fig. 3, and demonstrate the effects from changing the eccentricity of the nanoparticle geometry (spheres, discs, and needles) in the Maxwell-Garnett mixing rule on $\varepsilon_{r\text{-}out}$ and substrate. The plots indicate the particle shape in the upper-left corner and assume air is used to pressurize the capillary ($\varepsilon_{r\text{-}in}$ = 1) and push the dispersion out of the antenna, similar to the effects in Fig. 3b.

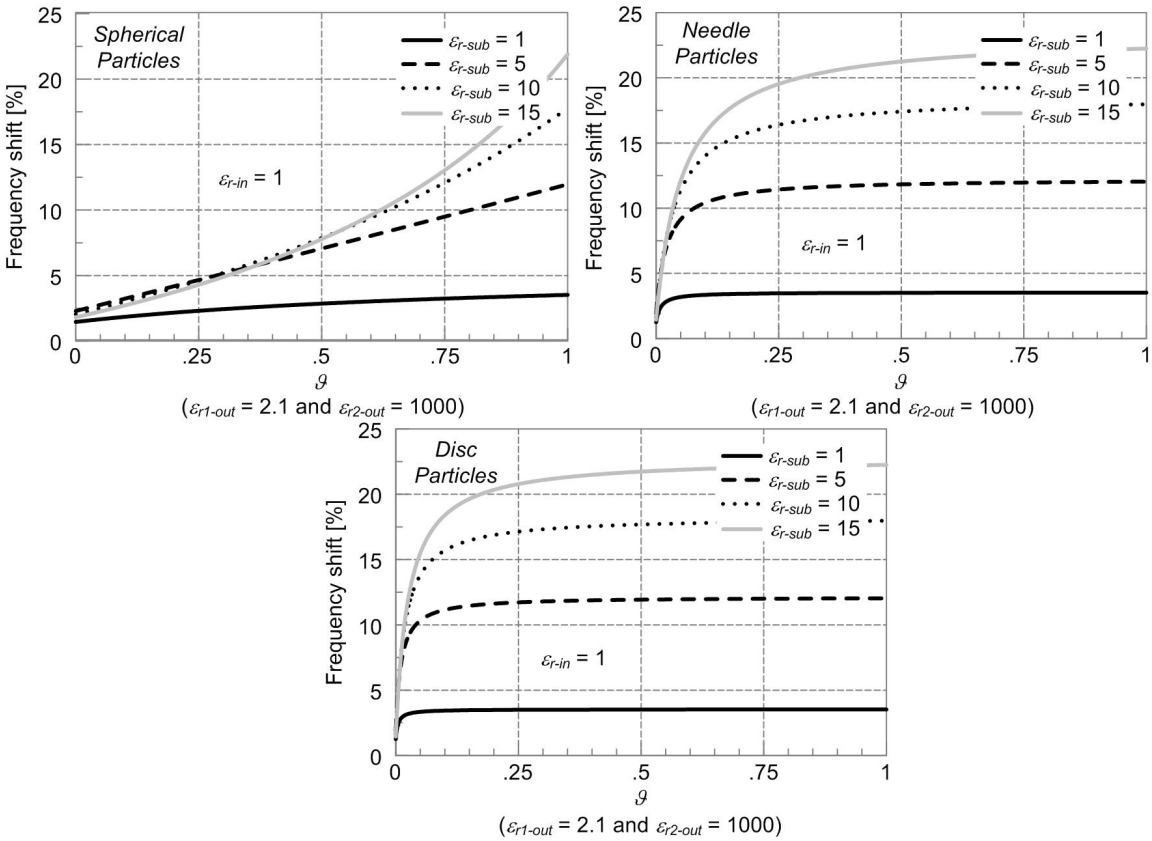

Fig. 4. Plots of frequency shift showing the impact of the nanoparticle's eccentricity (spheres, discs, and needles) and mixing formulas for the dispersion shown in Fig. 2.

Each of these plots uses the data from the dispersion properties plotted in Fig. 2; calculated from Eq. 1 and its variants to account for particle eccentricity (spheres, discs, and needles). The major difference in these curves and those in Fig. 4 are their abscissa, which is shown as the volume fraction ϑ of the $\varepsilon_{r\text{-}out}$ material dispersion to better correlate the plotted frequency shift against the properties of the mixture. Several design-related observations can be made from this more comprehensive, but theoretically attainable, frequency shifts shown in Fig. 4. The two of particular interest relate to the particle shape and linearity o the response, and amount of material required to achieve this effect. For the spherical particles, the non-linear function of volume fraction on the effective medium properties (see Fig. 2) combines with the non-linear effect of the perturbation to provide a relatively linear response to an increase in the volume fraction. This indicates that a polydispersed spherical particle system can tolerate a control system with limited capabilities to adjust the volume fraction so long as the viscosity of the dispersion remains acceptable. The needle- and disk-shaped particles have an opposite effect; they show a more linear response in volume fraction ϑ of the $\varepsilon_{r\text{-}out}$ material dispersion, but a very non-linear saturation of the frequency shift. This indicates that a volume fraction of high aspect ratio particles will requires less material to achieve the desired response but a more precession material delivery system. Results for other capillary topologies will be discussed in the presentation of this material.

4. Single Capillary Compensation Mechanism for Antenna Deformation

The first potential application of the substrate-integrated capillary relates to the electromagnetic performance of conformal antennas on polymorphic structures and/or control surfaces that can alter their shape or texture. These “smart” structures have typically included flexible materials on the skin of the structure (e.g., [19], [20]) where the conformal antennas would reside. The effect of this physical deformation on the antenna’s performance depends on a myriad of factors (design, deformation, materials, etc.), so a number of possible side-effects on the antenna’s electromagnetic performance exist. For smaller low power systems like micro air vehicles (MAVs), a mechanism to compensate for this behavior would ideally operate in a cognitive or autonomous manner. Ergo, facilitate a bend-assisted displacement of nanoparticle dispersions within the antenna’s substrate (conceptually similar to a fire billow) to maintain the desired performance over various degrees of shape shifting.

This application examines an antenna similar to Fig. 2 from the previous section; a linearly polarized microstrip patch antenna with a substrate-integrated capillary that is aligned with the antenna’s H-plane. The original reporting of this bent-antenna structure and its performance were reported in [1], [21], and the majority of these results have been omitted. The item of interest for this work is demonstrating the impact of the dispersion properties on the ability of this mechanism to compensate the sharp bend through the center of this structure by displacing a high permittivity dispersion with air to utilize the effect shown in Fig. 3b. This will effectively reduce the electrical length on that side which counteracts the electrical lengthening from the bend. The co-location of each of

these effects on the same side of the probe feed is required to maintain the impedance match, which can be conceptualized using the antenna's transmission line model.

Fig. 5 shows the antenna with a sharp bend at its center (coincident with the H-plane) and a summary of the antenna's simulated [22] VSWR as it bends from 0º (flat) to 90º. Plots a-c in this figure correspond to (a) an antenna design with no capillary, (b) a dispersion in a capillary with $\varepsilon_{r\text{-}out}$ = 10 and $\varepsilon_{r\text{-}in}$ = 1, and (c) a dispersion in a capillary with $\varepsilon_{r\text{-}out}$ = 25 and $\varepsilon_{r\text{-}in}$ = 1 ($\varepsilon_{r\text{-}sub}$ = 2.66 for all cases). The initial dispersion in the capillary was taken into account in the design of each antenna in (b) and (c) to ensure they were impedance matched at 3 GHz when flat with W' = 0 ($\varepsilon_{r\text{-}out}$ under the whole patch). The curves in (a) illustrate the electromagnetic effects of bending (assuming the conductor stretches across the compressed substrate) appear similar to a length-extension on the side of the probe which the bend occurs. The difference in (b) and (c) reside in their ability to maintain the impedance bandwidth as the antenna bends to 90 º. This is a predictable result by considering the greater potential for dielectric loading with a higher dielectric constant material, but it relates back to the dispersion's effective medium properties and the trends seen in Fig. 3b.

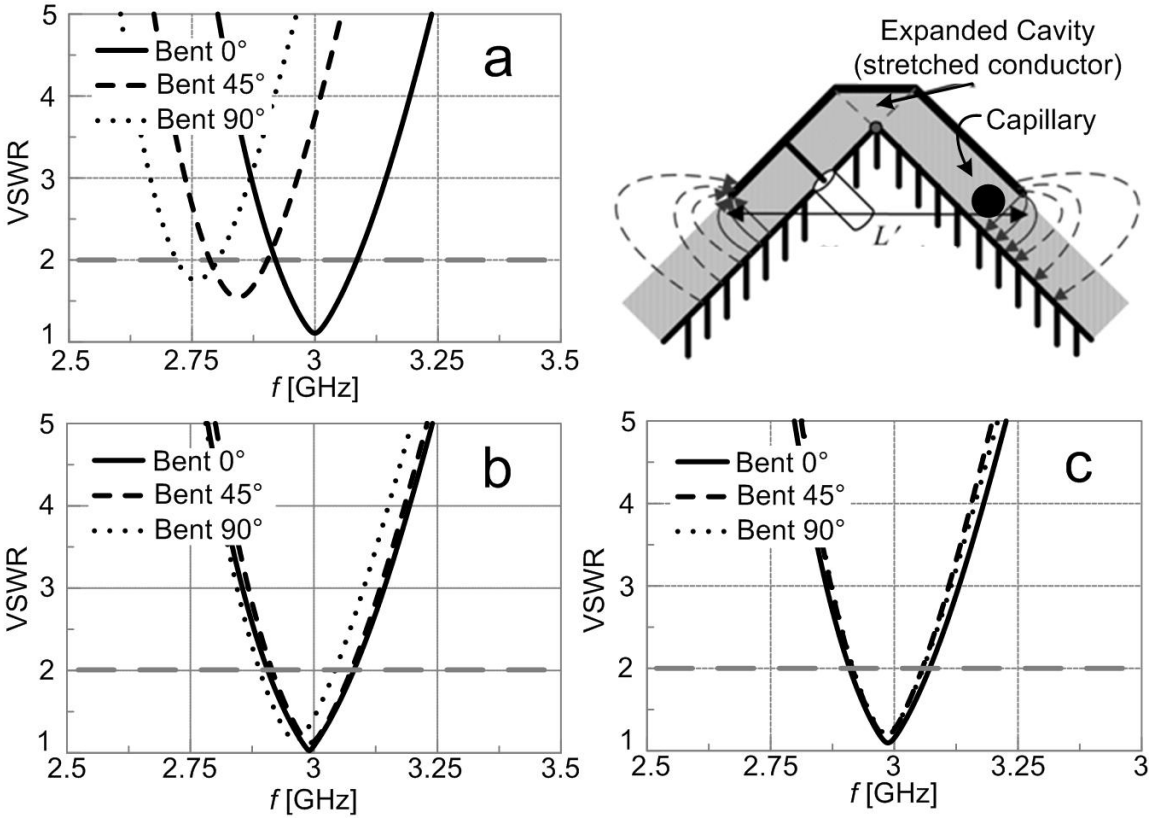

Fig. 5. The antenna with a sharp bend at its center and a summary of the antenna's simulated VSWR as it bends from 0º (flat) to 90º; (a) an antenna design with no capillary, (b) a capillary with $\varepsilon_{r\text{-}out}$ = 10 and $\varepsilon_{r\text{-}in}$ = 1, and (c) a capillary with $\varepsilon_{r\text{-}out}$ = 25 and $\varepsilon_{r\text{-}in}$ = 1.

5. Small Arrays of Frequency Reconfigurable Patch Antennas

The use of a multiple capillary system and nanoparticle dispersions have been examined in [23]-[24] as a means to reconfigure the impedance bandwidth of a microstrip patch antenna. This has been extended in [25] to examine their performance in small arrays. An item of particular interest from this more resent work was the use of miscible (or 'mixable') fluids for the dispersions in the capillaries. Specifically, [25] examined the displacement of a low dielectric fluid with a closely matched permittivity to the antennas' substrate (making it benign with respect to the operation of the antenna) with a dispersion of a higher dielectric constant derived from mixing high dielectric materials into the same fluidic medium. Figs. 6 and 7 show the H-plane and E-plane array orientations, respectively, that were designed for operation at 3 GHz and testing microfluidic reconfiguration of arrays with corporate (E-plane) and series (H-plane) capillary systems. The simulated and fabricated arrays are shown on the left and right, respectively, for each configuration. Each array has a center-to-center spacing of l0 at 3GHz, which results in an edge-to-edge separation of S_e = 15 mm in H-plane orientation and S_e = 22 mm in the E-plane configuration. Each designs use Sylgard 184 [26] (PDMS) substrates (ε_r = 2.66, μ_r =1) [55] of height h = 5 mm. All of the patches have a resonant length of 37 mm and width of 27.9 mm, and were chemically etched on 5 mil thick Duroid 5870 and mechanically fastened to the antenna and aluminum substrate. There are three capillaries total per radiator, with a diameter d = 3 mm; each is aligned with the antennas' H-planes.

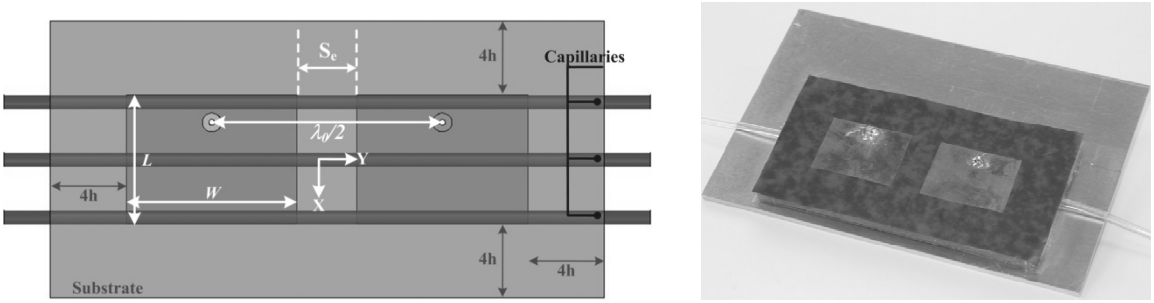

Fig. 6. Simulated (left) and fabricated (right) H-plane arrays with the series-type capillary configuration embedded into the substrate.

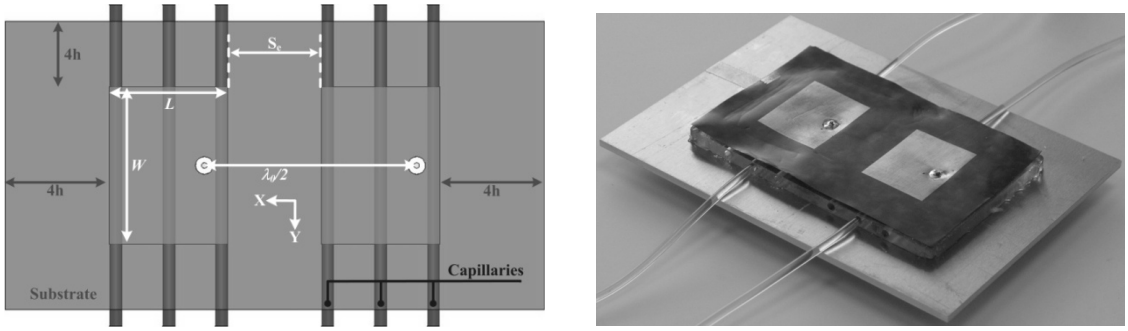

Fig. 7. Simulated (left) and fabricated (right) E-plane arrays with the corporate-style capillary configuration embedded into the substrate.

In both the experiments and measurements, the center capillary in each antenna in each array configuration was filled with (non-ionic) mineral oil with ($\varepsilon_{r1} \sim 2.1$ and tan $\delta_l \sim 0$) and sealed since it would have little effect in the performance of the antenna using dielectric nanoparticles in the TE_{10} patch mode where there is a null in the standing electric field distribution. Each of the perimeter capillaries were also filled with this oil in their initial state (hence, $\varepsilon_{r\text{-}out} = 2.1$). Polydispersed Barium Strontium Titanate (BSTO) ($\varepsilon_r \sim 1000$ and tan $\delta \sim 0.01$) [27] was treated with a nominal amount of Nanosperse [28] surfactant ($\varepsilon_r \sim 8$ and tan $\delta \sim 0.11$), and then dispersed into the low-loss petroleum distillate with a volume fraction of $\vartheta = 58\%$ to create a dispersion with $\varepsilon_{r\text{-}in} \sim 10.7$ and tan $\delta_{eff} \sim 0.003$ (approximated using (1)). This dispersion was routed accordingly from a single syringe using fluidic splitters and tubing into the antenna, and then pumped into the antenna arrays in discrete steps. These displacement steps are shown in Figs. 8 and 9 along with the simulated coupling (S_{21} and S_{12}) for the H-plane and E-plane, respectively, such that material is flowed half-way and fully underneath each antenna (5 configurations *a-e* for the H-plane array and three configurations *a-c* for the E-plane array).

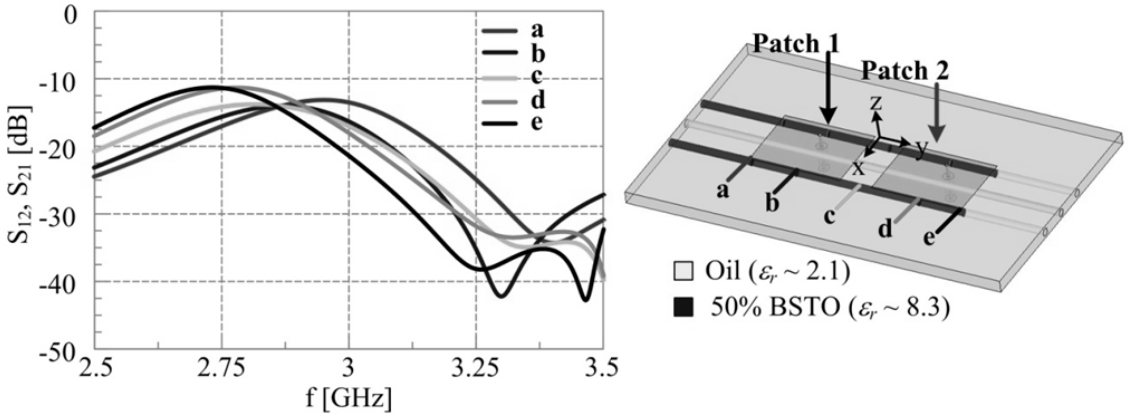

Fig. 8. Displacement steps (right) and simulated mutual coupling for H-plane array (left).

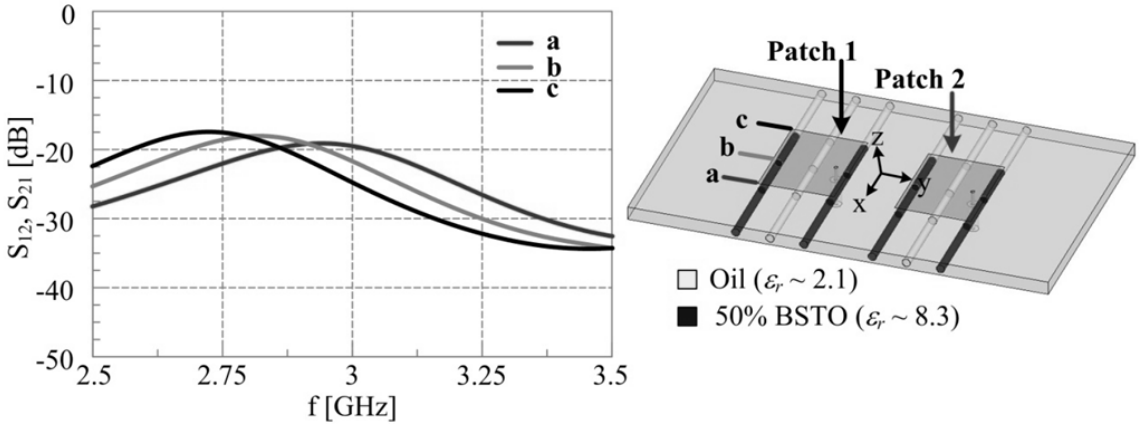

Fig. 9. Displacement steps (right) and simulated mutual coupling for E-plane array (left).

As the dispersions progress through the array in both array configurations, the edge-to-edge electrical length decreases as the antennas become electrically longer from the increased aggregate dielectric material properties underneath the patches. This effect is shown by the increase in coupling as the dispersion makes its way through the array. In addition, the H-plane mutual coupling is higher than the E-plane because the edge-to-edge spacing was less than the E-plane's spacing. These results show a strong correlation between increasing the electrical length of the elements by increasing the dielectric strength of the dispersion. This decreases the electrical separation between the elements which increases the mutual coupling.

Figs. 10 and 11 show the simulated and measured VSWR of each antenna in the H-plane and E-plane configurations, respectively. The letters located in the upper left corner of each plot correspond to the dispersion locations shown in Fig. 8 (H-plane) and Fig. 9 (E-plane). The "non-stick" properties of the PDMS substrate material and poor adhesion of the Duroid substrate created many of the non-ideal effects seen in both of these plots. Additional issues arose from the pressure-seal that created a lagging or leading effect.

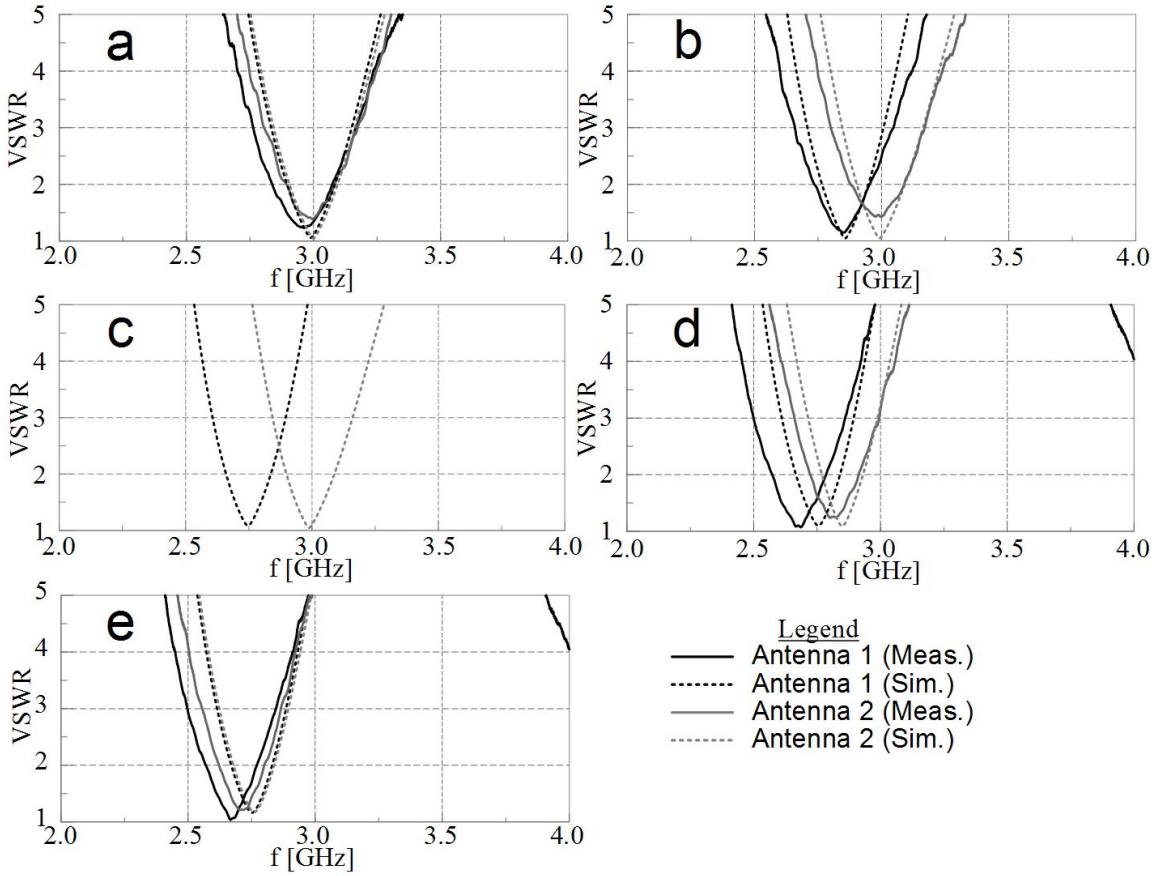

Fig. 10. Simulated (dashed) and measured (solid) VSWRs of each antenna in the H-plane array configuration; the letters *a-e* located in the upper left corner of each plot correspond to the dispersion locations shown in Fig. 8.

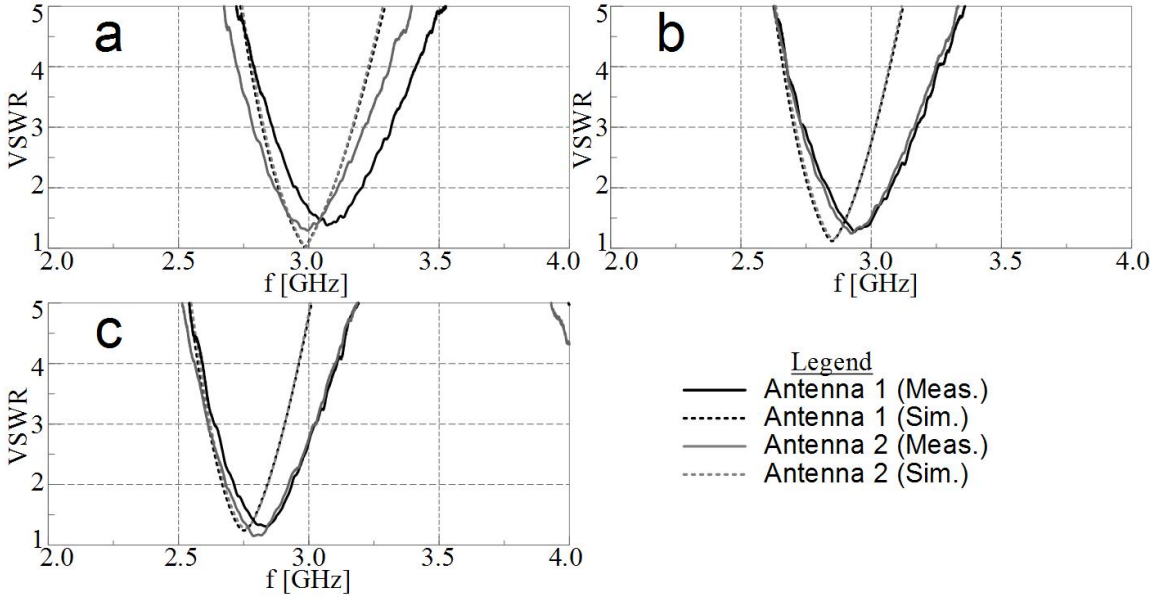

Fig. 11. Simulated (dashed) and measured (solid) VSWRs of each antenna in the E-plane array configuration; the letters *a-c* located in the upper left corner of each plot correspond to the dispersion locations shown in Fig. 9.

In these configurations, the H-plane array elements were reconfigured sequentially and the E-plane array elements were reconfigured simultaneously. A full analysis of these results will be included in the presentation of this material, but the effects from the blending of the miscible fluids as the material flowed through the arrays can be seen in these plots. This impacted the H-plane array more than the E-plane array due to the longer fluid path, and created a situation that resulted in the VSWR at positions 10*c* and 10*d* to be nearly identical (measured results were removed as a result of this to better show the simulated results).

Fig. 12 shows a summary of the simulated radiation patterns in the plane of beam-forming for both array configurations; the primary (xz) cut-plane and E_ϕ polarization in H-plane array (left) and (yz) cut-plane and E_θ polarization in the E-plane (right). All three dispersion locations *a-c* are shown for the E-plane configuration since a common frequency for beam-forming resulted from their simultanious reconfiguration. For the H-plane configuration, ony the locations *a* and *e* are shown since the antennas were reconfigured sequentially and therefore only shared two positions of the dispersion where this was possible. A full description of the radiation behavior will be provided in the presentation of this material, but several (somewhat predictable) effects can be seen from the data provided in Fig. 12. The most noticable property of these arrays is the decreasing beamwidth observed as the dispersion reconfigures the the antennas' matched impedance bandwidth lower in frequency. This is related back to the same effect that increase the coupling as the dispersion made its way through the array; namely, the effect of decreasing the electrical seperation of the elements and radiating edges of the antennas.

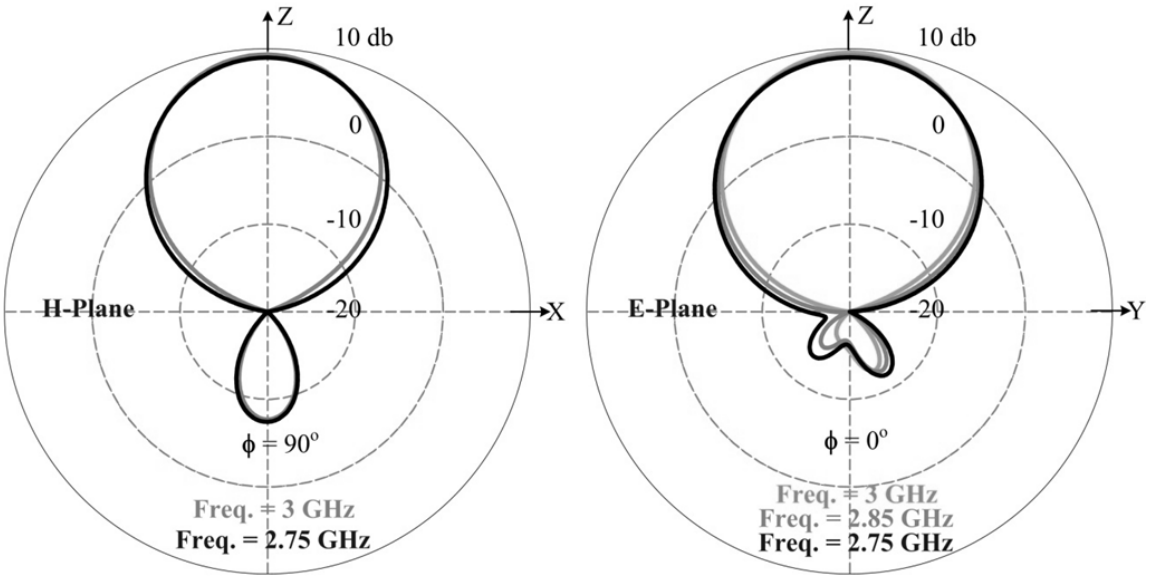

Fig. 12. Summary of radiation patterns for H-plane (left) and E-plane (right) array configurations shown in Figs. 8 and 9, respectivily.

6. Summary

This manuscript has provided a summary of the ongoing work related to the use of capillary-based antenna reconfiguration mechanisms (vascular networks) that were inspired by the biologically mechanisms of the cuttlefish. Specifically, this work discussed the displacement and/or flow of functionalized nanoparticles dispersions within the substrate of the microstrip patch antenna. The discussion began with a very brief recap on the use of the nanoparticle dispersions and demonstrated the impact of particle geometry on the mixing formulas used to approximate the effective medium properties of the dispersion. The analytical analysis that followed this examined the theoretical limits and behavior of a linearly polarized microstrip patch antenna with a dispersion-filled substrate-integrated capillary that is aligned with the antenna's H-plane. Several sets of design curves were generated for this. This single capillary system as then examined for its ability to compensate the effects of a sharp bend located at the center of the resonant length dimension, which was coincident with the H-plane and the embedded capillary system. The proof-of-concept design used the reconfigurable properties of this capillary mechanism to compensate the bending of a patch antenna up to 90º. Additional capillaries were then added and the array behavior using miscible fluids were then examined; the additional capillaries were also aligned with the H-plane and integrated into the substrate. The dispersion-filled capillaries were then utilized with arrays of flat (non-deformed) microstrip patch antennas to facilitate reconfiguration and the frequency agility of a single element into the behavior of two-element E-plane and H-plane arrays. The use of parallel (corporate) and series capillaries (vascular networks) networks, along with the effects from using miscible fluids as components in the nanoparticle dispersions were also discussed using the measured and simulated results of the two arrays.

7. Acknowledgements

Funding for this work was provided in part by the U. S. Air Force Office of Scientific Research (AFOSR) under grant # FA9550-08-1-0329 and in part by the U. S. National Science Foundation (NSF) under grant # ECCS-0846865.

8. References

[1] G. H. Huff, S. Goldberger, and S. A. Long, “The RF cuttlefish: Overview of biologically inspired concepts for reconfigurable antennas and smart skins” *in proc. 2008 Antenna Applicat. Symp.*, Monticello, IL, Sept. 2008, pp. 291-305.

[2] M. L. VanBlaricum, T. L. Larry, G. H. Huff, “A design approach for Reconfigurable RF surfaces and apertures,” *in proc. Soc. of Eng. Sci.: 45th Annu. Tech. Meeting*, Champaign, IL, Oct., 2008.

[3] G. H. Huff, “Electromagnetically functionalized colloidal dispersions and microfluidic reconfiguration mechanisms for phase-reconfigurable reflectarray elements,” *in proc. 2008 URSI Gen. Assy.*, Chicago, IL, Aug. 2008.

[4] Sean Goldberger and G. H. Huff, “Frequency reconfiguration of a microstrip patch antenna enabled by colloidal dispersions,” *in proc. 2008 URSI Nat. Radio Sci. Meeting*, Boulder, CO, Jan. 2008.

[5] J. McDonald and G. H. Huff, “Microfluidic mechanisms for reconfigurable dielectric resonator antennas,” *in proc. 2008 URSI Gen. Assy.*, Chicago, IL, Aug. 2008.

[6] D. C. Prieve, "Particle transport: Salt and migrate," *Nat. Mater.*, vol. 7, pp. 769-770, Oct. 2008.

[7] M. L. Y. Sin, Y. Shimabukuro, and P. K. Wong, “Hybrid electrokinetics for separation, mixing, and concentration of colloidal particles,” *Nanotech.*, vol. 20, , [on-line] http://stacks.iop.org/Nano/20/165701, April 2009.

[8] A. Rida and M. A. M. Gijs, “Manipulation of Self-Assembled Structures of Magnetic Beads for Microfluidic Mixing and Assaying,” *Anal. Chem.*, vol. 76, pp. 6239–6246, Nov. 2004.

[9] P. Takhistov, K. Duginova, and H.-C. Chang, "Electrokinetic mixing vortices due to electrolyte depletion at microchannel junctions," *J. Colloid Interface Sci.*, vol. 263, pp. 133-143, July 2003.

[10] P. Bahukudumbi, W. N. Everett, A. Beskok, M. A. Bevan, G. H. Huff, D. Lagoudas, and Z. Ounaies, “Colloidal microstructures, transport, and impedance properties within interfacial microelectrodes,” Appl. Physics Lett., vol. 90, 224102, May 2007.

[11] A. Sihvola, Electromagnetic Mixing Formulas and Applications. Padstow, Cornwall, TJ International, 1999.

[12] L. Jylhä, A. Sihvola, “Differential equation for the effective permittivity of random mixture of spheres,” *in proc. 2007 Int. URSI Comm. B – Electromag. Theory Symp. (EMTS 2007)*, Ottawa, ON, Canada, July 2007.

[13] D. Lagoudas, M. Bevan, G. H. Huff*, and Z. Ounaies, “Multi-scale modeling and characterization of electromagnetically tunable colloidal-based materials,” *in proc. Soc. of Eng. Sci.: 45th Annu. Tech. Meeting*, Champaign, IL, Oct. 13-15, 2008.
[14] J. C. Maxwell-Garnett, “Colours in metal glasses and metal films,” *Philos. Trans. R. Soc. London, Sect. A*, Vol. 3, 385–420, 1904.
[15] Y. T. Lo, D. Solomon, and W. Richards, “Theory and experiment on microstrip antennas,” *IEEE Trans. Ant. Propag.*, vol. 27, pp. 137-145, July 1979.
[16] J. R. Harrington, Time Harmonic Electromagnetic Fields. New York, NY: McGraw-Hill Book Company, 1961.
[17] G. H. Huff and S. A. Long, “Dynamic compensation mechanisms for deformable radiating structures based on colloidal dielectrics and fluidics,” *in proc. SPIE Smart Structures/NDE*, March, 2009.
[18] S. A. Long and G. H. Huff, “A substrate integrated fluidic compensation mechanism for deformable antennas,“ *in proc. 2009 NASA/ESA Conf. Adapt. Hardware Systems*, San Franscisco, CA, July 2009.
[19] V. K. Varadan and V. V. Varadan, "Design and development of smart skin conformal antenna with MEMS structural sensors and actuators," *Proc. SPIE*, Vol. 3046, p. 94-105.
[20] A. J. Lockyer, K. H. Alt, J. N. Kudva, and R. W. Kinslow, “Conformal load-bearing antenna structures (CLAS): initiative for multiple military and commercial applications,” *Proc. SPIE*, vol. 3046, June 1997, pp. 182-196.
[21] S. A. Long and G. H. Huff, “A study of microfluidic compensation mechanisms for deformable antennas,” *in proc. 2008 URSI Gen. Assy.*, Chicago, IL, Aug. 2008.
[22] Ansoft, HFSS© v9.1, Pittsburgh, PA 15219.
[23] S. Goldberger and G. H. Huff, “Frequency reconfiguration of a microstrip patch antenna enabled by colloidal dispersions,” *in proc. 2008 URSI Nat. Radio Sci. Meeting*, Boulder, CO, Jan. 2008.
[24] G. H. Huff, P. Bahukudumbi, W. N. Everett, A. Beskok, M. A. Bevan, D. Lagoudas, Z. Ounaies, “Microfluidic reconfiguration of antennas” *in proc. 2007 Antenna Applicat. Symp.*, Allerton Park, Monticello, IL, Sept. 2007, p. 241-258.
[25] S. Goldberger, F. Drummond, R. Anderson, J. Barrera, A. Bolon, S. Davis, J. Edelen, J. Marshall, C. Peters, D. Umana, and G. H. Huff, “Small array behavior of frequency reconfigurable antennas enabled by functionalized dispersions of colloidal materials,” *in proc. 2009 IEEE/URSI Int. Symp. Antennas and Propag.*, July, 2009.
[26] Dow Corning Corp., Sylgard© 184 Silicone Elastomer Kit, Midland, MI 48686.
[27] TPL, Inc., NanOxideTM HBS 1000 Barium Strontium Titanate Powder, Albuquerque, NM 87109.
[28] TPL, Inc., Nanosperse Surfactant, Albuquerque, NM 87109.

A Semiconductor Patch Antenna Built Upon the Depletion Region of a pn- or pin-Junction

Eduardo M. A. Oliveira, Angelo Puzella*, John McNeill, and Sergey N. Makarov

ECE Department, Worcester Polytechnic Institute, 100 Institute Rd.,

Worcester, MA 01609

*Raytheon Company, Sudbury, MA 01776

makarov@wpi.edu

Abstract: The present study introduces the concept of a semiconductor patch antenna (SPA) and estimates its efficiency. The antenna loss model is the classic Jackson's model valid for a generic patch antenna resonator that consists of a long dielectric (lossy) channel between two conductor (lossy) plates: the patch and the ground plane. To estimate the antenna channel height, we use an analytical approximation for the depletion layer width (the abrupt pn-junction). To estimate the conductor loss, we use the semi-empirical Drude model for the doped Si. To estimate the dielectric loss, we use carrier concentrations in the depletion region that are close to the intrinsic conductivity of an undoped or compensated Si.

The result of this study is in the following: at common doping concentrations the SPA efficiency is extremely low in the low GHz range (L to X-bands), due to a wide skin layer and a relatively narrow depletion layer with or without intrinsic Si. On the other hand, the efficiency very significantly increases in the mm-wave band and in a low THz band due to a much smaller skin layer depth.

Keywords: patch antennas, integrated antennas, 60 GHz band, THz antennas

1. SPA concept

We suggest to use the depletion region of a semiconductor pn-junction (Fig. 1) as a transmission line in the direction *along*, but not *across* the pn-junction (Fig. 2). The depletion region is free of charge carriers at zero and negative bias voltages, i.e. has a very low conductivity. At the same time, it has certain static depletion capacitance per unit length, much as the parallel-plate transmission line has the distributed static capacitance per unit length.

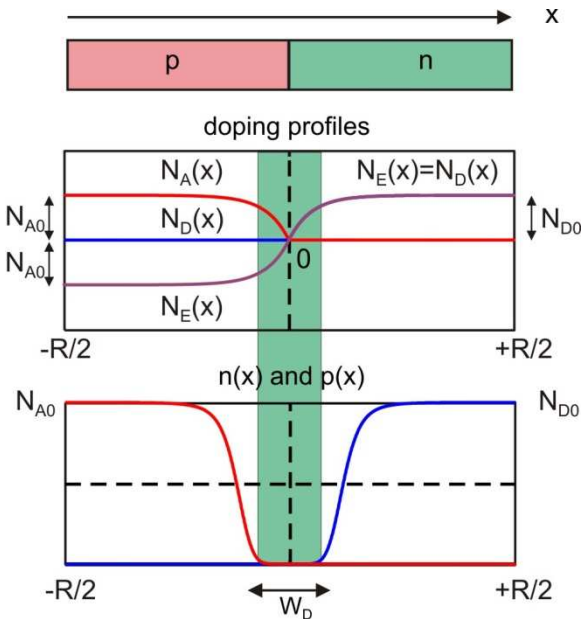

Fig. 1. Doping profiles and carrier concentration profiles through a typical Si pn-junction including the depletion region. A numerical solution for the symmetric Si pn-junction with exponential doping profiles, with doping concentrations $N_{D0} = N_{A0} = 10^{16}$ cm^{-3} and with the total length of $R =$ 2μm at zero bias voltage is given. The width of a metallurgical junction is $0.1\mu\text{m}$. The depletion region is marked by a rectangle.

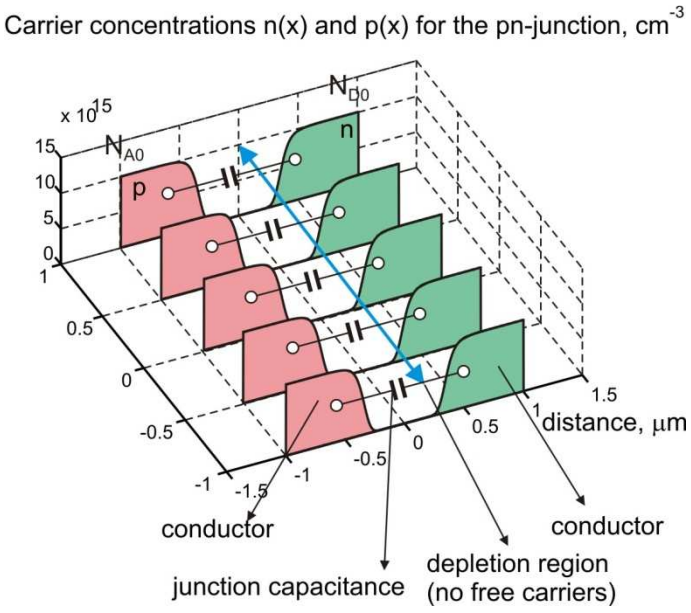

Fig. 2. The pn-junction as a potential transmission line in the direction *along* the junction (marked by an arrow). Carrier concentrations are shown. Note the scale for the width of the transmission line. A numerical solution for the symmetric Si pn-junction with exponential doping profiles, with $N_{D0} = N_{A0} = 10^{16}$ cm^{-3} and with the total length of $R =$ 2μm at zero bias voltage is given. The width of a metallurgical junction is $0.1\mu\text{m}$.

Thus, the pn-junction in the direction along the junction has two necessary ingredients of a transmission line: a lengthy carrier-free region between two high carrier-concentration zones (conductors), and an appreciable capacitance for this region per unit length - see Fig. 2. Note that static (immovable doping ions) charges also exist on that transmission line. This circumstance should not prevent the RF transmission line operation.

Once we have agreed that the pn junction may serve as a transmission line in its longitudinal direction, we could introduce a λ/2 open-open transmission line resonator - the patch antenna. Fig. 2* shows the concept. Compared to the metal transmission line resonator, the pn-junction has different carrier types (holes) in the p-side. However, the necessary RF charge distribution may still be achieved. The only difference is that the positive surface charge in the p-side is formed by excess hole concentration, whereas for metal it is formed by the lack of free electrons. Similarly, the negative charge is formed by the lack of holes. Widening the ground plane gives the required patch antenna pattern.

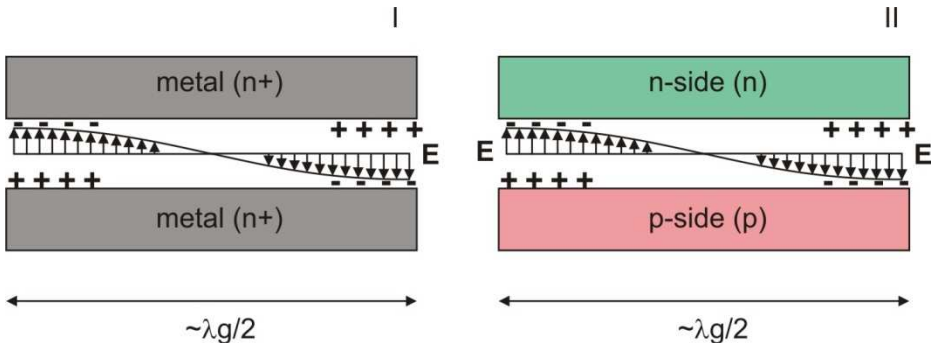

Fig. 2*. I - A λ/2 open-open transmission line resonator on the base of metal transmission line; II - the same resonator on the base of the wide pn-junction. Only the RF *E*-field is shown.

The concept of the semiconductor patch antenna shall be appealing for two reasons:

1. an ability to change the antenna height (depletion layer width) by simply varying the reverse-bias voltage and;
2. an ability to combine the antenna and the rectifying diode in one (at small positive bias voltages).

However, the stumbling stone with this concept appears to be the antenna efficiency. We will see that the efficiency limitations almost completely eliminate the first possibility, but still allow us to pursue the second one.

2. Efficiency of a generic patch antenna

Any patch antenna is a half-wave open-open quasi-TEM resonator with two supporting (imperfect) conductors (patch and metal ground plane) and a (lossy) dielectric filler. Its efficiency is to be estimated based on the general approach summarized in [1],[2]. The total patch antenna *Q*-factor is given by

$$\frac{1}{Q}=\frac{1}{Q_{sp}}+\frac{1}{Q_{sw}}+\frac{1}{Q_d}+\frac{1}{Q_c} \qquad (1)$$

where Q_{sp}, Q_{sw}, Q_d, Q_c are the space-wave, surface-wave, dielectric loss, and conductor loss *Q*-factors. When the surface-wave loss (loss into the outgoing surface waves) is assumed to be negligibly small or reduced using potentially well-known means [2] the antenna's radiation efficiency, *E*, is expressed in the form

$$E = \frac{\dfrac{1}{Q_{sp}}}{\dfrac{1}{Q_{sp}} + \dfrac{1}{Q_d} + \dfrac{1}{Q_c}} = \frac{Q}{Q_{sp}} \tag{2}$$

since every partial *Q*-factor is inversely proportional to the corresponding (radiated or dissipated) partial power, respectively. The partial *Q*- factors may be found by tracking energy radiated or dissipated in the half-wave resonator due to a specific loss mechanism per unit time.

We briefly recall those *Q*-factors. We consider a half-wave patch with the length $L \approx \lambda_0 /(2\sqrt{\varepsilon_r})$ where index 0 denotes the free-space wavelength and ε_r is the relative dielectric constant. The corresponding *Q*-factor of the radiated field [2] may be approximately written in the form

$$Q_{sp} \approx \frac{3}{32}\sqrt{\varepsilon_r}\,\frac{\lambda_0^2}{hW} \tag{3}$$

where *h* is the patch antenna (channel) height, and *W* is the channel width. The most important conductor loss *Q*-factor is expressed in terms of the skin layer depth, δ, [2]

$$Q_c \approx \frac{\eta_0}{2}\frac{k_0 h}{R_s^{av}}, \quad R_s = \frac{1}{\sigma\delta} \tag{4}$$

with R_s^{av} (Ω) being the average surface resistance of the patch and the ground plane, respectively, and σ (S/m) being the corresponding volume conductivity. In a good conductor, $\delta = \sqrt{\dfrac{2}{\omega\mu_0\sigma}}$. The general expression for the skin layer depth is given in Appendix A. The dielectric (channel) loss factor is given by

$$Q_d = \frac{1}{\tan\delta}, \quad \tan\delta = \frac{\sigma_i}{\omega\varepsilon_r\varepsilon_0} \tag{5}$$

where σ_i is the effective conductivity of the depletion layer (intrinsic Si). Thus, for the estimation of the semiconductor patch antenna efficiency we need to estimate

i. conductivities of the doped Si (both donor and acceptor doping) as a function of frequency and at different doping concentrations;
ii. loss tangent of the intrinsic (or compensated [3]) Si.

3. Depletion (or intrinsic) layer characterization

The free carrier concentration in the bulk of the depletion region of an unbiased pn-junction is close to the intrinsic carrier concentration. This fact can be observed using the direct numerical solution of Poisson equation for the unbiased pn-junction for arbitrary doping profiles - see Ref. [4]. Therefore, in order to characterize the dielectric loss in the depletion region, attenuation properties of the intrinsic (or compensated) Si are needed. The theoretically estimated attenuation constant, α, of intrinsic Si is very small above the absorption edge at $\lambda_0 \approx 1\mu m$ (below 300 THz) and is often ignored [5],[6]. For a low-loss dielectric material one has

$$\sigma = 2\alpha\sqrt{\frac{\varepsilon}{\mu}}, \quad \tan\delta = \frac{\sigma}{\omega\varepsilon} 2\alpha \frac{1}{\sqrt{\mu\varepsilon}\omega} = 2\alpha\frac{c}{\omega}, \quad c = c_0/\sqrt{\varepsilon_r} \tag{6}$$

On the other hand, Ref. [3] reports the attenuation constant values that in average do not exceed $\alpha \approx 6\text{cm}^{-1}$ from about DC to 21 THz. The experimental data of Ref. [3] from 1 to 21THz approximately follows the dependence

$$\alpha \approx 4.0\times10^{-14}\,\omega\,\text{cm}^{-1} \tag{7}$$

In view of Eq. (7) the loss tangent $\tan\delta$ in Eq. (6) becomes roughly independent of frequency and equal to 6.9×10^{-4}. This value will be used in what follows[1]. The refractive index (or phase speed $c = c_0/\sqrt{\varepsilon_r}$) does not change significantly with frequency [3].

4. Conductivities of doped Si

4. 1. Static conductivity approximation

The macroscopic conductivity of the doped semiconductor [S/cm] is given by the product of carrier mobility, carrier concentration, and the carrier charge,

$$\sigma_n = q\mu_n n, \quad \sigma_p = q\mu_p p \tag{8}$$

where μ_n, μ_p are the mobilities of electrons and holes in Si, [$\text{cm}^2/(\text{V}\cdot\text{s})$], n and p are the corresponding carrier concentrations [cm^{-3}] and q=1.60218×10^{-19} C is the electron's charge. The mobilities in Si decrease with increasing concentrations. At equilibrium (and at room temperature) one has [8]

[1] According to Ref. [3], higher values of loss tangent, on the order of 2×10^{-3}, may be expected in the GHz range. The estimates given below have been recalculated for this higher value of the loss tangent. Virtually no differences have been observed.

$$\mu_n = \frac{1318}{\left(1+\frac{N_D+N_A}{10^{17}}\right)^{0.85}} + 92, \quad \mu_p = \frac{420}{\left(1+\frac{N_D+N_A}{1.6\times10^{17}}\right)^{0.7}} + 50 \tag{9}$$

Here, N_D and N_A are the donor and acceptor concentrations [cm^{-3}]. Usually, one assumes equilibrium conditions and full ionization of dopant atoms, i.e. $n = N_D$, $p = N_A$. Eqs. (9) then yield the required conductivities in terms of the doping concentrations.

4. 2. Conductivities at 30 THz and higher

Ref. [5] suggests the following approximation for the attenuation constants [1/cm]

$$\alpha_n = 1.0\times10^{-18}\lambda_0^2 n, \quad \alpha_p = 2.7\times10^{-18}\lambda_0^2 p \tag{10}$$

that is obtained by fitting the experimental data. Here, *n* and *p* are the corresponding carrier concentrations [cm^{-3}], λ_0 is the free-space wavelength *in micrometers*. This approximation is valid in the frequency band from 30 to 75 THz or for $4\mu\text{m} \le \lambda_0 \le 10\mu\text{m}$ [5]. It is also valid for carrier concentrations from 1×10^{16} to 1×10^{19} cm^{-1}. In a good conductor [7],

$$\sigma_n = \frac{2\alpha_n^2}{\omega\mu}, \quad \sigma_p = \frac{2\alpha_p^2}{\omega\mu}, \tag{11}$$

We may again assume equilibrium conditions and full ionization of dopant atoms, i.e. $n = N_D$, $p = N_A$.

4. 3. Drude model at GHz and low THz frequencies

Neither of two models discussed above is applicable in the GHz and in the low THz range. Instead, we will use the simple semi-empirical classic Drude model described in Appendix A (Refs. [9]-[11]). The physical conductivity of either p- or n-side is given by

$$\sigma(\omega) = \frac{\sigma_{\text{DC}}}{1+(\omega\tau)^2} \tag{12}$$

Two parameters to find are the static conductivity σ_{DC}, and the scattering time (or average collision time) τ. The static conductivity is found from the measured data on doped Si wafers that are reported in the wafer specification. The conductivity is found simply by inverting the static resistivity ρ_{DC} [Ω cm] (measured with the four-probe method),

$$\sigma_{\text{DC}} = \frac{1}{\rho_{\text{DC}}} \tag{13}$$

Typical resistivity values for doped Si vary from 0.001 Ω cm (high doping) to 100 Ω cm (light doping), for either donor or acceptor doping.

Scattering times in doped Si (Phosphorus for *n*, Boron for *p*) depend on doping concentration or, which is the same, on the DC resistivity (13) itself. They are found by interpolation and/or extrapolation of the measured data from Refs. [9], [10] as described in Appendix A. After the conductivity has been calculated, we find the skin layer depth as described in Appendix A.

Finally, we need the relation between measured resistivities and expected doping concentrations N_D and N_A. They are found from Ref. [12] (Phosphorus/Boron doping) as described in Appendix B.

Thus, by knowing the resistivities from the wafer specifications, we restore

i. N_D and N_A ;
ii. dynamic conductivity $\sigma(\omega)$ on either side of the pn-junction;

Augmented with a reasonable assumption about doping profiles, this information is sufficient to find

i. the width of the depletion region or the channel height and;
ii. the skin layer depth.

When the skin layer depth is much less than the channel height, the patch antenna so constructed may be shown to have a reasonable efficiency. Otherwise, the patch antenna becomes too lossy. The channel (depletion region) is unable to confine the resonating quasi-TEM wave and the patch antenna cavity is no longer a true resonator.

5. Antenna efficiency - plain pn-junction

The static depletion layer width, *h*, of the pn junction with abrupt doping profiles (full ionization) is given by [6]

$$W = \sqrt{\frac{2\varepsilon}{q}\frac{(N_{A0}+N_{D0})}{N_{A0}N_{D0}}(\varphi_{bi}-V)} \tag{14}$$

where

$$\varphi_{bi} = V_T \ln\left(\frac{N_{A0}N_{D0}}{n_i^2}\right) \tag{15}$$

is the built-in voltage and *V* is the bias voltage. ε is the dielectric constant of intrinsic Si. Eq. (14) for the depletion layer width and Eq. (A5) for the skin layer depth have been programmed in a simple MATLAB script [13]. The script accepts the input resistivities of a pn Si wafer and outputs the depletion layer width and the skin layer depth; the latter is plotted as a function of frequency. The result is shown in Fig. 3 for three different reverse-bias voltages: *V* = 0V, -10V, and -1000V. The thin solid curve is the skin layer

depth in the p-side, the thin dashed curve is the skin layer depth in the n-side. The thick line is the static width of the depletion layer; the width increases with increasing the reverse bias voltage. The results in Fig. 3 a) to e) are given for five representative values of the resistivity:

$$\rho_{DC} = 0.001, 0.01, 0.1, 1, \text{ and } 10 \ [\Omega \text{ cm}] \quad (16)$$

which essentially cover the available resistivity variations. The corresponding doping concentrations are listed on top of each graph. One can see that, irrespective of the values of doping concentration and applied bias voltage, the depletion layer width never reaches the skin layer depth. In other words, the skin layer depth is too large compared to the width of the depletion region. This means that the patch antenna concept on the base of a pure pn-junction is not feasible. The corresponding antenna efficiency (not given in Fig. 3) has been calculated; it's upper limit for different cases in Fig. 3 does not exceed 1.0%.

6. Antenna efficiency - pin-junction

A straightforward way to extend the channel width is to either use the pin-junction instead of the pn-junction, or a separating buried oxide (SiO_2) layer between p-and n-doped regions. The second case is less interesting from the practical point of view since the ability to control the channel is lost.

The pin-junction case is somewhat more flexible. The typical pn-junction includes a layer of intrinsic (or compensated) Si between p- and n-doped regions. The built-in voltage is again given by Eq. (15). When the intrinsic layer is thick enough, and the doping concentrations are high enough, the particular value of the negative bias voltage has little influence on the width of the depletion region, which now includes the i-region, and two small carrier-free regions on either side of the pin-junction. This is in contrast to the pn-junction where the applied bias voltage largely influences the width of the depletion region.

As an example, Fig. 4 shows the carrier profiles (numerical simulation) and the associated static electric parameters for a wide pin-junction with the following parameters;

i. N_D and N_A of 4×10^{16} cm^{-3} ; $\varphi_{bi} = 0.79$V
ii. i-region width of 200 μm;
iii. doping profiles of 30 μm in width (given by a raised cosine).

Approximation of the electric field region described in Ref. [4] was used to model the pin-junction. Fig. 4a shows the corresponding doping profiles, Fig.4b - the free-carrier profiles, Fig. 4c gives the electric potential distribution, Figs. 4d, e show charge density and the electric field distribution, respectively. The applied bias voltage is -1000V.

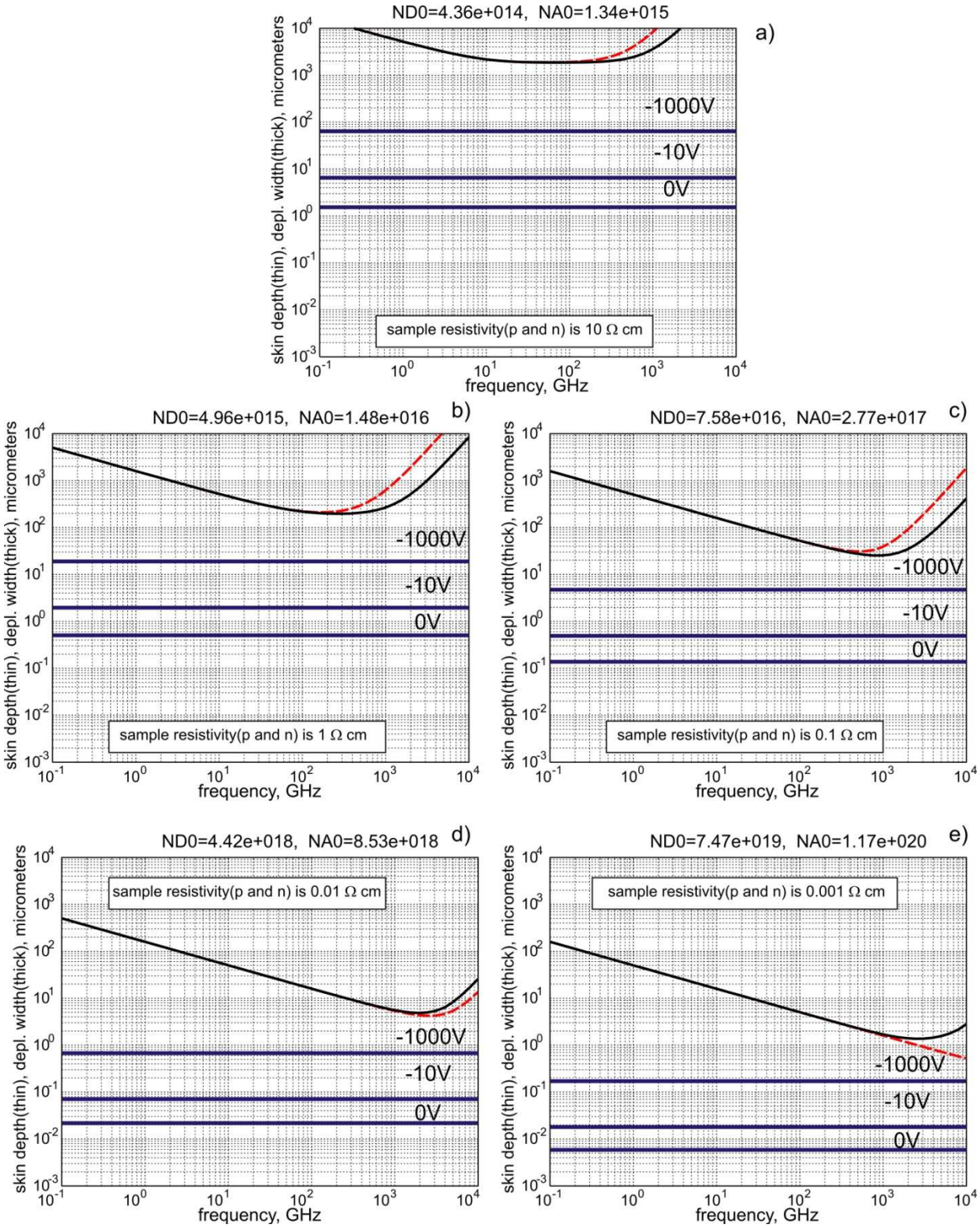

Fig. 3. Depletion layer width (thick solid lines) versus skin layer depth (thin curves: dashed – p, solid – n) at different doping concentrations and at different bias voltages.

The (large) reverse-bias voltage slightly widens the depletion region (the i-region) as seen in Fig. 4b. For larger terminal doping concentrations, this effect becomes less profound, but it increases for smaller doping concentrations. The carrier concentration in the entire depletion region is close to the intrinsic concentration, $n_i \approx 1\times10^{10}$ cm^{-3}. The solution given in Fig. 4 is accurate both qualitatively and quantitatively.

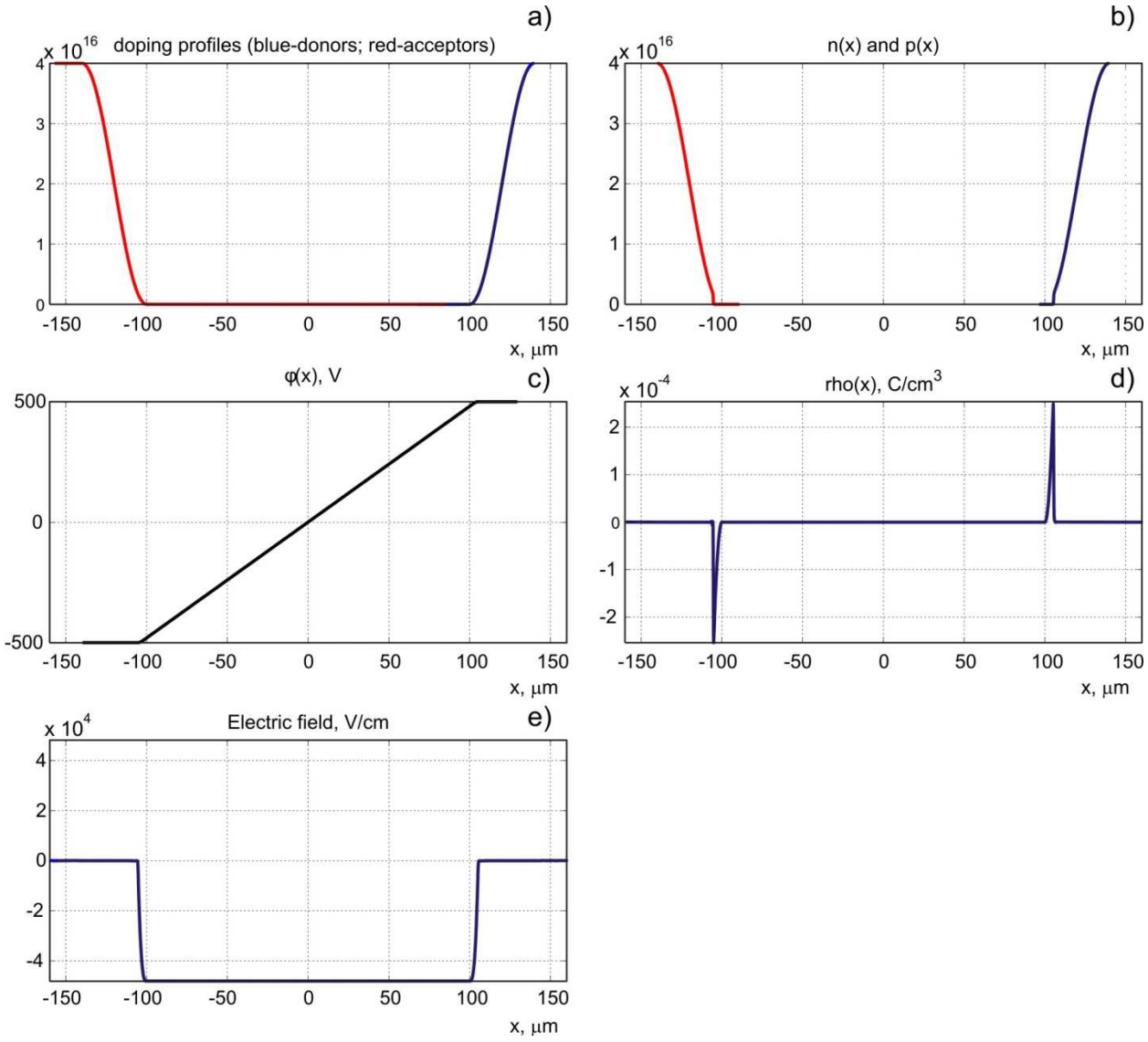

Fig. 4. a) - Doping profiles; b) - free carrier concentrations; c) - electric potential, d) - charge density, and e) - electric field for the pin junction with $N_D = N_A = 4\times10^{16}$ cm^{-3}, and the i-layer width of 200 μm. The p-side is on the left, the n-side is on the right. The bias voltage is -1000V.

However, a positive bias voltage leads to a flood of free carriers into the intrinsic region so that this region becomes conducting, quite similar to the depletion region of the pn-junction. As an example, Fig. 5 shows the same pin junction profiles as in Fig. 4, but for the forward bias voltage of +0.6V, which is slightly less than the built-in voltage of 0.79V. One can see very significant carrier concentrations in the intrinsic region, both of

them are equal to 1.0×10^{15} cm^{-3}. The solution in Fig. 5 ignores carrier recombination in the depletion region and is valid only qualitatively.

The larger the width of the intrinsic Si layer is the better antenna efficiencies can be obtained. Si power pin diodes may have a large width of the intrinsic or compensated Si. As a base example we consider an experimental wide pin-junction from Ref. [14] that has

i. the width of the intrinsic (strictly speaking, n$^-$) region h of 370μm;
ii. N_D and N_A of 4×10^{19} cm^{-3} (resistivities of 0.0018 and 0.0028 Ω·cm, respectively);
iii. total diode area of approximately 10 mm^2.

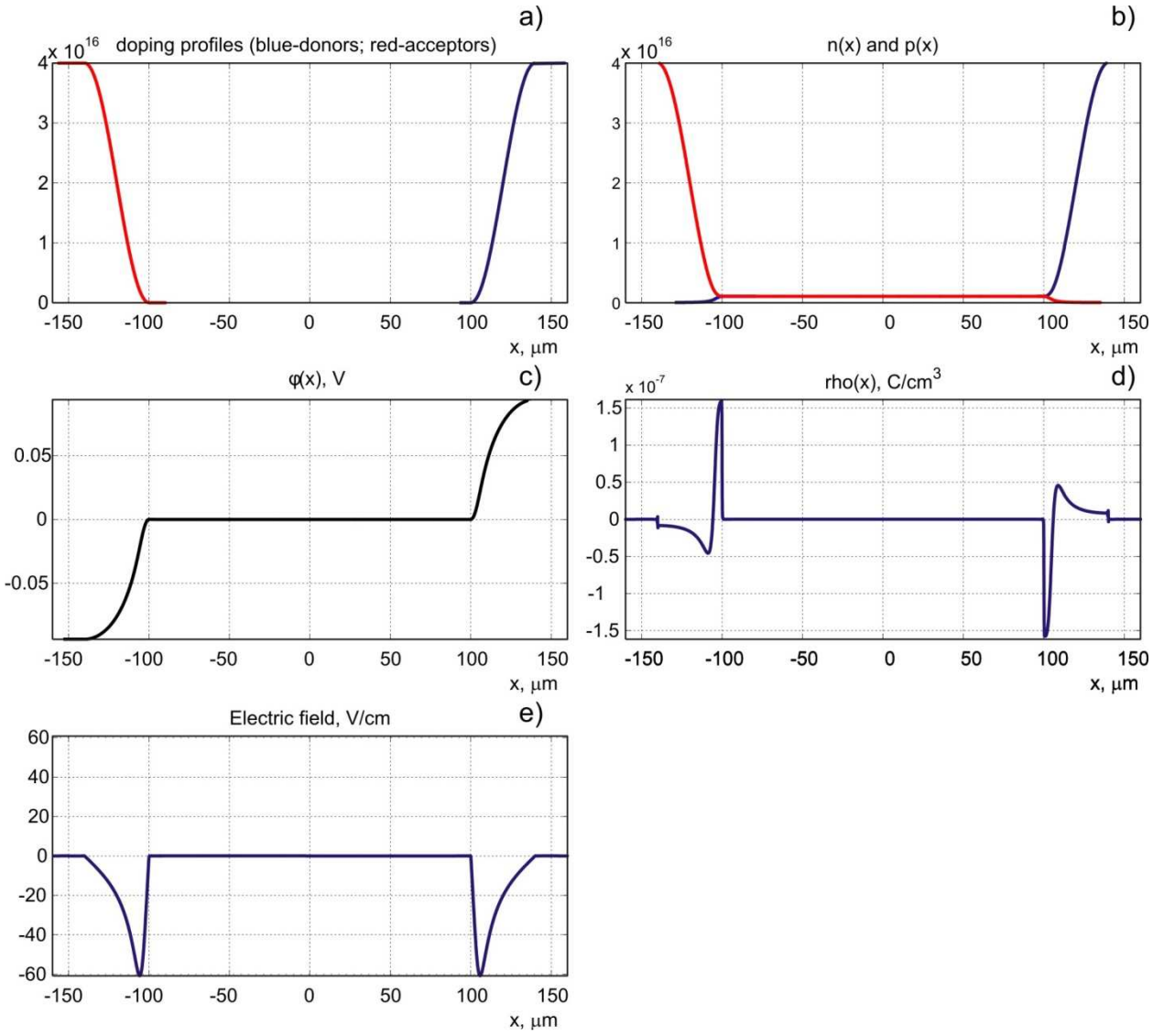

Fig. 5. The same data as in Fig. 4, but for the forward-bias voltage of +0.6V.

Fig. 6 illustrates the skin layer width versus the channel width for the present case and the resulting antenna efficiency. The efficiency was calculated for the square patch ($W = L$). The antenna height is exactly the width of the i-Si (or weakly-doped Si) region (370μm). The minimum antenna thickness in Fig. 6c is 370μm plus twice the skin layer width from either side. The calculations are assembled in a MATLAB script [13]. From Fig. 6 one can see that the present pin-junction may serve as a patch antenna starting with frequencies $f \geq 50\,\text{GHz}$ (the efficiency is greater than 50%). At 50 GHz, the minimum antenna thickness is 0.4 mm. To move down to lower frequencies (e.g. to the X-band), the antenna thickness should be larger. It also seems from Fig. 6 that the Si pin-junction best serves in the 60 GHz band and in the low-THz range.

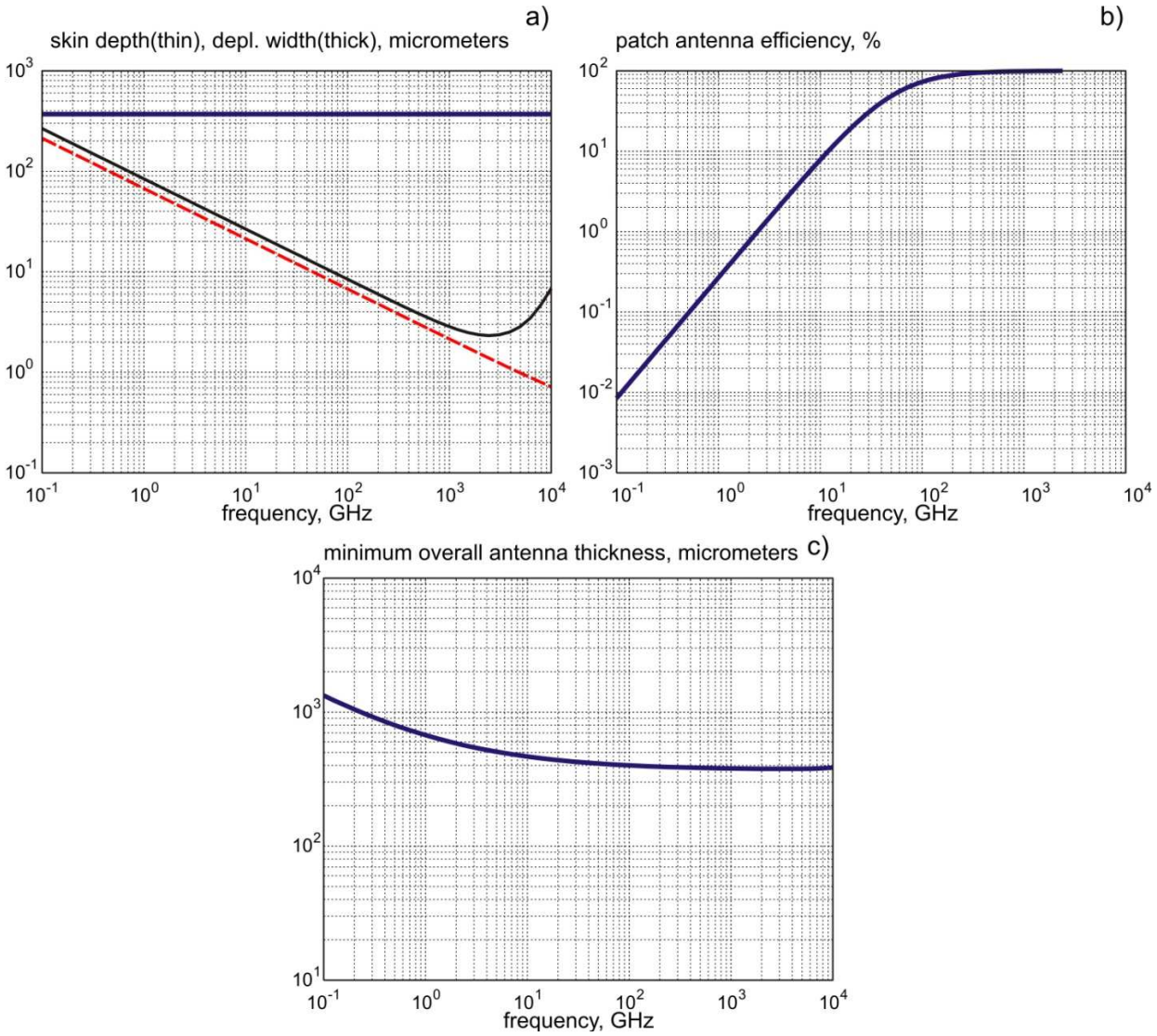

Fig. 6. Patch antenna efficiency on the base of a pin-junction from Ref. [14]. a)- Depletion layer width (thick solid line) versus skin layer depth (thin curves: dashed – p, solid – n); b) – patch antenna efficiency found from Eq. (2) (the square patch); c) – minimum allowable antenna total thickness (channel width plus twice the skin layer width for each side); all parameters are functions of frequency.

7. A pn-junction with a SiO_2 buried oxide layer

The material of this section is mostly intended to show how "not to build" the semiconductor patch antenna. Before the present estimates have been done and understood, we had ordered a series of 100mm Si wafers from Silicon Quest International, Inc. The wafers have the parameters listed in Table 1. We cut a wafer into a number of rectangular patches, 20×13mm in size, as shown in Fig. 7. The expected resonant frequency of one such patch is

$$L = \frac{0.49 c_0}{\sqrt{\varepsilon_r}\, f_{\text{res}}} = 2.13 \text{ GHz} \qquad (17)$$

Table 1 Initial Si test wafers <1-0-0> for the semiconductor patch antenna with a buried SiO_2 layer. The carrier concentration is estimated according to Appendix B.

Layer/Thickness	Doping	Carrier concentration, $1/cm^3$
N 20±0.5μm	Sb (Antimony) 0.005 - 0.020 OHM-CM	~4×10^{18}
Buried oxide, 0.25μm±5%	SiO_2	None
P 500±15μm	B (Boron) 0.005 - 0.020 OHM-CM	~1×10^{19}

Fig. 7. A Si wafer cut into single die patches 20×13mm in size.

The built-in voltage of the junction is approximately 1.0 V, the (effective) depletion layer width is about 0.022μm+0.25μm. It can be seen that the antenna parameters hardly satisfy the necessary requirements. First, the thickness of the *n*-layer is certainly smaller than the skin layer depth (on the order of 100μm) at the expected resonant frequency of 2.13 GHz. Furthermore, the channel width is too small to expect any significant efficiency according to Fig. 3. Therefore, there is no wonder that the present antennas have ultimately not been working when supported by a two-electrode flexible metal band feeding holder, which is soldered to the SMA male connector as shown in Fig. 8. By

varying the antenna position within the holder we are able to achieve the best match to 50 Ohm, but we are still unable to improve the antenna efficiency.

Fig. 8. Antenna support by two feeding electrodes.

However, for one of the patch samples, we have yet obtained a clean S_{11} resonance at 2.21 GHz as shown in Fig. 9. This value deviates by 4% from the theoretical prediction. The resonance was highly repetitive and was established for four consecutive measurements with the resonant frequency deviation of about 1%. The reason for such a behavior of this particular sample is not quite clear. One possible reason is the deviation of wafer parameters for the specified ones.

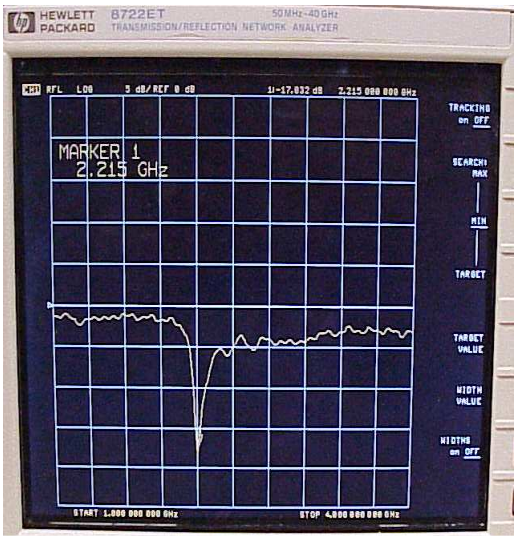

Fig. 9. A "strange" wafer sample. The S_{11} data is given for 5dB/200 MHz per division; the frequency span is from 2 GHz to 4 GHz.

8. Discussion and conclusions

Out of three considered candidates - the pn-junction patch antenna, the pin-junction patch antenna, and the semiconductor patch antenna with the buried isolator (SiO_2) - the pin-junction setup seems to be most promising. Realistically, it may possess an acceptable antenna efficiency at frequencies above 50 GHz or so. The semiconductor antenna is perhaps best suitable for the 60 GHz band and the low-THz band.

The pin-junction patch antenna is simultaneously one wide pin diode. In other words, the semiconductor antenna potentially combines the radiating element and the rectifying diode element in one. This circumstance might be important from the viewpoint of a coupling loss problem arising between the antenna and the RF integrated circuit at high GHz and low THz frequencies. This question is currently under investigation.

Apart from this, the concept of the semiconductor patch antenna may perhaps be useful to mitigate the effect of surface metal roughness, which appears significant above 10 GHz [15],[16] and at THz frequencies [17].

Other antennas that are related to the subject of the present research include:

1. At GHz frequencies, conventional metal patches and strips with discrete switching diodes are suggested in the literature; see, for example, Refs. [18]-[20]. In these antennas, discrete semiconductor diodes are used to connect two (or more) distinct parts of the same metal antenna in order to change its resonant frequency electronically.
2. At mm-wave frequencies, integrated on-chip metal antennas include deposited metal spirals [21]-[24] and tapered-slot antennas with long metal wings [25].
3. In the THz frequency range, the conventional approach is also a metal antenna [26]-[32]. It is predominantly a long-wire traveling-wave antenna made out of tungsten, with typical diameters in the range of 10-100 μm, and with relatively large lengths varying from 4λ to 100λ. The well-known problem with metal antennas in the THz band is weak coupling to the on-chip mixer or rectifier [29]-[32].
4. Quite recently dielectric resonator antennas on Si have been proposed at 60 GHz and realized at 7.5 GHz [33]. The semiconductor is used as the dielectric material for the DRA. By modifying its loss tangent optically it is possible to tune the (lossy) bandwidth.

We note that none of the configurations listed above uses the SPA concept. On the other hand, the SPA resonator cavity is somewhat similar to the traveling-wave region of optical laser pn-junction diodes.

References

[1]. D. R. Jackson and N. G. Alexopoulos, "Simple approximate formulas for input resistance, bandwidth, and efficiency of a resonant rectangular patch," *IEEE Trans. Antennas Propagation*, vol. 39, pp. 407-410, March 1991.

[2]. D. R. Jackson, *Microstrip Antennas*, in Antenna Engineering Handbook, 4th ed., John L. Volakis, Ed., Ch 7., McGraw Hill, New York, 2007.

[3]. M. N. Afsar, H. Chi, and X. Li, "Millimeter wave complex refractive index, complex dielectric permittivity and loss tangent of high purity and compensated Si," *Conf. on Precision EM Meas.* CPEM'90, Ottawa, June 1990, pp. 238-239.
[4]. B. R. Chawla and H. K. Gummel, "Transition region capacitance of diffused p-n junctions," *IEEE Trans. on Electron Devices*, vol. ED-18, no. 3, March 1971, pp. 178-195.
[5]. D.K. Schroder, R. N. Thomas, and J. C. Swartz, "Free carrier absorption in silicon," *IEEE Journal of Solid-State Circuits*, vol. 13, no. 1, Feb. 1978, pp. 180-187.
[6]. M. Sze and K. K. Ng, *Physics of Semiconductor Devices*, Wiley, New York, 2007, 3rd edition.
[7]. C. A. Balanis, *Advanced Engineering Electromagnetics*, Wiley, New York, 1989.
[8]. C. C. Hu, *Modern Semiconductor Devices for Integrated Circuits*, Prentice Hall, Upper Saddle River, NJ, 2010.
[9]. M. van Exter and D. Grischkowsky, "Optical and electronic properties of doped silicon from 0.1 to 2 THz," *Appl. Phys. Lett.*, vol. 56, no. 17, 23rd April 1990, pp. 1694-1696.
[10]. Tae-In Jeon and D. Grischkowsky, "Nature of conduction in doped silicon," *Physical Review Lett.*, vol. 78, no 6, Feb. 10th, 1997, pp. 1106-1109.
[11]. Tae-In Jeon and D. Grischkowsky, "Characterization of optically dense, doped semiconductors by reflection THz time domain spectroscopy," *Appl. Phys. Lett.*, vol. 72, no. 23, 8th June 1998, pp. 3032-3034.
[12]. *Properties of Crystalline Silicon*, Robert Hull, ed., Emis Series, INSPEC, 1999, pp. 413-416.
[13]. http://ece.wpi.edu/ant/04Allerton09_2/
[14]. M. Isberg, P. Jonsson, N. Keskitalo, F. Masszi, and H. Bleicher, "Physical models in device simulation of SI power pin diodes for optimal fitting of simulation results to measured data," *Compel* (*Int. Journal for Computation and Mathematics in Electrical and Electronic Engineering*), vol. 16, no. 3, 1997, pp. 144-156.
[15]. Gu, X., Tsang, L., and Braunisch, H., "Estimation of roughness-induced power absorption from measured surface profile data," *IEEE Microw. Wireless Compon. Lett.*, Vol. 17, No. 7 (2007), pp. 486–488.
[16]. Tsang, L., Gu, X., and Braunisch, H., "Effects of random rough surface on absorption by conductors at microwave frequencies," *IEEE Microw. Wireless Compon. Lett.*, Vol. 16, No. 4 (2006), pp. 221–223.
[17]. N. Laman and D. Grischkowsky, " Missing Conductivity in the THz Skin-Depth Layer of Metals," *Lasers and Electro-Optics, 2007*. CLEO 2007, 6-11 May 2007, pp. 1 - 2.
[18]. D. Piazza, N. J. Kirsch, A. Forenza, R. W. Heath, and K. R. Dandekar, "Design and evaluation of a reconfigurable antenna array for MIMO systems," *IEEE Trans. Antennas Propagation*, vol. 56, no. 3, March 2008, pp. 869-881.
[19]. L. Ming-Iu and J. Shyh-Kang, "Compact pattern reconfigurable antenna array based on L-shaped slots and PIN diodes for adaptive MIMO systems," 2008 *IEEE Antennas and Propagation Society International Symposium*, San Diego, CA, July 2008, AP-S 2008, 4p.

[20]. S. Gruszczynski, K. Wincza, J. Borgosz, J. G. Hallatt, and I. Aldred, "Reconfigurable antenna for 24 GHz Doppler sensor applications with low-cost pin diode switches," 2007 *IEEE Antennas and Propagation Society International Symposium*, Honolulu, Hawaii, June 2007, pp. 5829-5832.

[21]. R. M. Emrick and J. L. Volakis, "On chip spatial power combining for short range millimeter-wave systems," 2008 *IEEE Antennas and Propagation Society International Symposium*, San Diego, CA, July 2008, APS.2008.4618919. 4p.

[22]. R. M. Emrick and J. L. Volakis, "Inductively loaded millimeter-wave spiral array on silicon," 2007 *IEEE Antennas and Propagation Society International Symposium*, Honolulu, Hawaii, June 2007, pp. 4389-4392.

[23]. R. M. Emrick and J. L. Volakis, "Antenna requirements for short range high speed wireless systems operating at millimeter-wave frequencies," 2006 *IEEE MTT-S International Sym.*, San Francisco, CA, June 2006, pp. 974-977.

[24]. H. Abe, M. Sato, K. Itoi, S. Kawai, T. Tanaka, T. Hayashi, Y. Saitoh, and T. Ito, "Microwave operation of on-chip antenna embedded in WL-CSP [RFID applications]," IWAT 2005. *IEEE International Workshop on Antenna Technology: Small Antennas and Novel Metamaterials*, March 2005, pp. 147 - 150.

[25]. Lu Yang, N. Ito, C. W. Domier, N. C. Luhmann, and A. Mase, "18–40-GHz Beam-shaping/steering phased antenna array system using Fermi antenna," *IEEE Trans. Microwave Theory Techniques*, vol. 56, no. 4, April 2008, pp. 767-773.

[26]. G. Gallot, S. P. Jamison, R. W. McGowan, and D. Grischkowsky, "Terahertz waveguides," *J. Opt. Soc. Am. B*, vol. 17, no. 5, May 2000, pp. 851-863.

[27]. Tae-In Jeon, J. Zhang, and D. Grischkowsky, "THz Sommerfeld wave propagation on a single metal wire," *Appl. Phys. Lett.*, vol. 86, no. 16, April 2005, id 161904.

[28]. K. Mizuno, R. Kuwahara, and S. Ono, "Sub-millimeter detection using a Schottky diode with a long-wire antenna," *Appl. Phys. Lett.*, vol. 26, no. 11, June 1975, pp. 605-607.

[29]. H. Kraeutle, E. Sauter, and G. V. Schultz, "Properties of a sub-millimetre mixer in an open-structure configuration," *Infrared Physics*, vol. 18, 1978, pp. 705-712.

[30]. K. M. Evenson, M. Inguscio, and D. A. Jennings, "Point contact diode at laser frequencies," *J. Appl. Phys.*, vol. 57(3), Feb. 1985, pp. 956-960.

[31]. Hua Cao and Ajay Nahata, "Coupling of terahertz pulses onto a single metal wire waveguide using milled grooves," *Optics Express*, vol. 13, no. 18, Sep. 2005, pp. 7028-7034.

[32]. J. A. Deibel, K. Wang, M. D. Escarra, and D. M. Mittleman, "Enhanced coupling of terahertz radiation to cylindrical wire waveguides," *Optics Express*, vol. 14, no. 1, Jan. 2006, pp. 279-290.

[33]. A. Ayazi, A Motafakker-Fard, and B. Jalali, "Optically tunable Si RF antenna," *21st Annual Meeting of the IEEE Lasers and Electro-Optics Society*, Nov. 2008. LEOS 2008, pp. 83-84.

Appendix A. Drude conduction model and skin depth for doped Si

The Maxwell wave equation in terms of phasor **E** (equation for **H** has the same form) and assuming time dependence $e^{j\omega t}$ has the form

$$\nabla^2\mathbf{E} = j\omega\mu\sigma\mathbf{E} - \omega^2\mu\varepsilon\mathbf{E} = \gamma^2\mathbf{E}, \qquad \gamma^2 = j\omega\mu\sigma - \omega^2\mu\varepsilon \tag{A1}$$

The Drude model assumes complex conductivity in Eq. (A1) of the type

$$\sigma = \frac{\sigma_{\mathrm{DC}}}{1 + j\omega\tau} \tag{A2}$$

where τ (sec) is the average collision time (or the scattering time) of free charge carriers, and $\sigma_{\mathrm{DC}} = 1/\rho_{\mathrm{DC}}$ is the DC conductivity of the doped Si (S/cm). The DC resistivity ρ_{DC} (Ω·cm) is reported in wafer datasheets.

Substitution of Eq. (A2) into Eq. (A1) yields

$$\gamma^2 = j\omega\mu\frac{\sigma_{\mathrm{DC}}}{1 + j\omega\tau} - \omega^2\mu\varepsilon = j\omega\mu\left[\frac{\sigma_{\mathrm{DC}}}{1 + (\omega\tau)^2}\right] - \omega^2\mu\left[\varepsilon - \frac{\tau\sigma_{\mathrm{DC}}}{1 + (\omega\tau)^2}\right] \tag{A3}$$

Comparing Eq. (A1) and Eq. (A3) we define the frequency-depending conductivity $\sigma(\omega)$ and the frequency-dependent dielectric constant $\varepsilon(\omega)$,

$$\sigma(\omega) = \frac{\sigma_{\mathrm{DC}}}{1 + (\omega\tau)^2}, \quad \varepsilon(\omega) = \left[\varepsilon - \frac{\tau\sigma_{\mathrm{DC}}}{1 + (\omega\tau)^2}\right] \tag{A4}$$

so that the propagation constant γ (Np/m) in Eq. (A3) again has the same form as in Eq. (A1). Clearly, $\sigma(\omega)$ decreases with frequency; $\varepsilon(\omega)$, however, slightly increases.

The rest of the microwave relations are then written in terms of $\sigma(\omega)$, $\varepsilon(\omega)$ instead of σ and ε. In particular, the skin depth is given by [7]

$$\delta = \text{skin depth} = \frac{1}{\alpha} = \frac{1}{\omega\sqrt{\mu\varepsilon(\omega)}\left(\frac{1}{2}\left[\sqrt{1 + \left(\sigma(\omega)/\omega\varepsilon(\omega)\right)^2} - 1\right]\right)^{1/2}} \tag{A5}$$

Alternatively, in terms of the complex dielectric constant, $\varepsilon(\omega) = \varepsilon'(\omega) - j\varepsilon''(\omega)$, one has

$$\varepsilon''(\omega) = \frac{\sigma(\omega)}{\omega} \tag{A6}$$

The scattering times are functions of doping concentration, or functions of the DC resistivity of a Si sample. They are estimated using the experimental data of [9],[10]. The results are given in Table A1.

Table A1. Scattering times in doped Si (Phosphorus, Boron) as a function of DC resistivity [9], [10].

n-type ρ_{DC} (Ω·cm)	n-type $\tau \times 10^{-13}$ sec	p-type ρ_{DC} (Ω·cm)	p-type $\tau \times 10^{-13}$ sec
8.15	2.95	9.61	1.54
1.15	2.49	0.92	1.05
0.21	1.90	0.17	0.80

Fig. A1 shows interpolation and extrapolation of the data from Table A1 using a cubic interpolation in MATLAB over a wider range of sample resistivities. The interpolation/extrapolation results on scattering time from Fig. A1 have been used in the main text.

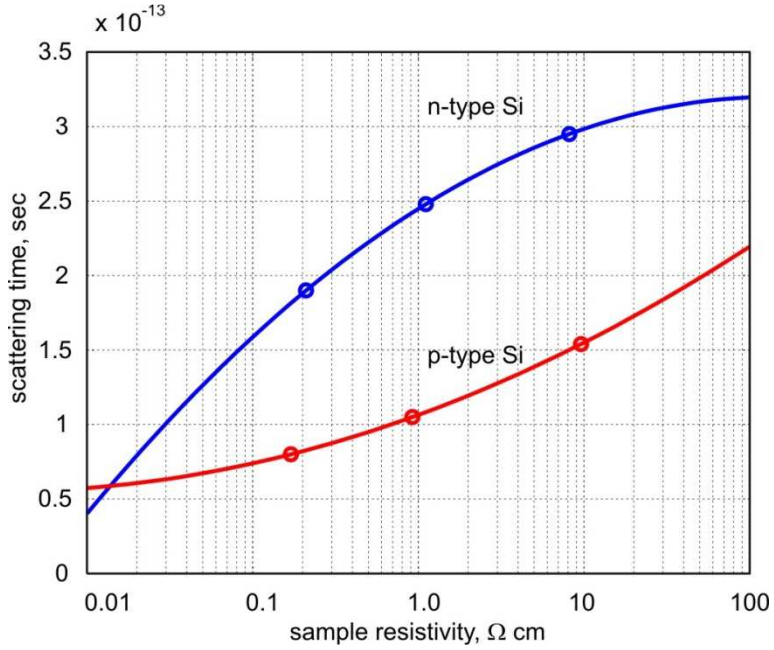

Fig. A1. Interpolation/extrapolation data on the scattering times for doped Si at different DC resistivities of a doped Si sample.

Appendix B. Resistivities versus doping concentrations (Si)

The data from Ref. [12] (Table A2 on p. 414) is interpolated. Donor doping is Phosphorus, acceptor doping is Boron. All resistivities (labeled as nres and pres) are in Ωcm, doping concentration (ND) is in cm^{-3} .

nres(1) = 1.60e-4;
nres(2) = 7.70e-4;
nres(3) = 5.78e-3;
nres(4) = 2.36e-2;
nres(5) = 8.38e-2;
nres(6) = 5.23e-1;
nres(7) = 4.48e+0;
nres(8) = 4.29e+1;
nres(9) = 4.30e+2;
nres(10)= 4.30e+3;

pres(1) = 1.30e-4;
pres(2) = 1.17e-3;
pres(3) = 8.87e-3;
pres(4) = 4.35e-2;
pres(5) = 2.02e-1;
pres(6) = 1.44e+0;
pres(7) = 1.33e+1;
pres(8) = 1.31e+2;
pres(9) = 1.30e+3;
pres(10)= 1.30e+4;

ND(1) = 1e+21;
ND(2) = 1e+20;
ND(3) = 1e+19;
ND(4) = 1e+18;
ND(5) = 1e+17;
ND(6) = 1e+16;
ND(7) = 1e+15;
ND(8) = 1e+14;
ND(9) = 1e+13;
ND(10)= 1e+12;

PHASE CENTER STABILITY OF PLANAR SPIRAL ANTENNAS

Matthew J. Radway[1], Thomas P. Cencich[2], and Dejan S. Filipović[1]
[1]University of Colorado, Boulder, CO 80309-0425
[2]Lockheed Martin Space Systems Company, Littleton, CO 80125

Abstract: Planar spiral antennas are excellent prime-focus reflector feeds for certain applications due in part to the frequency stability of their beamwidth, phase center, and axial ratio. Phase center is a particularly important parameter, but one that is often neglected in the available literature on spiral antennas. In the 1960s and 1970s various studies of spiral antenna phase center were reported, but these studies were often narrow in scope. For instance, the numerical models often neglected any possible contribution from the arm termination or cavity backing, and measurements relied on limited information from principal-plane cuts. Today, commercial numerical antenna analysis tools allow the consideration of additional effects in the model, as well as the output of dense pattern data. This pattern data can be used to gain an improved understanding of phase center. This work studies the effects that field-of-view, mode of excitation, number of arms, arm termination, and reflective cavity backing have on the phase center and its associated error of the planar spiral antenna. An algorithm that calculates a unique three-dimensional phase center position is discussed and used to account for possible modeformer amplitude and phase imperfections.

1 Introduction

Soon after their introduction, planar spiral antennas were recognized for their usefulness as broadband feeds for prime-focus reflector antennas. Cheo, Rumsey, and Welch [1] theoretically analyzed the spiral and discovered that for small growth rates the constant phase surface is nearly spherical in shape, and therefore the concept of phase center is well-defined for the planar spiral. Lantz [2] noted that the spiral antenna's broad, symmetric pattern could produce relatively uniform illumination of the reflector surface and allow precisely controlled edge illumination over a broad bandwidth. He used a combination of two reflective-cavity backed four-armed spirals separately fed to obtain dual-mode monopulse operation at 136 MHz, 235 MHz, and 406 MHz simultaneously. Similarly, spiral antennas have been found to be useful as lens feeds [3].

2 Definition of Phase Center and Phase Center Variation (PCV)

The IEEE defines phase center as *the location of a point associated with an antenna such that, if it is taken as the center of a sphere whose radius extends into the far field, the phase of a given field component over the surface of the radiation sphere is essentially constant, at least over that portion of the surface where the radiation is significant*. Balanis [4] gives the following concise definition: *The reference point which makes* [the far-field

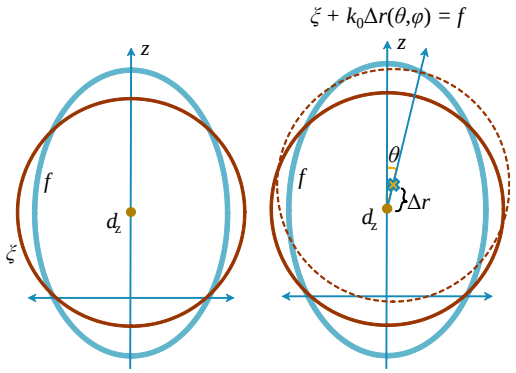

(a) Phase Center. (b) Phase Center Variation.

Figure 1: Illustrations of the concepts of phase center and phase center variation (PCV)

phase] *independent of* [observation angle]... Yet another definition provided by Kildal [5] is simply ... *the phase reference point which maximizes the feed efficiency* ....

Each of these definitions has important deficiencies; for instance, Kildal's definition is specific to antennas used as reflector feeds, and is meaningless for antennas used in GPS systems, for example. Balanis' definition assumes the existence of a reference point that makes the far-field phase independent of observation angle; however, such a point does not strictly exist for physically realizable antennas. While for some antennas the error is very small (e.g. for electrically small dipoles in free space), there are many antennas for which this definition breaks down. The IEEE definition modifies this somewhat by allowing only a portion of the far field surface to be considered, yet ultimately suffers from the same deficiency as the Balanis definition.

The GPS literature deals with this reality by instead allowing the phase center to be a function of azimuth and elevation. Then a mean phase center is defined which is independent of azimuth and elevation, and a quantity called phase center variation (PCV) (a function of azimuth and elevation) is defined to describe the error committed by the assignment of the mean phase center. While this representation is formally correct, it seems abusive to use the term phase center in this way, since the IEEE defines phase center as a point in space.

For the purposes of this paper, we use an alternate definition of phase center that allows for a unique point to be determined. Referring to Fig. 1(a), *given a general far-field phase function* (shown schematically by the ellipse f), *the phase center* d_z *is the center of the sphere* (shown schematically by the circle ξ) *that minimizes phase error magnitude* $|f-\xi|$ *in a suitable sense*. This definition accomplishes three objectives. First, it defines the phase center as a point in space that can be uniquely determined provided that a suitable fitting algorithm is used. Second, the phase center is explicitly defined to be in an approximate sense, so that even antennas with non-spherical phase surfaces can be assigned a unique phase center. Third, it is sufficiently general so as to be useful in diverse situations. Under this definition of phase center the phase error $f-\xi$ plays an important role. Another quantity frequently encountered in the GPS literature is the previously mentioned PCV, where

we give the following interpretation: *The PCV Δr is the displacement about the phase center d_z in the direction θ, ϕ required to make the actual phase function f and the ideal phase function ξ coincident.* Figure 1(b) demonstrates the definition in two dimensions, where it can be seen that an expression for PCV is

$$\Delta r = (f - \xi)/k_0 \tag{1}$$

where k_0 is the propagation constant of free space. That is, PCV only differs from the phase error by the multiplicative constant k_0.

3 Some Past Studies of Spiral Antenna Phase Center

Barbano [6] used a phaseless two-probe technique to measure the phase center of high growth rate spiral antennas at a single frequency. These measurements, taken in three different planes, were found to be in agreement with the theory of [1]. Wheeler [7] later used an assumed current distribution to calculate the phase center of wire spirals of infinite radius and infinitely small feed region. He found that for interferometer applications the growth rate of such antennas should be no greater than $a = 0.1$/rad to ensure that the phase error is sufficiently small. Dyson [8] measured apparent phase centers for two-armed conical log-spiral antennas by weighting the contribution to phase center more heavily for angles near broadside. Atia and Mei [9] use Hu's method [10] to determine the phase center of a numerically simulated four-armed conical spiral antenna using the slope of the far-field phase.

4 Phase Center Computation

4.1 Algorithm

The method most commonly used to determine the phase center of measured principal plane data is one given by Hu [10], in which the far-field phase is plotted and a straight-line fit is performed on the phase data. The slope of the fitted line is d_z/λ, where d_z is the phase center location. This method is straightforward and is especially useful when postprocessing range data manually. In practical cases the phase data will not be perfectly linear, which may be either due to measurement noise or due to inherent phase front nonuniformity. In such case it becomes necessary to fit the line to the data, which suggests the method of least squares.

At this point we note that Hu's method only provides a one-dimensional result, which may be insufficient if lateral displacement can not be neglected. If lateral displacement is to be known it is natural to instead choose to fit the phase surface, which we expect to be roughly circular in shape. A number of algorithms for fitting a circle to a general function are available [11].

One simple way that introduces the general method is to use Fourier analysis to identify the center points. A circle located at the origin in the x, y coordinate system is parameterised by

$$x = \rho\cos(\phi) \tag{2}$$
$$y = \rho\sin(\phi) \tag{3}$$

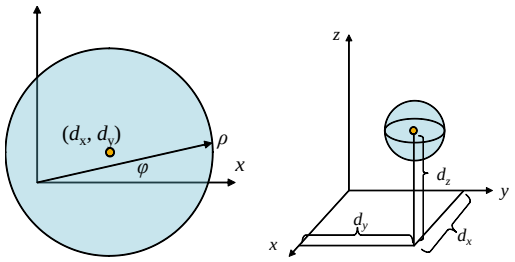

(a) 2-D. (b) 3-D.

Figure 2: Interpretation of the coefficients d_x, d_y, and d_z as the x, y, and z phase center coordinates respectively.

where ρ is a constant. If the circle is no longer located at the origin, we can retain this parameterisation by allowing ρ to become a function of ϕ (Fig. 2(a)). The center coordinates of the circle are

$$d_x = \frac{1}{\pi}\int_0^{2\pi} \rho(\phi)\cos(\phi)d\phi \tag{4}$$

$$d_y = \frac{1}{\pi}\int_0^{2\pi} \rho(\phi)\sin(\phi)d\phi \tag{5}$$

which are the first-order Fourier coefficients of ρ. When ρ does not describe a circle, but instead describes a simple closed parametric curve, then the coefficients are the center coordinates of the circle that fits ρ in a least-squares sense. The extension to the case of a three-dimensional surface is straightforward. In this case the parameterisation of a simple closed surface is given by

$$x(\theta,\phi) = r(\theta,\phi)\sin(\theta)\cos(\phi) \tag{6}$$

$$y(\theta,\phi) = r(\theta,\phi)\sin(\theta)\sin(\phi) \tag{7}$$

$$z(\theta,\phi) = r(\theta,\phi)\cos(\theta) \tag{8}$$

with the center coordinates of the least-squares best-fit sphere given by

$$d_x = \frac{2}{\pi^2}\int_0^{2\pi}\int_0^{\pi} r(\theta,\phi)\sin(\theta)\cos(\phi)d\theta d\phi \tag{9}$$

$$d_y = \frac{2}{\pi^2}\int_0^{2\pi}\int_0^{\pi} r(\theta,\phi)\sin(\theta)\sin(\phi)d\theta d\phi \tag{10}$$

$$d_z = \frac{1}{\pi^2}\int_0^{2\pi}\int_0^{\pi} r(\theta,\phi)\cos(\theta)d\theta d\phi \tag{11}$$

This method works very well for closed surfaces. However, in practical circumstances we want to restrict the fitting algorithm to a portion of the main beam, while ignoring sidelobes and pattern nulls which degrade the quality of the fit. The Fourier method requires integration over a closed surface, so we must extend the algorithm by invoking the more general Method of Least Squares to estimate the Fourier coefficients.

4.1.1 Least Squares Computation of Phase Center

Rusch and Potter [12] used a least squares procedure to calculate the phase center of an antenna in a two-dimensional principal plane. In this section we extend this procedure to three dimensions. A general expression for the far field of an antenna in free space is

$$U(r,\theta,\phi) = F(\theta,\phi)\frac{e^{j\psi(r,\theta,\phi)}}{r} = F(\theta,\phi)\frac{e^{-jk_0 r}}{r}e^{jf(\theta,\phi)} \tag{12}$$

where $F(\theta,\phi)$ and $f(\theta,\phi)$ are real functions that describe the far field amplitude and phase, respectively. An ideal (spherical) phase function has the form

$$f(\theta,\phi) = C + d_x\sin(\theta)\cos(\phi) + d_y\sin(\theta)\sin(\phi) + d_z\cos(\theta) \tag{13}$$

where d_x, d_y, and d_z are the Cartesian coordinates of the phase center as before. Although a physically realizable phase function will not exactly have this form, we can approximate it with the following trigonometric polynomial

$$\xi(\theta,\phi) = a_0 + a_1\sin(\theta)\cos(\phi) + a_2\sin(\theta)\sin(\phi) + a_3\cos(\theta) \tag{14}$$

Following the least squares procedure, the constants a_n are chosen to be those that minimize

$$I = \int_{\phi_1}^{\phi_2}\int_{\theta_1}^{\theta_2}[f-\xi]^2 d\theta d\phi \tag{15}$$

where the upper and lower limits of integration act in lieu of a weighting function, thereby uniformly weighting inside a specified field-of-view and neglecting contributions outside it. Considering I to be a function of the a_n, we wish to determine the values that minimize I.

$$\frac{\partial I}{\partial a_0} = 0 \qquad \frac{\partial I}{\partial a_1} = 0 \qquad \frac{\partial I}{\partial a_2} = 0 \qquad \frac{\partial I}{\partial a_3} = 0 \tag{16}$$

These equations form a linear system that can be solved for the a_n.

4.2 Validation

The phase center computation algorithm was validated (Fig. 3) against the analytical results in [1] for the infinite-radius, infinite-armed equiangular spiral. In that paper, it was shown that for tightly-wrapped spirals the phase center was located an electrical distance $k_0 d_z = a$ behind the antenna, where k_0 is the propagation constant of free space, d_z is the location of the phase center, and a is the growth rate.

For validation, the Moment Method code *FEKO* was used to compute the radiation patterns of two-armed wire spirals. Before computing the phase center it is necessary to first unwrap the phase and then subtract away the inherent $2\pi m$ azimuthal phase progression, where m is the desired mode of excitation, in order to obtain a closed phase surface that is suitable for the sphere fitting routine. The previously discussed phase center computation algorithm was used, where trapezoidal integration was used to evaluate the integrals that have the unknown phase function in the integrand. The resulting four linear equations were then solved numerically to yield the phase center.

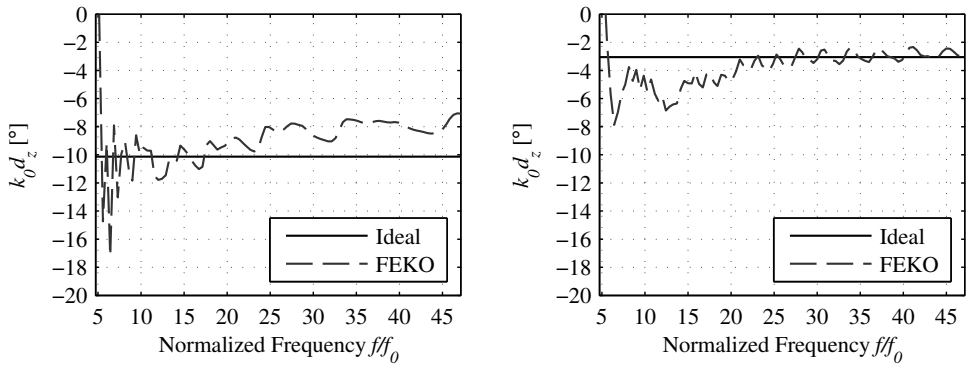

(a) Phase center vs. frequency for growth rate $a = 0.1$.

(b) Phase center vs. frequency for growth rate $a = 0.03$.

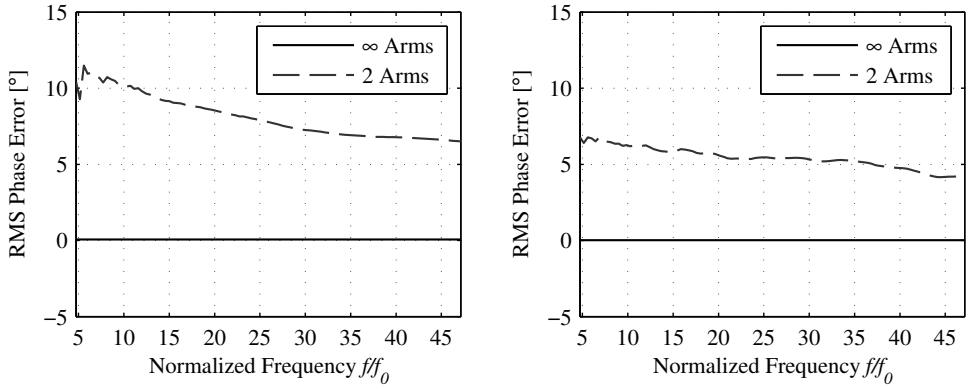

(c) Phase error vs. frequency for growth rate $a = 0.1$.

(d) Phase error vs. frequency for growth rate $a = 0.03$.

Figure 3: Validation of the phase center computation algorithm against the infinite-armed case analyzed in [1]

It was found that good agreement between this theory and results computed with *FEKO* were obtained if the antenna structure in *FEKO* was sufficiently large ($f/f_0 \approx 10$). Since a two-armed equiangular spiral with a fine feed region ($r_{feed}/r_{max} < 0.01$) was used for this validation, contaminating effects of feed region radiation and of higher-order modes are believed to be negligible compared to the contaminating effects due to the spiral truncation.

5 Studies

5.1 Effects of Field-of-View

The phase error and PCV can be decreased by reducing the field-of-view over which the least-squares procedure is performed. For investigation of the effect of field-of-view, a *FEKO* model of a four-armed free-standing equiangular spiral with a growth rate of $a = 0.0616$/rad and excited in Mode 1 was chosen. Figure 4 shows that when considering a narrow field-of-view, small undulations in the phase surface curvature produce relatively large changes in the computed phase center position. This effect has been observed to be insensitive to the far-field sampling density within the field-of-view.

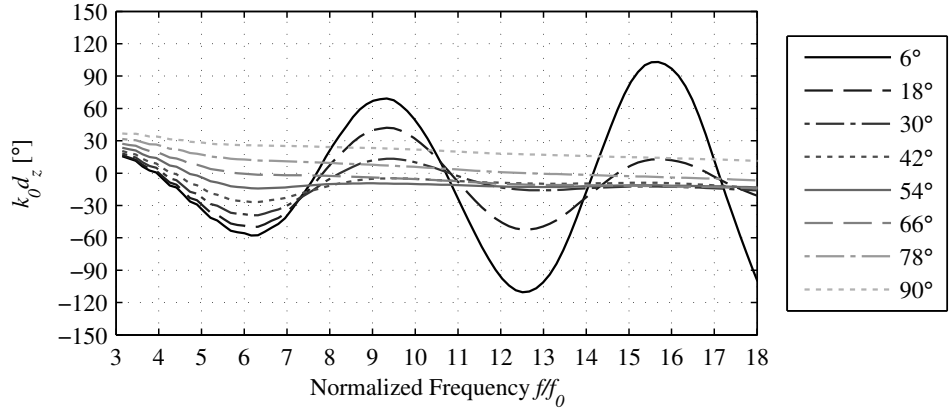

Figure 4: Decreasing the field of view increases the sensitivity of the algorithm to small changes in the phase surface curvature close to broadside.

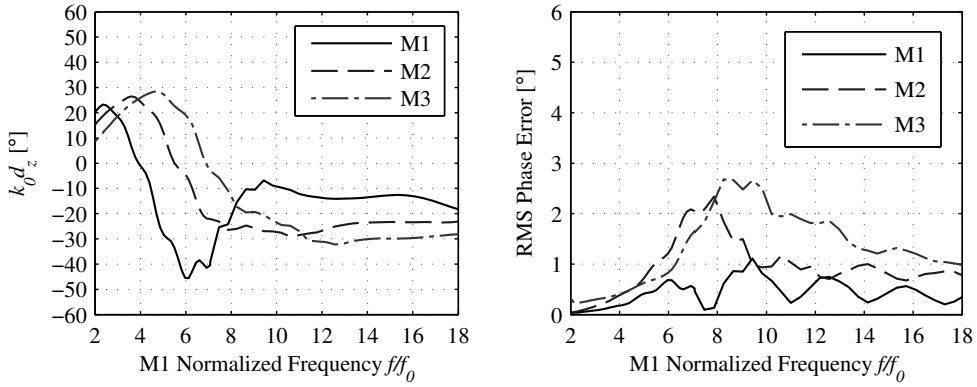

(a) Phase center.

(b) Phase error.

Figure 5: Effect of changing the excitation mode. As the mode number is increased, the undulations are shifted higher in frequency due to the larger radiation region for increasing modes.

5.2 Effects of Excitation Mode

Since multi-armed spirals are most often used in monopulse systems, it is highly desirable for all modes to share a common phase center. Figure 5(a) shows the phase centers for an eight-armed spiral with growth rate $a = 0.14121$/rad as modeled in *FEKO*. The phase center for each mode was calculated over its respective 3-dB beamwidth (M1: $0° \leq \theta \leq 38°$, M2: $18° \leq \theta \leq 60°$, M3: $27° \leq \theta \leq 66°$). The phase centers are co-located within $20°$ for frequencies above approximately nine times the cutoff frequency f_0. Below f_0, the phase centers exhibit undulation which is presumably due to the effect of end termination as discussed previously. The phase error increases for higher modes because the patterns progress lower in elevation, where the phase surface is increasingly nonspherical.

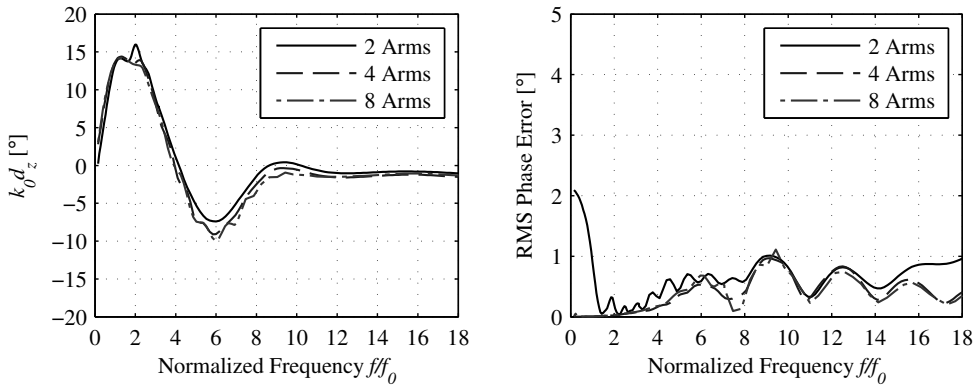

(a) Phase center.

(b) Phase center variation.

Figure 6: Effect of number of arms on the phase center of spiral antennas. Little effect is seen for the phase center, but the two-armed spiral has poorer phase error near the cutoff frequency f_0.

5.3 Effects of Number of Arms

Figure 6 shows that increasing the number of spiral arms has little effect on the phase center stability. This study was performed using free-standing spiral models in *FEKO* with a growth rate of $a = 0.0616$/rad. However, the phase error associated with that phase center is large for the two-armed spiral for frequencies below the cutoff frequency, while the four- and eight-armed spirals have low phase error for all frequencies. This is because the two-armed spiral becomes linearly polarized near the cutoff frequency, which violates the assumption of a Mode 1 azimuthal phase progression. If the phase center of the two-armed spiral below cutoff is desired, then no azimuthal phase progression should be assumed.

5.4 Effects of Growth Rate

From Fig. 7(a), where numerous phase centers are shown for a large range of growth rates, we can see that the phase center stability is not affected much by changing the growth rate. However, the phase error improves markedly with decreasing growth rate down to $a \approx 0.06$/rad, beyond which diminishing returns are seen. This is in qualitative agreement with the results from [1].

5.5 Effects of End Termination

Figure 8 illustrates the effect of adding an absorptive termination to the outside of the spiral. The particular spiral under study is an eight-armed spiral with four turns (0.1421/rad) modeled in FEKO. The unloaded spiral is 15 cm in diameter, while the loaded spiral is 20 cm in diameter with a 2.5 cm wide absorbing ring so that the unloaded diameter is also 15 cm. The inner diameter is sized to accomodate a bundle of eight 47 mil diameter semi-rigid coaxial cables. Figure 8(a) shows that the variation of phase center with respect to fre-

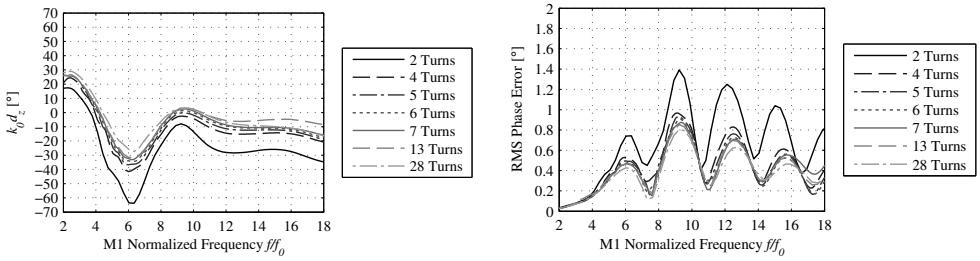

(a) Phase center. (b) Phase error.

Figure 7: Effect of the growth rate on the phase center of spiral antennas. Little effect is seen for the phase center, but lower phase error is observed for lower growth rates.

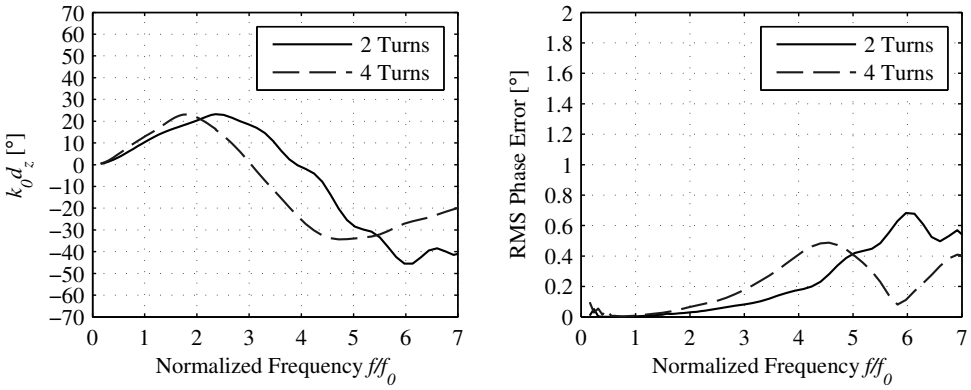

(a) Phase center. (b) Phase error.

Figure 8: Effect of resistively terminating the spiral arms.

quency has been shifted lower, but the amplitude of the variation has not been diminished. This shift may be due to the increased size of the spiral due to the terminating portion. For the phase error, we see a similar effect of shifting lower in frequency.

5.6 Effects of Reflective Cavity Backing

Typically a unidirectional radiation pattern is desired from a spiral antenna; however, the planar spiral inherently radiates equally both upward and downward. An absorbing cavity is most often used to accomplish this, because it causes the least degradation in the broadband properties of the radiation pattern. However, additional gain can be achieved in certain circumstances when the spiral is used with a reflective cavity backing. Figure 9(a) shows that placing the unterminated spiral discussed in the previous section two inches above an infinite PEC plane causes large amplitude oscillations in the phase center, with an accompanying large phase error. We can see that upon adding the termination of the previous section to the spiral, the large-amplitude oscillations are highly dampened, and the phase error associated with that phase center is highly decreased, nearly to the level of

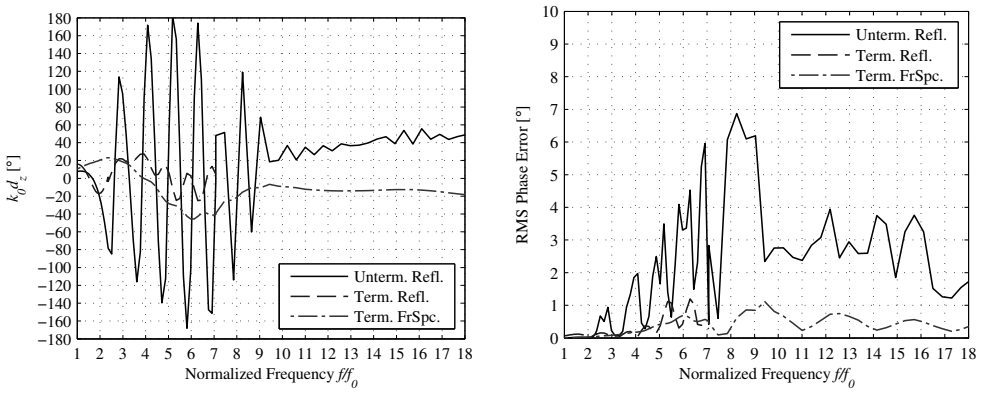

(a) Phase center.

(b) Phase error.

Figure 9: Reflecting cavity backed spiral. Adding resistive termination to the arms appears to help reduce the oscillations in the phase center.

the spiral in free space.

5.7 Effects of Beamformer Errors

Since physically realizable spiral beamformers have amplitude and phase imbalances, it is desirable to know how these imperfections affect the phase center of the spiral. The modal content of the beamformer outputs can be analyzed by performing a DFT. For a four-armed isolated spiral, only Modes 1, 2, and 3 can be excited. Any other modes (e.g. -1, 5, etc.) are excited only when energy is not radiated by these three. We will now study how the introduction of spurious modes can affect the phase center of a Mode 1 pattern. In this study the low-level spurious modes were mathematically superimposed individually on the ideal Mode 1 beamformer at a level 25 dB below that of Mode 1. This level corresponds to those observed in practical beamformers. Since Modes 1 and 2 combine to form a beam that is non-symmetrical in both amplitude and phase with respect to the spiral axis, we expect to see movement of the phase center in the lateral direction (Fig. 10(a)). However, since Modes 1 and 3 combine to form a symmetric beam, we expect to see very little lateral movement of the phase center, and this is confirmed in Fig. 10(b). If the phase center is allowed to move off-axis, then the Mode 2 contaminated pattern shows less phase error, and therefore a more well-defined phase center (Fig. 11(a)). By contrast, Mode 3 contamination can not be compensated by moving off axis, so its effect on phase error is greater.

6 Conclusions

The purpose of this paper was to investigate the phase center stability of spiral antennas. Along the way, we re-examined several existing definitions of phase center and found that each had their own deficiencies, leading us to present an alternate definition of the concept. A commonly-used term phase center variation (PCV) was reinterpreted in light of this alternate definition and was found to be simply related to the phase error committed by assigning a unique phase center.

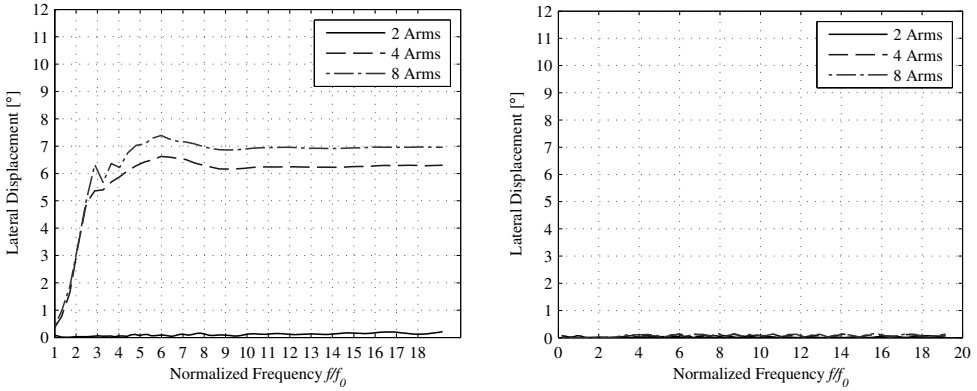

(a) Mode 2 contamination.

(b) Mode 3 contamination.

Figure 10: Lateral phase center displacement versus frequency for two types of contamination on a four-armed spiral. Mode 2 contamination causes significant lateral displacement, while Mode 3 contamination produces relatively very little displacement.

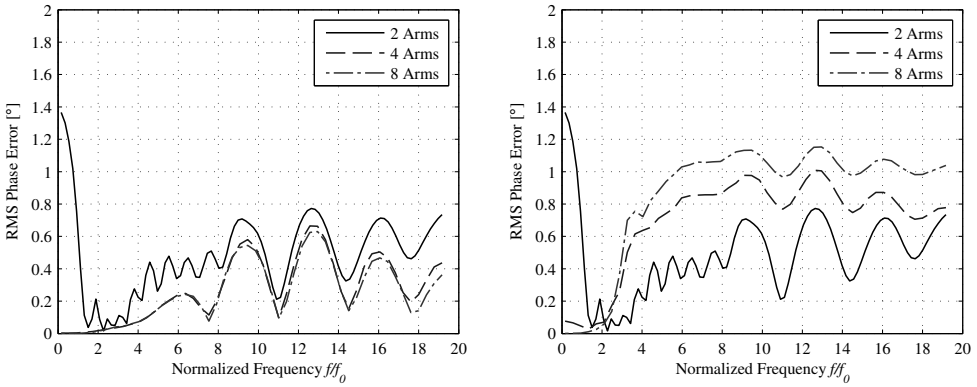

(a) Mode 2 contamination.

(b) Mode 3 contamination.

Figure 11: RMS phase error versus frequency for two types of contamination on a four-armed spiral. Lateral displacement from Mode 2 allows there to be little additional phase error degradation. Phase error is higher for the Mode 3 case since the phase center does not move to compensate.

Next, an algorithm for computing the three-dimensional phase center of antennas was presented. The additional capability to determine lateral displacements was useful for analyzing the effect of beamformer errors on phase center.

Increasing the number of arms of the spiral from two to four substantially improved the phase error near the cutoff frequency because the two-armed spiral loses the assumed $2\pi m$ phase progression. Decreasing the growth rate improved the phase error up to a point ($a \approx 0.06$/rad) after which diminishing returns were observed. Resistive termination of the spiral arms was seen to have little effect for spirals in the absence of a reflecting cavity, but was very useful once a reflecting cavity was introduced.

Finally, the effects of beamformer errors were examined and it was found that, for a four-armed spiral, contamination from Mode 2 produced a significant lateral offset with small phase error, while contamination from Mode 3 produced comparatively insignificant lateral offset but increased the phase error.

Acknowledgments

The authors acknowledge the support of the Office of Naval Research, United States Navy, under grant #N00014-07-1-1161, administered by Dr. Peter Craig.

References

[1] B. R.-S. Cheo, V. H. Rumsey, and W. J. Welch, "A solution to the frequency-independent antenna problem," *IRE Transactions on Antennas and Propagation*, vol. 9, no. 6, pp. 527–534, November 1961.

[2] P. A. Lantz, "A two-channel monopulse reflector antenna system with a multimode logarithmic spiral feed," in *Sixteenth Annual Symposium on USAF Antenna Research and Development Progress*, 1966.

[3] W. R. Free, F. L. Cain, C. E. Ryan, C. P. Burns, and E. M. Turner, "High-power constant-index lens antennas," *IEEE Trans. Antennas Propagat.*, vol. 22, pp. 582–584, 1974.

[4] C. A. Balanis, *Antenna Theory: Analysis and Design*, 3rd ed. Hoboken, New Jersey: John Wiley and Sons, Inc., 2005.

[5] P.-S. Kildal, "Combined e- and h- plane phase centers of antenna feeds," *IEEE Trans. Antennas Propagat.*, vol. 31, no. 1, pp. 199–202, January 1983.

[6] N. Barbano, "Phase center distributions of spiral antennas," in *WESCON/60 Conference Record*, vol. 4, August 1960, pp. 123–130.

[7] M. S. Wheeler, "Phase characteristics of spiral antennas for interferometer applications," in *IRE International Convention Record*, vol. 12, March 1964, pp. 143–152.

[8] J. D. Dyson, "The characteristics and design of the conical log-spiral antenna," *IEEE Trans. Antennas Propagat.*, vol. 13, no. 4, pp. 488–499, July 1965.

[9] A. Atia and K. Mei, "Analysis of multiple-arm conical log-spiral antennas," *IEEE Trans. Antennas Propagat.*, vol. 19, no. 3, pp. 320–331, May 1971.

[10] Y. Y. Hu, "A method of determining phase centers and its application to electromagnetic horns," *Journal of the Franklin Institute*, vol. 271, pp. 31–36, January 1961.

[11] G. Taubin, "Estimation of planar curves, surfaces and nonplanar space curves defined by implicit equations, with applications to edge and range image segmentation," *IEEE Trans. Pattern Anal. Machine Intell.*, vol. 13, pp. 1115–1138, 1991.

[12] W. V. T. Rusch and P. D. Potter, *Analysis of reflector antennas*. New York, New York: Academic Press, Inc., 1970.

VHF THROUGH L-BAND ANALOG AND DIGITAL MODEFORMERS

Nathan Sutton, Paul Kasemir, Matthew Radway and Dejan S. Filipović
Department of Electrical, Computer, and Energy Engineering
University of Colorado, Boulder, CO 80309-0425

Abstract: Well designed beam and modeformers are necessary for high quality performance of phased arrays, accurate direction finding systems, etc. Traditionally, modeformers are realized as hybridly or monolithically integrated analog sub-systems. In this paper several analog hybrids are used to create a modeformer baseline. Their wideband operation is evaluated for loss, amplitude and phase misbalances, weight, complexity, etc. Most of these factors contribute to the errors in beam-pointing and geo-location, as well as antenna pattern contamination. Recent advances in digital integrated circuits have contributed to not only improved performance of analog to digital and digital to analog converters and FPGAs but also to their reduced cost. Thus, we are now able to realize complete modeforming functionality in a digital domain and thus enhance the performance of modeformers. This paper demonstrates the design of digital and analog modeformers and compares their performance from 100MHz to 1GHz for mode 1 operation of planar four-arm spiral antennas.

1. Introduction

Compared to the more common two-armed spiral antenna, multi-armed spiral antenna apertures inherently produce far-field patterns with a high degree of modal purity, and with correspondingly low levels of axial ratio (AR) [1] and azimuthal gain variations (often denoted as WoW). The additional arms improve the performance by suppressing the radiation of spurious modes [2]. However, the important benefits of a multi-armed aperture will not be completely realized unless it is paired with a high-quality beam-forming network (BFN). Therefore care must be taken to ensure that the BFN ports are properly amplitude- and phase-balanced, potentially over multidecade bandwidths, while maintaining acceptable size and weight of the BFN. In analog BFNs, component parasitics and overmoding limit performance at high frequencies, while size and weight limit performance at low frequencies.

This paper demonstrates two types of BFNs that together address low- and high-frequency performance. The paper is organized as follows. First, we discuss the effects of BFN errors on the pattern characteristics. Next, we demonstrate the performance of two analog BFNs designed and built with commercially available hybrids and a broadband lumped element 90° hybrid. Then, we demonstrate a digital BFN constructed using commercial components such as a field-programmable gate array (FPGA), analog to digital converter, and digital to analog converter. We conclude by comparing the far field characteristics produced by each BFN when paired with a four-armed spiral aperture.

2. Effects of Modeformer Errors

A spiral antenna analog BFN is constructed from a combination of wideband hybrid components that typically have individual amplitude and phase imbalances of about 0.8 dB and 5°, respectively. A 0.5m diameter four-armed seven-turn self-complementary spiral is used for the simulations. Figs. 1 and 2 show the effects of these individual errors, distributed to produce spurious Modes -1 and 3, on the far field of a four-armed spiral antenna. At low frequencies any presence of spurious Mode -1 degrades the broadside AR (Fig. 1), until Mode +3, which has the same excitation, is able to radiate efficiently beyond $3f_0$. However, radiation of Mode +3 causes degradation of off-broadside WoW (Fig. 2). Both of these parameters are important in typical applications, so proper design of the BFN is important.

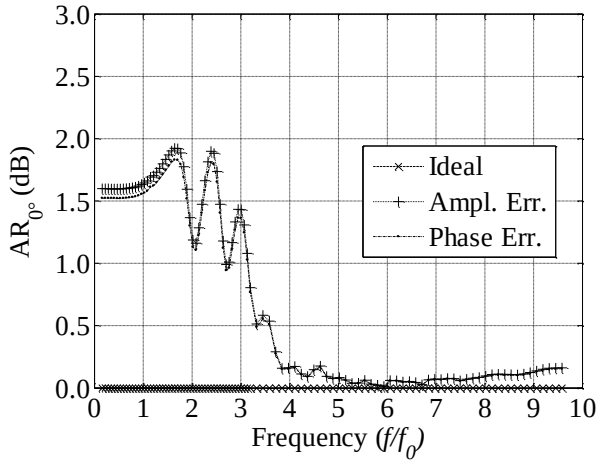

Fig. 1. Broadside axial ratio (AR) as a function of frequency, highlighting the effect of typical beam-forming network (BFN) amplitude and phase errors. The ideal beamformer produces perfect AR at broadside.

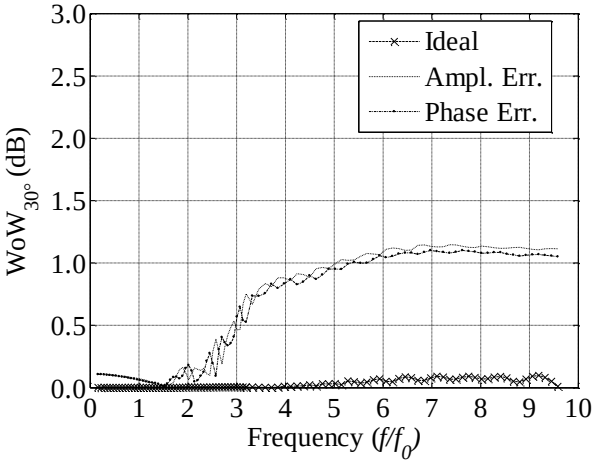

Fig. 2. Azimuthal gain variation (WoW) at 30° from broadside, highlighting the effect of typical beam-forming network amplitude and phase errors. The ideal beamformer produces very little WoW at this angle.

3. Analog Modeformer

Two analog modeforming networks (MFNs) are created both of which follow the block diagram of Fig. 3. The circuit in Fig. 3 achieves two purposes: equal amplitude power division, and mode 1 phase progression at the outputs. Equal amplitude is accomplished by a symmetric traversal through two hybrids for each output. Mode 1 phase progression is achieved by using the 90° and 180° phase delays in the correct configuration to produce the 0°, 90°, 180°, and 270° outputs at the far right of the figure.

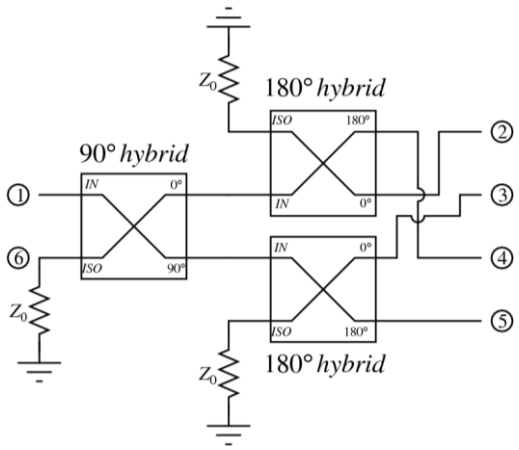

Fig. 3. Analog BFN block diagram. All isolated ports on the utilized hybrids are terminated in matched loads. Port 1 is the input port on the left, and ports 2-5 are the output ports with a phase progression of 0°, 90°, 180°, and 270° from port 2 to 5.

The first MFN consists entirely of commercially available 90° and 180° hybrids from Pulsar Microwave fabricated to operate over a few frequency bands. The low frequency band, 100-500MHz, uses the QE-18-412 90° hybrid and the high frequency band, 500-1000MHz, is constructed with the QS2-01-464 90° hybrid. Both bands use the same JT-06-411 180° hybrid which is rated to operate from 20-1000MHz. Individually these components are rated no worse than 1.2dB magnitude misbalance, 7° phase misbalance, and 1.5dB of insertion loss over their operating frequency ranges [4]-[6]. These components are connected according to Fig. 3 using phased matched cables to ensure correct phase progression and tested on a 2 port Agilent 8719ES network analyser. Ideally these MFNs should produce equal output magnitudes of -6dB and a 90° phase progression between output ports.

As shown in Fig. 4, the input reflection coefficient is below -15dB across the entire 100-1000MHz range. This can be attributed to the internal lumped element design creating an excellent match situation regardless of frequency. However, the isolation deteriorates below 10dB for frequencies less than 400MHz.

From the data the output magnitudes are all within -8.13±1.13dB. This range points to an insertion loss of 2.13dB which is proportional to the loss through the 90° hybrid, 1.2dB max, plus the loss through a single 180° hybrid, 1.5dB max. Fig. 5 shows the output magnitude misbalances with respect to the 0° output. The discontinuities at

500MHz is from the two frequency band measurements. The maximum magnitude misbalance from this data is about 1.75dB, which is proportional to the sum of the rated misbalances of the two individual hybrids.

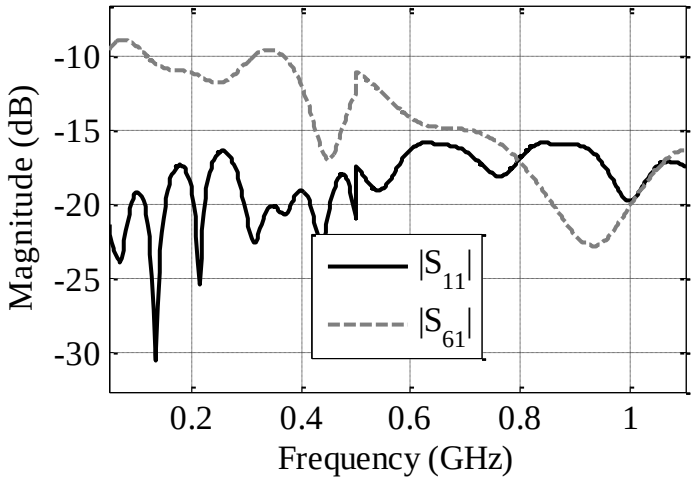

Fig. 4. Input reflection coefficient and isolation for MFN. Isolation measured as power received in isolated port of 90° hybrid (bottom left resistor of Fig. 3) from the input port 1. All measurements taken with respect to 50Ω.

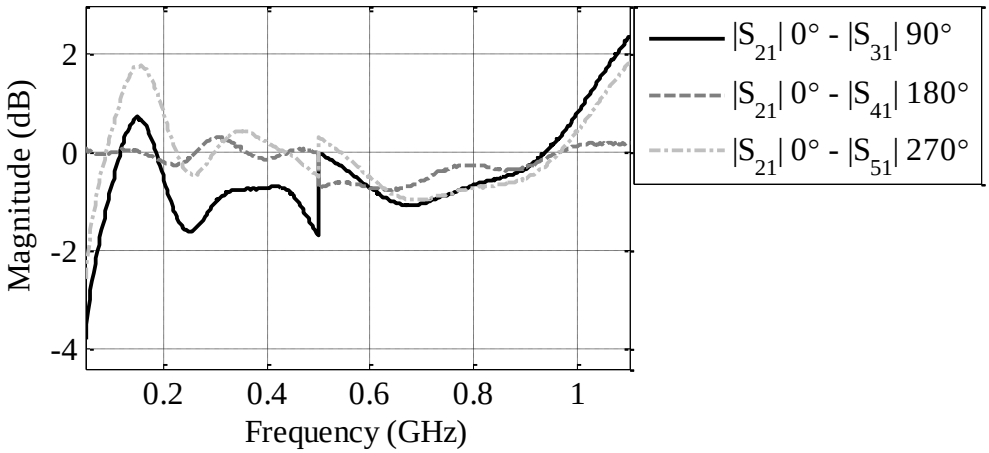

Fig. 5. Analog MFN magnitude misbalances. All three misbalances are measured with port 2 as the reference.

Fig. 6 shows the phase difference between adjacent ports. Phase misbalance is within 10° of the desired 90° phase progression on the output ports. This comes from phase misbalance in the hybrids, 3° and 7° for the 90° and 180° hybrids respectively, as well as some mismatch with the two connecting cables.

In order to evaluate the effects of BFN nonidealities on multi-armed spiral performance, a moment method model [3] of a 0.5m diameter four-armed self-complementary spiral aperture ($f_0 \approx 191$ MHz) was excited using the BFN outputs as weights. The resulting broadside AR is shown in Fig. 7, where the BFN errors have their greatest effect at frequencies below $3f_0$.

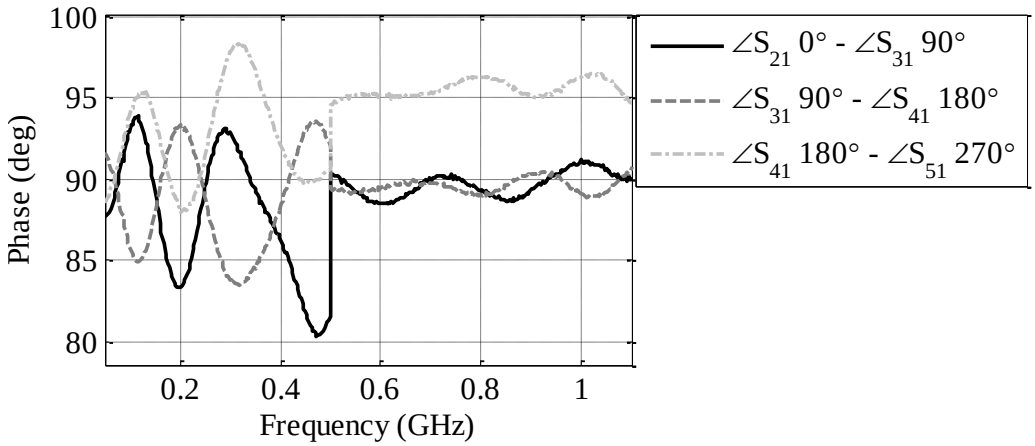

Fig. 6. Analog BFN phase misbalance. Only 90° phase misbalance is shown to clearly see the misbalance value.

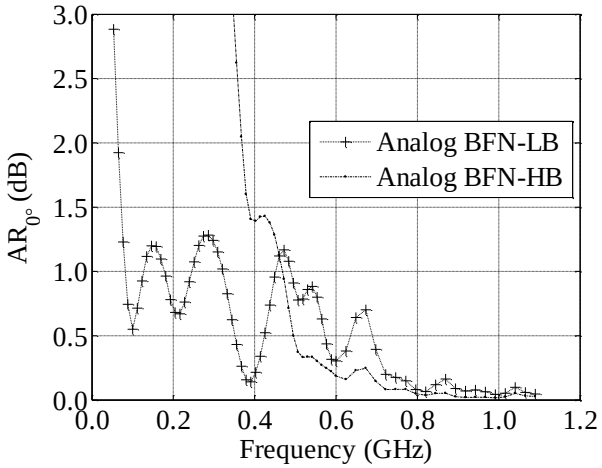

Fig. 7. Broadside AR of a 0.5 m diameter four-armed spiral fed by the analog low-band BFN (100-500 MHz) and analog high-band BFN (500-1000 MHz)

The effect of BFN errors on WoW at 30° from broadside is shown in Fig. 8, which worsens as higher order spurious modes begin to radiate efficiently at higher frequencies.

A second MFN using a 100MHz-1GHz lumped element 90° hybrid design according to [7] was evaluated using the AWR design environment [8]. The reason to create this second MFN is to eliminate the two separate frequency bands of the previous MFN. To create the 90° hybrid a second order cascade [7] is scaled to 100MHz-1GHz and connected as shown in Fig. 3 to the measured data for the commercially available 180° hybrids. Fig. 9 shows the broadband 90° hybrid prototype consisting of two center tapped coupled inductors. The coupled inductors of this lumped circuit act as an analog to coupled lines in distributed circuits. To fabricate the circuit two separate magnetic toroid cores are required with two sets of bifilar windings on each core. The exact number of turns and overlap is dependent on the frequency range of choice (inductance value), the core material, and the magnet wire.

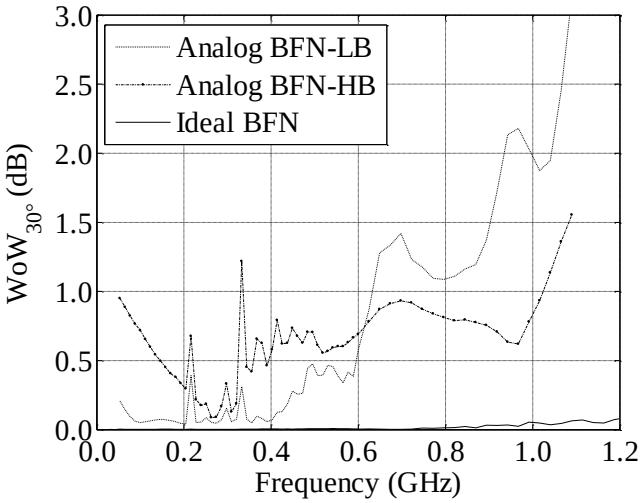

Fig. 8. WoW at 30° from broadside of a 0.5 m diameter four-armed spiral fed by the analog low-band BFN (100-500 MHz), by the analog high-band BFN (500-1000 MHz), and by an ideal BFN

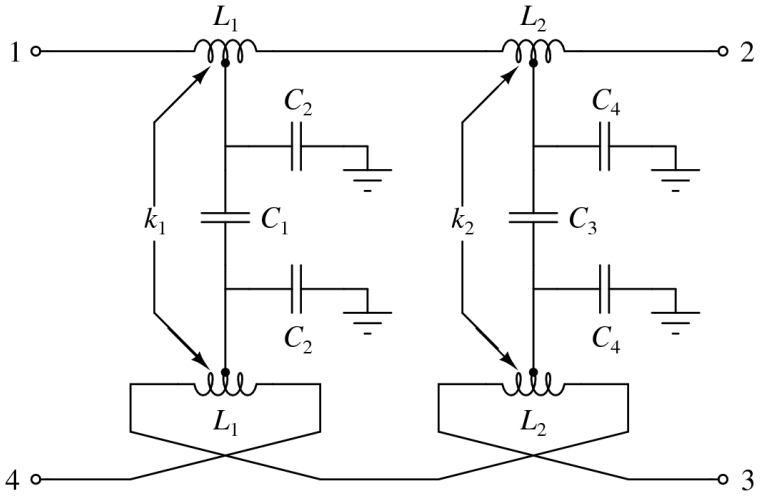

Fig. 9. Ideal lumped element model of second order cascade 90° hybrid prototype. Equations for circuit values can be found in [7].

Using the design lumped element 90° the MFN is simulated to find the input match and isolation (Fig. 10), magnitude misbalance (Fig. 11), and phase difference (Fig. 12). The isolation is improved over the previous MFN only for the low frequency band (less than 500MHz). An important note here is that from this data it can be concluded that the isolation between the two input ports is heavily reliant on the 90° as opposed to the 180° hybrids because the isolation changes completely with the same 180° hybrids.

Fig. 11 shows the magnitude misbalance of the updated MFN is less than 0.8dB across the entire 100-1000GHz band. As with the previous misbalances the ports sharing a 180° hybrid have better misbalance which is to be expected because the two hybrids are identical. The difference here is that the majority of this misbalance is incurred in the 180° hybrid as the ideal 90° hybrid has a maximum misbalance of 0.4dB. An important point to remember is that the output magnitudes for this

beamformer are misleading because there is no loss in the 90° hybrid. However, the fabricated misbalance will be close to the same value because the loss should be equivalent for each path through the hybrids.

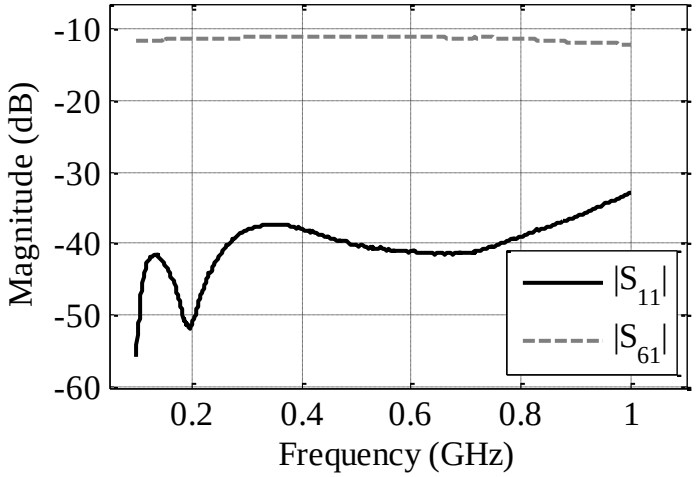

Fig. 10. Input reflection coefficient and isolation for new lumped element MFN. Isolation definition same as Fig. 4.

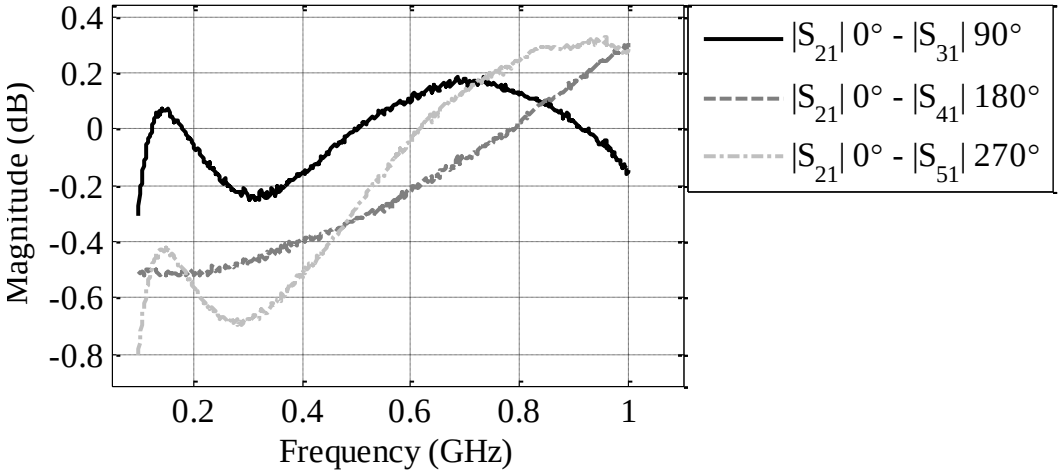

Fig. 11. Designed lumped element MFN magnitude misbalance with respect to the through port.

Phase difference for this is much improved over the previous design with a maximum of 6° from Fig. 12. Like the magnitude misbalance this plot shows that the biggest misbalances occur between outputs that don't share a 180° hybrid (ports 3 and 4 in this case). This is directly tied to the lumped element design because that hybrid has less than 1° of phase misbalance. When fabricated this would increase, but from the results in [7] a typical phase difference is 3°.

For the purpose of comparison in the discussion section the first analog MFN that has two bands and is constructed entirely from commercially available hybrids will be referred to as A-1. The second hybrid constructed from the broadband lumped element 90° hybrid and the pulsar 180° hybrid will be referred to as A-2.

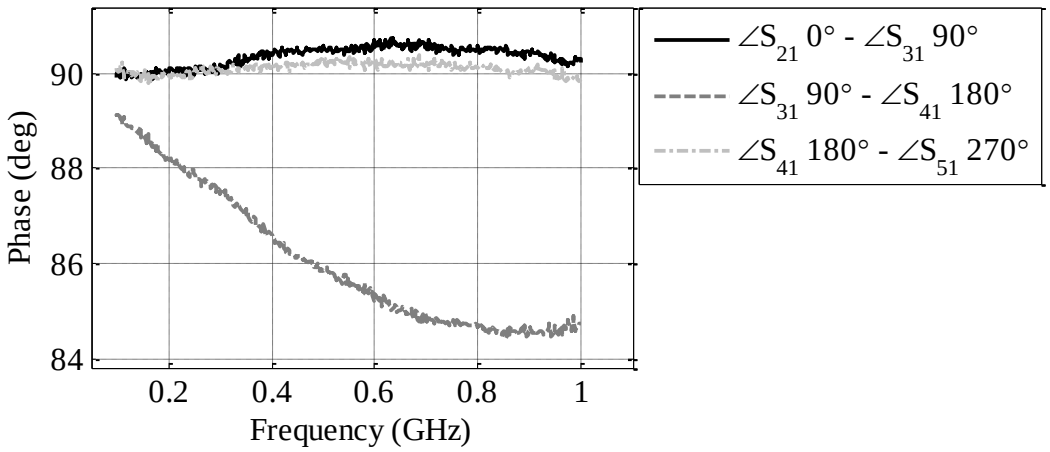

Fig. 12. Designed lumped element MFN phase difference for adjacent ports (90° only).

4. Digital Modeformer

The appeal of a digital beamformer is that all the data is stored as samples and can be manipulated without any loss. The mode 1 operation of a 4-arm antenna requires four signals, one at each of the following phases 0, 90, 180, and 270°. In a digital system, it is very easy to produce a 180° phase shift. With the simple assumption that the signal is a sine wave centered around zero then the negative of that signal is also the 180° phase shift. The simplest method to negate a digital sample is to negate all the bits within the sample. With this 180° shift capability of the digital system, we can create the four required phases from two inputs, one at 0° and the other at 90°. Fig. 13 shows a possible realization of a beamformer using both analog and digital components. The analog components are the initial 90° phase shift block and the 4-arm antenna while the digital component is the FPGA. The interface between the digital and analog domains is carried out by utilizing analog to digital converters (ADC) and digital to analog converters (DAC).

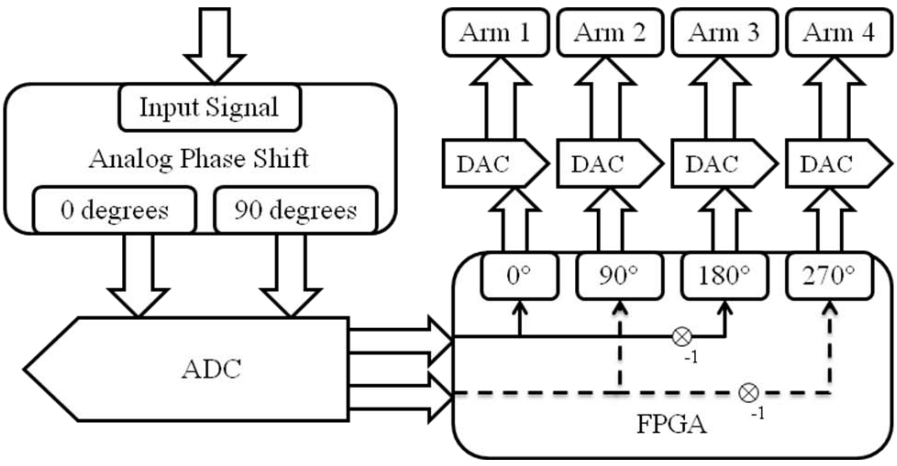

Fig. 13. Analog/digital hybrid beamforming network.

ADCs sample an analog signal and convert it into a digital representation using a number of bits. For an 8-bit ADC there are 2^8 = 256 discrete values that can be represented. The ADC will specify an input voltage range for the analog signal which will then be equally divided into the 256 values. DACs perform the conversion in the opposite direction, i.e., from digital to analog domain. Each sequence of bits taken as an input into DAC is converted into an output analog signal within a specified range. FPGA is usually used to implement a user defined logic function, which makes it fairly easy to create a design where the FPGA can perform nearly any digital operation the user desires. For our purposes the FPGA is programmed with a design that reads data values from the ADC and then creates the two desired outputs for the DAC, one at 0° and the other at 180°. The other reason the FPGA is useful is its ability to do parallel operations, so we can have two chains of 180° phase shift as shown in Fig. 13.

The analog input is sampled at a constant rate to create a digital stream of 8-bit samples. The stream is then manipulated and output at the sampling frequency to recreate the 0° signal and produce the 180° signal. The sampling frequency plays a big role in the capability of the digital BFN because of the sampling theorem. The sampling theorem by Nyquist states that the maximum frequency present in an analog signal must be half the sampling frequency in order to have an accurate representation of the signal in the digital domain.

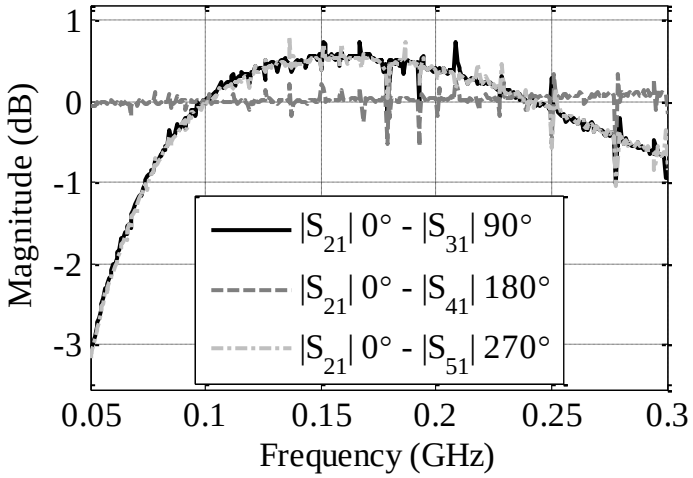

Fig. 14. Digital BFN magnitude misbalances.

The beamforming system shown in Fig. 13 was built and tested using a sampling frequency of 500MHz. The analog hybrid has bandwidth of 100-500MHz, so the effective range of the hybrid BFN is from 100-250MHz. Fig. 14 shows the magnitude misbalance of the system over a range of frequencies that includes the effective range. As seen, about 1dB amplitude misbalance is obtained. This variation could theoretically be removed by using the FPGA to multiply up the amplitude by a correction factor which is frequency dependent. Fig. 15 shows the phase misbalances between the different phases. As seen, a fairly large drift between phases is obtained. This result is caused by the unequal routing on the fabricated printed circuit board (PCB). The electrical length of the traces carrying clock signal is slightly different for each of the DAC chips, thus leading to a small linear phase between the channels. A

closer look at the graphs shows several spikes in the plots at certain frequencies, which are likely due to the chosen sampling frequency.

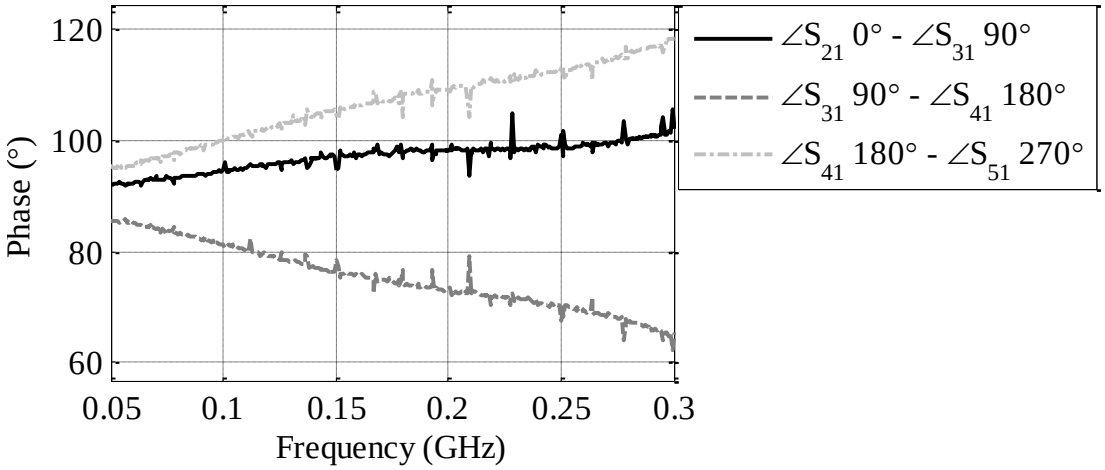

Fig. 15. Digital BFN phase misbalances.

5. Digital/Analog Comparison

Comparing the digital BFN to the analog BFN shows that the digital system performs better as far as magnitude misbalance, but the phase misbalance of the analog system is superior. From Fig. 5 and Fig. 14 the magnitude misbalance is ±2dB for the analog system compared with ±1dB for the digital system. It is important to notice that the performance of the digital BFN is also heavily influenced by the quality of the analog hybrid. At the moment, the digital realization of a frequency independent 90° hybrid counterpart is under development and when realized it will significantly improve the performance of the digital beamformer. Fig. 6 and Fig. 15 show that the analog BFN is better for phase misbalance with 90°±8° while the digital BFN is 90°±28°. Layout of the digital board is a likely cause for most of the phase distortion and can be mitigated with greater care on phase matching on the PCB.

One of the other big differences between the analog and digital BFNs is that the analog is completely passive while the digital is active. The digital BFN shown here consumes approximately 10 W. While this needed power may be undesirable in some applications, it also enables enhanced range of system level capabilities. Specifically, the FPGA allows us to have intelligence within the BFN, so we can control a number of things such as the manipulation of various waveforms, control the system operation over a serial communications link, etc.

6. Discussion

In order to evaluate the errors of the discussed MFNs a prototype spiral antenna is designed and fabricated. Fig. 16 shows the antenna geometry as a whole (left) and the transition region (right). Archimedean growth was used in the transition region on the top layer to create a four turn spiral with a four to one metal to slot ratio (a = 0.873 mm/rad). The increased metal to slot ratio is used to reduce the nominal impedance

over a self-complementary structure. The tight wrap is employed to provide enough length for impedance matching at lower frequencies. Equiangular growth is used for the final turn of the spiral, which is self-complementary (a = 0.336). Future antenna miniaturization was in mind with this section so the loose wrap creates ample space for termination treatments. The antenna was fabricated using 62.5mil FR4 and its final diameter was 16.5".

Fig. 16. Fabricated spiral antenna geometry. Full spiral geometry (left) and magnified transition region (left) images.

To provide validation for the simulated results the antenna was measured and the results for mode 1 VSWR were compared as shown in Fig. 17.

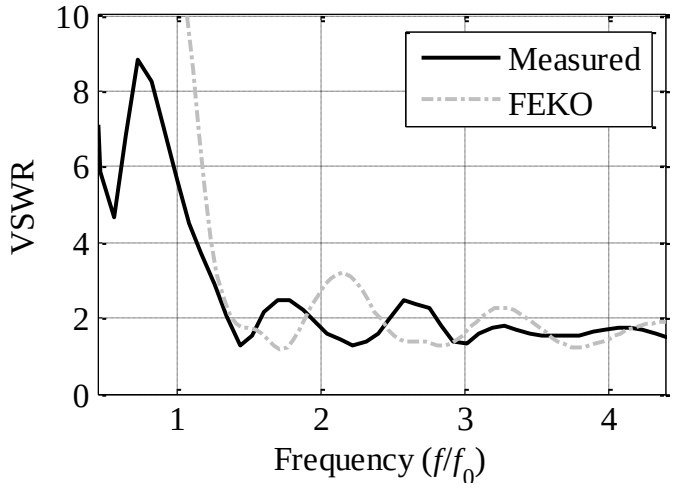

Fig. 17. Modal VSWR for simulated and measured antenna.

VSWR is less than three to one for $f > 1.25f_0$, and there is solid agreement between the two methods. Simulated data assumes an infinite dielectric, which creates some discrepancies with the measurements. Also there is some measurement error from the feed bundle and the imperfect absorber used.

In addition to the VSWR the far-field of the antenna was simulated using the three MFNs discussed as well an ideal MFN. For the far-field data the simulated results were scaled such that f_0 corresponds to 100MHz which is the low frequency cut-off of all the MFNs. Average axial ratio at broadside is reported in Table 1 to emphasize the effect of the MFN on the purity of the spiral patterns. The ideal data has the best axial ratio across all frequencies at less than 0.008dB. A self-complementary spiral ideally has 0dB axial ratio at broadside, so these small values come from mesh asymmetries and the transition region. The digital MFN shows the worst result, which is directly related to the large phase difference seen in Fig. 15. Of the two analog MFNs the axial ratio for A-2 is reduced for all frequencies because the magnitude misbalance and phase difference are lower.

Fig. 18 shows the co- and cross-polarized gain at $\varphi = 0°$ for the four antennas at three different frequencies for the mode 1 spiral. Co-polarized gain is relatively unaffected by the misbalances produced from the MFNs. However, the cross-polarization level, especially at broadside, is increased for all three nonideal MFNs. This is illustrated prominently in Fig. 18(b), and the effect is minimal at higher frequencies. A-2 shows the closest to ideal performance over all frequencies because the misbalances for this MFN are the smallest of all three.

In addition to the broadside axial ratio a cut at $\theta = 30°$ is studied to evaluate the pattern symmetry or WoW. Table 2 shows the WoW $\theta = 30°$ at for frequencies from one to eight times f_0. The table shows that the WoW is increased over the ideal case; however, the increase in WoW only reaches 1.6dB in the worst MFN. This result mirrors the axial ratio data with the increased imbalances created increased WoW. For all the MFNs the WoW is increasing as the frequency increases because of the higher order modes radiating more efficiently at higher frequencies.

Fig. 19 shows the co-polarized gain patterns for the four MFNs at $\theta = 30°$. It is important in these plots to recognize the scale changes. The three scales are (a) 0.5-0.75dB, (b) 1.5-2dB, and (c) 2-4dB. The scales are changed so that the imperfections of each pattern can be clearly seen for all four MFNs. From these patterns it is easy to see that the nonideal MFNs are increasing the WoW, and again the digital (shown only in the first two patterns) is the worst.

f/f_0	1	2	3	4	5	6	7	8
Ideal	0.005	0.004	0.005	0.003	0.005	0.005	0.008	0.005
A-1	0.277	0.449	0.295	0.023	0.024	0.012	0.046	0.100
A-2	0.157	0.026	0.067	0.020	0.004	0.010	0.010	0.026
Digital	0.554	0.701	--	--	--	--	--	--

Table 1. Average axial ratio in dB at broadside.

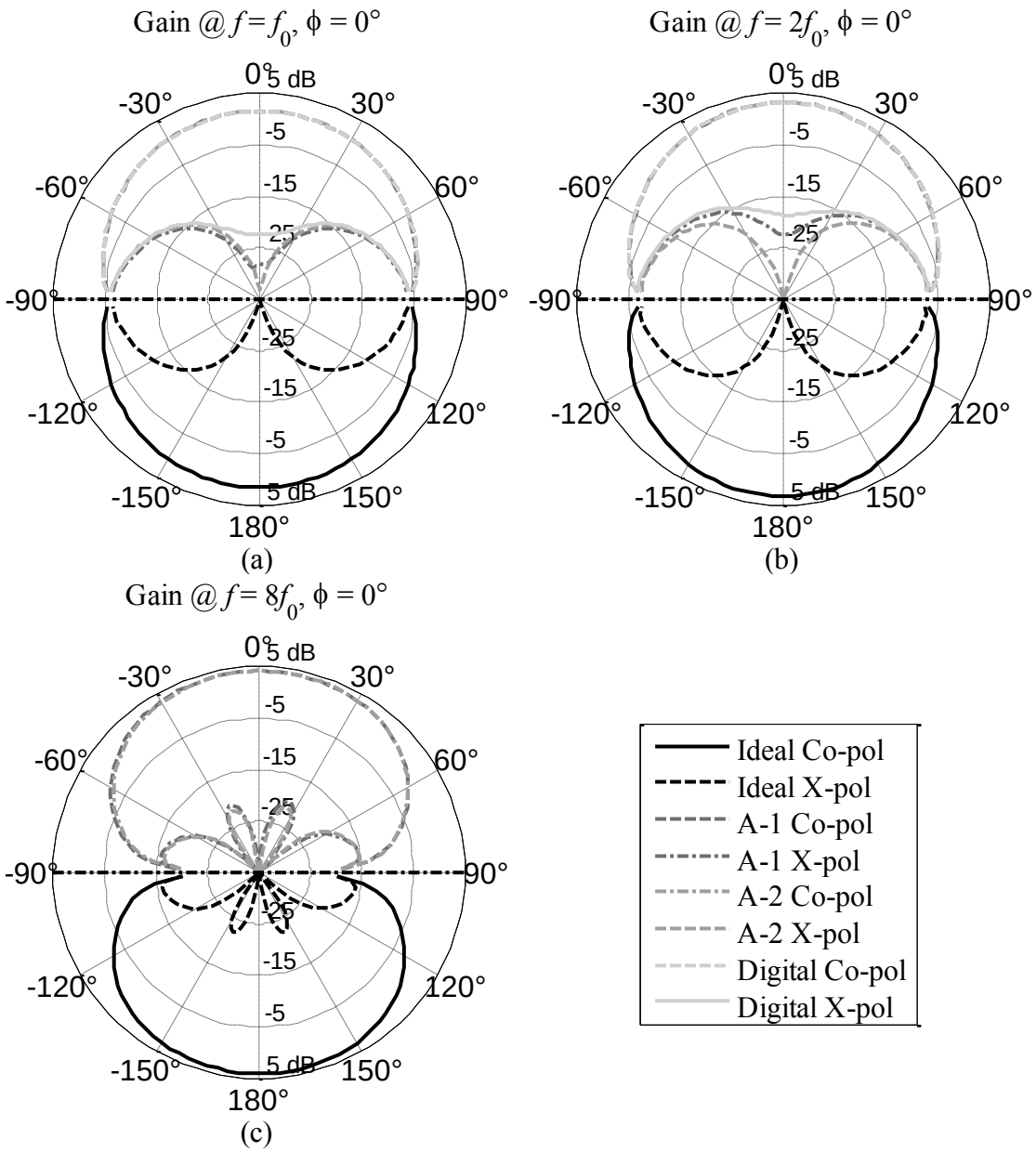

Fig. 18. Theta cuts for antenna far-field for four MFNs show co- and cross-polarizations over a 40dB range. The three patterns are for (a) $f = f_0$, (b) $f = 2f_0$, and (c) $f = 8f_0$. In each plot the nonideal patterns are shown in the top half-circle and the ideal case is shown in the bottom half. The final plot (c) does not contain digital data because the digital MFN is valid only up to $f = 2.5f_0$.

f/f₀	***1***	***2***	***3***	***4***	***5***	***6***	***7***	***8***
ideal	0.024	0.041	0.068	0.057	0.375	0.497	0.665	0.799
A-1	0.106	0.254	0.414	0.163	0.903	1.013	1.585	1.442
A-2	0.086	0.184	0.323	0.426	0.690	0.885	1.137	1.268
digital	0.160	0.290	--	--	--	--	--	--

Table 2. WoW for $\theta = 30°$ in dB.

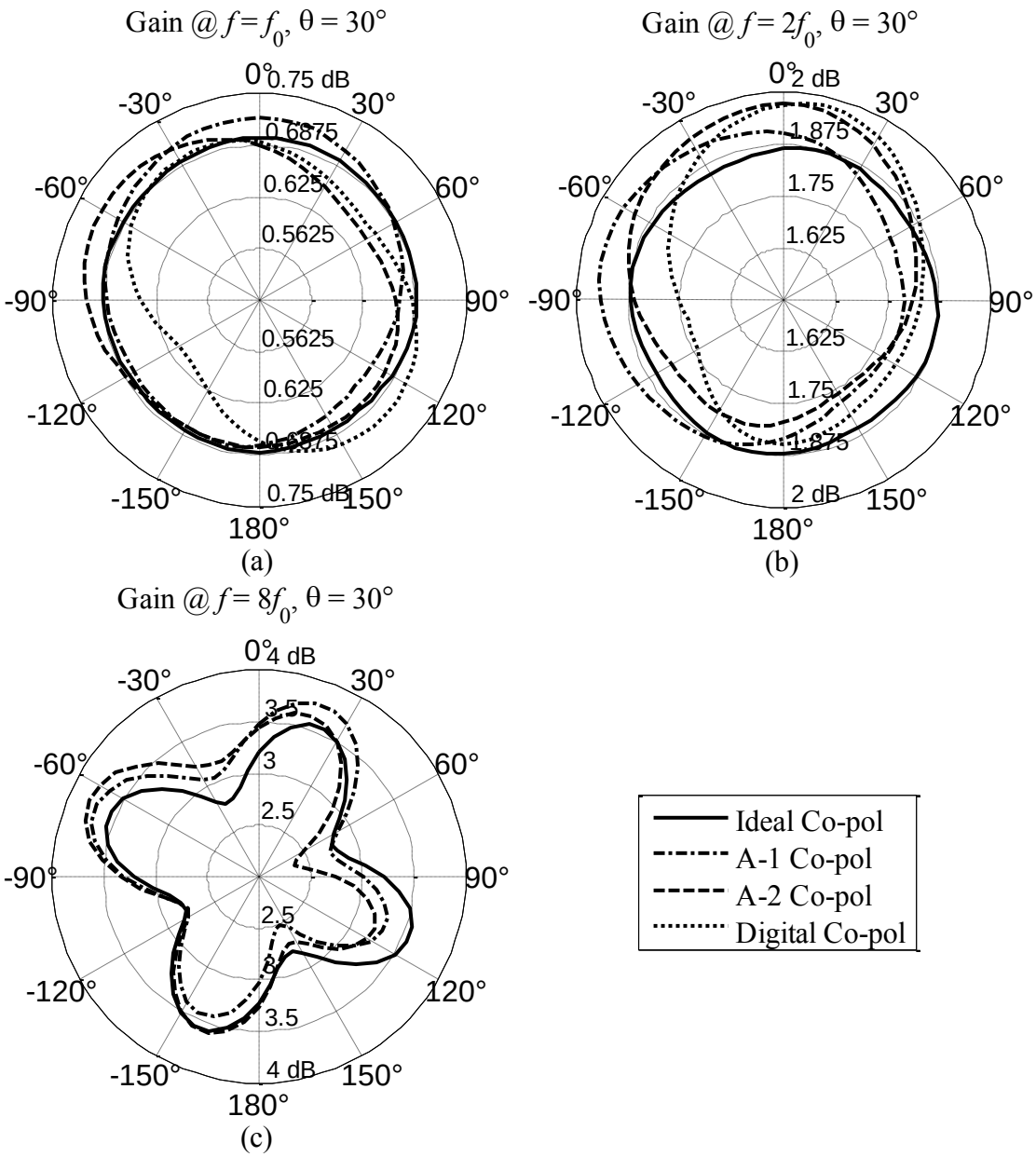

Fig. 19. Phi cuts for antenna far-field for four MFNs showing co-polarization over three different gain ranges. The three patterns are for (a) $f = f_0$, (b) $f = 2f_0$, and (c) $f = 8f_0$. The final plot (c) does not contain digital data because the digital MFN is valid only up to $f = 2.5f_0$.

From the two pattern figures as well as the tables it again must be emphasized that the MFN has a significant impact on the pattern quality and its design and performance are critical. Also from this data it can be seen that not only does the A-2 hybrid cover the entire band with one MFN it has better performance that the commercially available version. Future improvements in digital MFN will further reduce the misbalances and thus enhance the overall pattern stability.

Acknowledgements

This work is sponsored by the Office of Naval Research grant #N00014-07-1-1161. The authors would like to thank W. Neill Kefauver from the University of Colorado.

References

[1] M. J. Radway, W. N. Kefauver, and D. S. Filipović, "On the Use of Spiral Antennas for Electronic Attack", *Proceedings of the 2008 Antenna Applications Symposium*, pp.154-164, Robert Allerton Park, University of Illinois, 2008.
[2] R. G. Corzine and J. A. Mosko, *Four-Arm Spiral Antennas.* Norwood, Massachusetts: Artech House, Inc., 1990.
[3] EMSS, *FEKO 5.3*, EM Software and Systems, Stellenbosch, S. A., 2007.
[4] http://www.pulsarmicrowave.com/products/hybrids/180.htm
[5] http://www.pulsarmicrowave.com/products/hybrids/90deg_51-1251.htm
[6] http://www.pulsarmicrowave.com/products/hybrids/90deg_21-41_stripline.htm
[7] Andrews, D.P. and C.S. Aitchison, "Design of Cascaded Lumped Element Quadrature Hybrids," *IEE Proceedings on Microwaves, Antennas, and Propagation*, Vol. 148, No. 5, Oct 2001, pp. 275-279.
[8] AWR Corp, *AWR Design Environment 2008*, Applied Wave Research Inc., 2008.

REFLECTOR IMPULSE RADIATING ANTENNA DESIGN WITH A WIDEBAND STRIP-LINE BALUN FOR 20 kV IMPULSE

Byeongkwan Kim[1*], Joonho Byun[2], Frances J. Harackiewicz[3], and Byungje Lee[1]
[1]Department of Wireless Communications Engineering
Kwangwoon University
447-1, Wolgye-Dong, Nowon-Gu, Seoul, 139-701, Korea
[2]Digital Media & Communications R&D Center
Samsung Electronics Co., Ltd.
416, Matan-3dong, Yeongtong-gu,
Suwon-City, Gyeonggi-do, 433-742, Korea
[3]Department of Electrical and Computer Engineering
Southern Illinois University
Carbondale, Illinois 62901-6603

Abstract: A reflector impulse radiating antenna (IRA), which can handle a 20 kV impulse input signal, is proposed. The proposed antenna consists of a parabolic reflector, a wideband strip-line balun, and two pairs of feed arms with ground plane. A diameter of the reflector is 1600 mm, and a ratio of focus and diameter (F/D) is 0.38. The proposed strip-line balun can be easily designed and fabricated to avoid the voltage breakdown. The balanced signal fed at the feed arms goes through the balun and then terminated by resistors at the edge of reflector. The feed arms are comprised of two pairs by designing the reflector effectively. The impedance bandwidth (VSWR < 2.5) of the proposed antenna is 1715 MHz (285 - 2000 MHz, 150 %) and its peak gain at boresight (θ = 0 °) is about 17.4 dBi at 1500 MHz.

1. Introduction

Since damage on electronic device by electromagnetic pulse (EMP) was known in 1960s, a research about electronic weapon using high-amplitude electromagnetic pulse (HEMP)

has been begun [1]. For transmitting HEMP to specific direction, high-power electromagnetic source and antenna have been studied [2]. The design of the antenna using the HEMP source is approached by two aspects. The first aspect is a capacity of a high power related to a dielectric breakdown. If the breakdown occurs, a radiation efficiency is decreased and then a reflected power, which generated by the breakdown, can destroy the source. To prevent the breakdown in HEMP system, it is important to consider a material and its dielectric breakdown voltage. The second aspect is a wideband operation with a high gain. The operating frequency of an antenna is wideband because the short rise-time signal, like an impulse, has wideband characteristic in frequency domain. When the rise-time of a Gaussian impulse signal is 500 ps, an energy level of the signal is concentrated on between DC and 1.5 GHz in frequency domain. Therefore, the operation frequency of the antenna covers at least above 1.5 GHz. To obtain these characteristics such as high power handling capacity, wideband operation, and high gain, TEM horn antennas [3], dielectric lens antennas [4], and impulse radiating antennas (IRAs) [5] have been researched. Although the reflector IRAs have been much more interested because of their higher gain, they need a wideband balun as well as a high power and wideband balun. Since a twin coaxial balun (TCB), which needs a 100 Ω coaxial cable, is used for IRAs in general [6], a customized 100 Ω coaxial cable or a conventional 95 Ω cable is used. In this work, the reflector IRA, which is fed by a strip-line balun instead of a TCB, is proposed to transmit a 20 kV impulse signal (rise-time = 500 ps). The proposed strip-line balun designed based on the TCB can achieve a 100 Ω line easily and build a splitter into the strip-line. In addition, the strip-line can handle higher voltage than the coaxial cable in the same dimension. The proposed IRA has mainly two parts. One part is the radiating elements and the parabolic reflector composed of a pair of feed arms and terminated by resistors. The diameter of reflector is 1600 mm (D) and the ratio of focus and diameter is 0.38 (F/D). Another part is the strip-line balun consisted of strip-line filled with the Teflon.

2. Radiating Elements Design

The reflector IRA can transmit the impulse signal with a high gain by locating V-type traveling antenna at a focus of parabolic reflector [7], [8]. Figure 1(a) and (b) show IRA structures having a pair of feed arms whose input impedance is $400\,\Omega$. The design concept of IRA feed arm is based on a biconical vee antenna [8], [9]. Structures of two

feed arms can be approximately derived from an equation (1), which indicates characteristic impedance of two parallel transmission lines [10],

$$Z_0 \approx 120\sqrt{\frac{\mu_r}{\varepsilon_r}}\ln\frac{s}{a} = 276\sqrt{\frac{\mu_r}{\varepsilon_r}}\log\frac{s}{a} \quad (1)$$

where the μ_r is a relative permeability and the ε_r is a relative permittivity of the material. The *s* is a distance between the two lines and *a* is a radius of line. Therefore the impedance of feed arms is 400 Ω when the ratio of *s* and *a* is 28.1. In case of Figure 1 (b), the characteristic impedance of the coplanar feed arms can be approximately equal to the characteristic impedance of conical feed arms when a_e is 4*a*, where the a_e is the width of coplanar feed arm that is design to reduce an aperture blockage [8]. Each feed arm for both Figure 1(a) and Figure 1(b) is terminated by a resistor (200 Ω). In addition, the length of the gap for feed arms is 30 mm in order to handle a 20 kV impulse signal without a breakdown in air (30 kV/cm) [11]. Figure 2 shows the simulated [12] antenna performances with varying overall dimension of IRA having a pair of coplanar feed arms (see Figure 1(b)) when it maintains the input impedance of 400 Ω and the F/D of 0.38. Figure 2(a) shows that three different sizes of antennas are designed so that the VSWR is less than 2.5. Figure 2(b) shows the relative terminated power which is the ratio of the power at resistors of each feed to the input power, and Figure 2(c) shows the antenna efficiencies. It is noticed that while most power is consumed by resistors in the lower frequency band, the radiated power is much more dominant in the higher frequency band. Also, the radiated power is increased as the antenna size becomes larger.

3. Structure of Proposed IRA

Figure 3 shows the overall view of the proposed antenna with dimensions. In general, two pairs of feed arms are used in order to design the reflector effectively and match the impedance efficiently between output of the balun and the input of the feed arms [5], [10]. Each pair of feed arms is crossed at an angle (α) of 90 degrees. The proposed strip-line balun is located at center of two pairs of feed arms. In this location, the ground plane acts as the ground for the balun. In addition, it does reduce the cross polarized field of feed arms. Figure 4 shows a structure of the proposed strip-line balun. The strip-line of balun

is located between two ground planes and the strip-line is filled with Teflon ($\varepsilon_r = 2.08$, 900 kV/cm). A height of the strip-line is 10 mm, and two ground planes are shorted by the metal wall (W_3 = 40 mm, W_4 = 20 mm). The 50 Ω line, which is input part of the balun (W_1 = 8.75 mm), is divided into two 100 Ω lines (line 1 and line 2, W_2 = 2.28 mm) by a splitter. By shorting the strip line 2 and the ground of strip line 1, the balance signal is generated between the strip line 1 and the ground of strip line, so that its output impedance becomes 200 Ω. Ground plane and metal wall of two 100 Ω lines are partially covered with a ferrite material to reduce a current on the exterior of 100 Ω line ground [6]. Figure 5 shows the connection between the input parts of feed arms and the output part of the balun. The distance of gap of input of feed arms was initially designed with 30 mm for handling 20 kV. However the distance of gap of proposed antenna becomes 40 mm after placing a 10 mm height of the balun. Then, the gap between the ground plane and the input part of the feed arms is 15 mm. Figure 6 shows the fabricated antenna. The antenna shown in Figure 6 used the parabolic reflector of the commercial satellite antenna (D = 1600 mm, F/D = 0.38) to cover the lower frequency below 300 MHz. The resistors between the feed arms and the reflector are the metal film resistors (200 Ω, 2 Watts), and they are arrayed by seven strings [11].

4. Simulation and Experiment Results

Figure 7 shows the simulated results of the proposed antenna by using CST's MWS simulator [12]. It is noticed that while the power below 300 MHz is almost consumed by resistors, the power above 300 MHz is mostly radiated before the input signal arrives at resistors. In these simulation results, the balun structure is omitted from the proposed antenna because the size of the problem is too big to get accurate results. Figure 8 shows the measured result of the proposed strip-line balun by the back-to-back balun measurement [13]. The measured results indicate that the balun is fairly operated from 200 to 1600 MHz. Figure 9 shows the measured return loss of the proposed antenna including the strip-line balun. The measured impedance bandwidth ranges from 285 to 2000 MHz under VSWR < 2.5. Figure 10 shows the simulated radiation patterns in the y-z plane. Figure 11 shows the simulated and measured gains on the boresight ($\theta = 0°$) from 200 to 2000 MHz.

5. Conclusion

The reflector IRA having a simple balun structure is proposed. To handle 20 kV impulse signal, the length of the air gap between the input part of the feed arms and the ground plane is maintained by 15 mm, and Teflon is used for the balun. The proposed reflector IRA has wide bandwidth (285 - 2000 MHz, VSWR < 2.5) and high gain (17.4 dBi at 1500 MHz). Its overall size is 620 mm × 1600 mm × 1600 mm. In the future, the accurate measured results of the proposed antenna may be available, and this antenna will be improved to get the broader band operation, higher gain, and higher power handling capability

6. Acknowledgments

This work was supported by the Ministry of Knowledge Economy and Korea Electronics Technology Institute (KETI) Research Grant.

7. References

[1] C. E. Baum, “Reminiscences of High-Power Electromagnetics”, IEEE Trans. Electromag. Compat., vol. 49, pp. 211-218, May 2007.

[2] D. V. Giri, High-power Electromagnetic Radiators, pp. 55-136, Cambridge, Massachusetts and London: Harvard University Press, 2004.

[3] D. A. Kolokotronis, Y. Hung, and J. T. Zhang, “Design of TEM Horn Antennas for Impulse Radar”, IEEE High-Freq. Postgrad. Student Colloq., pp. 120-126, September 1999.

[4] W. S. Bigelow, E. G. Farr, L. H. Bowen, D. E. Ellibee, and D. I. Lawry, “Design and Characterization of a Lens TEM Horn”, Sensor and Simulation Notes 490, April 2004.

[5] M. Majid and R. S. Yahya, “On the Characterization of a Reflector Impulse Radiating Antenna (IRA): Full-Wave Analysis and Measured Results”, IEEE Trans. Ant. Propagat., vol. 54, pp. 812-822, March 2006.

[6] G. D. Sower, D. P. Mclemore, and W. D. Prather, “Quad Coaxial Balun”, Measurement Notes 44, August 1993.

[7] C. A. Balanis, Antenna Theory, pp. 549-600, 3rd ed., New Jersey: John Wiley & Sons, 2005.

[8] E. G. Farr, “Optimizing the Feed Impedance of Impulse Radiating Antennas Part I: Reflector IRAs”, Sensor and Simulation Notes 354, January 1993.

[9] J. D. Kraus, Antennas for All Applications, pp. 378-400, 3rd ed., New York: McGraw Hill, 2002.

[10] P. A. Rizzi, Microwave Engineering, pp. 182-185, New Jersey: Prentice Hall, 1988.

[11] L. H. Bowen, E. G. Farr, and W. D. Frather, “A High-Voltage Cable-Fed Impulse Radiating Antenna”, Sensor and Simulation Notes 507, December 2005.

[12] CST Microwave Studio, Version 2008, CST GmbH, Darmstadt, Germany.

[13] H. T. Kim, S. Lee, J. H. Park, Y. K. Kim, and Y. Kwon, “Ultra-wideband Uniplanar MMIC Balun Using Field Transformations”, IET Elect. Lett., vol. 42, pp. 359-361, March 2006.

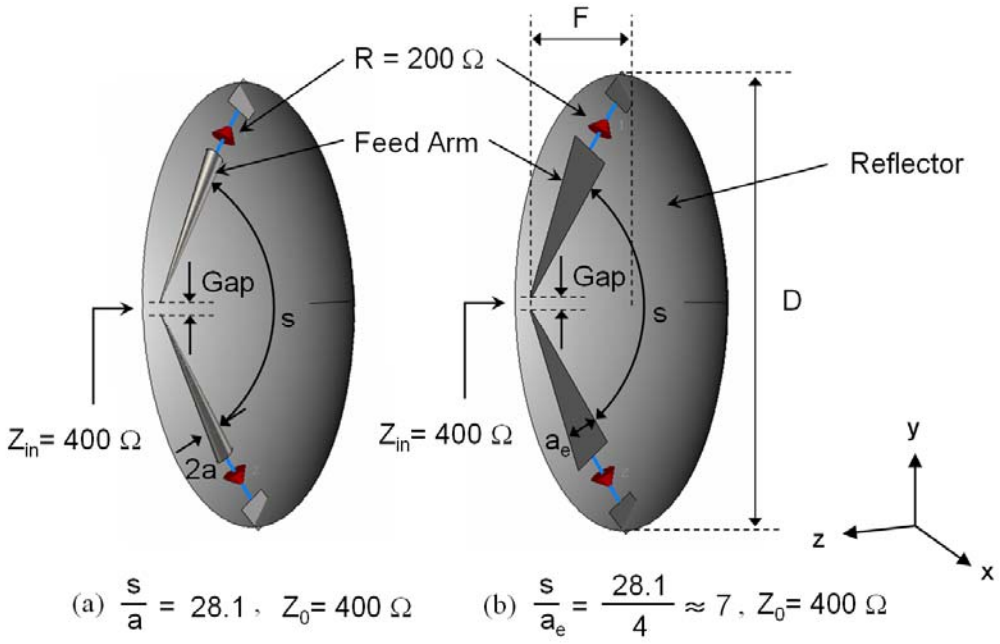

Figure 1. Radiating Elements of IRA Having a Pair of Feed Arms; (a) Conical Feed Arms, (b) Coplanar Feed Arms

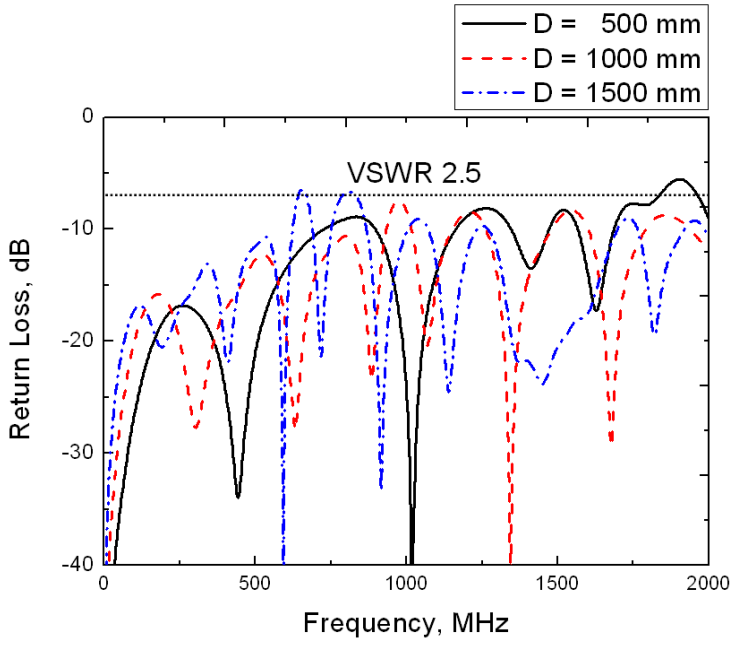

Figure 2 (a). Simulated Return Losses with Varying Overall Dimension of IRA Having a Pair of Coplanar Feed Arms

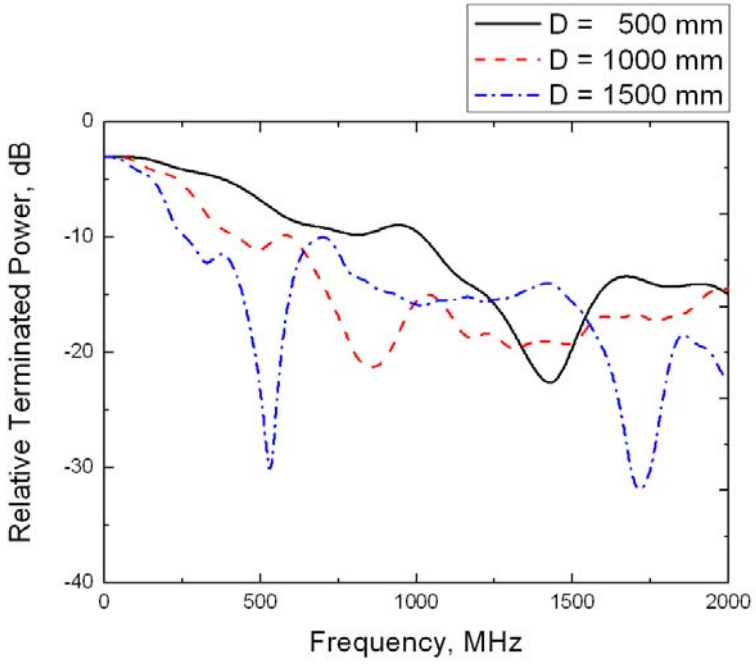

Figure 2 (b). Simulated Relative Terminated Powers with Varying Overall Dimension of IRA Having a Pair of Coplanar Feed Arms

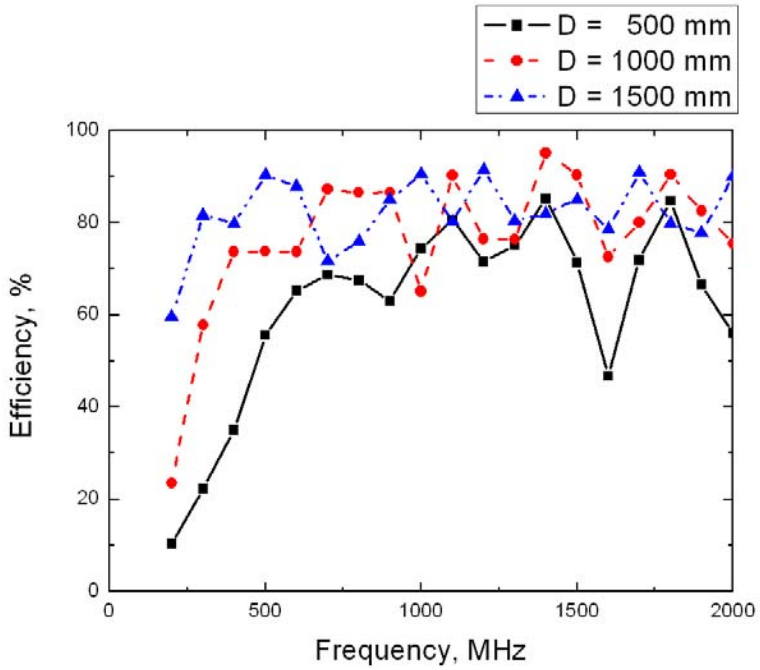

Figure 2 (c). Simulated Efficiencies with Varying Overall Dimension of IRA Having a Pair of Coplanar Feed Arms

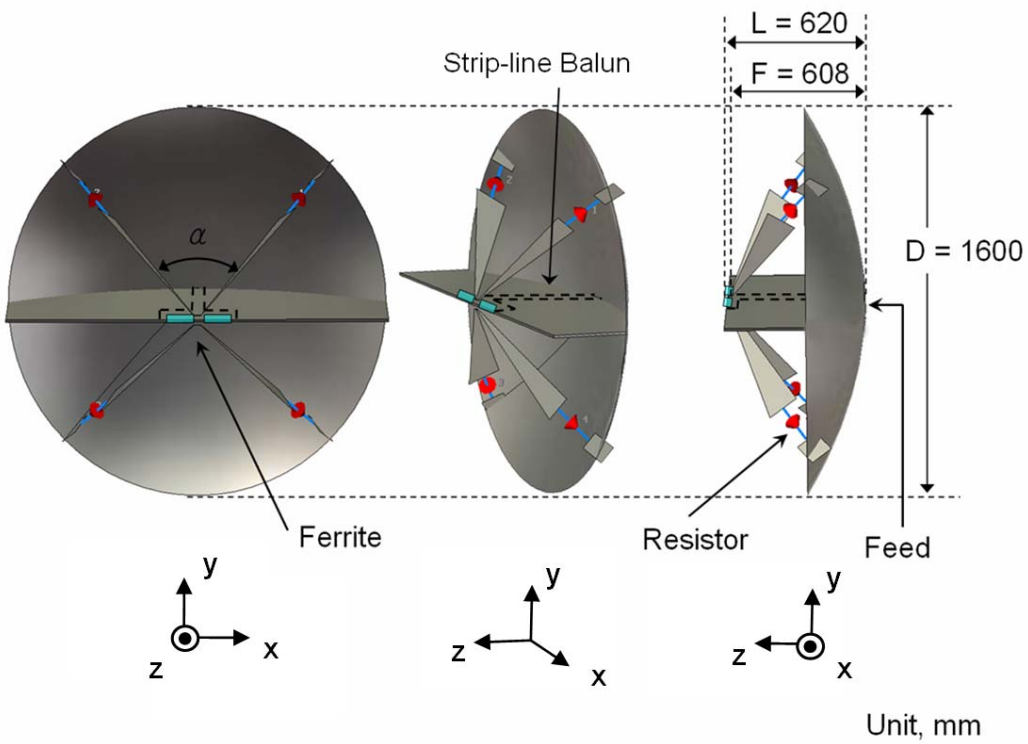

Figure 3. Overall View of Proposed Antenna

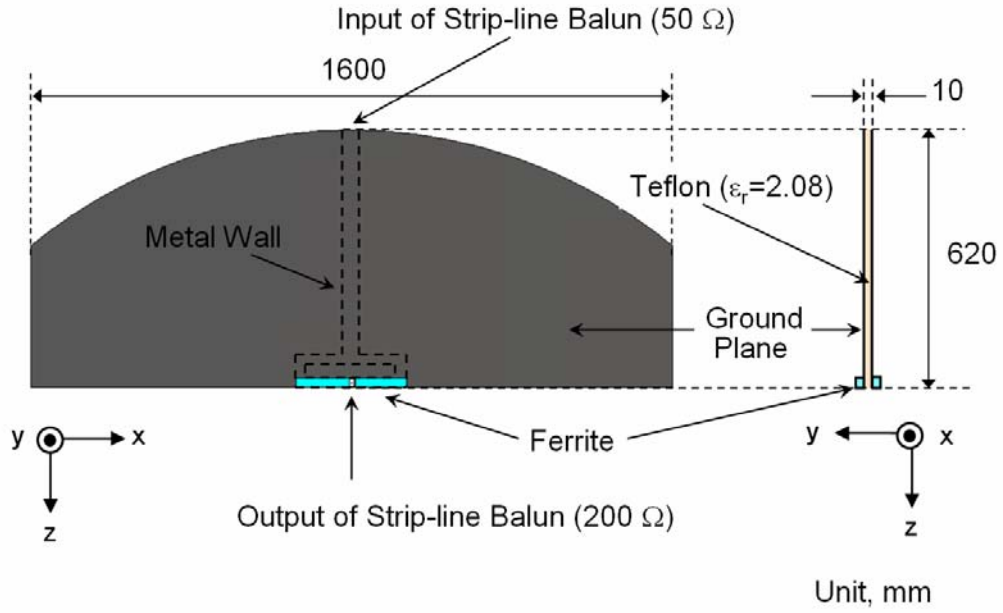

Figure 4 (a). Top and Side View of Strip-line Balun

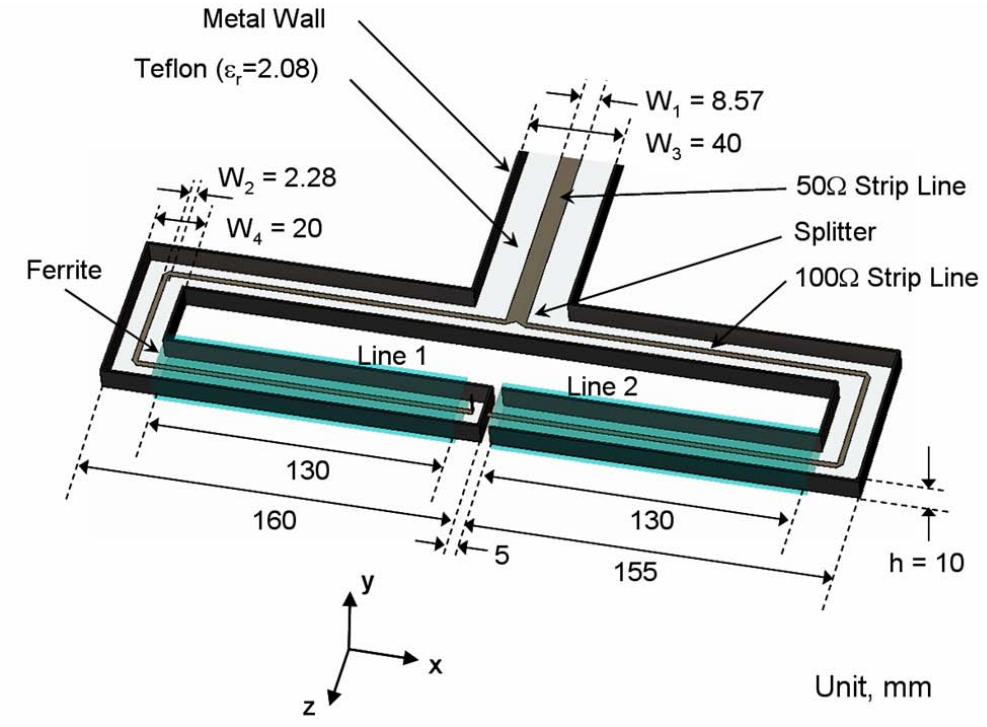

Figure 4 (b). Detailed View of Strip-line Balun

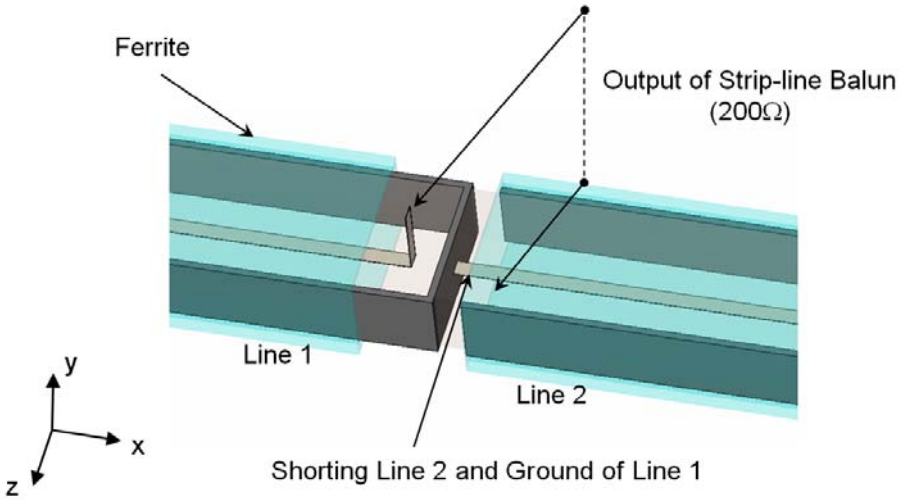

Figure 4 (c). Output Part of Strip-line Balun

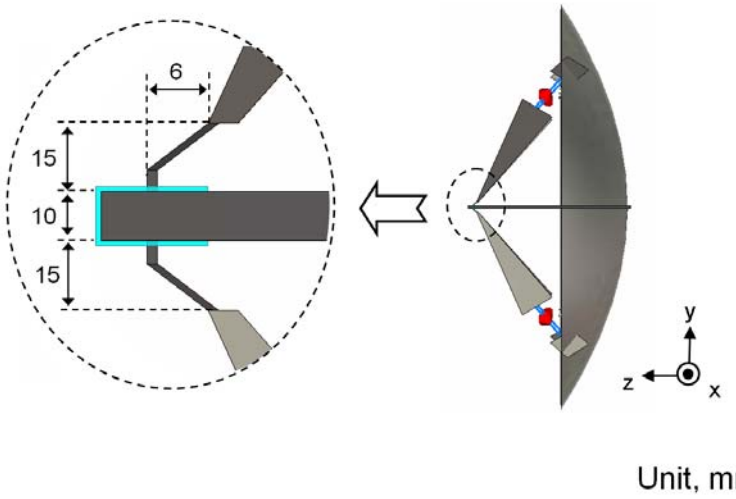

Figure 5. Connection between Input Parts of Feed Arms and Output Part of Balun

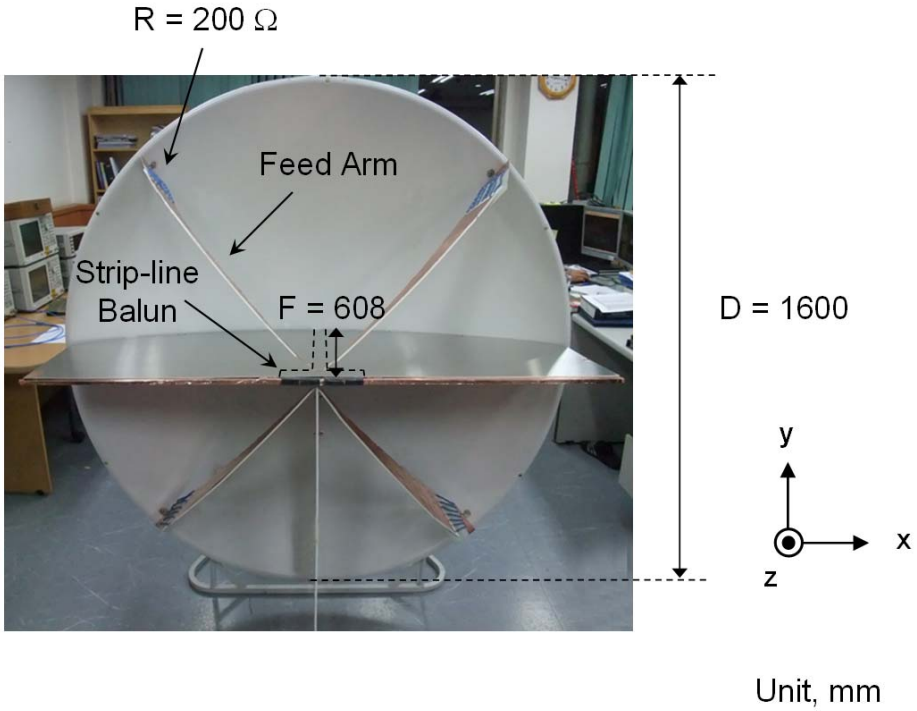

(a)

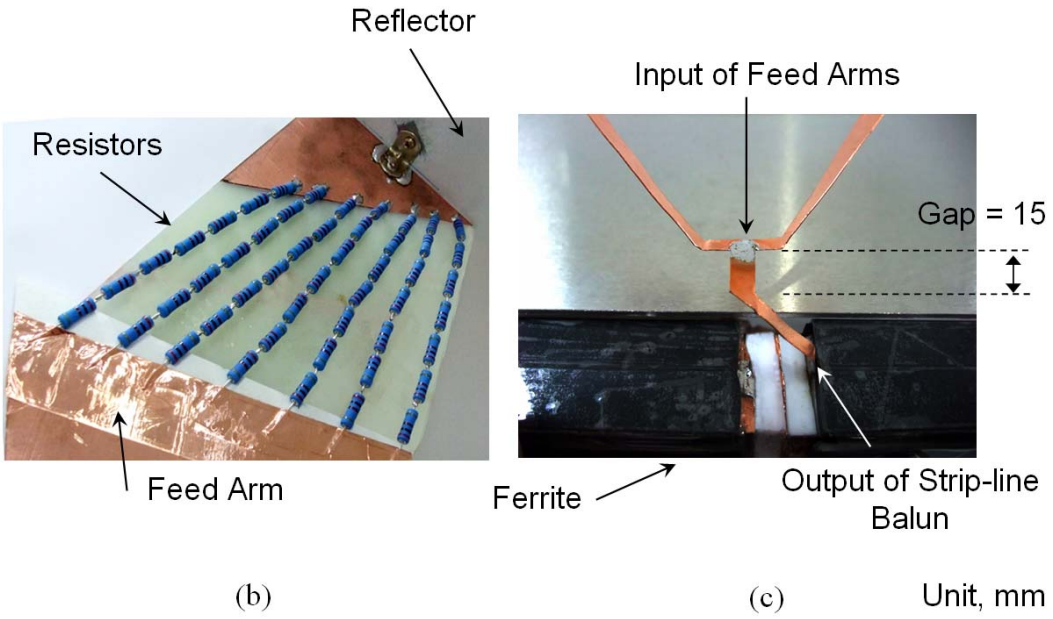

Figure 6. Photograph of Fabricated Antenna ; (a) Overall view, (b) Seven Strings Resistors, (c) Input of Feed Arms and Output of Strip-line Balun

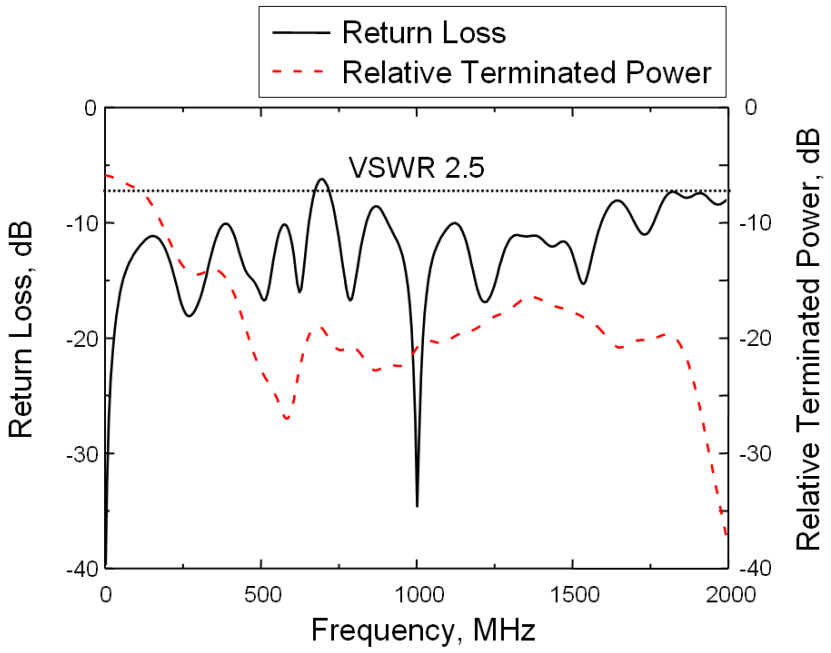

Figure 7. Simulated Return Loss and Relative Terminated Power of Proposed Antenna

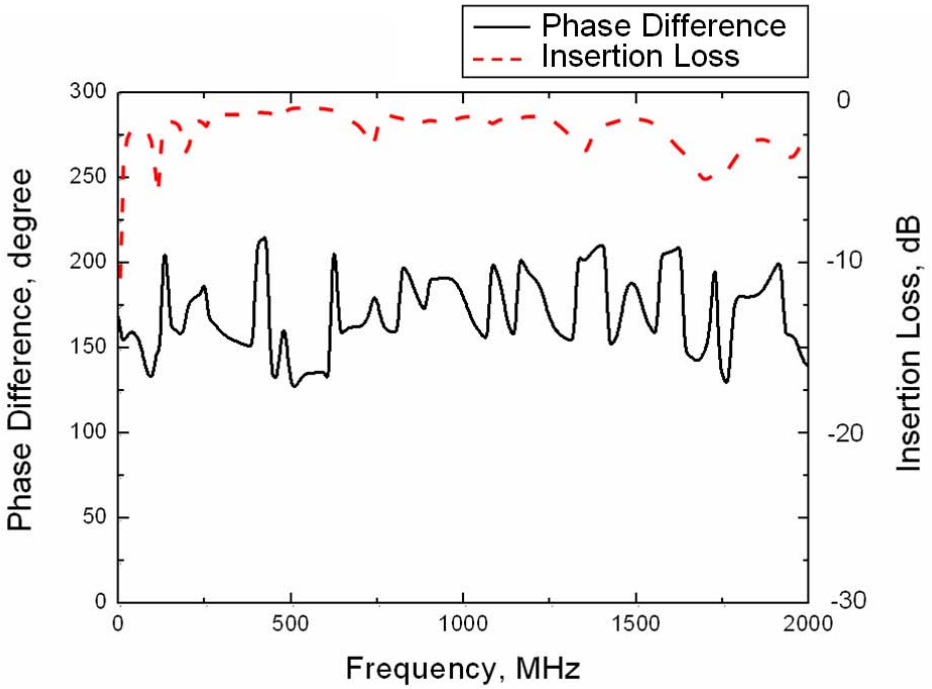

Figure 8. Measured Insertion Loss and Phase Difference of Proposed Strip-line Balun

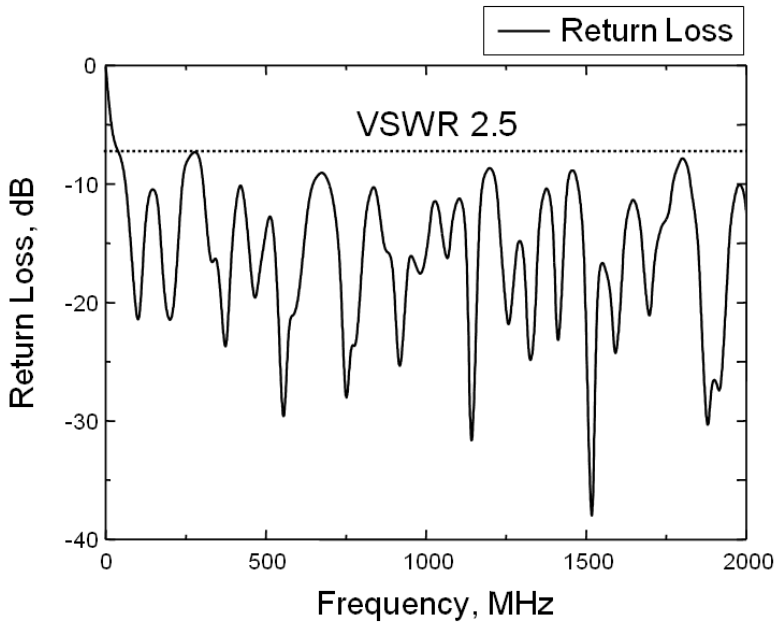

Figure 9. Measured Return Loss of Proposed Antenna

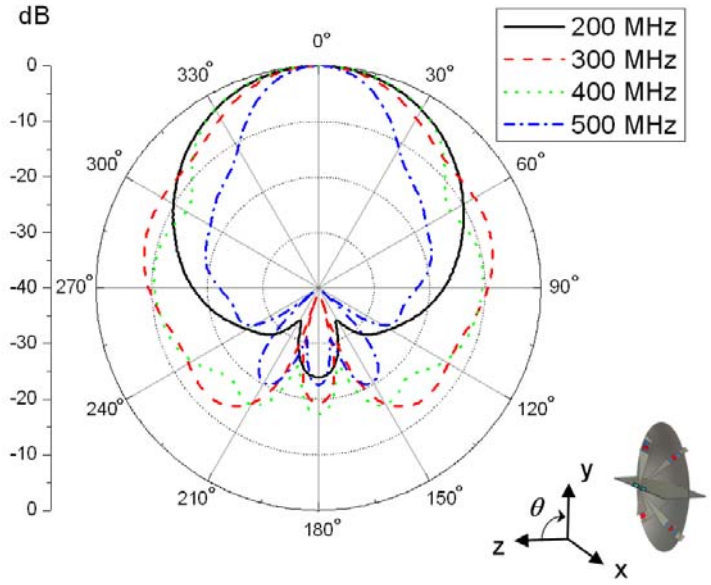
dB
0
-10
-20
-30
-40
-30
-20
-10
0
0°
30°
60°
90°
120°
150°
180°
210°
240°
270°
300°
330°
200 MHz
300 MHz
400 MHz
500 MHz
θ
y
z
x

(a)

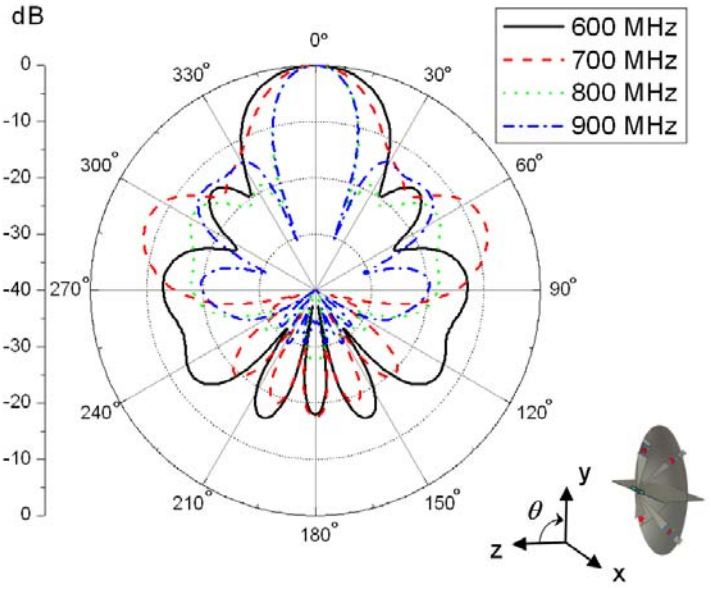
dB
0
-10
-20
-30
-40
-30
-20
-10
0
0°
30°
60°
90°
120°
150°
180°
210°
240°
270°
300°
330°
600 MHz
700 MHz
800 MHz
900 MHz
θ
y
z
x

(b)

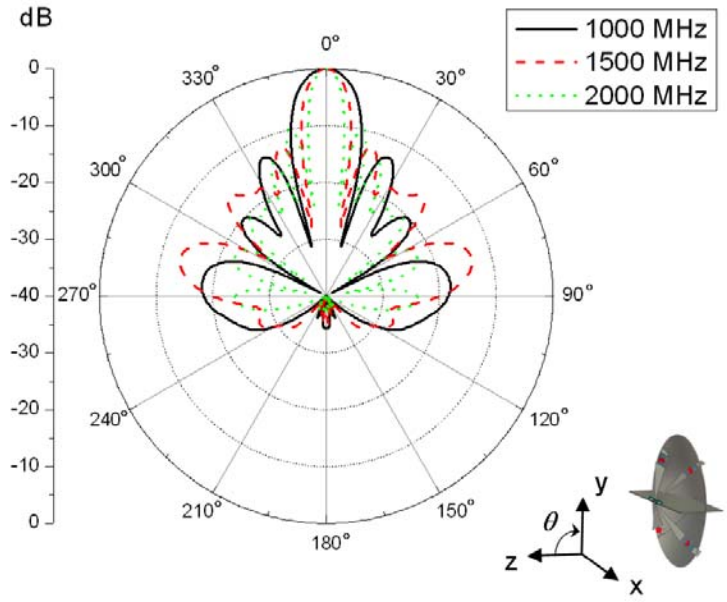

(c)

Figure 10. Simulated Radiation Patterns (y-z plane) at ; (a) 200 - 500 MHz, (b) 600 - 900 MHz, (c) 1000 - 2000 MHz

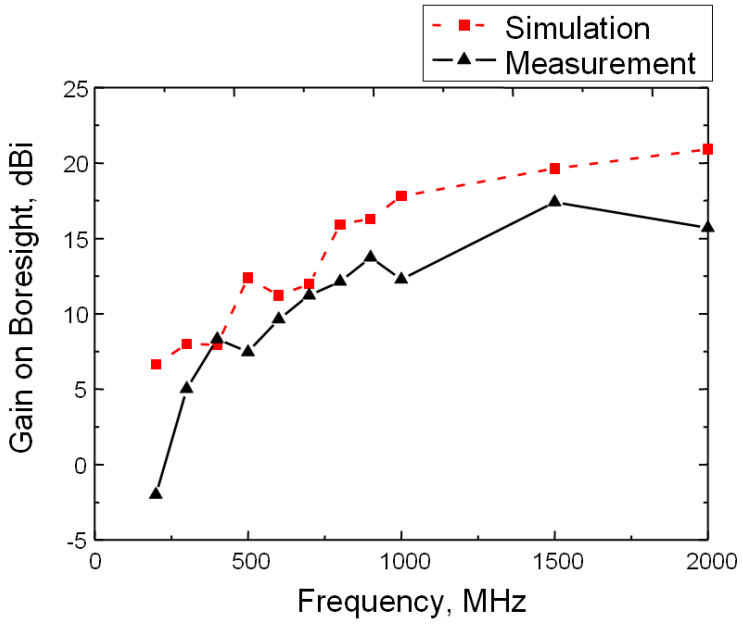

Figure 11. Antenna Gains on boresight (θ = 0°)

Wide-Band Dual Patch Aperture Coupled Antenna

Youn M. Lee
U.S. Army Research Laboratory
2800 Powder Mill Road
Adelphi, MD 20783
youn.lee@us.army.mil

Abstract

An aperture coupled dual patch microstrip antenna is designed with a geometry that greatly enhances it's bandwidth. The achieved bandwidth is 73% and 80% for standing wave ratio of 1.5:1 and 2.0:1, respectively. To reduce the size of the antenna, a 0.062-inch thick FR-4 fiberglass is used as a substrate material for both patches. However, Rogers Duroid 5880 was used for aperture and feed line substrate material. The design uses poplar wood to hold the three dielectric sheets together. Application of this antenna is for ultrawideband radar. The antennas may become elements of a physical array of receivers in order to form a cross-range aperture.

1. Introduction

Without a doubt, a microstrip patch antenna is very attractive for many applications because of its low cost, simplicity in fabrication, and conformability. To design a wide-band patch antenna, many researchers have used an aperture to excite a patch or stacked patches [1-6]. For stacked patches, a parasitic element is placed above a lower patch. For this type of design, a bandwidth of 30 – 35% was achieved [7]. In addition, a near resonant aperture with a thick antenna substrate can provide similar performance [8-10]. By using a radiating aperture and dual stacked patches, 69% impedance bandwidth (VSWR of less than 2:1) was achieved. However, VSWR of 1.5:1 bandwidth was 21% [11].

There were a few different approaches reported in exciting the aperture [11-12], however dual offset feed lines were used in this effort. For antenna-element substrate material, 0.062-inch thick fiberglass material was used to reduce the antenna size, while Rogers Duroid 5880 was used as feed line substrate material. The design employs Poplar wood to maintain the gap between them.

As a first step, dual feed line and an aperture on opposite sides of the substrate material was modeled. After fine-tuning the transmission line width, the aperture length and width were adjusted to tune the low end of the desired frequency band. Subsequently, a patch was added and the air gap between the patch and feed layer was adjusted for which the return loss and the desired frequency band were optimized. Upon completion of adjustment, a second patch was added on top of the first patch with an air gap in between them. Results of these efforts are delineated in the following section. Two prototypes were fabricated and their performances are reported in the following sections.

2. Design Procedure

A customer placed a stringent limitation on the antenna size. Therefore, I made a decision to use FR-4 fiberglass as an antenna substrate. The dielectric constant of the FR-4 that I used in computation was 4.4, and the loss tangent was 0.02. These values are frequently used by many researchers and are used by HFSS software [13]. On the other hand, a fiberglass manufacturer posted its value as 5.2 measured at 1 MHz and the dissipation factor as 0.025 also measured at the 1 MHz. For aperture and feed line substrate material, Rogers Duroid 5880 was used to minimize loss within the feed structure. The dielectric constant of the Duroid 5880 is 2.2 measured at 10 GHz, and the loss tangent is 0.0009 also measured at 10 GHz [14].

A relatively thin dielectric material, 0.0094 wavelength at the highest frequency (1.8 GHz), was used as the antenna substrate. A positive aspect of using the thin dielectric material is improvement in the surface wave efficiency, which Targonski et al described in [11].
One possible drawback of using the thin dielectric material can be the slight warping of the material when fabricated, which would probably happen when these antenna elements are put together using Poplar wood. It may have reduced the impedance bandwidth a little, but I did not verify it because of difficulty in correcting the problem. To check the severity of warpage, the antenna was placed on a flat surface. Then, the heights of antenna elements were measured at three places, two edges and the center. The difference of height between the edges and the center portion of each element was on average 0.024 inch and 0.007 inch, for Duroid 5880 and the FR-4 material, respectively. The fiberglass is very stiff, but the Duroid material is fairly flexible. The dielectric material was about 7.7 inches wide. However, the 0.024 inches is about 0.002 wavelengths at 1 GHz, which may have a negligible effect.

The design was started by calculating the width of the microstrip line for 100 ohm and 50 ohm for 0.062” thick material and the dielectric constant of 2.2. The line widths were adjusted to 1.2mm and 4.8mm after the computer simulations As briefly mentioned in introduction, the dual offset feed line was used, and Targonski et al [11] reported details of the design. The two parallel sections of the 100-ohm line are 57.4 mm long, when measured from the corner to the end (see figure 1). The other section of the 100-ohm line, perpendicular to the parallel 100-ohm line is 98.8 mm long when measured from inner edges of the 100-ohm parallel transmission lines. A single stub is used on the 50-ohm line to optimize impedance matching. The stub is located -50 mm from the center of the aperture (to left in the figure 1) and is 4 mm long. A quarter-wave matching transformer is not used as part of a power splitter between the 50-ohm line and 100-ohm line because of the lack of room to add it. The whole transmission line is shifted 2 mm to the left in reference to the center of the aperture as shown in Figure 1.

To avoid complications, the first model had transmission lines and a ground plane on opposite sides of the Duroid 5880, 182 mm by 150 mm and 1.57 mm thick, with an aperture as shown in Figure 1. The desired minimum frequency range for a SWR of 2:1 or less was from 0.75 GHz to 1.25 GHz. The initial aperture size was 10 mm by 152 mm. It was placed at the center of the dielectric material at the center portion of the ground plane. The starting length was determined by choosing a nominally short 10 mm. The width of the aperture was chosen as 1.5 times the ½ wavelength in dielectric material at the desired center frequency of 1 GHz. Figure 2 shows the return loss of the model, and its resonant frequency at around 0.79 GHz. Figure 3 exhibits

impedance locus in the Smith chart. The trace starts at 0.6 GHz, at the top- left and ends at 1.0 GHz.

Next, a patch was added on top of the aperture using 0.062-inch thick FR-4 dielectric material. The initial length of the patch was 100 mm, which is ½ of the wavelength in dielectric material at the desired center frequency of 1 GHz. The initial width of the patch was 150 mm. Won-Gyu Jang and Jae-Hoon Choi used the air gap on their multiband aperture-stacked patch antenna design [15]. The height of the air gap between the feed layer and the patch was 24mm. Figure 4 shows two small loops in the Smith chart that indicate presence of some mutual coupling between the aperture and the patch.

A second patch was then added on top of the first patch. The initial air gap between the first and second patches was 24mm; the same distance between the feed layer and the first patch. Figure 5 is the computed impedance trace in the Smith chart of the dual patch aperture coupled antenna. As shown in tables 1 and 2, the computed and measured SWR bandwidths are very similar. Figure 6 shows the computed and measured SWR of the aperture-coupled antenna with dual patch.

3. Front to Back Ratio, Gain and Radiation Patterns

Since the application of the antenna is for radar, Back radiation needs to be minimized. To accomplish that, a reflector was placed by following the steps provided by Won-Gyu Jang et el [15]. The 4mm wide and 98 mm long reflector was placed 70 mm below the feed line, To probe further, another reflector was added. The front to back ratio was calculated for the following configurations: (1) Two reflectors were placed just below the parallel portions of the 100-ohm transmission line, and (2) two reflectors were placed equally spaced within the dielectric material. The size of the each reflector is the same as that of the single reflector. The results are tabulated in tables' three to six, and are graphed in Figure 8.

Figure 9 shows the measured and computed realized-peak gain as a function of frequency from 0.75 GHz to 1.75 GHz. The computed realized-peak gains are higher than the measured gain. A possible cause of the discrepancy is that the dielectric constants and the loss tangent data used in the simulation were not a function of frequency.

Figure 10 shows the measured radiation pattern of E plane at 1.05 GHz. Figure 11 displays the measured radiation pattern of H plane at 1.05 GHz. These patterns were measured near the desired frequency of 1 GHz. However, radiation patterns change as a function of frequency.

4. Conclusion

This paper presented a very broadband aperture coupled dual patch antenna. Dual offset feed lines were used to feed the aperture. The measured bandwidth of the antenna was significantly higher than the previously reported microstrip patch antenna. The SWR of 1.5:1 was especially higher at 73%. Through computation, it showed that the two reflectors work much better than the single or no reflectors in improving front to back ratio.

Table 1. Measured SWR of Antenna Number 1.

SWR	Low Freq.	High Freq.	center freq.	BW
2:01	7.64E+08	1.79E+09	1.28E+09	80.34%
1.5:1	7.85E+08	1.69E+09	1.24E+09	73.13%

Table 2. Computed SWR.

SWR	Low Freq.	High Freq.	center freq.	BW
2:01	7.50E+08	1.75E+09	1.25E+09	80.00%
1.5:1	7.73E+08	1.67E+09	1.22E+09	73.43%

Table 3. Computed front to back ratio (H field) of aperture coupled dual patch antenna without a reflector. Dot dashed green line represents the data in figure 8.

Frequency, GHz	Front, dB	Back, dB	Front/back ratio
0.75	7.27	5.36	1.91
0.85	6.8	5.49	1.31
0.95	6.23	6.52	-0.29
1.05	5.17	7.06	-1.89
1.15	7.68	5.61	2.07
1.25	8.14	5.56	2.58
1.35	8.69	4.9	3.79
1.45	7.68	4.67	3.01
1.55	8.06	6.37	1.69
1.65	5.17	7.39	-2.22
1.75	1.88	7.2	-5.32

Table 4. Computed front to back ratio (H field) of aperture coupled dual patch antenna with a reflector. Solid blue line represents the data in figure 8.

Frequency, GHz	Front, dB	Back, dB	Front/back ratio
0.75	6.01	5.6	0.41
0.85	6.75	5.5	1.25
0.95	7	5.7	1.3
1.05	8.7	4.2	4.5
1.15	9.88	-2.69	12.57
1.25	9.58	-0.5	10.08
1.35	9.48	0.8	8.68
1.45	9.71	1.97	7.74
1.55	8.97	4.97	4
1.65	6.34	6.93	-0.59
1.75	2.92	7.39	-4.47

Table 5. Computed front to back ratio (H field) of aperture coupled dual patch antenna with two reflectors equally spaced. Short dashed pink line represents the data in figure 8.

Frequency, GHz	Front, dB	Back, dB	Front/back ratio
0.75	6.05	6.64	-0.59
0.85	6.13	6.55	-0.42
0.95	6.83	5.74	1.09
1.05	8.35	4.29	4.06
1.15	9.56	1.94	7.62
1.25	10.13	-0.95	11.08
1.35	10.36	-3.76	14.12
1.45	10.63	-3.93	14.56
1.55	10.07	-0.28	10.35
1.65	7.49	2.37	5.12
1.75	3.25	2.91	0.34

Table 6. Computed front to back ratio (H field) of aperture coupled dual patch antenna with two reflectors placed just below the parallel 100-ohm transmission line. Dashed black line represents the data in figure 8.

Frequency, GHz	Front, dB	Back, dB	Front/back ratio
0.75	5.33	6.35	-1.02
0.85	6.02	6.3	-0.28
0.95	6.94	5.92	1.02
1.05	8.51	4.66	3.85
1.15	9.77	1.85	7.92
1.25	10.34	-2.57	12.91
1.35	10.66	-6.49	17.15
1.45	11.02	-2.48	13.5
1.55	9.66	1.89	7.77
1.65	5.99	3.16	2.83
1.75	1.75	3.93	-2.18

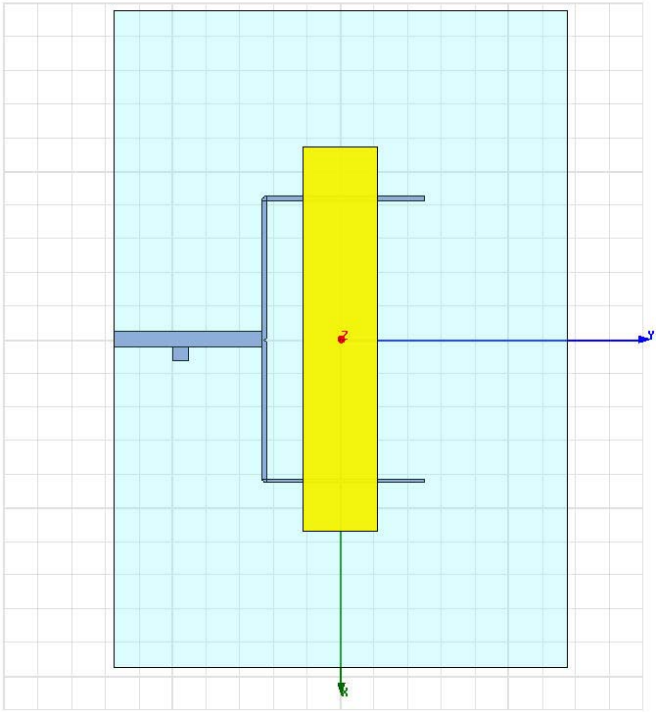

Figure 1. A top view of the HFSS model is shown with the aperture. The feed lines are on the surface of the Duroid 5880. The aperture size is 10 mm by 145 mm and is located at the center of the ground plane.

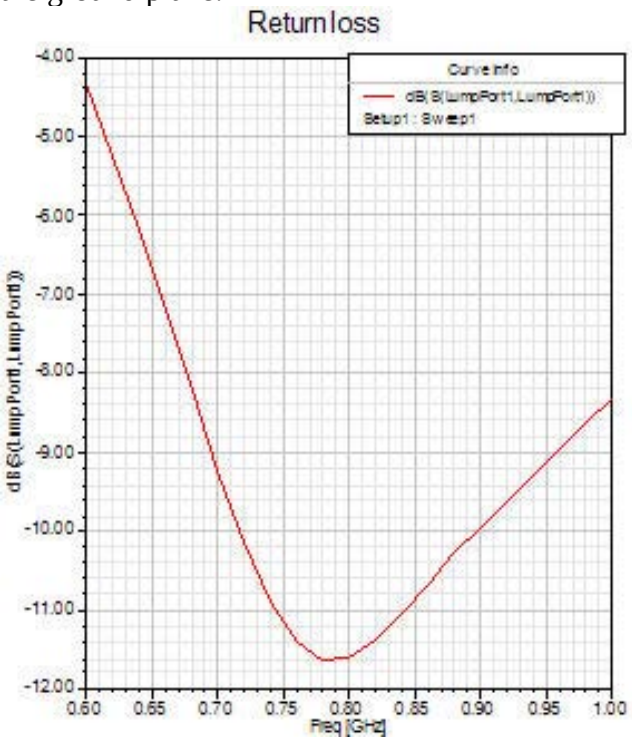

Figure 2. Simulated return loss of the model shown in figure 1. The resonant frequency of the model shown in figure 1 is 0.79 GHz, near the low end of the operating frequency range.

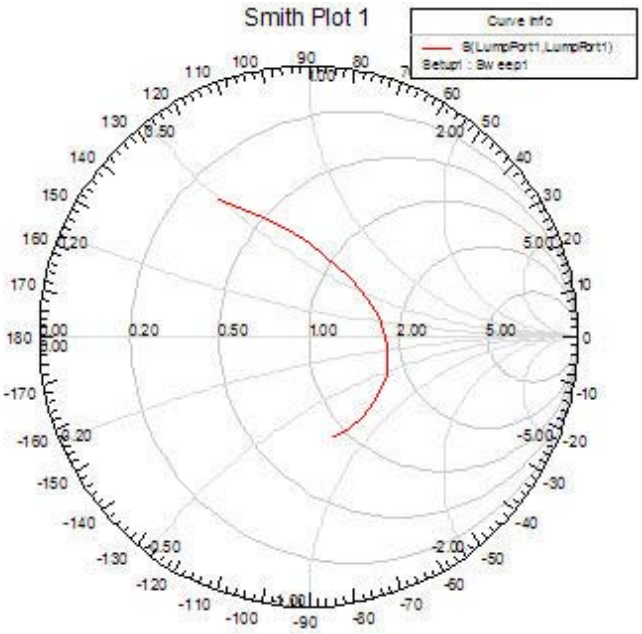

Figure 3. Simulated impedance locus is shown on the Smith chart from 0.6 GHz to 1 GHz. Starting point is at the top at 0.6 GHz for the model shown in figure 1 without any antenna elements.

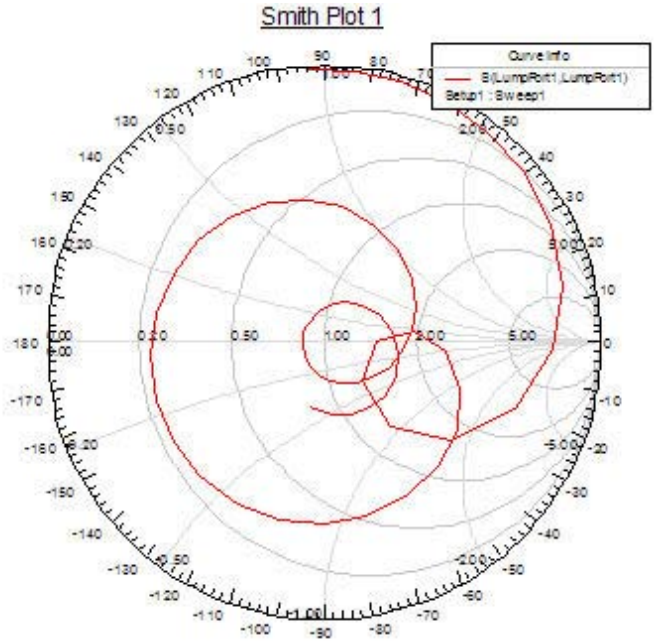

Figure 4. Computed impedance locus of the patch antenna fed by an aperture. Presence of two loops indicate mutual coupling between the aperture and the patch. The resonance occurs at 0.96 GHz and 1.68 GHz. The aperture size is 12 mm by 88 mm, and the patch size is 95.3 mm by 145 mm. The patch dielectric material is 0.062-inch thick FR-4 fiberglass.

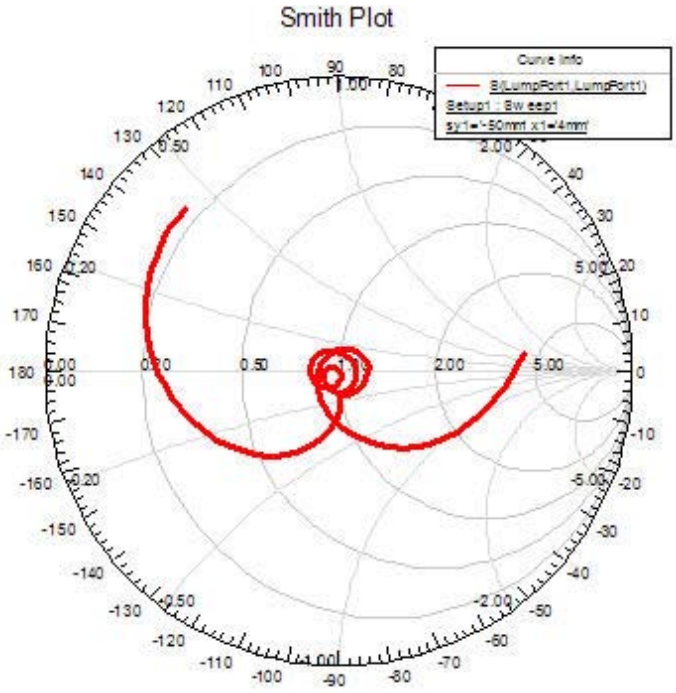

Figure 5. Impedance trace of the aperture coupled antenna in the Smith chart with dual patch.

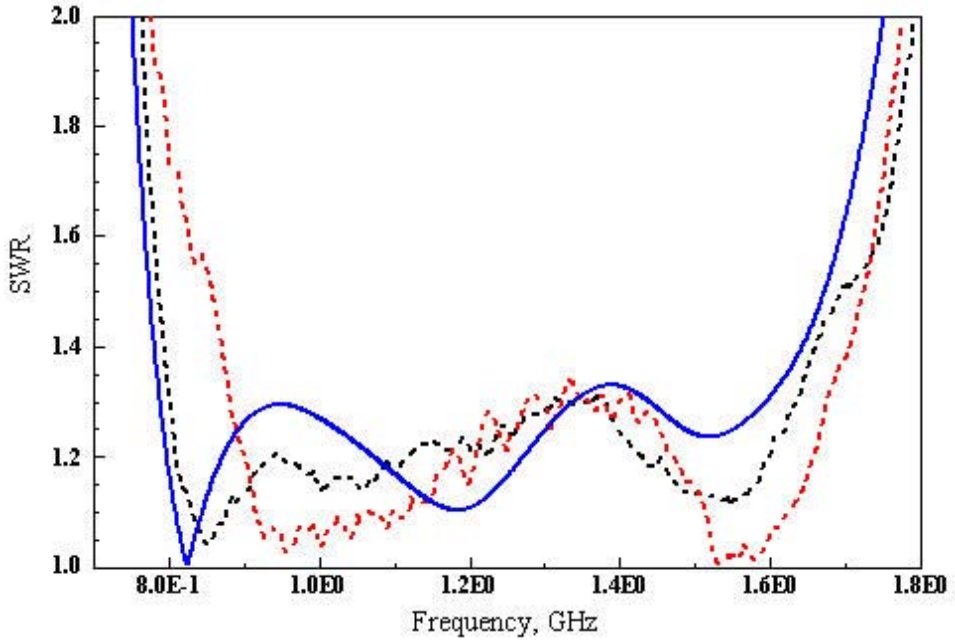

Figure 6. Computed and measured SWR of the aperture-coupled antenna with dual patch. Solid blue line is the computed results, black dashed line is the measured SWR of antenna no.1, and red dashed line is antenna no.2.

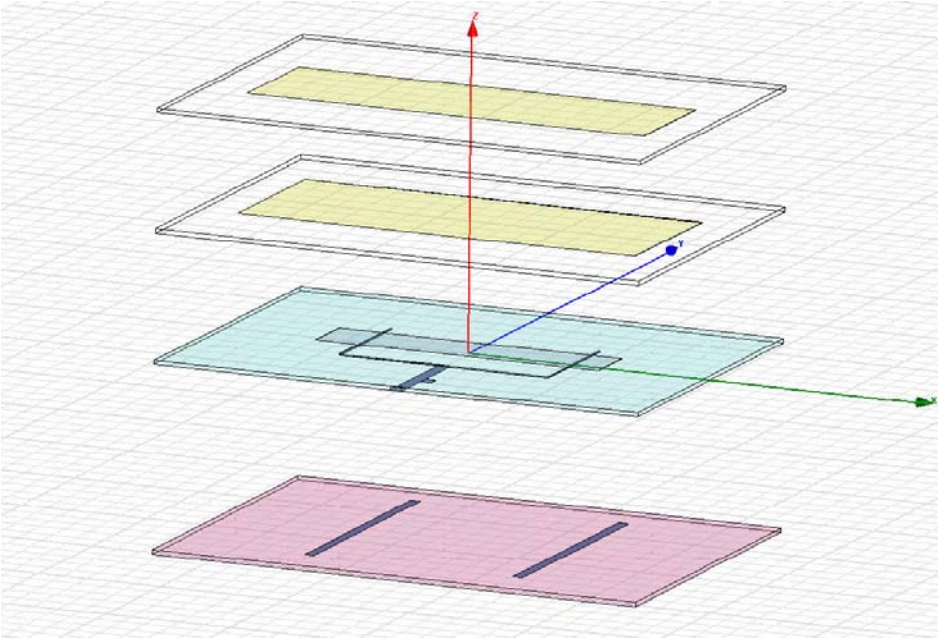

Figure 7. Exploded view the aperture-coupled dual patch antenna is shown with two reflectors.

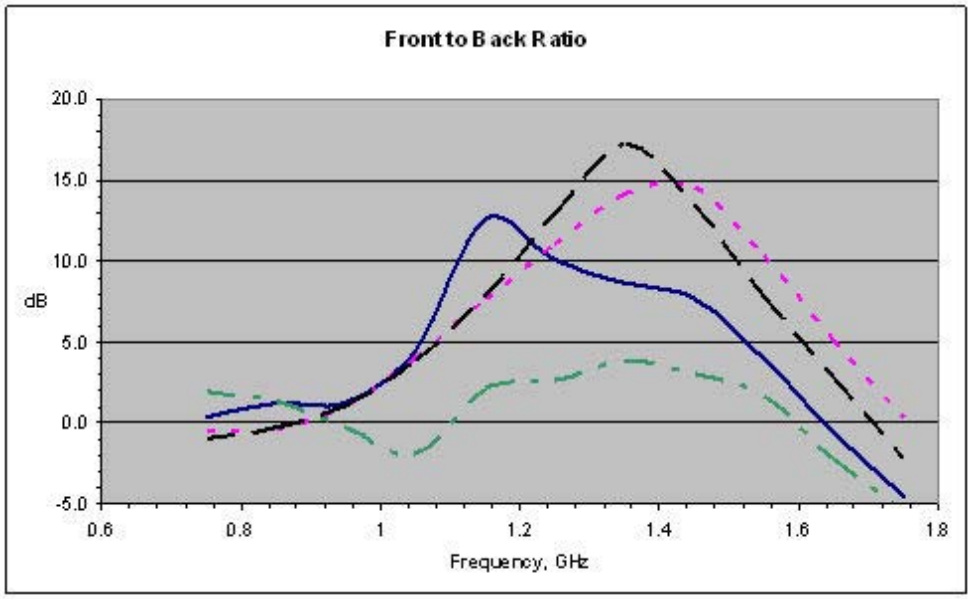

Figure 8. Computed front to back ratio is shown as a function of frequency. Dot dashed green line represents no reflector, solid blue line represents single reflector, Short dashed pink line represents two reflectors equally spaced, and dashed black line represents two reflectors just below the parallel portion of the 100-ohm transmission line.

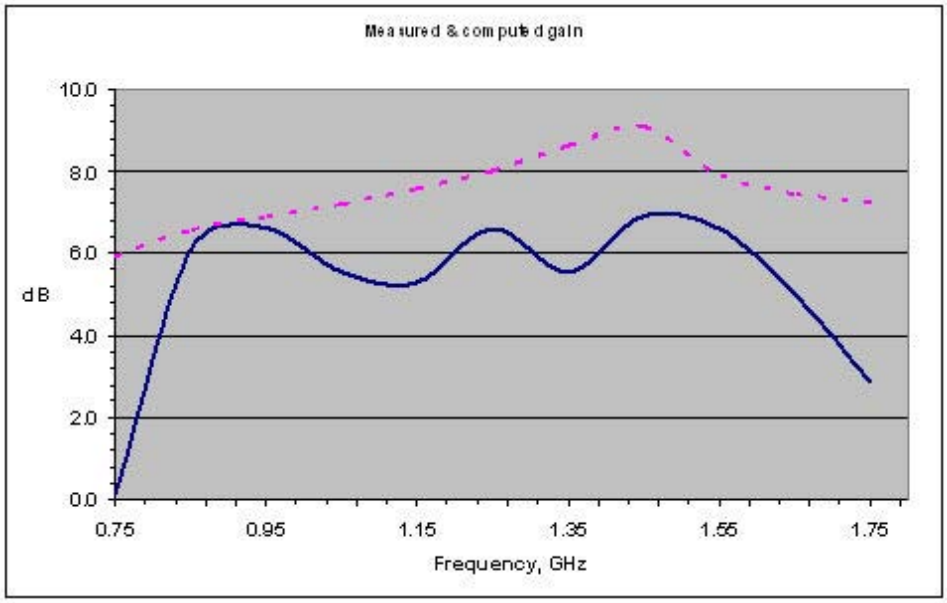

Figure 9. Computed realized gain curve, dashed line in pink and measured gain curve, blue in solid line. No reflectors are present.

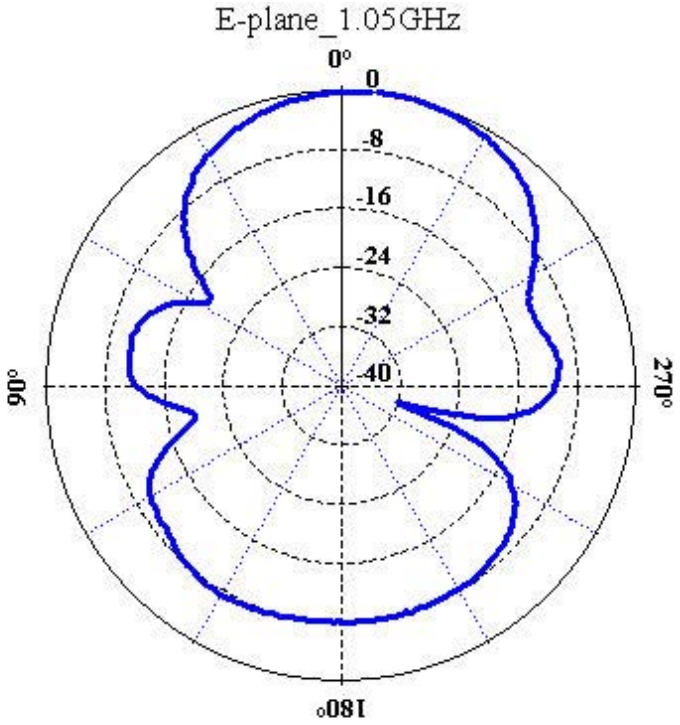

Figure 10. Measured E plane radiation pattern at 1.05 GHz.

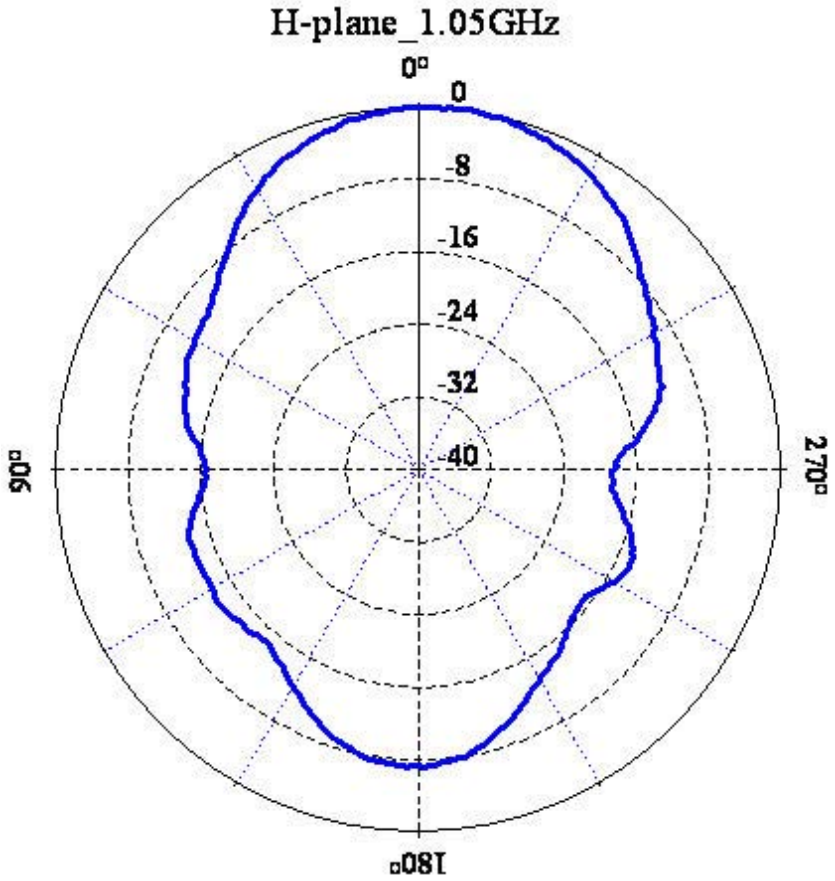

Figure 11. Measured H plane radiation pattern at 1.05 GHz.

5. References

[1] Waterhouse, R.B.; Novak, D.; Nirmalathas, A.; Lim, C.; "Broadband printed millimeter-wave antennas", IEEE Transactions on Antennas and Propagation, vol. 51, Issue 9, pp. 2492 – 2495, September 2003 Digital Object Identifier 10.1109/TAP.2003.816318

[2] Rowe, W.S.T.; Waterhouse, R.B.; "Theoretical investigation on the use of high permittivity materials in microstrip aperture stacked patch antennas", IEEE Transactions on Antennas and Propagation, Vol. 51, Issue 9, pp. 2484 - 2486 September 2003, Digital Object Identifier 10.1109/TAP.2003.816383

[3] Ghorbani, K.; Waterhouse, R.B.; “Dual polarized wide-band aperture stacked patch antennas”, IEEE Transactions on Antennas and Propagation, Vol. 52 Issue 8, pp. 2171 – 2175, August 2004, Digital Object , Identifier 10.1109/TAP.2004.832484

[4] Ghorbani, K.; Waterhouse, R.B.; **“**Ultrabroadband printed (UBP) antenna”, IEEE Transactions on Antennas and Propagation, Vol. 50Issue 12, pp. 1697 – 1705, December 2002, Digital Object Identifier 10.1109/TAP.2002.807423

[5] Kyungjin Oh; Bongjun Kim; Jaehoon Choi; **“**Design of dual and wide band aperture stacked antenna with double-sided notches,” IEEE 2004 International Symposium on Antennas and Propagation Society, Vol. 3, pp. 3091 – 3094, June 2004, Digital Object Identifier 10.1109/APS.2004.1332032

[6] Hong-Xing Zheng; Shi-Quan Zhang; “A new structure of broadband millimeter wave antenna”, IEEE 2004 International Symposium on Antennas and Propagation Society, Vol. 1, pp. 269 – 272, June 2004, Digital Object Identifier 10.1109/APS.2004.1329623

[7] F.E. Gardiol and J. F. Zurcher, “Broadband Patch Antennas – A SSFIP Update”, IEEE Antennas and Propagation Society Symposium Digest, Baltimore, MD, pp. 2-5, July 1996.

[8] J. F. Zurcher, “The SSFIP: “A Global concept for High Performance Broadband Planar Antennas”, Electron. Lett., vol. 24, pp 1433-1435, November 1988.

[9] F. Croq and A. Papiernik, “Wide-band Aperture Coupled Microstrip Antenna”, Electron Lett., vol., 26, pp. 1293-1294, August 1990.

[10] J. R. Sanford and A. Tengs, “A two Substrate dual polarized Aperture Coupled Patch”, IEEE Antennas and Propagation Symposium Digest, Baltimore, MD, pp. 1544-1547 July 1996.

[11] S. D. Targonski, R. B. Waterhouse, and D. M. Pozar, “Design of Wide-Band Aperture-Stacked Patch Microstrip Antennas”, IEEE Transactions on Antennas and propagation, Vol. 46, No. 9, September 1998.

[12] Rowe, W.S.T.; Waterhouse, R.B. “Integratable wide-band dual polarized antennas with rear field cancellation”, IEEE Transactions on Antennas and Propagation, Vol. 51, Issue 3, pp. 469 – 477, March 2003., Digital Object Identifier 10.1109/TAP.2003.809835

[13] Ansoft Corporation, www.ansoft.com

[14] Rogers Corporation Selector Guide, http://www.rogers-corp.com/mwu/prodsel.htm

[15] Won-Gyu Jang and Jae-Hoon Choi, “Design of a Wide and Multiband Aperture Stacked Patch Antenna with Reflector”, Microwave and Optical Technology Letters, vol. 49, No. 11, Nov. 2007.

RECONFIGURATION OF VIVALDI AND LOG PERIODIC ANTENNAS

P S Hall[1], M R Hamid[1], F Ghanem[1], A Mirkamali[2] and P Gardner[1]

[1]University of Birmingham, UK
p.s.hall@bham.ac.uk
[2]Zanjan University, Iran
ali_mirkamali@znu.ac.ir

1 INTRODUCTION

The increasing congestion of the radio frequency spectrum, by the addition of new bands and applications, has lead to growing interest in controlling antenna performance in the frequency domain. Whilst there has always been a need to achieve a certain bandwidth in a typical antenna requirement, and in some cases to achieve frequency agility, there are now increasing examples where band switching and the inclusion of stop bands are necessary. For example, many configurations have been developed to place a stop band at WLAN and Wi-Fi frequencies, between 5 and 6 GHz, in ultra wideband antennas, operating from 3 to 10 GHz, for short range high capacity communications systems, [1,2,3]. Mobile phone handsets are increasingly making use of the chassis as the radiating element, in which switched external matching circuits can be quickly reconfigured to meet the needs of multi-standard demands, [4,5,6]. The concept of cognitive radio takes multiple standard operation further by incorporating spectrum search functions into radios thus giving them the potential to select their own band of operation, with interference controlled by strict operating protocols, [7,8,9]. Thus frequency control and reconfiguration is an increasingly important theme in much current research on small antennas for personal communications. However to the authors knowledge there has been little published on the frequency reconfiguration of other very wideband antennas.

In this study two types of very wideband antennas have been examined, to assess their suitability for frequency reconfiguration. One, the Vivaldi, represents the class of frequency independent antennas, whilst the log periodic, as its name implies consists of many conventional antenna elements with size scaling. The two types demonstrate different approaches to frequency band control. In the first, it is necessary to introduce resonators whilst in the second switching of the radiating elements can be performed. The two methods of course imply that the control will be of a switched nature between well

defined bands of operation, although fine tuning can be achieved by devices such as varactor diodes. The underlying issues in both types, is the minimization of the number of control elements needed, and the resultant degree of control achieved. In the latter assessment it is appropriate to use filter terminology, such as pass band loss, roll off at band edge and out of band isolation.

2 RECONFIGURABLE VIVALDI ANTENNAS

2.1 Switched Gaps in Slot Edge

In a conventional tapered slot Vivaldi antenna, the wide band action arises due to progressive radiation along the slot, where radiation at high frequencies occurs closer to the slot throat and lower frequencies further from the throat and closer to the wider part of the slot. In this study we show how coupling resonators to gaps in the slot edge affects the radiation properties at frequencies corresponding to the position of the gap and resonator, whilst leaving other frequencies unaffected. In this way it is thus possible to 'switch off' parts of the band. Fig. 1 shows the proposed antenna structure, [10]. The Vivaldi without gaps and rings has a bandwidth of about 2 to 8 GHz. The edges of the tapered slot have eight ring slots, connected through gaps which can be open or short circuited. The single rings at the high and low frequency ends of the taper form high and low stop filters, and are used to give operation in the low and high parts of the band respectively. The central section has two coupled slots which form a band pass filter, which can be used to give operation in the middle part of the band. The tapered slot and the feeding line is located on Taconic TLY-5 substrate which has ε_r = 2.2 and tanδ = 0.0009. The substrate size is L = 70mm x W = 72mm x h = 0.787mm. The antenna length D = 60mm and the aperture size H = 40.6mm. The tapered slot consists of a circular slot stub with radius 2.3mm and an elliptical shape with horizontal and vertical radius = 20mm and 40mm respectively. The tapered slot is fed with a W_f = 2.75mm wide feed line terminated in a R_f = 5.1mm radius quarter circle. The ring slots each have an inner and outer radius of 3mm and 5mm respectively.

A wideband operation is achieved when all ring slots are disconnected from the tapered slot, by short circuiting the gaps in the slot edge, providing a smooth flow of current through the tapered profile. To provide a sub band operation around 7.4 GHz, the two uppermost gaps are open circuited, hence creating a low frequency stop band. On the other hand, when the two lowermost ring slots are connected to the tapered slot by open circuiting the gaps in the edge, a high frequency stop band is created, in this case giving a sub band operation around 2.5 GHz. A 5 GHz sub band operation is achieved by open circuiting the four rings in the middle of the tapered slot.

Metal bridges size 2mm x 2mm have been use as an approximation of the switching devices, in both the simulation and in the measured antennas. The presence of a metal bridge represents the ON state and absence the OFF state. We believe this approximation provide an acceptable demonstration of the basic switching concept. The size of these bridges has also been chosen to be similar to typical electronic switch size. In the final version the bridges will be replaced by real RF switching devices.

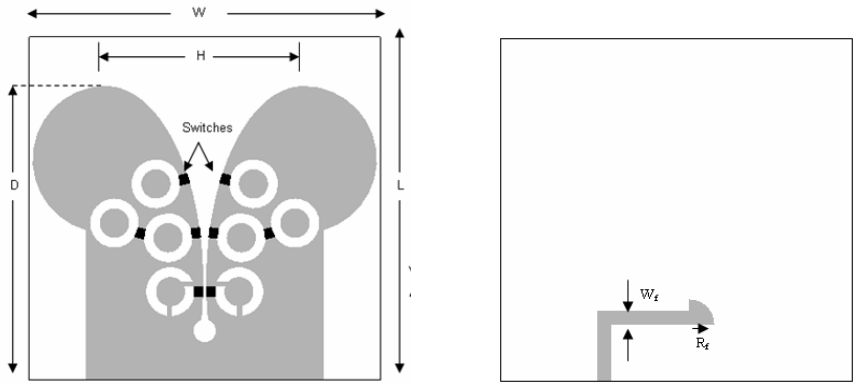

Fig 1 Vivaldi tapered slot antenna with switchable gaps in slot edge

Fig. 2 shows the measured return loss for the switchable slot tapered antenna. The return loss for wideband mode is less than 10dB over the 2.1 – 7.9GHz band. The return loss for the other three sub bands, around 2.5 GHz, 5 GHz and 7.4 GHz is less than 10dB. The measured gain is 4.94dBi at wideband mode (2.5 GHz), 4.46dBi at 2.5 GHz sub band mode, 3.39dBi at 5 GHz sub band mode and 3.72dBi at 7.4 GHz sub band mode. Out of band rejection in the 5 GHz sub-band case is worse than for the other sub-bands. Radiation patterns are in general well behaved, and there is a good agreement between the simulated and measured patterns.

A design methodology has also been developed by simulating the image parameters of each section of the tapered slot containing a ring slot. The attenuation - frequency plot derived gives a very good indication of the contribution of the ring to the overall antenna performance, and allows some optimising of the band positions. However interactions between the rings give rise to unwanted resonances that can be seen in the S_{11} results. It is also expected that if a longer tapered slot antenna were used, then more resonators could be incorporated, giving better control of the pass bands, or finer stepping of the pass bands up through the overall bandwidth. As the switched gaps are effectively in a large ground plane, then switch bias isolation can be provided by narrow slits in the ground plane. Work is currently underway to design and construct an electronically switched version of the antenna.

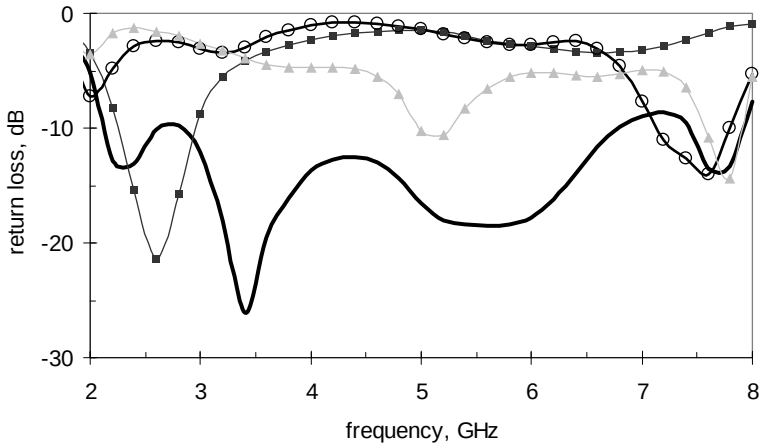

Fig. 2 Measured frequency response (S_{11}) of the switchable tapered slot antenna.
—— wideband, -■- 2.5GHz band, -▲- 5GHz band, -○- 7.4GHz band

2.2 Coupled Resonators

An alternative method of controlling the bandwidth of the Vivaldi antenna is with microstrip line resonators placed across the tapered slot, printed on the reverse side of the substrate. Fig 3 shows a configuration that demonstrates the potential of this approach. The Vivaldi antenna is the same as is described in section 2.1 and has an overall bandwidth of around 2 to 8 GHz. The L shaped microstrip resonator has dimensions of 10 mm x 17 mm and a width of 0.2 mm. A varactor diode is placed 7 mm from the top of the resonator and the capacitance is changed from 1 pF to 0.001 pF. The simulation results in Fig 4 shows the S_{11} achieved. It can be seen that a stop band is introduced whose centre frequency can be shifted from about 4.2 to 5.5 GHz. Below this frequency S_{11} is little affected, but above it there are changes, in particular in the upper frequency of operation. It will also be noted that the capacitance values necessary to give this stop band control are very small compared to the variation of typical PIN diodes, and may thus be difficult to realise in this technology. However, the study demonstrates that stop band control can be achieved using coupled resonators, with relatively high Q factors compared to those achieved using gaps and ring resonators in section 2.1. Parametric studies of similar resonators at the same location on the tapered slot indicate that by changing the varactor position and resonator shape and length, stop bands can be created over wider bandwidths than shown here. However in general the Q factor of the stop band reduces as the frequency is increased, presumably due to radiation losses in the resonator itself. Further work will include study of the position of the resonator along the tapered slot line and the

design of the bias circuit, although it is expected to be possible to realise simply with microstrip components.

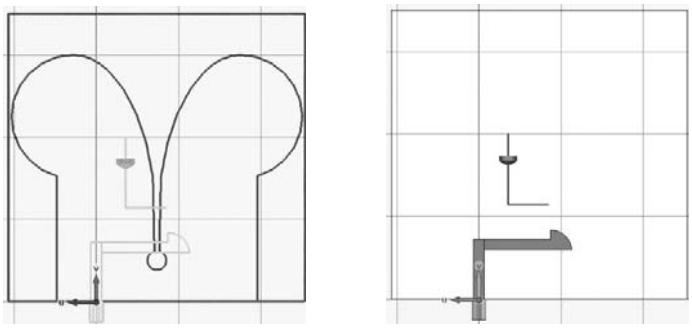

Fig 3 Varactor controlled resonator coupled to tapered slot in Vivaldi antenna(varactor is arrow shaped symbol on L shaped resonator)

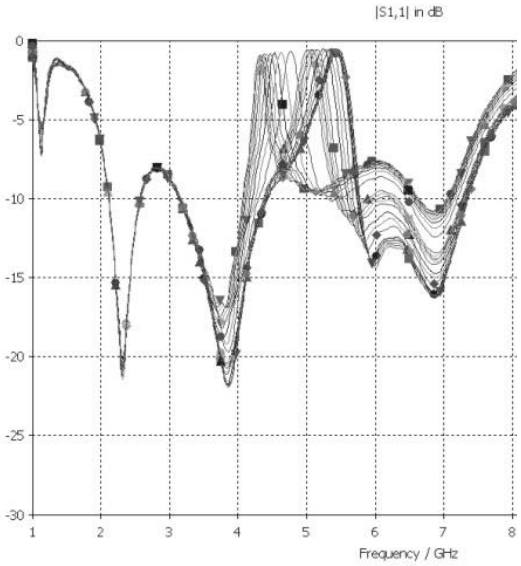

Fig 4 Simulated S_{11} of antenna of Fig 3
(contours are for various varactor capacitance in range 0.001 to 1 pF)

3 RECONFIGURABLE LOG PERIODIC ARRAYS

3.1 Dipole Array

Switches can be incorporated into a log periodic dipole array to reconfigure the band or bandwidth of operation, [11]. Fig 5 shows a schematic of a conventional

wideband printed log periodic dipole array which has been made reconfigurable by the inclusion of switches. One side of the transmission line and half of alternate dipoles are etched on the top side of the substrate and the rest on the under side. It is clear that the priority position for the switches is at the base of the dipoles. This then gives a transmission line that supports, in principle, an arbitrarily chosen set of dipoles. However, our simulations of such an array, in which we represent the switches with metal bridges as in section 2.1, indicate that this leads to rather poor control of the radiation pattern. This is primarily due to coupling to lower frequency dipoles beyond (or to the left in the figure) those switched on, both through the feed line and through radiation. In addition, when the high frequency dipoles are switched off to give low frequency operation, it is necessary to put harmonic traps in the low frequency dipoles to mismatch their higher harmonic resonances. These traps are shown on the 3 dipoles to the left in Fig 5 and consist of short lengths of open circuited two strip transmission line. We have also switched these traps off in the simulation and experiments, when required. The total number of switches for this 8 element array is 36. In a non-switched version of the array it is possible to feed with a coaxial cable at the high frequency end and attach the outer of the cable to the feed line to form a balun structure. In this case the switches in the feed line preclude this, and in our experimental arrays the coax was lead away from the substrate, in a plane perpendicular to the array plane. This was found to increase the radiated cross polarisation.

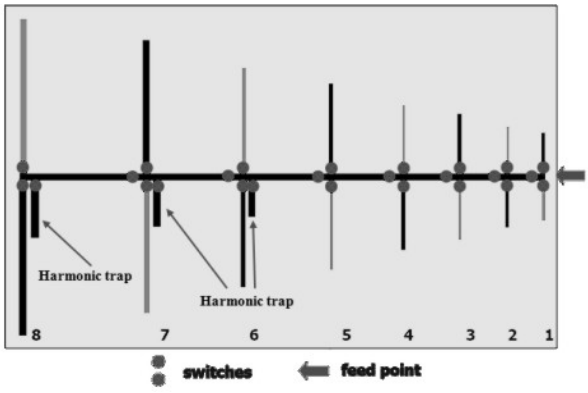

Fig. 5 Schematic of the wideband reconfigurable printed switched log periodic dipole array

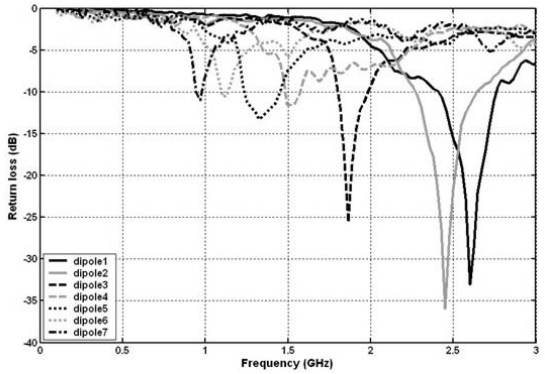

(a)

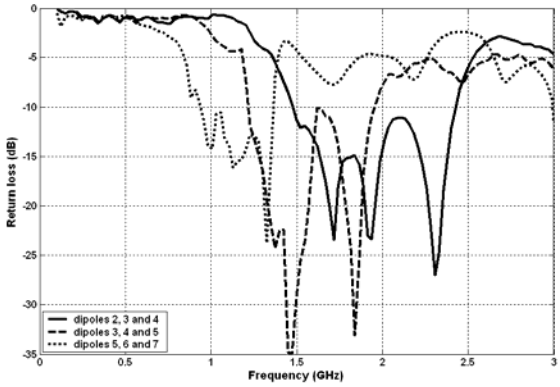

(b)

Fig. 6 Measured return loss of the reconfigurable LPDA
(a) when one of the dipoles is switched on, (b) when groups of 3 dipoles are switched on

Fig 6 shows the measured return loss of the reconfigurable log periodic dipole array in two configurations. Firstly, in Fig 6a, all switches are off except those of a single dipole, and the seven curves are for dipoles 1 through 7. Because the length to width ratio of the dipoles changes down the array, the change in bandwidth seen in the figure is expected. It can also be noted that the return loss at frequencies higher than the dipole resonance is less than at lower frequencies. In filter terms this means that the out of band rejection is relatively poor above the pass band. The same phenomenon can be seen in Fig 6b, where groups of 3 dipoles are switched on. When less dipoles are switched in than would normally be in the array active region, then the directivity reduces. When only 1 element is switched in the nominally omnidirectional pattern is distorted and the cross polarisation increased. There are significant challenges in the design of switched log periodic arrays, not the least being the bias circuit. We are currently designing the

PIN diode version of the array shown, and hope to show some results at the conference. However, our studies so far show the potential performance of such an array.

3.2 Microstrip Patch Array

The problems of biasing many switches in the dipole array suggest that it may be easier to apply switches to a microstrip based array. In particular a configuration in which one switch can control each radiating element would seem to be ideal. The configuration shown in Fig 7 and 8 has the potential to do this, [12]. It consists of a log periodic patch array, with an expansion factor of 1.02. Each patch is coupled to a feed line through a slot aperture in a ground plane, and this should allow a single switch to be placed at the centre of the aperture. The $50\,\Omega$ feed line and slot apertures are etched on a 0.787mm thick RT Duroid 5880 substrate with the dielectric constant of 2.2. The patches are printed on a similar 0.254mm thick substrate and spaced from the slots by a Rohacell foam with dielectric constants of 1.09 and thickness of 2mm. The patches are polarised at right angles to the array axis, in the same orientation as the conventional log periodic patch array, to allow simple feeding and spacing at half the feed line wavelength (with opposite offset in adjacent patches) to give a beam just off broadside. To get an analogous arrangement with aperture coupling the slots are oriented along the array length and the feed line must cross alternate slots from the opposite direction. The meandered feed results, as shown in Fig 7.

Fig 7 Reconfigurable microstrip patch log periodic array

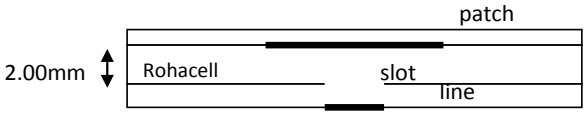

Fig 8 Cross section of reconfigurable microstrip patch log periodic array

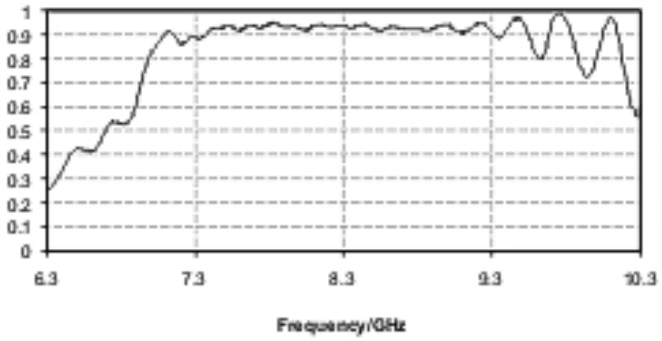

Fig 9 Simulated efficiency of non-switched log periodic patch array of Fig 7

Because it is usual to terminate the array in a matched load, we have found efficiency an easier measure of the reconfiguration of the array, where efficiency is defined as $1-|S_{11}|^2-|S_{21}|^2$. Fig 9 thus shows the simulated efficiency, in a scale of 0 to 1.0, of the array of Fig 7. It can be seen that it operates efficiently from around 7 to 9.5 GHz. Fig 10 shows the efficiency when groups of five switches are open circuit with all other switches short circuit, and the groups are the first five, second five, etc. Switches in the simulation are represented by metal bridges of size 1 x 1 mm, placed across the centre of the slots. Simulated radiation patterns are on the whole well formed and show reasonable similarity with those at the same frequency from the non-switched array.

Fig 10 shows that some degree of frequency reconfiguration can be achieved, with four bands clearly seen, corresponding to the switched on patch groups. There are, however, ripples in the various bands which are very pronounced at low frequencies. The high frequency band has fewer ripples, but the roll off at the band edge is less strong. There are some features of the design that might account for these issues. Additional simulations indicate that a switch across the slot aperture does not completely switch off the patch, but some leakage around the switch occurs. Thus there is some low level excitation of the patches not in the desired group. Also, we have made no attempt to suppress higher order modes in the patches, and this will also give rise to patch excitation outside the desired band. There is a change in the impedance seen by the feed line when the switch is short circuited and this might be responsible for some of the ripples seen in the desired band. In the switched and non switched versions there is radiation from the feed line, which is independent of the switch states. Measures have been taken to screen the feed line, with some improvements. A prototype has been fabricated and results will be reported.

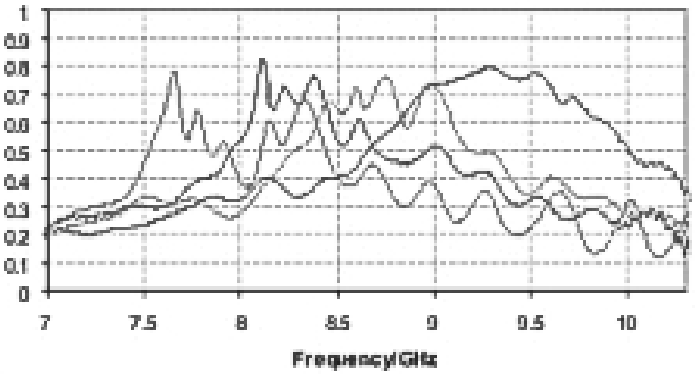

Fig 10 Simulated efficiency of switched log periodic patch array of Fig 7 (Different curves are for different groups of slots switched off, left hand peak - patches 1 to 5, next peak – patches 6-10, next peak – patches 11-15, right hand peak – patches 16-20)

4 CONCLUSIONS

Four different antennas configurations have been shown that allow reconfiguration of the band of operation. As the Vivaldi antenna has a continuous radiating structure, filtering elements are integrated with the structure, which, as expected, have relatively low quality factors. Examples are shown that change the wideband properties into narrower pass bands, located at various frequencies and that place narrow stop bands in the wide operating band. In the Vivaldi with gaps in the radiating edges coupled to ring slots, there are significant design difficulties due to the interactions between the rings. Nevertheless in the relatively simple example shown some degree of band switching is achieved. In the Vivaldi with a microstrip resonator coupled across the slot, narrow stop bands tunable across part of the band are demonstrated, with the prospect that additional resonators can extend the tuning band. One of the features of the log periodic arrays is the large number of control elements needed, and the search for simplifying configurations seems to be the primary challenge. In addition when parts of the array are switched out, the remaining parts do not necessarily operate in the same way, and caution is needed to achieve stable operation. In all types getting bias to the control elements is a challenge. Nevertheless, it is shown that reconfiguration of these antennas is possible and may result in antennas with system advantages.

5 REFERENCES

1. W. Hong, Y. Zhang, C. Yu, et al. “Compact Ultra-Wideband Antenna with Multiple Stop Bands,” in iWAT, 4-6 March 2008, pp. 32-34.

2. Makris I., Manteuffel D., Seager R.D., “Miniaturized reconfigurable UWB antennas for the integration into consumer electronic products,” in European Conference on Antennas and Propagation (EuCAP), 2007, pp. 1-6.
3. Ruvio G., Ammann M. J., Chen Z.N., “Wideband reconfigurable rolled planar monopole antenna,” IEEE Trans. Antennas and Propag., vol. 55, no. 6, pp. 1760-7, June 2007
4. Manteuffel D. and Arnold M., “Considerations for Reconfigurable Multi-Standard Antennas for Mobile Terminals,” in *iWAT,* Mar. 2008, pp. 231-4.
5. Kelly J. R., Hall P. S., Song P., “A Reconfigurable Wideband Handset Antenna Operating from 460MHz to 12GHz”, IEEE AP-S Int Symp on Antennas and Propagation, Charlston, USA, June 2009
6. Song, P, Hu, Z H, Kelly, J, Hall, P S and Gardner, P, “Wide Tunable Dual-Band Reconfigurable Antenna for Future Wireless Devices”, Loughborough Antenna and Propagation Conference, Loughborough, UK, 16-17 Nov 2009
7. Mitola J. III, "Cognitive radio for flexible mobile multimedia communications," IEEE Int. Workshop on Mobile Multimedia Communications, 15-17 Nov. 1999, pp. 3 – 10
8. Di Taranto, R; Nishimori, K; Popovski, P; Yomo,; Takatori, Y; Prasad, R; Kubota, S; “Simple Antenna Pattern Switching and Interference-Induced Multi-Hop Transmissions for Cognitive Radio Networks“, DySPAN 2007, 2nd IEEE International Symposium on New Frontiers in Dynamic Spectrum Access Networks, . 17-20 April 2007, pp 543 – 546
9. Hall, P S, Gardner, P, Kelly J, Ebrahimi, E, Hamid, M R, Ghanem, F Herraiz-Martinez, F J and Segovia-Vargas, D, “Reconfigurable Antennas Challenges for Future Radio Systems”, 3rd European Conference on Antennas and Propagation, EuCAP 09, Berlin, Germany, March 2009
10. Hamid, M R, Gardner, P and Hall, P S, “Switchable Wideband-Narrowband Tapered Slot Antenna”, Switchable Wideband-Narrowband Tapered Slot Antenna”, Loughborough Antenna and Propagation Conference, Loughborough, UK, 16-17 Nov 2009
11. Mirkamali, A. and Hall, P.S., ‘Log Periodic Printed Dipole Array for Wideband Frequency Reconfiguration’, Institution of Engineering and Technology Seminar on Wideband, Multiband Antennas and Arrays for Defence or Civil Applications, 13-13 March 2008, pp 95 – 110

12. Hamid, M R, Gardner, P and Hall, P S, “Reconfigurable Log Periodic Aperture Fed Microstrip Antenna”, Loughborough Antenna and Propagation Conference, Loughborough, UK, 16-17 Nov 2009

Utilizing Radiation Properties of Pattern Reconfigurable Antennas in Adaptive Arrays

T. L. Roach* and J. T. Bernhard
Electromagnetics Laboratory, Department of Electrical and Computer Engineering
University of Illinois at Urbana-Champaign, Urbana, IL 61801
http://antennas.ece.illinois.edu; e-mail: tlroach, jbernhar@illinois.edu

In an adaptive array setting, R.T. Compton Jr. and others demonstrated that pattern reconfigurable antennas can offer an added degree of freedom to mitigate the effects of grating nulls. This particular technique, which requires having antenna elements with specified beam tilts, seeks to maintain good output signal-to-interference-plus-noise ratio (SINR) when the array element spacing is relatively large. However, the methodology only specifies the requirements of an additional antenna element based on prior knowledge of the original array elements, which can lead to a limited possible solution space. Thus, this particular approach does not fully leverage the capabilities of the available pattern reconfigurability. The present work focuses on exploring ways to overcome this limitation by utilizing radiation reconfigurable antennas in an adaptive array setting not only in terms of their beam tilting capability but their null-forming ability as well. Incorporating pattern variability in this way supports more flexibility in adaptive array processing. Results of inclusion of pattern reconfigurability into an adopted optimization routine will be demonstrated.

1. Introduction

Pattern reconfigurable antennas, as discussed in [1] along with a variety of other reconfigurable antenna types, possess an added degree of freedom that may enhance or expand system performance. Prior investigations, (e.g., [2-6]) have begun to examine the capabilities of pattern reconfigurable antennas with beam tilts. However, questions still remain about the capabilities and limitation of these antennas in phased arrays. One particular system wherein the inclusion of pattern reconfigurable antennas offers the potential to increase functionality is adaptive arrays.

In general, an adaptive array antenna system controls its pattern in response to the signal environment [7]. Such systems look to automatically sense and suppress the presence of interference noise sources (friendly or hostile) while simultaneously enhance desired signal reception without prior knowledge of the signal/interference environment. In an array setting composed of relatively large spaced elements grating nulls—spurious nulls that degrade overall system performance—can occur. Larger elemental spacing could

prove beneficial, however, due to reduced mutual coupling effects between elements and hence increase the effectiveness of devices that are more sensitive to mutual coupling in an array setting.

The work presented by the authors in [8, 9] introduces a method to mitigate grating nulls in a linear array comprised of antenna elements. This particular technique, which requires having antenna elements with specified beam tilts (the fundamental capabilities of pattern reconfigurable antennas), seeks to maintain good output signal-to-interference-plus-noise ratio (SINR) when the array element spacing is relatively large. In a previous study, the authors in [10] investigated the functional benefits of utilizing radiation reconfigurable antennas with beam tilts adopting this methodology. The results demonstrate how performance potential increases with the inclusion of pattern variability. However, the methodology only specifies the requirements of an additional antenna element based on prior knowledge of the original array elements, which can lead to a limited possible solution space. Thus, this particular approach does not fully leverage the capabilities of the available pattern reconfigurability.

The present work focuses on exploring ways to overcome this limitation by utilizing radiation reconfigurable antennas in an adaptive array setting not only in terms of their beam tilting capability but their null-forming ability as well. Thus the task turns to integrating pattern variability directly into the algorithm. In this way the approach is more systematic by allowing the algorithm itself to determine the range of possible solutions. Furthermore, the methodology adopts a convex optimization routine developed by the authors in [11, 12], the flexibility of the routine offers the means toward applying the integration process. Ultimately, the findings will specify what requirements are necessary in the element design for pattern reconfigurable antennas to have an impact in adaptive arrays.

This paper proceeds as follows. Section 2 first brings to light the concept of null reconfigurability and illustrates the concept's potential use for radiation reconfigurable antennas in an adaptive array framework. Next, Section 3 discusses the process on pattern variability into an optimization routine. Graphical results are displayed for different case scenarios. Finally Section 5 contains the conclusion.

2. Null Reconfigurability

This section exemplifies the potential use for radiation reconfigurable in an alternative way—once again, in an adaptive array setting with a simple illustrative example. Recall, the overall objective of the research aims to specify the requirements for the element design which can have an impact in improving adaptive array performance. The forthcoming sections present ongoing steps toward achieving this goal.

2.1 Overview and methodology

Thus far the implementation of pattern reconfigurable antennas has focused on tilting the maximum of the mainbeam in a specified direction, i.e., the beam tilts [10]. True this characteristic of the antenna element's pattern is of great importance to the functionality of the system. However, just as important may be the null (or depression) the pattern reconfigurable antenna can offer in a specified direction apart from the pattern's maximum. Thus, the notion of pattern variability very well includes all the distinct features within the antenna element capabilities.

To illustrate some of the advantages, consider a scenario which showcases an adaptive array composed of isotropic elements (such benchmark elements are commonly used in the literature [7]) and an array composed of pattern reconfigurable antennas. The reconfigurable antennas have a specified maximum and null point. To simplify the analysis, model these elements using a tilted dipole element of the cosine variety. The elements are then represented by

$$f_j(\theta) = cos(\theta - \theta_{n\,j}), \tag{1}$$

where the main beam maximum resides at $\theta_{n\,j}$ with $\theta_{n\,j} = 0^{\circ}$ corresponding to broadside and a pair of nulls residing at $\theta_{n\,j} \pm 90°$.

The basic constituents of the analysis involve evaluating the adaptive array specific parameters in a "static" state utilizing the general adaptive array concepts presented by Compton in [7]. Comparisons between results are made for the isotropic array and the model RCFG array for three different cases. In each case, the constants consist of the arrays having $N = 5$ elements spaced $d = 1\lambda_0$ apart, a strong interference environment (interference-to-noise ratio (INR) equal to 40 dB), and the signal-to-interference ratio (SNR) equal to 0 dB. Also, in the reconfigurable antenna array, all element beam tilts, $\theta_{n\,j}$, are identical (i.e., all the elements tilt their main beam maximum and null in the same direction according to just θ_n). The varying parameters in each case include the signal environment (θ_d and θ_i) and the pattern reconfigurable antenna beam/null tilting parameter, θ_n. Lastly, the SINR (dB), voltage pattern (dB), and element weight profile (magnitude and phase) plots are illustrated for each case in the next subsection.

2.2 Case study results

Table 1 outlines the exemplifying parameters involved with the two different case scenarios. In *Case 1* the beam tilts are not directed toward the desired signal ($\theta_d \neq \theta_n$) and the interferences signal falls into the null of the model reconfigurable antenna (RCFG) pattern ($\theta_i = \theta_n - 90°$). In *Case 2* the interference signal falls into the grating null (GN) and into the null of the element patterns ($\theta_i = \theta_{GN}$ and $\theta_n = \theta_{GN} + 90°$).

Table 1. Listing of the signal environment parameters and direction of the beam tilts in for the model pattern reconfigurable element. Note, the element null lies at θ_n - 90°.

Case #	θ_d (°)	θ_n (°)	θ_i (°)	θ_{GN} (°)
1	**20**	45	-45	**-41**
2	45	**73**	**-17**	-17

Figures 1 and 2 depict the results of the different case studies listed in Table 1. In each case the first column of plots represents the SINR vs. θ_i, and the radiation pattern vs. θ, respectively, using isotropic elements. Similarly, the second column presents the same but utilizing the model RCFG elements. The third column details a magnitude and phase weight profile computed by the adaptive array algorithm, e.g., least mean square (LMS), for both types of antenna elements.

Utilizing both antenna element types, the results for Case 1 (Figure 2) display their differences in a few ways. The adaptive algorithm adjusts the weights to place a null in the pattern at θ = -45° and steers the overall pattern main beam to θ = 20°, the incoming direction of the desired signal. However, the individual beam tilts of the reconfigurable antenna elements are not directed toward the desired signal. The effect amounts to less than a dB of loss in maximum SINR of the RCFG plot versus the isotropic plot, essentially a scan loss effect from the beam tilt directions. Due to the null in the element factor, the RCFG array depicts an overall pattern with lower sidelobe levels compared to the isotropic array results. Unlike the isotropic array, having the interferer fall into the null of the element pattern allows for a uniform amplitude distribution and progressive phase profile in the weights—a results predicated upon being able to direct the null of the elements in the direction of the interferer.

In Case 2 (Figure 2) considers the situation when the interference signal falls into the grating null (θ_{GN} at θ_i = -17°). No doubt an undesirable result, as illustrated by the isotropic array pattern and weight plots. Since the interference signal falls into the grating null, the pattern suffers mightily, overall values are less than -30 dB. The source of the problem lies in the magnitude of the weights which are effectively zero for each element. The adaptive algorithm in conjunction with the isotropic elements has no way of dealing with the interference signal coming from this direction, thus it resorts to basically shutting down the array by zeroing out the weights.

One way to deal with the problem lies within the notion of configuring the null of the reconfigurable antenna's pattern along the same direction of the grating null (i.e., θ_n = θ_{GN} + 90° = 73°). Doing this allows grating null alleviation in the SINR plot, main beam steering along the desired signal direction, and desirable weight profile—a uniform

amplitude and a progressive phase distribution. With such a weight profile, complexities in hardware may be reduced and the potential for increased system efficiency.

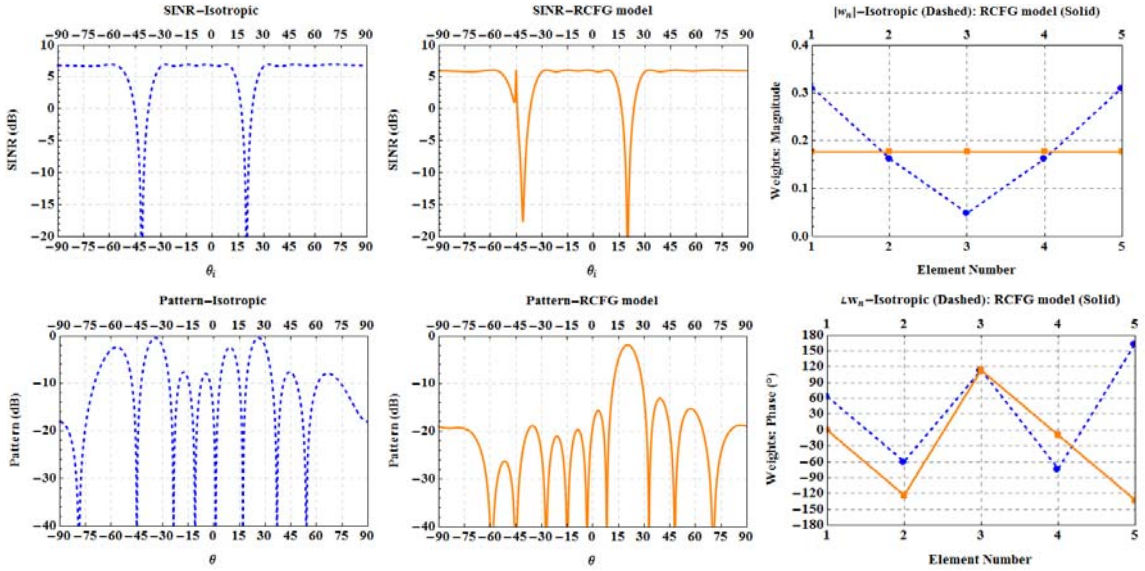

Figure 1. Adaptive array results (SINR, pattern, and weight profile) comparing an array composed of isotropic elements (dashed curves) to an array of model pattern reconfigurable elements (solid curves). The parameters of operation are indicated for Case 1 in Table 1.

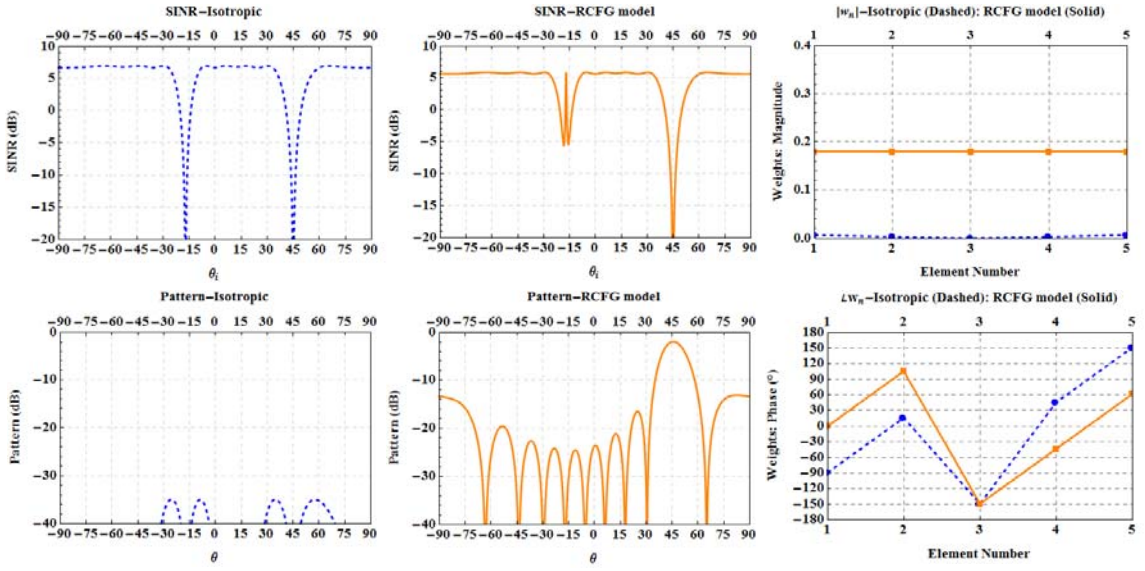

Figure 2. Adaptive array results (SINR, pattern, and weight profile) comparing an array composed of isotropic elements (dashed curves) to an array of model pattern reconfigurable elements (solid curves). The parameters of operation are indicated for Case 2 in Table 1.

Previously the work in [10] centered on using pattern variability in conjunction with elements that can reconfigure their main beam to a prescribed spatial direction. This study evaluated pattern variability in term of null reconfiguration which, as seen in Case 2, provides an alternative way for grating null mitigation. Overall, the work gives insight into the potential null reconfigurability has to offer when used in an adaptive array setting. True the dipole model symbolizes an ideal element but it represents a starting point and provides direction to what requirements of practical radiation reconfigurable antennas are necessary to elevate performance.

3. Pattern Variability Integration

In continuing with the notion of exploring methods which intend to fully leverage the capabilities of the available reconfigurability, this section investigates a method which integrates pattern variability into the algorithm. This method presents a more systematic approach in which the algorithm itself then determines the range of possible solutions. The section will first highlight the salient points behind the adopted routine and then discuss the framework behind incorporating the reconfigurable antenna (RCFG) element into the routine. Next, graphical results are displayed for a couple example scenarios.

3.1 Description of the optimization routine

The authors in [11, 12] present a method of finding the optimum sidelobe-minimizing weights for an arbitrary linear array that holds for any scan direction, beamwidth, set of pattern nulls, and type of antenna element used. The array problem is presented in convex form (i.e., a convex optimization problem with various constraints), which is rapidly solvable in a straight forward manner and whose solutions are guaranteed to be globally optimum [11]. Apart from these attributes, the interest of the routine lies in its flexibility in terms of constraint allowance on the array weights. The work focuses incorporates pattern variability into the optimization process utilizing this degree of freedom.

The very basic constituents of the routine include the following (see the work in [11, 12] for specific details describing the methodology). Consider the output of the total radiation pattern of an *N*-element linear array conveyed as a function of the element weights ($\vec{w}$) and spatial angle θ. The relationship can be expressed in the standard relations, i.e.,

$$T(\vec{w},\theta) = \sum_{n=1}^{N} w_n f_n(\theta) \exp[j\frac{2\pi}{\lambda_0} d_n \cos\theta], \tag{2}$$

where $f_n(\theta)$ is the each element's radiation pattern, d_n is the linear distance of each element from the reference location, and λ_0 is the free space wavelength at the operational frequency. Note in this case the array geometry is set up such that broadside is at $\theta = 90^\circ$

The task of finding the optimum sidelobe-minimizing weights is a solution to the optimization problem given by

$$\min_{\vec{w} \in C^N} \left\{ \max_{\theta \in \Theta} \left| T(\vec{w}, \theta) \right| \right\}$$
$$\text{subject to} \left\{ \begin{array}{c} T(\vec{w}, \theta_d) = 1 \\ \dfrac{d}{d\theta} \mathrm{Re}\{T(\vec{w}, \theta_d)\} = 0 \\ T(\vec{w}, \theta_i) = 0, \;\; i = 1, 2, ..., K \end{array} \right\}. \tag{3}$$

In (3) the objective function is the sidelobe level (SLL) which is to be minimized subject to the listed constraints and Θ represents the region outside the mainbeam which is to be suppressed (e.g., the sidelobes). Furthermore, the constraints at θ_d impose the normalized radiation pattern be equal to unity and that the magnitude of the total radiation pattern is maximum. Also, C^N is the set of all N-element vectors with complex components and K is the number of specified nulls at an angle θ_i. The simplicity in the process comes into play when the authors in [11] write the array pattern in terms of its real and imaginary parts and thus pose the problem in convex form. As a result, the constraints can be written as a matrix set of linear equalities and inequalities. In this form, the *fminimax* function in MATLAB® offers one of many ways to solve the problem.

3.2 Reconfigurable model integration

With an effective convex optimization routine at hand in terms of operation, the task now turns to implementing model reconfigurable antennas into the procedure—thereby allowing the optimization process to select the best solution for the scenario at hand. The results will then give insight into the necessary requirements for the element design. Since the routine sets forth the weight vector $\vec{w}$ as the variable of interest (its real and imaginary parts), the method of interest pertains to modeling each individual pattern RCFG element as a subarray of isotropic elements within the full N-element array. Figure 3 details a graphic of the array geometry including the 2-element subarrays which will representative each individual pattern RCFG element.

Depending upon its geometry, each individual subarray can carry its own unique pattern in terms of the location of its main beam maximum and null location(s). In reference to Figure 3, d_{sub} represents the distance between each subarray element and d_{Main} represents the distance between each subarray (i.e., RCFG element). In this work, d_{sub} is identical for all subarrays. Also, all N antennas are attached to its own complex weight, w_n.

In addition to the constraints imposed on the element weights via the optimization routine, as indicated in (3), the current methodology looks to impose two additional linear constraints on the weights. They exist as:

- The pair of weights representing each subarray are complex conjugates of each other, i.e., $w_{n+1} = w_n^*$, for n = 1,3,5,…,N-1 (i.e., odd numbered elements)
- In conjunction with the above, a constraint on the spatial location of the allowable main beam maximum (beam tilt angle) for each subarray. The region of constraint permits individual beam tilts to fall within ± 30° of broadside, $\theta = 90°$.

Again the flexibility of the routine allows such constraints to be imposed. The first constraint forces identical weight magnitudes on the elements within each subarray; this may prove useful when associating the subarray model to the RCFG element. The second constraint stems from limitations in a practical pattern reconfigurable antenna's beam steering range. Thus, the three types of weight constraints exist as: (1) No additional constrains, (2) complex conjugate constrains, and (3) complex conjugate with beam steering constraints. The constrains will be labeled Case 1, Case 2, and Case 3, respectively, for notational simplicity in reference to the results presented in Section 4.3.

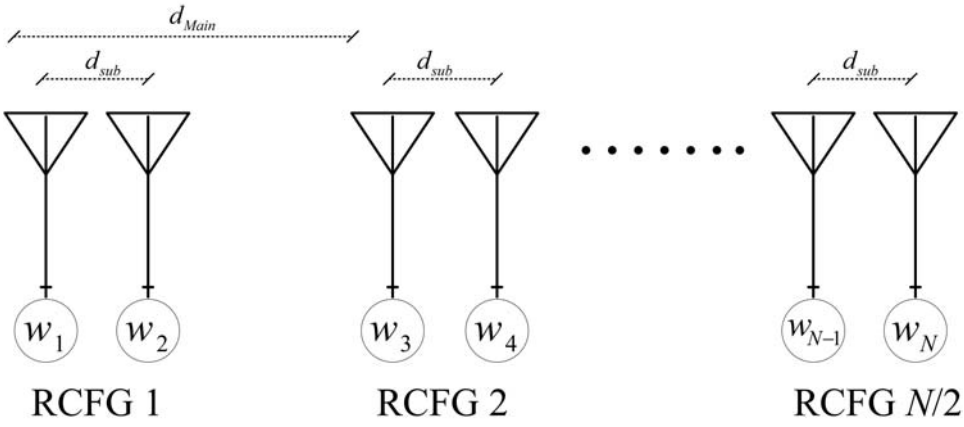

Figure 3. Graphic entailing the array geometry utilized in the optimization routine. The array consists of $N/2$ subarrays (spaced d_{Main} apart), each models a pattern RCFG element and contains two isotropic elements, spaced d_{sub} apart.

After the routine returns the weights, the idea is to analyze the resulting patterns for each subarray and link it to the patterns of the RCFG element, it is here where insight can be gained into what type or range of patterns the reconfigurable antenna needs to uphold the performance offered by optimization routine. Note, the adaptive array concept still applies here because the goal of placing a maximum along the desired signal direction and placing a null along the interference direction does not change—effectively enhancing the SINR.

3.3 Results

This section will graphically detail the results pertaining to a couple example cases utilizing the aforementioned optimization routine subject to the three different weight

constraints discussed in section 3.2. In each scenario, N = 10 (thus 5 RCFG elements), d_{sub} = 0.5λ_0, and d_{Main} = 1.0λ_0. Also, three clustered interference signals at θ_i = {120°, 122°, and 124°} impinge on the array and the null-to-null beamwidth is set to 30°. Figure 4 and Table 2 presents details applied to a scenario when θ_d = 90° (broadside) and Figure 5 and Table 3 illustrates when θ_d = 45°.

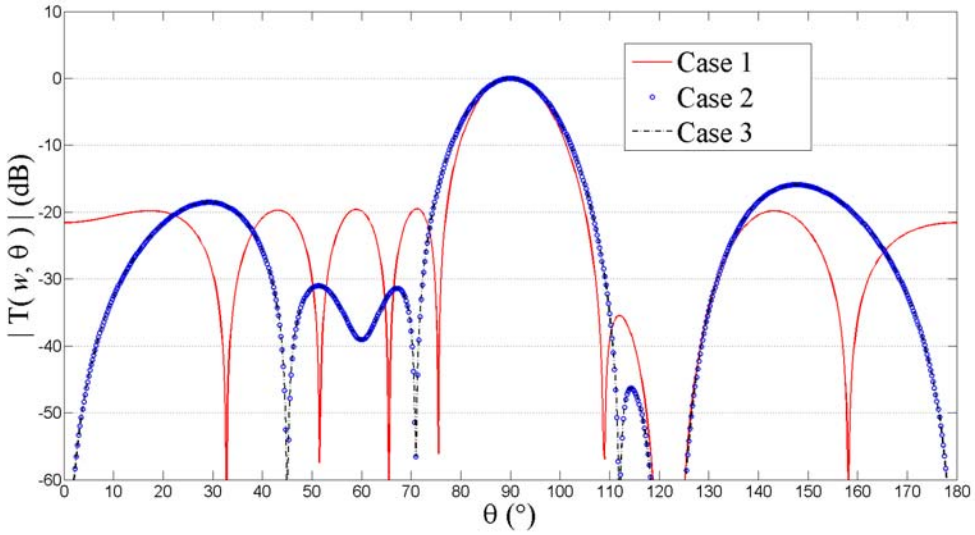

Figure 4. Magnitude of the radiation pattern vs. θ for a 5-element model RCFG array spaced 1.0λ_0 apart; θ_d = 90° and θ_i = {120°, 122°, and 124°}. In concert with the optimization routine, Case 1: no additional weight constraints, Case 2: subarray weight complex conjugate constraints, Case 3: complex conjugate constraints and subarray beam tilts constraints.

In Figure 4, all plots handle the single environment well, i.e., the routine places a pattern maximum along the desired signal direction and nulls out the interferers along the direction specified. Compared to the constrained cases, Case 1 does a better job in establishing the required beamwidth and slightly lower SLL overall. The discrepancies between the cases stem from the additional constraints, namely the magnitude and phases of the weights. Such constraints can make it more difficult for the optimization routine to meet all of the desired pattern characteristics. Table 2 lists the calculated beam tilt, dictated by $\theta_{substeer}$, for each subarray. Overall for each case, the individual beam tilts center around 90°, an expected result due to the desired signal's angle of arrival. As a final note, the amplitude dynamic ratio (ratio of max-to-min $|w_n|$), for Cases 1-3 exist as 2.79, 4.25, and 4.25, respectively.

Table 2. Listing of the resultant beam tilt angles for each RCFG element (subarray) in the calculated radiation pattern showcased in Figure 4.

Subarray	**1**	**2**	**3**	**4**	**5**
$\theta_{substeer}$ (°) ***Case 1***	76	89.7	92.0	89.7	75.9
$\theta_{substeer}$ (°) ***Case 2***	86	89.7	92.2	89.7	86.1
$\theta_{substeer}$ (°) ***Case 3***	86	89.7	92.2	89.7	86.1

When the desired signal arrives from 45°, the routine handles the problem somewhat different compared to the previous broadside scenario. Figure 5 showcases the results, again for each case. The routine meets the requirements of having the mainbeam equal to 0 dB and nulls along the interference for each case. However, the constrained cases suffer in overall pattern performance compared to the unconstrained case. In Case 1, the main beam maximum at θ_d represents the overall pattern maximum. Such is not the result in Cases 2 and 3, in fact instances occur when the routine pushes the pattern above the 0 dB mark. A result predicated upon, again the additional weight constraints and the initial formulation of the optimization problem. Since the routines desires to steer the overall mainbeam toward θ_d, elemental phasing comes into play, unfortunately the constraints make it more difficult to achieve progressive phasing toward the desired signal direction.

Analogous to Table 2, Table 3 lists the beamtilt results for each subarray in this particular scenario. Note in Case 1, the values are not exactly centered on θ_d = 45° and the beam tilts vary much more across the model RCFG elements than before. Also, the beamsteer constraint visibly comes into play in Case 3 with the values being restricted to within ±30° of broadside (between 60° and 90°), another determining factor in Case 3's difficulties since the desired signal arrives from outside this region. In addition, the amplitude dynamic ratio, for Cases 1-3 exist as 10, 11, and 6.5, respectively—a larger set of values due to the steering and nulling requirements.

In all, this section has presented a couple example scenarios pertaining to different constraint types when implementing pattern variability (via the subarray model) in the chosen optimization routine and in effect let the routine pick the best possible range of beam tilts. As the results in Figures 4 and 5 illustrate, the overall pattern performance can vary depending on the signal environment in conjunction with the weight constraints. Consistency remained in terms of the meeting the mainbeam and nulling requirement. The overall pattern performance, on the other hand, can be looked at as an added bonus from an adaptive array point of view with the SINR counting the most.

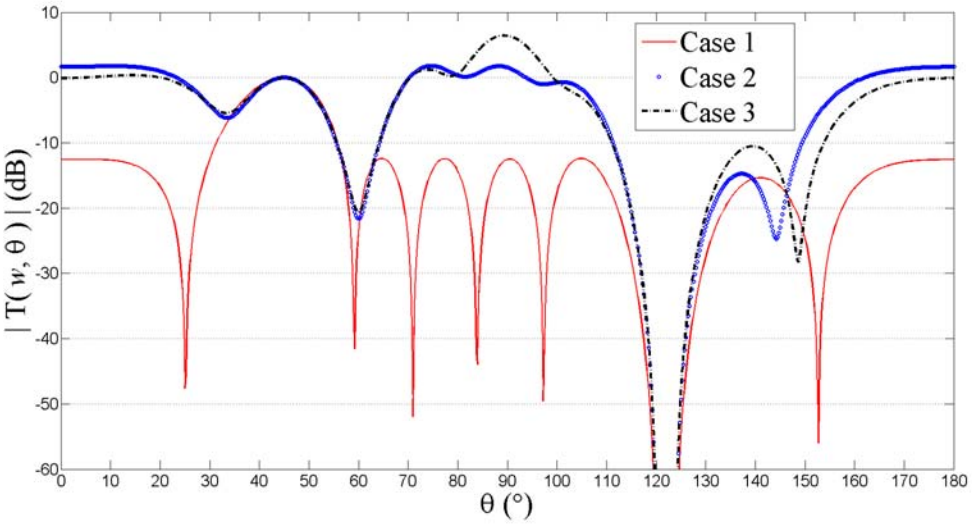

Figure 5. Magnitude of the radiation pattern vs. θ for a 5-element model RCFG array spaced $1.0\lambda_0$ apart; θ_d = 45° and θ_i = {120°, 122°, and 124°}. In concert with the optimization routine, Case 1: no additional weight constraints, Case 2: subarray weight complex conjugate constraints, Case 3: complex conjugate constraints and subarray beam tilts constraints.

Table 4. Listing of the resultant beam tilt angles for each RCFG element (subarray) in the calculated radiation pattern showcased in Figure 5.

Subarray	**1**	**2**	**3**	**4**	**5**
$\theta_{substeer}$ (°) ***Case 1***	57	56	49	56	57
$\theta_{substeer}$ (°) ***Case 2***	71	70	118	129	51
$\theta_{substeer}$ (°) ***Case 3***	73	75	95	60	60

4 Conclusion

In summary, this work has continued to explore the functional benefits of utilizing radiation reconfigurable antennas in an adaptive array setting. The potential impact of these antenna types relies not only in their beam tilting capability but their null-forming ability as well. Section 2 demonstrated another utility of pattern reconfigurability, those with null-forming capabilities. Steering the null of the elements along the direction of the interferer provides an alternative way for grating null mitigation, resulting in potential reduced hardware requirements. Section 3 investigated integrating pattern reconfigurable

elements into an optimization routine to fully leverage the capabilities of the available reconfigurability. Utilizing the subarray model to represent the antenna elements provided insight to what patterns are necessary from the returned weight values—essentially allowing the means to synthesize the reconfigurable element's pattern. With this acquired knowledge the capability exists to take away some of the complexity out of the necessary element weights and hardware requirements and apply it to the reconfigurable element.

At this point in the research many directions for future work present themselves. These include going forward with transitioning the patterns provided by employing the subarray model to the design aspects of the pattern reconfigurable element, specifying specifically the makeup of the element's radiation pattern. Also, investigate other variations of the subarray model within the confines of the optimization routine (e.g., using more than two-elements or non-isotropic elements), and variations that include the null-forming capabilities of the model which can be integrated into the routine as well. The results could prove useful in ultimately determining the requirement for the element design and validate the impact these antennas have in adaptive arrays.

5 Acknowledgments

This work is sponsored in part by the Vodafone-Illinois Graduate Fellowship, a GEM Fellowship, and the IMGIP Graduate Fellowship Program of Illinois. The author would like to thank fellow cohort Michael P Daly for his insight into this topic.

6 References

1. J.T. Bernhard, *Reconfigurable Antennas*, Morgan and Claypool Publishers, 2007.

2. J. -C. Chiao, S.-Y. Cheng, J. J. L. Chang, I. M. Chio, Y. Kang, and J. Hayasaka, "MEMS reconfigurable antennas," *Int. J. of RF and Microwave Computer-Aided Eng.*, vol. 11, pp. 301 – 309, September 2001.

3. K. Hietpas, G. H. Huff, and J. T. Bernhard, "Investigation of phased array beamsteering using reconfigurable antennas," in *Proc. IASTED Int. Conf. on Antennas, Radar, and Wave Propagation*, July 2004, pp. 41 – 44.

4. S. Zhang, G. H. Huff, J. Feng, and J. T. Bernhard., "A pattern reconfigurable microstrip parasitic array," *IEEE Trans. Antennas Propagat*., vol. 52, pp. 2773-2776, Oct. 2004.

5. S. Zhang, G. H. Huff, G. Cung, and J. T. Bernhard (2005), Three variations of a pattern-reconfigurable microstrip parasitic array, *Microwave Opt. Technol. Lett.*, vol. 45, pp. 369 – 372, June 2005.

6. G. H. Huff and J. T. Bernhard., "Integration of packaged RF MEMS switches with radiation pattern reconfigurable square spiral microstrip antennas," *IEEE Trans. Antennas Propagat*., vol. 54, pp. 464-469, February 2006.

7. R. T. Compton, Jr., *Adaptive Arrays – Concepts and Performance*, Englewood Cliffs, NJ: Prentice-Hall, 1988.

8. R. T. Compton, Jr., "A method of choosing element patterns in an adaptive arrays," *IEEE Trans. Antennas Propagat*., vol. 30, pp. 489-493, May 1982.

9. A. Ishide, and R. T. Compton, Jr., "On grating nulls in adaptive arrays," *IEEE Trans. Antennas Propagat*., vol. 28, pp. 467-475, July 1980.

10. T. L. Roach and J. T. Bernhard, "Antenna element pattern reconfigurability in adaptive arrays," in *Proc. 2008 Antenna App. Symp.*, Monticello, IL, 2008, pp. 86-103.

11. P.J. Bevelacqua and C. A. Balanis, "Minimum sidelobe levels for linear arrays," *IEEE Trans. Antennas Propagat*., vol. 55, pp. 3442-3449, December 2007.

12. P.J. Bevelacqua, "The utility of convex optimization for weight selection in arrays," in *Proc. IEEE AP-S Int. Symp.*, June 2009, pp. 1-4.